ROYAL MELBOURNE INSTITUTE OF TECHNOLOGY

TECHNISCHE HOCHSCHULE INGOLSTADT

DOCTORAL THESIS

Postprocessing and Simulation Methods for Additively Manufactured Continuous Fibre Reinforced Plastics

---

Michael HANDWERKER

M. Eng. (Technische Hochschule Ingolstadt)

B. Eng. (Technische Hochschule Ingolstadt)

A thesis submitted in fulfillment of the requirements for the degree of Doctor of Philosophy

School of Engineering

College of Science, Technology, Engineering and Maths

RMIT University

August 2022

Declaration of Authorship

I, Michael Handwerker, certify that except where due acknowledgement has been made, this research is that of the author alone; the content of this research submission is the result of work which has been carried out since the official commencement date of the approved research program; any editorial work, paid or unpaid, carried out by a third party is acknowledged; and, ethics procedures and guidelines have been followed.

In addition, I certify that this submission contains no material previously submitted for award of any qualification at any other university or institution, unless approved for a joint-award with another institution, and acknowledge that no part of this work will, in the future, be used in a submission in my name, for any other qualification in any university or other tertiary institution without the prior approval of the University, and where applicable, any partner institution responsible for the joint-award of this degree.

I acknowledge that copyright of any published works contained within this thesis resides with the copyright holder(s) of those works.

I give permission for the digital version of my research submission to be made available on the web, via the University's digital research repository, unless permission has been granted by the University to restrict access for a period of time

Michael Handwerker

Ingolstadt, 03.08.2022

“A goal without a plan is just a wish.”

Antoine de Saint-Exupéry

Acknowledgements

This doctoral thesis was created as part of a cooperation between RMIT University in Australia and Technische Hochschule Ingolstadt in Germany. I am very grateful to both universities to have been selected for this program. While working on the thesis I was employed as a project engineer in Prof. Jörg Wellnitz's engineering firm. For this I am also very grateful as it provided financial support and allowed me to get a lot of practical experience.

I would like to thank my supervisors, Prof. Dr.-Ing. Prof. h.c. Jörg Wellnitz and Dr.-Ing. Hormoz Marzbani without whom this thesis would not have been possible. It was an honour to work with you.

The vast treasure of Prof. Jörg Wellnitz's experience is astonishing to me to this day and I was fortunate enough, that he shared it with me. Since his research interest cover many different fields (lightweight design, aerospace engineering, hydrogen power trains,…) I would call him the Swiss army knife of professors. In our technical discussions he was always able to steer me in the right direction. During my times of doubt, he motivated me to keep going.

Dr.-Ing. Hormoz Marzbani provided valuable advice throughout my thesis. He is a self-made man whose research career is truly impressive and inspirational to me. His positive attitude and shared experiences kept motivated through tough times. He always had an open ear for me and took the time to guide me. Without his guidance and support this thesis would not have been possible.

Professor Dr. Ulrich Tetzlaff is a researcher by heart and supported my work from the very beginning. While his main research focus lies with metals, he also has in-depth knowledge about composite materials. Our discussions in the laboratory gave me valuable insight and often a notch in the right direction.

Professor Dr. Martin Bednarz came to the university shortly before I started with my thesis and was responsible for the purchase of the 3D printer used in this thesis. He supported me from the start and always had an open ear for me. Due to his experience in additive manufacturing, he provided me with a lot of valuable advice.

Professor Dr. Jörg Bienert, who is an acoustic and vibrations expert, supported my vibration analysis and was kind enough to include me in several industrial projects. This gave me an interesting insight into this field and I learned a lot from him.

Very helpful advice was also given during the milestone presentations. I appreciate the valuable tips and feedback that I received from all the panel members. But in particular I would like to thank Prof. Dr. Reza Nakhaie Jazar who showed great interest in my work and was a panel member in all milestone reviews.

Furthermore, I would like to acknowledge my fellow PhD students for their help and stimulating discussions. Namely, Dr. Georges Lemos for his help with the XRD measurements, Simon Keim for his help with the REM microscopy and Albin Gottwalt for his help with the nanoindentation measurements. Also, I would like to thank Sebastian Kuba and Fabian Wein from “Schanzer Racing” for their help with the analysis and failure calculations of the universities race car.

I would also like to thank the laboratory technicians Stefan Saumer, Christian Biber, Thomas Flieger, Markus Bauch, Karl Kirmaier and Josef Haas for their support of my experiments. And of course, I am thankful to the Technische Hochschule Ingolstadt for allowing me to use the laboratories and machines. I would also like to thank the administrative staff at both universities, in particular Astrid Moser (THI) and Nabila Hamed (RMIT).

A big thank you goes to several researchers in my field who shared their advice with me on different topics: Prof. Dr. Christoph Strobl, Prof. Dr. Shuguang Li, Dr. Elena Sitnikova, Dr. Lei Wan, Dr. Stephanie Bruckmeier, Ross Mclendon, Prof. Dr. Josef Mair, Peter Schwarz and Dr. Michael Okereke. While I am very thankful to all my teachers who made me who I am today, I would like especially thank Andreas Eichner. He encouraged me to follow the path that I am on today. I also would like to thank my friends and former colleagues Christoph Storr, Thomas Bigus and Florian Klein for giving me the opportunity to work with them during my studies.

Lastly, I would like to thank my family for their support throughout this journey. Without them this thesis would not have been possible. My parents, Brigitte and Thomas supported me with love, time and money throughout my Bachelor, Master and now PhD studies; my brother Thomas, who is currently acquiring his Master’s degree. Our regular talks kept me motivated when the going got rough and he provided me with good advice in difficult situations. My grandparents, Rosamunde, Karin and Günter who shared their valuable life lessons with me. Their love and moral support helped me hold my head up high in difficult times.

Table of Contents

List of Figures

List of Tables

List of Abbreviations

DSC	Differential scanning calorimetry
ILSS	Interlaminar shear strength
IR	Infrared
PA 6	Polyamide 6
SEM	Scanning electron microscopy
TGA	Thermogravimetric analysis
UTS	Ultimate tensile strength
XRD	X-Ray diffraction

List of Symbols

A	Cross-sectional area	mm²
β	Friction angle	°
C	Elasticity	GPa
E	Young's modulus	GPa
Δ	Separation of the cohesive layer	µm
l	length of the unit cell	µm
m	mass	kg
G	Fracture energy rate	J/m²
H	Melting enthalpy	J
K	Degree of Crystallinity Compliance of the cohesive layer Ratio of yield stress in triaxial tension/compression	- GPa/m -
φ	Fibre volume content	-
p	Equivalent pressure stress Inclination parameter for Puck's failure criterion	MPa -
q	Mises equivalent stress	MPa
r	Third invariant of the deviatoric stress	MPa
ρ	Density	kg/m³
ε	Strain	-
σ	Stress	MPa
u	Displacement	µm
R	Fracture strength	MPa
θ	Diffraction angle of the XRD analysis and angle of the action plane	°
τ	Shear stress	MPa
T	Interface strength	MPa
θ_{fp}	Angle of the fracture plane	°
RF	Reaction force of the reference node	N
V	Total volume of the unit cell	µm³

v	Poisson’s ratio	-

Dedicated to all my teachers.

Abstract

A new technology based on fused filament fabrication that allows the manufacturing of continuous fibre reinforced composites has been developed in the recent years. Fibres are being embedded in a plastic that is molten and laid out on two-dimensional layers. These layers are stacked on top of each other, thereby creating a three-dimensional part. However, alignment of the polymer chains during the extrusion causes an insufficient bonding between the layers. Furthermore, the printing process causes a high air-void ratio. These effects lead to a reduced strength and stiffness.

To address these drawbacks, this study investigated the influence of a thermal treatment process on the mechanical performance of continuous and chopped fibre reinforced polyamide 6 in the build-up direction. A correlation between the annealing temperature and the mechanical performance was found. The Young's modulus increased by a factor of three, while the ultimate tensile strength (UTS) increased by 186% for the continuous glass fibre reinforced material. A temperature dependent transition from the gamma to the alpha phase was observed while the crystallinity only slightly changed. For the continuous fibre reinforcement an increase in the air-void ratio was observed.

Based on these findings, the influence of a post pressure treatment process on the mechanical performance in build-up direction and perpendicular to fibre direction within the layer was investigated to address the high air-void ratio. Annealing at a pressure of 1 MPa was found to homogenize the material and led to a significant increase of both the tensile strength (55 MPa) and Young's modulus (5 GPa). Increasing the pressure to 3 MPa only slightly increased the mechanical performance, whereas a further increase to 6 MPa caused no significant changes. While at 1 MPa the air-voids are significantly decreased within the part, 3 MPa were required to decrease the air-void ratio close to the fibre bends.

In order to evaluate potential use-cases it is important to understand the materials failure behaviour. Simple failure theories used for homogenous materials, like the von Mises failure criterion, are not able to predict the failure of composite materials. Due to the vastly different properties of the fibres and the matrix the failure process is more complex. To investigate the

failure behaviour of the postprocessed material a micromechanical model was developed. Based on sophisticated models for the constituents a unit cell was used for virtual testing. It was found that, despite the low fibre volume content, Puck's failure criterion was applicable. Consequently, the it was used to simulate the materials potential uses in the front spoiler of the university's student race car.

Chapter 1

Introduction

In recent years design and manufacturing of lightweight structures have gained more importance. Especially in the aviation and automotive industry the requirement for lower emissions and greater range has led to the development of new technologies for the manufacturing of lightweight materials. Looking back in history, steel was replaced by aluminium which is now getting competition from composite materials [1]. The most noted representative of such composite materials are fibre reinforced plastics. The performance of these non-isotropic materials mostly depends on fibre orientation, fibre content, the type of plastic/fibre used and the manufacturing process [2]. Most used composite materials in the aviation industry are carbon fibres with a thermosetting polymer matrix. These high-performance composites are manufactured by stacking epoxy infused layers of unidirectional fibre mats (prepregs) on top of a mould and then curing it by applying pressure and high temperatures [1]. While the mechanical performance of parts produced this way is very good, they are very expensive to manufacture due to the complex mould shapes that are required. Thermosetting composite plastics have limited options of recycling because of the strong bonds between the polymer chains. One of the most common options is pyrolysis where the matrix material is thermally decomposed in an inert atmosphere and just the embedded fibres are reused. This way the matrix material is completely lost. Or the composite material is grinded into little pieces which are then used for short-fibre reinforced parts. Thermoplastic composites on the other hand can be separated using a dissolution process and all materials can be reused with only a minor reduction in stiffness. Also, thermoplastics could be recycled by thermoforming them into different parts, which is also not possible with thermosetting plastics [3] [4].

A new method for producing fibre reinforced plastics is the use of fused deposition modelling (FDM) sometimes also referred to as fused filament fabrication (FFF). In this process a thermoplastic filament is molten, extruded through a nozzle and deposited on the growing work. The required composite materials are created by adding continuous fibres to the filament. This manufacturing process gives engineers a lot of design flexibility and allows to produce optimized high-performance parts with complex geometries without requiring moulds or autoclaves. As a result, this process is a step towards the “print-it-all” fabrication process, since poor mechanical performance has been limiting the areas of application for 3D printed plastic materials [5]. Of course, issues like the high production time, the high costs and slow certification processes still need to be addressed before additive manufacturing can be used in large volume productions [6].

Due to the nature of the printing process unlike conventional fibre reinforced plastics the resulting material is not transverse isotropic. The adhesion between layers is not as good as the adhesion between individual strings forming a layer. One hypothesis suspects the cause in the alignment of polymer chains in flow direction during the printing process [7]. Other sources suspect the heat transfer from the fibres to prevent heat from the nozzle reaching the underlying layer as well as an uneven or slightly offset printing bed [8]. While the exact cause is still under debate, it is experimentally proven the matrix strength and stiffness in build-up direction is worse than that of perpendicular direction [8]. A well-known issue of the additive manufacturing process are residual stresses that are a result of the rapid heating and cooling cycles of the plastic [9]. Also, the interlaminar shear strength is very low compared to other fibre reinforced plastics [10]. More detailed information is provided in Chapter 2. The purpose of this thesis is to address these issues by applying a postprocessing treatment to the additively manufactured parts.

Furthermore, it is important to understand the materials failure behaviour in order to be able to use it efficiently. Inaccuracies in the methods used in a design process result in premature failure risk. This risk is usually taken care off by multiplying the actual load with a safety factor and designing the part in a way that it can handle those exaggerated loads. This way the costs of comprehensive testes are avoided, but the final product will be heavier and more expensive regarding the material costs. When it comes to lightweight design, the goal is to reduce the safety factor to a minimum. To do that the methods and theories used in the

design process must be very accurate. Especially when parts are responsible for human safety. Compared to isotropic materials, composite materials require much more sophisticated failure theories. In some works, the Hashin's failure criterion was applied to predict the failure of the additively manufactured composite [11] [12]. However, the authors did not provide sufficient evidence, that the failure criterion is applicable. Furthermore, it was shown in the "World Wide Failure Exercises" that Hashin's criterion is not as accurate as for example Puck's failure theory [13] [14] [15]. To pave the way for practical use of this material it was investigated how the material failure can be modelled on a macroscopic scale.

1.1 Methodology

After an extensive literature review an in-depth study of the annealing process was carried out to determine the effects of different annealing times and temperatures. Samples were annealed in a mineral oil bath to prevent oxidization and make use of the buoyancy effect, which helped to retain the shape of the samples at higher temperatures. Since the poor layer adhesion does affect the build-up direction most, focus was put on the changes in the tensile strength and Young's modulus of chopped and continuous fibre reinforced parts in that direction. Multiple analysis procedures, like for instance X-ray diffraction (XRD) and optical microscopy, were used to measure the changes in the materials (crystalline) structure.

Since the annealing study revealed an increase in air-voids, the influence of a pressure treatment process was investigated in a next step. In that study the temperatures and exposure times were fixed and different pressure levels were applied. While the previous study showed that paraffine oil is a suitable annealing medium, the simultaneous application of pressure was deemed too dangerous in the context of a university project. A failure of the container containing hot oil at high pressures would be a very serious health hazard. Consequently, a mould press was chosen for this study. The mould prevented the diffluence of the high viscosity polyamide and was expected to create an environment similar to that in an autoclave. To achieve a high practical relevance, pressure levels were chosen which can be achieved by commonly used autoclaves.

Based on the findings of the post-processing study the failure under combined loads was studied. To determine the applicability of failure theories for conventional composite materials the failure behaviour of the material was investigated using the finite element method. Based on sophisticated models for the constituents, a unit cell was used to determine the materials failure under combined loads. The obtained results were then transferred to a macroscopic failure criterion which was applied to the universities race car to evaluate potential use cases.

1.2 Research questions

To summarize, the following research questions will be studied in this thesis:

1. What temperatures and exposure times are required to make continuous fibre reinforced parts produced by fused filament fabrication transverse isotropic and improve their mechanical performance?
2. Which pressure levels are required to reduce the air-void ratio?
3. Which combined load cases lead to an inter-fibre-failure of postprocessed fibre reinforced plastics produced by fused filament fabrication?
4. What failure modes occurs in postprocessed fibre reinforced plastics produced by fused filament fabrication under combined loads?
5. How can the failure of the post-processed material be modelled on a macroscopic scale?

1.3 Thesis Outline

The chapters in this thesis are based on the research questions. In Chapter 2 a detailed overview of existing research that was published prior to the start of this thesis is presented. This will provide a detailed insight behind the methodology and motivation of this research project. Studies only relevant to particular research questions are included in the corresponding chapters.

Chapter 3 contains the results and discussion of the annealing study. In Chapter 4 the second research question is investigated and therefore contains the experimental setup and results of the pressure treatment process. Chapter 5 explains the micromechanical model in detail

and discusses the results of the failure stresses and failure modes under combined loads. In Chapter 6 the findings are summarized and future research recommendations are given.

Chapter 2

State of Research

Before undertaking any research project, it is important to determine the state of research. Because as Frank Westheimer once said: “A couple of months in the laboratory can frequently save a couple of hours in the library.” In this chapter a short comparison of existing printers will be given. Furthermore, the material properties of the additively manufactured continuous fibre reinforced composites are reviewed along with applicable testing standards. Furthermore, proposed optimization techniques that allow for tailored fibre placement are briefly discussed. These findings were published as a review Paper in the Journal “Progress in Additive Manufacturing” [16]. Studies that are particularly relevant for the undertaken research or were published during this thesis will be discussed in detail in the subsequent chapters.

2.1 Commercial printers

There are two basic working principals in processing continuous fibres using the FDM process. The continuous fibre used for reinforcement is either already present in the filament or fed into the nozzle separately. A summary of currently available FDM printers with the ability to process continuous fibre reinforcements is shown in Table 1. Markforged was the first company to sell an FDM printer capable of processing continuous fibre reinforcements in 2014 with a second generation released in 2016. The main restrictions of these two printers

are the closed source software which dictates the fibre path and the fact that only the manufacturers filament can be processed [17]. The Anisoprint Composer A3 and A4, which were released in early 2020 are almost the opposite. They mix the filament and fibres in the printing head and allow any materials to be used. Their software also allows adjustment of the fibre path and nozzle temperature [18]. This makes the Anisoprint composer perfect for research purposes since the influence of many factors could be investigated. Judging by the available information, the major difference between the Desktop Metal printer and the Markforged printer is the matrix material. Markforged uses polyamide and an unspecified amorphous plastic, whereas the Desktop Metal printers can process polyether ether ketone (PEEK) and polyetherketoneketone (PEKK) which both are plastics that can be used at higher temperatures than conventional plastics [19]. For manufacturing bigger structures, the CEAD CFAM Prime is currently the only option [20]. Since the Markforged printers were released to the market almost six years ago, most of the cited studies in this work used these printers.

Table 1: Commercial FDM printers that can process continuous fibre reinforcement

Company	Markforged [17]	Anisoprint [18]	CEAD [20]	Desktop Metal [19]
Printer	Mark One/Two	Composer A4/A3	CFAM Prime	Fibre series
Software type	Closed source	Open source	Closed source	Closed source
Build volume [mm³]	320 x 132 x 154	297 x 210 x 140 420 x 297 x 210	2000 x 4000 x 1500	310 x 240 x 270
Fibre material	Carbon, Glass and Aramid	Open material system	Carbon and Glass	Carbon and Glass
Working Principle	Impregnated filament	Mixer Head	Mixer Head	Impregnated filament
Available since	2014/2016	Early 2020	2018	Early 2020

2.2 Mechanical performance

It is important to state the testing direction when discussing the mechanical performance of composite materials. The system shown in Figure 1 is used for the present study. “X1” refers to the fibre direction, “X2” is perpendicular to the fibres and parallel to the printing bed and “X3” is perpendicular to both the fibres and the printing bed.

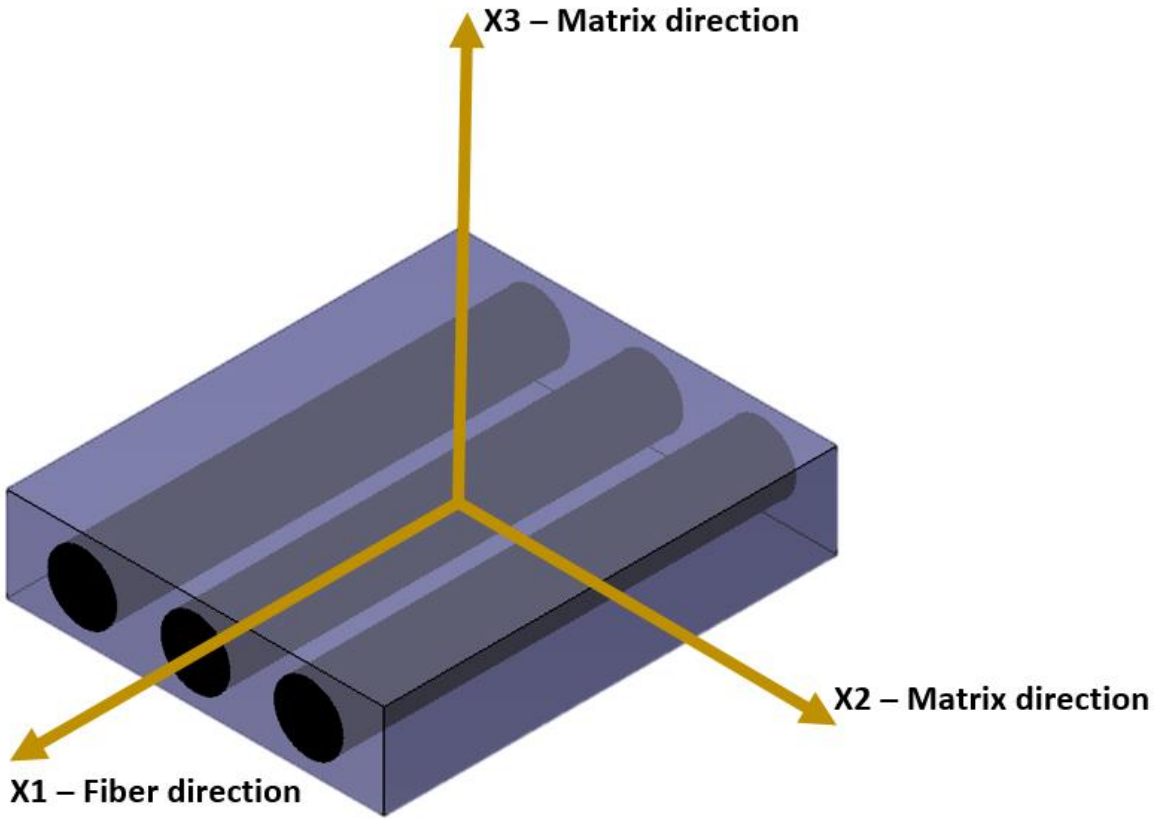

Figure 1: Coordinate system for fibre reinforced parts

An important property for composite materials is the shear strength. It can be distinguished between intra- and interlaminar shear strength with continuous fibre reinforced plastics. The former refers to shear stresses within one layer and thus affects the fibres, matrix as well as the fibre matrix bond. The latter refers to shear stresses between layers, which leads to delamination and is often abbreviated as “ILSS” [21] [22].

When conducting fatigue tests is important to take the testing frequency into consideration. Tests on long fibre reinforced plastics have shown that the fatigue strength decreases when increasing the testing frequency. This behaviour was attributed to hysteretic heat as well as the low thermal conductivity of thermoplastics [23]. Furthermore, it was found that creeping relaxes local stress accumulations and therefore has an influence on the durability [24]. Experiments conducted with thermosetting short glass-fibre reinforced composites have shown that many factors, like the manufacturing parameters, testing conditions and materials

have an influence on the predicted lifetime, so it is important to state these conditions, when publishing test results [25]. Table 2 contains a summary of mechanical test methods, the information that can be obtained as well as corresponding standards.

Table 2: Summary of test methods, their resulting information as well as applicable test standards

Method	Resulting Information	Standards
Tension, Compression	Stress-strain behaviour, Yield strength, ultimate strength, Young's Modulus	ASTM D3039 [26] ASTM D6641 [27] ASTM D3410 [28] ASTM D6484 [29] ASTM D5766 [30] ASTM D6742 [31] ASTM 6264 [32] ISO 527-4 [33] ISO 12817 [34] ISO 14126 [35] ISO 11566 [36]
Shear	Shear-stress-strain behaviour, shear modulus, shear strength	ASTM D5379 [37] ASTM D2344 [38] ASTM D3518 [39] ASTM 5467 [40] ASTM D4255 [41] ASTM D3846 [42] ISO 14130 [43] ISO 14129 [44] ISO 15310 [45]
Flexural	Flexural stress-strain behaviour, flexural modulus, flexural strength	ASTM D7264 [46] ASTM D6272 [47] ASTM D6415 [48] ISO 14125 [49]
Fatigue	Fatigue behaviour	ASTM D3479 [50]

As mentioned in the previous section, Markforged was one of the first companies to release a 3D printer that can process continuous fibre filament. This is the reason why their printers are used in most of the published research projects to date. Unless otherwise stated, the mechanical properties refer to parts manufactured by Markforged printers. In the following sections, the mechanical properties of Kevlar, glass and carbon fibre reinforced additively manufactured composites are presented. In section 2.5 the findings are summarised and discussed.

2.2.1 Kevlar fibre

2.2.1.1 Tensile and Flexural testing

The tensile strength and Youngs's Modulus of Kevlar reinforced parts were determined by Melenka et al. according to ASTM D638-14 [51]. The work compared samples with varying number of reinforced rings. A maximum ultimate tensile strength (UTS) of 80 MPa was determined with two layers being reinforced by five rings each. Because the start of the fibre path was in a high stress area, the determined values do not represent the full potential of the material and the authors recommend not to place the starting point of the fibre in the load path. Through optical microscopy a waviness in the Kevlar yarns was observed which is suspected to be caused by a lack of tension on the fibres during the printing process. These effects are both shown in Figure 2. Once the load is applied the fibres straighten which explains the observed non-linear stress-strain behaviour. Besides the acknowledged flaw of the starting point of the fibre being in the load path the applied standard is not intended for reinforced plastics.

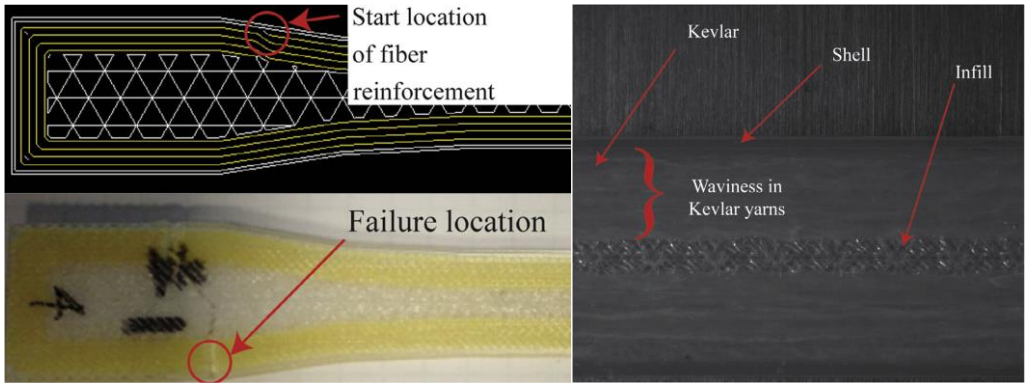

Figure 2: Location of the point of failure (left) and waviness of the Kevlar fibres (right) [51]

A similar test setup was used by Dickson et al. applying the ASTM D3039 standard for tensile tests [52]. With eight out of 32 layers reinforced a UTS of 164 MPa and a Young's Modulus of 6.7 GPa was measured. To avoid the start and end point of the fibre within the load path, the fibre ends were laid beyond the tabbing points. After the test, barely any residue of the matrix material could be found when examining the Kevlar fibres, which is an indicator of a weak bond between the matrix material and the fibre. The flexural strength and modulus with eight out of 32 layers being reinforced was 125,8 MPa and 6.65 GPa.

Adabi et al. found the main failure in tensile tests to be fibre tensile damage which showed as an almost lateral failure of the test piece [12]. With twelve out of 25 layers being reinforced in load direction an average UTS of 150 MPa and a Young's modulus of 8.7 GPa was determined.

2.2.1.2 Impact behaviour

V-notch test pieces and plates were used for Charpy testing and shot with a gas gun by Scrocco et al. to determine the impact behaviour of continuous Kevlar reinforced FDM parts [53]. Two reinforced layers perpendicular to the notch in a test piece (comp. Figure 3 left) designed according to ASTM E23 [54] resulted in an impact energy of 11.38 J. When the reinforced layers were parallel to the notch no significant strength increase was found (comp. Figure 3 right). Additionally, six-millimetre-thick plates were shot with spherical bearings at velocities between 208 m/s and 255 m/s with varying reinforcement. The projectiles managed to penetrate 2 mm of the Kevlar reinforcement at 208 m/s and the plate was very close to stopping the projectile traveling at 255 m/s.

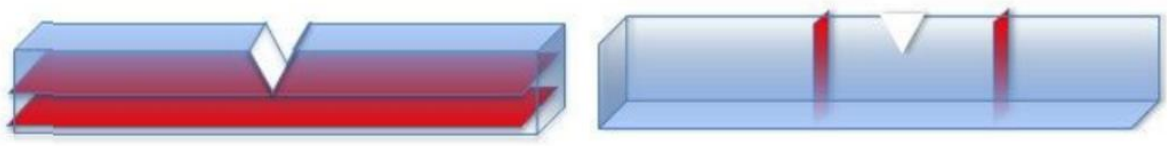

Figure 3: Notched test samples used for testing the impact behaviour of Kevlar reinforcements (shown in red) [53]

2.2.2 Glass fibre

2.2.2.1 Tensile and flexural testing

Dickson et al. determined the UTS of continuous glass fibre reinforced test specimens depending on the fibre volume ratio [52]. It was observed that more fibre reinforcement does

not lead to a proportional increase in UTS. This was suspected to be caused by air inclusions that got bigger and more frequently occurred as more fibres were used. 30 out of 32 layers reinforced resulted in an ultimate tensile strength of 444 MPa which exceeds the strength of Aluminium 6061-T6.

An average UTS of 450 MPa and Young's modulus of 7 GPa was determined by Goh et al. according to ASTM D3039 [55]. During tensile testing the specimens showed a sudden drop in tensile stress followed by slight rise before the sudden failure of the test piece, which is suspected to be caused by local fibre failure. Tensile and shear rupture were the failure modes causing fibre breakage. Fibre pull-out also was observed but was found to be insignificant compared to the fibre breakage. Delamination and de-bonding at the layer interfaces were observed, which indicates a weak bonding between adjacent layers. The fibre volume fraction of 35 % was determined by burning of the matrix.

Justo et al. determined an average UTS of 701 MPa and a Young's modulus of 68 GPa according to ASTM D3039 by extracting test pieces from a plate (comp. Figure 4) [56]. This was done to get homogenous fibre distribution within the test samples. The failure was reported to occur simultaneously in both the centre and close to the tabs. The number of reinforced layers is not stated and microscopic analysis revealed almost no waviness in the fibre paths but air gaps within the composite were observed.

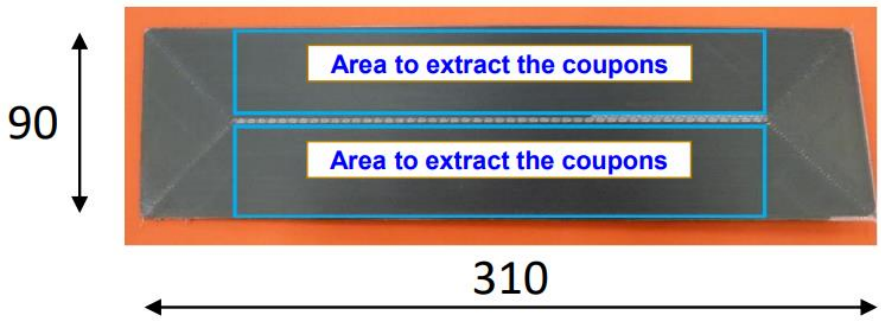

Figure 4: Extraction zones of the fibre reinforced plate [56].

An average flexural strength of 149 MPa and flexural modulus of 15 GPa was determined by Goh et al. according to ASTM D790 [55]. Testing showed that the flexural strength gradually decreased after reaching a 1 % strain. This is because individual localized buckling occurred in the compression layers due to the poor bonding of the layers which resulted in sequential failure of individual layers. Goh et al. suspects printing parameters used to manufacture the

samples to be the cause of this behaviour and similar results were obtained by Dickson et al. [52].

2.2.2.2 Shear testing

Samples with a +/- 45° pattern were used by Justo et al. who determined the shear strength according to ASTM D3518 to be 67 MPa and the shear modulus to be 0.88 GPa [56]. The stress-strain graph revealed two phases (comp. Figure 5). A convex phase that is caused by the fibres aligning themselves in load direction (scissor effect) followed by a concave phase that lasts until failure. The authors contributed that effect to the high strain as well as fibre pull-out. It was also observed that the failure zone decreased in width by 23 %.

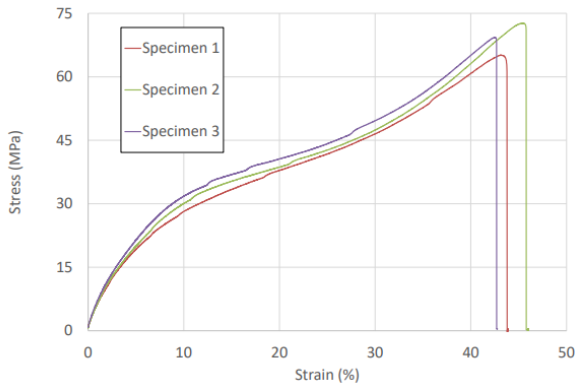

Figure 5: Stress-Strain diagram for the shear tests conducted by Justo et al [56].

2.2.3 Carbon fibre

2.2.3.1 Tensile and flexural testing

The UTS determined by Dickson et al. for samples with eight out of 26 layers being reinforced in a concentric pattern was 216 MPa with a Young's modulus of 13 GPa [57]. Fibre pull out was found to be the main cause of the failure and optical microscopy showed remaining residue on the Carbon fibres suggesting a strong bond to the matrix. Air inclusions that have a negative effect on the parts performance are shown in Figure 6. Their number and size increased with the fibre fraction.

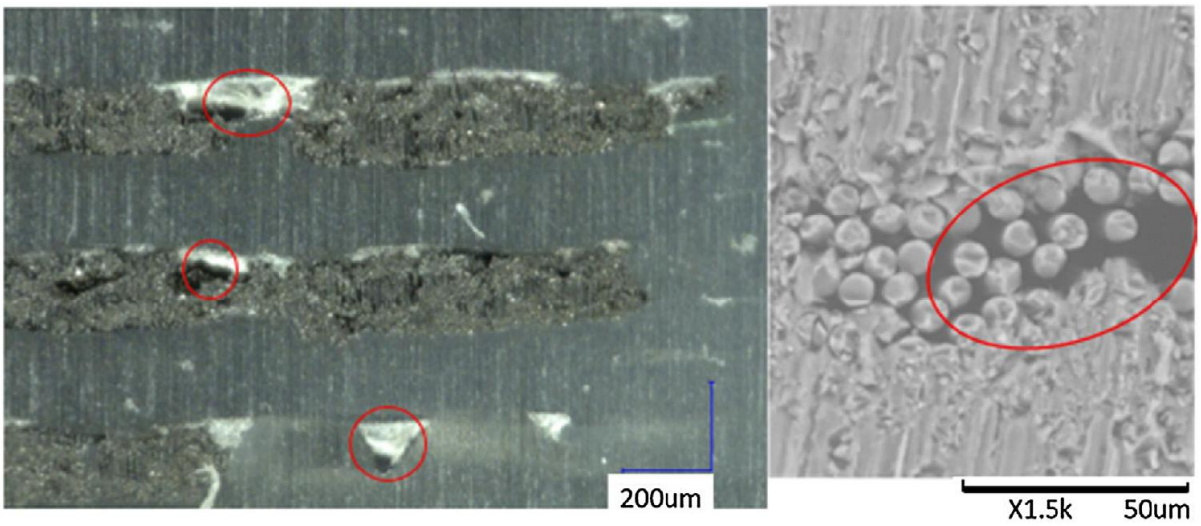

Figure 6: Air inclusions seen through an optical (left) and electron (right) microscope [57].

Blok et al. tested unidirectional samples which were cut out of a concentric printed plate with a fibre volume fraction of 27%. The average UTS was determined to be 986 MPa and the average Young's modulus to be 63 GPa [58]. Since these values are higher than the ones stated by the manufacturer and other researchers, a measurement error is very likely. High frequency fibre noise was audible at low stresses which did not occur again before failure. Waviness of the fibre strands is suspected to be the cause of the slight increase in stiffness with the load. The air voids reported by Dickson et al. between tracks and within them were also observed. In order to get a homogenous fibre distribution, the test samples used by Van der Klift et al. were cut out of a plate which resulted in an average UTS of 464 MPa and a Youngs Module 36 GPa with six out of ten layers reinforced [59]. The UTS varied between 138 and 171 MPa with two out of ten layers reinforced. It was also found that the number of voids increased when the fibre volume was increased.

When only partially reinforcing a part, the continuous fibres can either be stacked or placed all within a couple of layers. Lozada et al. found that placing the fibres within one layer rather than stacking them results in higher UTS [60]. A definite explanation couldn't be found, but the stacked specimens showed non-uniform wetting of the fibres. A fibre volume fraction of 54 % led to a UTS of 310 MPa and a Young's modulus of 24 GPa, which were determined according to ASTM D638.

An average UTS of 600 MPa and Young's modulus of 13 GPa was determined by Goh et al. with a fibre volume fraction of 41 %. The amount of fibre pull-out was found to be insignificant

compared to the fibre breakage which means, a good fibre matrix bond exists. A CT scan of the specimen revealed that there are air voids between adjacent layers as well as air voids within the filament [55].

For specimens reinforced with six out of ten layers the average UTS was determined to be 493.9 MPa and the Young's Modulus to be 45 GPa in accordance with ASTM D3039 [61]. With the fibres aligned 90° to the load direction the average UTS was 14 MPa with a Young's Modulus of 3.5 GPa. The ratio of longitudinal elastic modulus to fibre volume is found to be the same as for conventional thermosetting composites.

Adabi et al. found the main failure in tensile tests were both tensile and shear stresses. This was supported by test pieces breaking under an angle. An average UTS of 330 MPa and a Young's modulus of 37 GPa was determined with ten out of 20 layers being reinforced [12].

Using the JIS K7075-1991 standard Todoroki et al. determined the fibre volume fraction to be 30 %. The tests revealed a tensile strength of 701 MPa and a Young's modulus of 61 GPa [8]. When comparing the UTS' perpendicular to the fibre direction it was found that the bond between strands within one layer is stronger than the bond between layers. It is suspected that the heat flow from the printing nozzle did not reach the underlying layer but rather got distributed along the filament because of the high thermal conductivity of the fibres. This resulted in a 75% drop in strength and a 40% drop in stiffness when comparing the "X2" and "X3" testing direction and the air void ration increased from 7% to 11.3%. It is mentioned that a future study will investigate this phenomenon by simulating the printing process. A slightly offset or uneven printing bed that reduces the nozzle pressure was stated as an additional possible cause.

Blok et al. tested specimens with 0° fibre orientation according to ASTM D7264 [58]. An average flexural strength of 485 MPa and a flexural modulus of 42 GPa were determined with 30 out of 32 layers being reinforced. Limiting factors for the mechanical performance were found to be a poor fibre matrix bond as well as a high void content acting as premature failure initiators.

Similar results were obtained by Goh et al. found the average flexural strength to be 430 MPa and the flexural modulus to be 38 GPa [55]. At 1-% strain the flexural stress experienced a little drop before rupturing. The authors of the paper suspect the initiation of the crack that

caused the failure to be caused by the high compressive stress at the upper most surface which crushed the fibres and it propagated towards the neutral axis. When it reached the tensile side of the fibres, the stress became too high and the specimen ruptured. This behaviour is not unique to additively manufactured composites but is the same for conventional fibre reinforced plastics.

Zhang et al. used a custom build FDM printer with an integrated roller, that applied pressure and heat right after the filament was extruded [62]. It was found that this procedure will increase the mechanical performance, but too much pressure will cause a poor surface quality or even lead to printing failure. Carbon fibre reinforced samples with a PLA matrix achieved a maximum UTS of 645 MPa. Judging by the pictures provided in the article, this procedure is not yet on the level of commercial printers but still proves it could address the shortcomings of the FDM process.

2.2.3.2 Shear testing

Todoroki et al. used +/- 45° samples to calculate the shear strength according to JIS K7019, which is the Japanese equivalent of the ASTM D3518 standard [39]. A comparison between test pieces with their edges cut off and samples with a serpentine pattern revealed better results with the former. A shear strength of 90/52 MPa and shear moduli of 2.2/2.1 GPa were calculated. Since a rotation of fibre bundles to a lower angle was observed, the actual shear strength is lower [8].

2.2.4 Interlaminar Shear testing

Caminero et al. examined the Interlaminar shear behaviour of parts reinforced with continuous Kevlar®, glass and carbon fibres according to ISO 14130 [10]. The two different types of reinforced samples used are shown in Figure 7. Table 3 contains the number of reinforced layers for each of the different reinforcement materials and type of test pieces.

The results of the test are shown in Figure 8. As can be seen on the left side of Figure 8 the interlaminar shear strength increases for both glass and carbon fibre when increasing the fibre volume fraction, but the increase was not proportional to the added fibres. According to Caminero et al. this is most likely due to the increase in air gaps which have also been reported in other works. The reason for the shear behaviour of the Kevlar reinforced samples

is poor wettability of the Kevlar fibres which leads to a poor bonding between the matrix and the fibre. The thermosetting prepreg with a fibre volume of 59 % vastly outperforms the additive manufactured parts mainly because of the thermosetting matrix material as well as manufacturing process itself. The prepreg is processed in an autoclave under high pressure, which minimizes air gaps, whereas the additive manufactured materials are processed under atmospheric pressure. Also, the prepreg cures as one piece whereas the FDM produced parts are built layer by layer [10].

Table 3: Amount of reinforced fibre layers out of the total layers of fibre for each type of test piece [10].

	Type A	Type B
Carbon fibre	18/48	46/48
Kevlar® fibre	22/60	58/60
Glass fibre	22/60	58/60

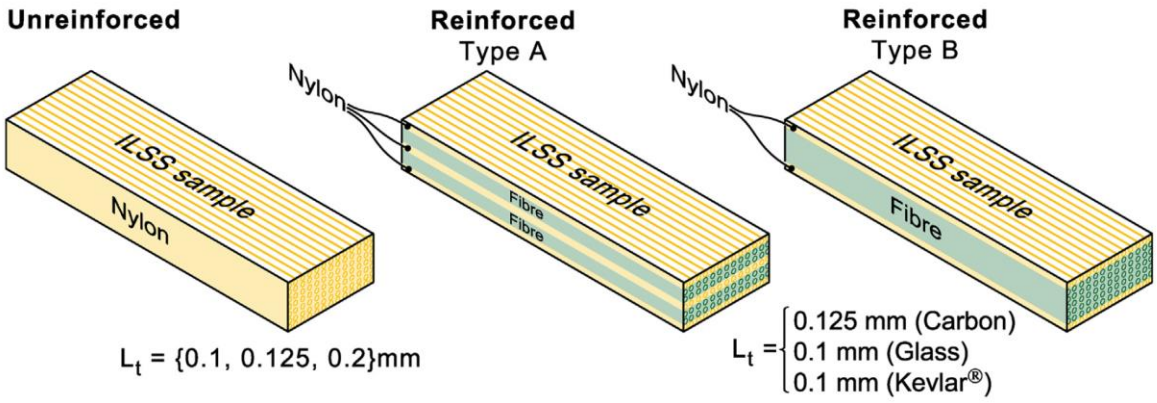

Figure 7: Test pieces used by Caminero et al. [10].

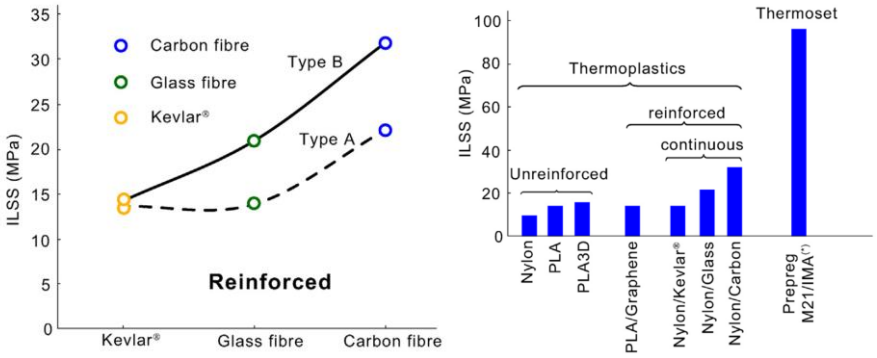

Figure 8: Average maximum interlaminar shear strength (ILSS). The influence of fibre volume on ILSS (left) and comparison of additive manufactured materials and pre-impregnated M21/MMA (thermosetting)(right) [10].

2.2.5 Fatigue testing

With a load ratio of 0.1 Imeri et al. evaluated the number of load cycles until failure according to ASTM E606M [63]. The specimens were either reinforced with up to three concentric rings, an isotropic reinforcement with fibres oriented in load direction or a combination of both. The load was varied in four steps and the number of cycles until failure was measured. Only cycles up to 10,000 could be detected because of testing equipment they used. Even though the acquired data didn't suffice for a reliable fatigue prediction model it was shown that the fill pattern has an influence on the fatigue performance. The isotropic fill pattern resulted in the highest number of endured load cycles. As in the UTS experiments, Carbon fibre was the strongest and Kevlar the weakest. An increase in fibre content led to an increase of the fatigue performance. While this work shows some correlation factors, its main flaw is the use of the ASTM E606 standard. Due to the "dog bone" shape of the test pieces the concentric reinforced samples were destined to perform worse than the isotropic reinforced ones. The fibre direction is not oriented in the load direction in the tapered part of the test piece. This would have not been an issue if rectangular test pieces (ASTM D3479) had been used.

Pertuz et al. also investigated the influence of different printing patterns and fibre orientations (0°, 45°, 60°) on the fatigue behaviour according to ASTM D7791 [64] with a load ratio of 0.1 [65]. Samples with fibres orientated in load direction were loaded with 95%, 90%, 85% and 80% of their ultimate tensile strength and the number of cycles until failure were measured. While the Kevlar and glass fibre reinforced samples only lasted a maximum of 550 and 2500 cycles respectively, the carbon fibre reinforced samples lasted up to 97.000 cycles at 80% of the ultimate tensile strength. Furthermore, the influence of the fibre angles was

tested using glass fibre specimens. Samples were loaded under the same conditions as before. It was observed, that with greater angles the matrix material absorbs most of the load, which lead to a very low fatigue resistance. The obtained data was fitted to Basquiṅs fatigue model for each of the tests. Unfortunately, the applied standard also uses “dog bone” shaped samples that have variations in the cross-sectional area. The authors themselves stated, that “a considerable number of specimens […] broke in the change of the transversal area section”. As with Imeri et al. this indicates that the mentioned location is a weak spot and the obtained data is only useful for samples that did not have curved fibre paths.

2.3 Material analysis

One of the most common procedures to analyse the thermal behaviour of a plastic is the differential scanning calorimetry (DSC). DSC measures the heat energy required to increase the temperature of a material, which allows the determination of the melting and glass-transition temperatures, the degree of crystallinity, cold crystallization processes, impurities as well as the effect of additives [66].

Another way to determine the glass-transition temperature as well as the viscoelastic behaviour of polymers is the dynamic mechanical analysis (DMA). A small load is applied in a cyclic manner and changes in stiffness and damping are measured. When the temperature is increased, the material stiffness will decrease and the viscosity significantly increases, when the glass-transition temperature is reached [67].

For evaluation of the thermal stability and the fibre content Thermogravimetric analysis (TGA) can be applied. The TGA procedure measures the sample mass by a micro scale as a function of time or temperature. Dynamic Thermogravimetry refers to a linear increase of the temperature, which will lead to different constitutes of the material deterioration at different times/temperatures. As a result, the mass loss at a certain temperature allows reaching conclusions about the material composition [68]. Static Thermogravimetry, where the temperature is held at a certain level, can also be used to burn of the matrix material. If this process is taking place under an inert atmosphere, it is referred to as pyrolysis [69]. Another way of determining the fibre volume fraction is by matrix digestion. In this procedure, the matrix material is dissolved by a heated-up acid. The fibres are then dried and weighed. Since

the weight of the total composite and the densities of the materials are known, the fibre volume fraction can be calculated with those values [70].

A very important aspect for composites manufactured by FDM is the determination of the air-void content, which can be determined by comparing the theoretical density of a material with the actual density. The actual densities are obtained by burning off the matrix like it is done with the pyrolysis process [71]. However, this method does not give any information about the void sizes and their distribution. X-ray microtomography can be used to obtain this important information. It can furthermore be used to visualize cracks and fibre distribution. A detailed description of how polymer composites can be analysed using this technique can be found in [72].

A summary of these test-methods and their corresponding international standards are listed in Table 4.

Table 4: Summary of calorimetric and chemical procedures to analyses composite materials, the information that can be obtained using those methods and the corresponding standards.

Method	**Resulting Information**	**Standards**
DSC	Glass-transition temperature, melting temperature, degree of crystallinity, plastic identification	ASTM D3418 [73] ASTM E1356 [74] ISO 11357 [75] [76] [77] [78] [79]
DMA	Glass-transition temperature, viscoelastic behaviour	ASTM D7028 [80]
TGA	Thermal stability, material composition, fibre volume fraction	ASTM E1641 [81] ASTM E1131 [82] ISO 11358 [83]
Matrix digestion, Pyrolysis	Fibre volume fraction, Air void ratio	ASTM D3171 [70]

		ASTM D2734 [71] ISO 11667 [84]
Microtomography	Air void ratio and crack, size and distribution; fibre alignment	ASTM E2533 [85]

An in-depth filament review of the raw filament for the Markforged printer was conducted by Pascual-Gonzalez et al. [86]. A thermodynamic analysis showed that the chopped carbon, glass and aramid fibres are embedded in Polyamide 6 (PA 6) based copolymer with a melting temperature of 199°C. With 4.8% the aramid filament had the highest water content and with 2.1% the carbon filament had the least, followed by glass fibre with 2.6%. Digestion, Pyrolysis and TGA were used to determine the fibre content. The sulphuric acid, that was used for digestion also dissolved the aramid fibres, which rendered this method useless for this type of fibre. Pyrolysis led to a high scattering of the determined values. Fibre volume fractions determined by TGA were 31.7% for the glass fibre, 40.4% for the aramid fibre and 36.4% for the carbon fibre filament. These values are a little bit higher than values determined by authors of [61] [8] and [55]. The discrepancy may be a result of the fibre density, which was not known and had to be estimated by all authors. While they found air voids in the raw filament, they concluded that the high crystallization temperature of polyamide, which was determined to be 160 °C, may also have an influence on the weak layer adhesion and the poor mechanical performance [86]. However, other studies have shown that there is enough time for crystallization despite the fast cool-down [7] [87] [88]. These studies found that there is also enough time for reptation and as a result the interpenetration depth is sufficient. The weak bonding is instead suspected to be caused by areas of aligned polymer chains close to the interface, which is referred to as residual alignment [88]. Residual alignment is caused by the flow of the molten plastic through the nozzle, which aligns the polymer chains along the flow direction at the filament nozzle interface. The aligned chains cannot anchor the adjacent material properly and thus weaken the material. A study analysing the weld strength of PLA has found, that lower printing speed and higher printing temperature can reduce this effect [88]. Furthermore, it was determined that the filament-filament interface makes up 12% of the total thickness. Despite the material used in this study having continuous fibre

reinforcement the underlying mechanisms are most likely similar. Since the material is also extruded through a nozzle, the polymer chains at the nozzle-filament interface will also align in flow direction. However, it is important to point out, that the previously cited studies are based on certain assumptions, like the axisymmetric cooling of the filament strand. This topic still requires a lot of research, to identify the exact mechanisms involved.

2.4 Optimization and Failure criteria

In automated processes, as mentioned in the introduction, conventional fibre reinforced plastics are usually manufactured by stacking unidirectional fibre mats on top of a mould and then cured under pressure and temperature. This means, that is not as simple to realize changes in local fibre orientations as it is with the additive manufacturing process, since all fibres within one fibre mat are aligned in the same direction in the raw material. So, local changes in the fibre direction would require for instance a patch, whereas with the additive manufacturing process only the printing path has to be altered.

If composite parts are manufactured by FDM the individual fibre paths can be defined during the development process. It is a well-known fact, that composite materials containing continuous fibres are the strongest, when loaded in fibre direction (on-axis loading). If the load is applied at an angle (off-axis loading), the strength decreases since the significantly weaker matrix material experiences higher stresses [89]. For a maximum utilization of the fibres, they must be positioned in a way that leads to a high tensile stress for the fibres (on-axis load). In a complex multilayered part, this is impossible to do by hand, so computer-based optimization processes are required.

It can be differed between approaches that model the fibre through parameterized curves (curve-based designs) and approaches were the finite elements contain information about material orientation (element-wise designs). The difference between the two is shown in Figure 9. Since this topic is worth an independent review paper, only a brief overview of recent work will be given.

With element-wise design, each element is assigned a parameter, that represents the fibre orientation. As a result, the stiffness of the element regarding a certain direction can be changed by changing the fibre orientation [90] [91]. As shown in Figure 9, at the beginning of

the process, the fibres in each element (represented by the lines) are aligned at random. The optimization process determines the ideal fibre orientation for each element. Post processing is required to transfer the individual element orientations into homogenous fibre paths [92]. To reduce the calculation time, the fibre orientation can be limited to a pre-defined number of values [93] [94]. The discrete material optimization (DMO) method developed by Lund [93], uses a matrix containing a pre-defined number of fibre orientations to limit the number of possible orientations. While the DMO theoretically allows an unlimited number of orientations, the shape function with penalization (SFP) approach is limited to four fibre orientations: 0°, +/-45° and 90° [95]. SFP uses the shape functions of the finite elements as weights to determine the optimal fibre orientation. The SFP was later extended to allow the use of eight fibre orientations [96]. A similar approach was taken by Gao et al. [97]. A different approach is to align the fibres along the principal stress directions. Malakhov et al. and Zhu et al. applied this principal to determine the fibre paths in structures with geometric discontinuities, such as holes and notches [98] [99].

Curve-based optimization processes on the other hand use parametrised curves that represent the fibre paths [100]. Contrary to element-wise optimization, no post-processing is required since the curves already represent the fibre paths. However, this technique still relies on local material orientations. Figure 9 illustrates this with the example of an additively manufactured lug that is loaded with compression inside the hole. Cubic splines with five parameters are used. The failure mode was evaluated using Hashin's failure criteria (comp. next paragraph) [11]. An approach inspired by fluids dynamics was perused by Yamanaka et al. [101]. They used streamlines that are usually used to model the flow of a fluid as a representation of the fibre path. The Tsai-Wu criterion was used to evaluate the material failure. This procedure was used to optimize a composite plate with a hole in the middle. Compared to a uniaxially reinforced ply, the optimized part showed a strength increase of 28%. A summary of these different optimization approaches can be found in Table 5.

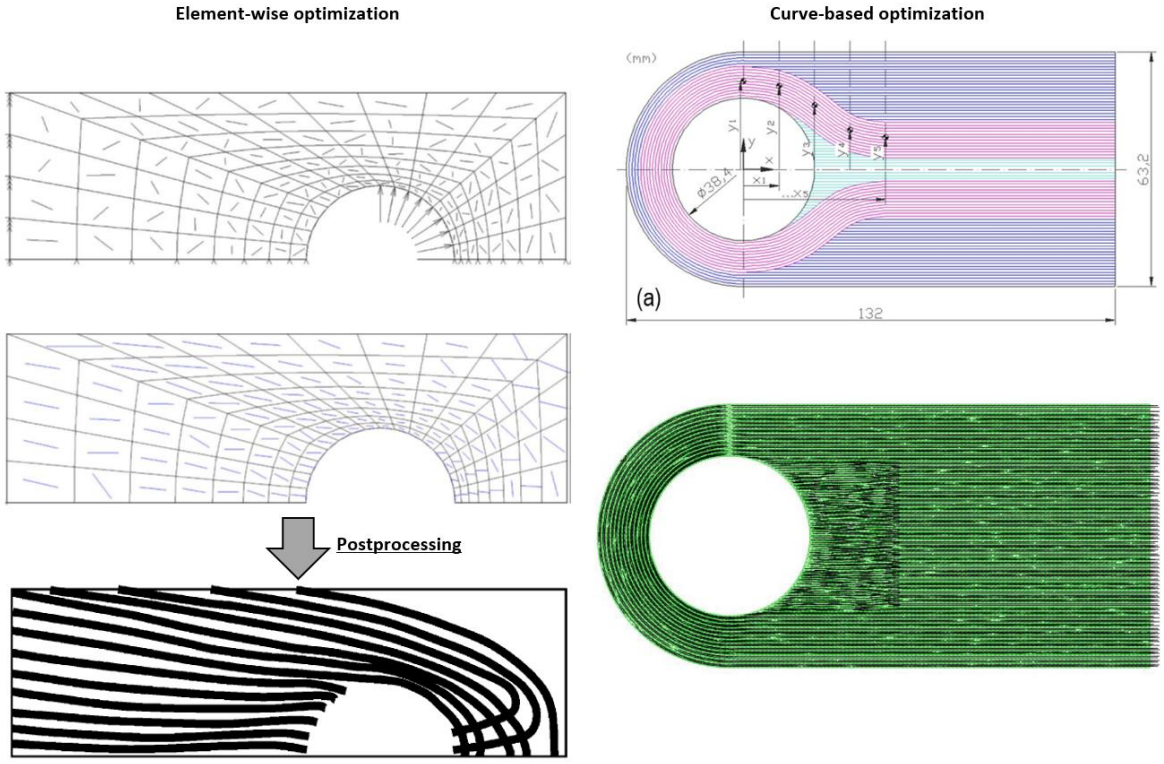

Figure 9: Difference between element-wise optimization [92] (left) and Fibre-path optimization [11] (right)

Table 5: Overview of element-wise and curve-based designs for the optimization of fibre reinforced plastics

Approach	Source
Element-wise designs	
The material orientation of a structure represented by a mesh was optimized to achieve maximum stiffness.	Kiyono et al. [94]
The discrete material optimization (DMO) method, which makes use of a matrix containing a limited pre-defined number of fibre orientations, is extended to take stress and strain-based failure criteria into account.	Lund [93]
By limiting the fibre orientations to 0°, +/-45° and 90° the Shape functions with penalization (SFP) method, the number of design variables is further reduced.	Bruyneel [95]
A bi-value coding parameterization scheme is used to determine the layer orientation for large-scale design problems.	Gao et al. [97]

The modelling of a curvilinear continuous reinforcement for structures with geometric discontinuities, such as holes and notches, is descried.	Malakhov et al. [98]
To optimize the critical buckling temperature and strain energy the element-wise fibre orientation was parametrized with an angle continuity constraint over the mesh in place.	Vijayachandran et al. and Acar et al. [90] [91]
Curve-based designs	
The multi-scale two-level (MS2L9) strategy, which first determines the optimal laminate stiffness properties and then the optimum fibre-paths, is used to maximize the first buckling factor of a VAT plate.	Montemurro and Catapuano [102]
The fibre-paths in a single-ply composite were optimized by using streamlines of the perfect flow.	Yamanaka et al. [101]
A family of parametrized curves is used to put the fibre-paths along the principal stress trajectories. This method was used to optimize a plate with a hole.	Zhu et al. [99]
By modelling the laminate as a Mindlin shell and the fibre as path functions the stiffness was maximized. Manufacturability is considered by examining the curvature and parallelism of fibre-paths.	Huang et al. [100]
To maximize the stiffness, the fibre-paths were optimized by using a level-set method.	Lemaire et al. [103]
An aeronautical lug which is under tension and compression load is optimized by using parametrized cubic spline interpolations representing the fibres. The failure mode was evaluated using Hashin's criteria.	Ferreira et al. [11]
The finite element method in combination with Abaqus' integrated Hashin's interlaminar damage initiation theory was used to determine the elastic properties of uni- and biaxial reinforced tokens.	Adabi et al. [12]

To optimize any part, the point of failure must be known. Contrary to isotropic materials like metals composite laminates can't be designed using equivalent tensile stresses (e.g., von Mises stress) to calculate the failure under combined loads. This is because the matrix and

fibres have vastly different physical properties resulting in different stresses under load. A composite material can either experience fibre failure or inter-fibre failure. When many fibres in a layer brake it is referred to as fibre failure. It is caused by high tensile or compression stresses. This failure mode is unacceptable because it leads to high stresses in adjacent layer which causes delamination and there for a complete part failure. Inter-fibre failure on the other hand can be a tolerable damage, depending on the kind of the stress that caused it. A compressive stress perpendicular to the fibres causes, for a brittle matrix material, a shearing off the layer. That layer starts acting like a wedge when further increasing the compressive stress making the whole part burst. Other stresses, like shear or tensile, will cause different kinds of matrix cracks. These cracks usually penetrate the whole layer and are only stopped when reaching a layer with a different fibre orientation. All inter-fibre failures have in common, that the fibre does not get damaged. Up to a certain amount, inter-fibre failure is tolerable [13].

To determine, whether a certain combination of loads leads to either fibre failure, inter-fibre failure or is tolerable, advanced failure criteria are required. In previous works that analysed the failure of continuous fibre reinforced parts manufactured by fused filament fabrication the Hashin's and Tsai-Wu criterion were used to take this effect into account [11] [12]. Hashin's criterion is simple to use, because it only relies on the physical parameters of the composite and it is already implemented in commercial FEM software like ABAQUS. But contrary to more advanced criteria, it can't predict different failure modes and the failure predictions are less precise [104].

2.5 Conclusion

When comparing the fibre volume content of continuous fibre reinforced thermoplastics discussed in this paper (30-35%) with those of conventional thermosetting composites (60-70%), the limiting factor for the mechanical performance is quickly found. Furthermore, air inclusions as well as the poor adhesion between layers significantly decrease the mechanical performance. This was confirmed by the low interlaminar shear strength which is an indicator for the poor bonding performance between layers.

A summary of the mechanical properties can be found in Table 6. The huge difference between the determined values is caused by the fact that the different authors used test

tokes that consisted of reinforced layers mixed with non-reinforced ones (most likely to keep the costs down). Other than that, the reviewed studies were very similar. The only authors that tested samples with 100 % reinforced was Todoroki et al. [8]. They determined a tensile strength of 700 MPa and a Young's modulus of 61 GPa for continuous carbon fibre reinforcement which based on the low fibre content are plausible values. As for the glass fibre reinforced parts, a UTS of up to 550 MPa and a Young's modulus of 25 GPa can be achieved. All the tested Kevlar samples contained only a few reinforced layers and therefor a very low fibre volume fraction thus no conclusion can be made towards their ultimate mechanical properties. Since both Dickson et al. and Adabi et al. tested Kevlar and glass fibre samples in an identical setup it can be said that the ultimate tensile strength is very likely the same and the Young's modulus of the Kevlar fibres is 30 % higher [52] [12]. This would be in accordance with performance data provided by the manufacturer [105]. Since no glass fibre/Kevlar parts with 100 % reinforcement were tested, no definite comparison between them and the continuous carbon fibre reinforcement can be made. But based on the results from the previous research, the carbon fibre filament seems to be 22 % stronger and 59 % stiffer than the glass fibre filament. The continuous carbon fibre reinforced reinforcement has a flexural strength of 485 MPa which is two and a half times that of the glass fibre reinforcement and more than three times than that of the Kevlar reinforcement. While these conclusions are based on very limited data, it seems like the carbon fibre filament outperforms both the glass fibre and the Kevlar filament regarding the tensile and flexural performance. No comparison can be made regarding the shear strength and strength perpendicular to the fibres (X2/X3 direction) because there is not enough data available. Due to the inadequate testing standards that led to failure in geometric weak spots as well as the limited data obtained no conclusion can be made towards the life expectancy under variable loading.

Table 6: Summary of the mechanical properties of the continuous carbon, glass and Kevlar fibre filament

Carbon fibre			**Glass fibre**			**Kevlar fibre**		
UTS (X1) [MPa]	Elastic Modulus [MPa]	Source	UTS (X1) [MPa]	Elastic Modulus [MPa]	Source	UTS (X1) [MPa]	Elastic Modulus [MPa]	Source
216	7730	[52]	444	-	[52]	80	9001	[51]
968	62500	[58]	450	7200	[55]	164	4370	[52]

304	23700	[60]	574	25860	[56]	150	8700	[12]
493	45200	[61]	140	6400	[12]			
600	13000	[55]						
701	60900	[8]						
330	37000	[12]						
UTS (X2) [MPa]	Elastic Modulus [MPa]	Source	UTS (X2) [MPa]	Elastic Modulus [MPa]	Source			
19	3970	[8]	9,84	1130	[56]			
16	3766	[61]						
Compression strength (X1) [MPa]	Compression Modulus [MPa]	Source	Compression strength (X1) [MPa]	Compression Modulus [MPa]	Source			
223	53000	[56]	82	19490	[56]			
317	51198	[61]						
Compression strength (X2) [MPa]	Compression modulus [MPa]	Source	Compression strength (X2) [MPa]	Compression modulus [MPa]	Source			
42	-	[56]	12,73	-	[56]			
Flexural strength [MPa]	Flexural modulus [MPa]	Source	Flexural strength [MPa]	Flexural modulus [MPa]	Source	Flexural strength [MPa]	Flexural modulus [MPa]	Source
250	13020	[52]	196	4210	[52]	125.8	6650	[52]
485	41600	[58]	149	14700	[55]			
430	38100	[55]						
Shear strength [MPa]	Shear modulus [MPa]	Source	Shear strength [MPa]	Shear modulus [MPa]	Source			
31	2260	[58]	67,77	880	[56]			
35	1803	[61]						
90	2270	[8]						

2.6 Research needs

The residual alignment of polymer chains and therefore low UTS in layup direction as well as the low interlaminar shear strength significantly limit the materials mechanical performance. These shortcomings could be addressed by subjecting the additively manufactured parts to a

heat treatment process. The heat energy could allow for successful inter-diffusion and consequently re-entanglement [7]. Also, the air-void ratio could decrease due to surface tension and decreased viscosity at higher temperatures [106] [107].

Furthermore, almost no research was done regarding the failure behaviour under combined loads for these additively manufactured composites. Conventionally manufactured continuous fibre reinforced composites usually have a significantly higher fibre volume fraction and use thermosetting matrix materials. This is why there is generally very little research published for low fibre volume fractions and thermoplastic matrix materials. Due to this fact, the materials discussed in this study cannot be used for lightweight applications yet. Because certain damage mechanism may cause premature failure. This risk is usually taken care off by multiplying the actual load with a safety factor and designing the part such that it can handle those exaggerated loads. That way the costs of comprehensive testes are avoided but the final product will be heavier. When it comes to lightweight design the goal is to reduce the safety factor to a minimum and use as little material as possible. This requires an accurate failure prediction which all optimization approaches rely upon.

Chapter 3

Annealing

Based on the state of research elaborated in the previous chapter, it seemed plausible, that annealing improves the overall material performance. In this chapter it is determined how the strength and Young's modulus of the additively manufactured composites in build-up direction were effect by a heat treatment. After a literature review regarding undertaken annealing studies the experimental setup is elaborated. Based on a pre-study the design of the experiment is formulated. Finally, the results are presented in detail and discussed. The findings were published as a research paper in the journal "Composites Part B: Engineering" [108].

3.1 Literature Review

This thesis focused on parts produced by a Markforged "Mark Two" 3D printer, which can process continuous carbon, glass and Kevlar fibre reinforced thermoplastics. The closed source software that controls the printer mandates that all parts must be surrounded by at least one layer of Onyx, which is Nylon mixed with chopped carbon fibres, on all sides. The manufacturer does not disclose any information about the materials. But as shown in the previous chapter the matrix material was identified as polyamide 6 (PA6).

Polyamide 6 is a semi-crystalline polymer with the chemical formula $(C_6H_{11}N0)_n$. It has two stable crystal structures (comp. Figure 10): The α form, which has a Young's modulus of 295GPa in chain direction and the γ form with a Young's modulus in chain direction of 135GPa. While the α form is thermodynamically most stable, the γ form occurs when fast cooled from the molten state [109].

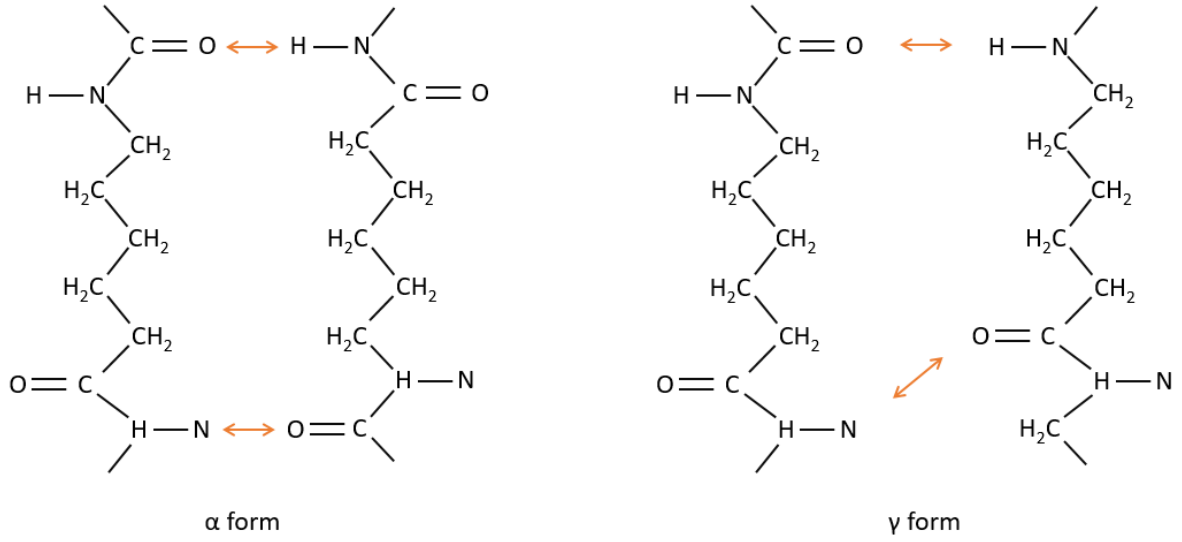

Figure 10: alpha (left) and gamma (right) form of Polyamide 6

The problem of poor layer adhesion is not unique to fibre reinforced plastics, because the cooldown issue affects all parts that are produced by fused filament fabrication. Heated printing beds and chambers can reduce this effect and may even be required for some materials, because the thermal stresses could become too high. Furthermore, low printing speeds and appropriate nozzle temperatures were also found to increase the layer adhesion [88]. But these countermeasures are limited by the fact, that the bottom layer needs to solidify before the next layer is printed on top of it. Nonetheless, there have been several different studies published, which are elaborated in the next paragraphs.

Wach et. al tested different annealing temperatures and times for polylactic acid (PLA), which is a thermoplastic commonly used for 3D printing applications. It has an average glass transition temperature T_g of 62.4°C and a melting temperature T_m of 153.4°C. When printed with a nozzle temperature of 215°C the samples showed a cold crystallization at 116.6°C which indicates that the cooldown process went too fast and parts of the amorphous state did not have enough time to crystallise. Samples were annealed at 85°C for 70 minutes and at 95°C for 15 minutes which led to a 11-17% increase of the flexural strength. The difference

can be explained by the number of nucleation sites of which more occurred at higher temperatures which led to slightly smaller crystals [110].

By annealing PLA samples at 80°C and 100°C for one-hour Benwood et al. obtained similar results. The measured tensile and flexural strength matched, and the impact strength exceeded those of injection moulded parts. This shows the great importance of the macromolecular structure formation for fracture mechanisms, which has also been shown in other works [111] [112]. The almost identical tensile strengths and moduli of the injection moulded part which has a crystallinity of 1.5% compared to a non-annealed part which has an 18% crystallinity showed, that these mechanical properties depend mostly on other factors like the thermal bonding of the filaments. The flexural strength and modulus on the other hand highly depend on the level of crystallinity [113]. Similar tendencies in the improvement of mechanical properties were obtained by Liao et al., Wang et al., Wangwang et al. and Simmons et al. [114] [115] [116] [117]. For short carbon fibre reinforced PLA Bhandari et al. found, that for an optimal increase in mechanical performance, the annealing temperature should lie between the glass transition temperature and the cold-crystallization temperature, because the formation of crystals at higher temperatures slows down the interlayer diffusion process [118].

Different authors also have achieved an increased crystallinity and improved mechanical performance by adding nucleating agents which promote the crystallization [116] [117]. Annealing still led to a better mechanical performance increase and since the scope of this work is to optimize the part performance without altering the filament, these options won't be further discussed.

Vaes et al. assessed the influence of the nozzle temperature, printing speed and printing bed temperature on the crystallinity of Polyamide 6 and Polyamide 6.6 with melting temperatures of 199°C and 198°C. An infrared camera was used to record the precise temperature development of individual layers which was fed into a fast-scanning calorimetry device that simulated the printing conditions. It was found that only the bed temperature had a significant effect on the crystallinity [119].

To overcome the issue of geometric deformation during the annealing process Dunn et al. used a dual printing head to increase an acrylonitrile butadiene styrene (ABS) part which has

a low glass transition temperature with a shell made from polycarbonate (PC), which has high glass transition temperature. By annealing the samples at 135°C for one week, 18 times the fracture toughness of non-annealed ABS was achieved. More temperature resistant shell materials could be used to increase the annealing temperature and significantly lower the annealing time [120].

Fouda et. al used density measurements to analyse the effect of annealing on nylon 6 fibres. Temperatures between 80°C and 185°C as well as exposure times varying between one and ten hours were chosen. After heating, the test samples were cooled to at room temperature. Four different processes were used, to explain the changes in density: Disorientation of the non-crystalline chains, recrystallization by nucleation and by growth of nuclei and crystal decomposition. Based on these assumptions, they concluded that the annealing is most effective at a temperature of 160°C for a duration of three hours. If heated longer, crystal decomposition is predicted to occur. The results were not backed up by mechanical testing. Since there was no mention of an inert gas being used, the crystal decomposition could have been caused by oxidation [121].

Different manufactures of conventional nylon products have published recommended values for the annealing parameters. Although none of them are backed up by experimental data, they all lie within a certain range and are most probably based on practical experiences. An overview is displayed in Table 7.

Table 7: Annealing parameters of Polyamide 6 recommended by plastic manufacturers

Heat up rate [K/h]	Annealing temperature [°C]	Annealing time [h per inch of thickness]	Cooldown rate [K/h]	Source
30 - 60	149	2-4	6 - 30	[122]
12	160	2	6	[123]
30	149	2	28	[124]
10-15	160-165	2	15-20	[125]

The values for the annealing temperatures agree with a US patent describing the annealing process of a nylon yarn [126]. While the sources have different recommendations for the

heat- and cooling rates, they all mention the oxidative behaviour of Polyamide at increased temperatures. The underlying chemical reactions have been studied in detail but shall not be further elaborated, because it would be beyond the scope of this work [127] [128].

Contrary to commonly used materials like PLA and ABS this thesis focused on the effects of annealing on the material strength of Polyamide 6 in build-up direction. Additionally, the material used in this study contains fibre reinforcement and an in-depth analysis of the cause of change in the materials mechanical properties was conducted. Furthermore, a wider temperature and time span was investigated up to the materials melting point. To allow for a practical application, no moulds were used in this process but rather a more innovative approach using paraffine oil.

3.2 Experimental setup

In this section the experimental setup is explained.

3.2.1 Materials

The fibre reinforced filaments from the company Markforged were processed on a Markforged “Mark Two” printer in a climatized laboratory. The material was processed as delivered, without being subjected to any thermal or dehumidifying procedures. Before processing the material was continuously stored in a dehumidified storage box at room temperature, as recommended by the manufacturer.

3.2.2 Optical Microscopy

Images of the fracture surfaces of the different test samples were taken by a Leica MZ6 with an Axiocam 305 color camera attached to it.

3.2.3 Infrared spectroscopy

Even though it is known that the polymer used in the chopped carbon and continuous glass fibre filament is a polyamide 6 based copolymer, the material has not yet been investigated using infrared spectroscopy. A Brunker “Alpha E”, which uses the attenuated total reflection (ATR) technique, equipped with a Germanium crystal was used for the analysis. Data was collected every 4 cm^{-1} over a range of 4000 – 600 cm^{-1} with 64 scans per sample.

3.2.4 Caloric Characterization

A “DSC821e” differential scanning calorimeter from “Mettler Toledo“ with a “FRS5” sensor was used to analyse the unprocessed and processed filaments with a temperature rate of 10 K/min with 5 mg samples in standard 40 µl pierced aluminium pans starting from 20°C going up to 230°C according to ASTM D3418 [73]. The temperature was held for five minutes to erase the thermal history after which the samples were cooled down to 0°C using liquid nitrogen at a rate of 10 K/min. The heat and cooling cycles were then repeated with the same parameters. Calibration of the measurement device was carried out according to the user manual and formerly mentioned standard by using Indium as a reference material of which the melting point and enthalpy is known. The test chamber was flooded with 50 ml/min of nitrogen and each measurement was repeated twice. Due to the stiffness of the fibre reinforced raw filament, it had to be chopped into multiple pieces to fit inside the pan. For the analysis of the printed parts, samples were extracted with a sharp cutting tool. All the samples extracted from printed parts contained at least fifteen layers. After extraction they were stored for two weeks in a room with an air moisture level of 50% at a temperature of 23°C.

3.2.5 X-Ray Diffraction

Changes in the crystal structure were analysed by using X-Ray Diffraction (XRD). When an X-Ray beam hits an atom, the beam is scattered. Since in crystalline structures atoms are arranged in regular arrays the scatters will add constructively when the path-length difference equals an integer multiple of the X-Ray wavelength. This is expressed in Bragg’s law

$$d = n\lambda/(2sin\theta)$$

where the spacing between the crystal arrays (*d*) is expressed as a function of the wavelength of the x-rays (λ) as well as the angle of the beam (θ) with n being a natural number [129]. By varying the angle of the beam, reflective peaks will occur in the diffraction pattern, allowing the calculation of the distance between the arrays. Measurements were conducted using a Malvern Panalytical Empyrean. The machine is equipped with a cobalt cathode (wavelength = 1.7890100 Å) and the voltage and current were set to 40 kV and 30 mA. The intensity data was collected from 10° to 40° every 0.02° for a period of 0.7s.

3.2.6 Mechanical Testing

Tensile testing was performed on an Instron 5966 machine. To achieve a quasi-static load, the strain rate was set to 0.01/min as recommended by ASTM D3039. Notch effects and other influential factors, which could happen as a result from using mechanical gages were avoided by using an Instron 2663-901 video extensometer. It measures the strain by tracking points on the test token. The samples were tested right after the annealing process. While Polyamide is known to absorb water, it is a rather slow process. The test samples used in this study would reach equilibrium after roughly nine months [130].

All test samples were designed according to ASTM D3039. The standard describes the minimum length as “gripping + 2*width + gage length”. To get a uniform application of force, a 20mm gripping length was chosen. With a gage length of 20mm and width of 4mm, this results in a minimum length of 68mm. The recommendation in the standard for a 90° tensile test is a length of 175mm, which is based on practical experience. To keep the costs down, a length of 110mm was chosen as happy medium between the minimum length and the recommendation [131]. To avoid bending stresses from misaligned grips, the grip alignment was calibrated before the measurements. The ultimate tensile strength (UTS) was calculated as the force applied at the point of failure divided by the initial cross section.

As mentioned in the previous chapter, the coordinate axes were named in accordance with works regarding conventional fibre reinforced plastics. “X1” is in fibre direction, “X2” is perpendicular to “X1” and on the same plane and “X3” is perpendicular to the printing bed (often referred to as lay-up or build-up direction). In transverse isotropic materials, the stiffnesses and strengths in “X2” direction are the same as in the “X3” direction (comp. Figure 1). This chapter focused on the material strength in the “X3” direction for both the chopped carbon and continuous glass fibre reinforced material.

X3 Tensile sample

Rectangular tubes were printed from which the samples for the build-up strength test were extracted as shown in Figure 4 on the left side. For the continuous fibre-reinforced samples a “concentric” fill pattern was selected and “Start Rotation percent”, which determines the location of the starting point, was chosen to be either 1%, 26%, 51% or 76%. This put the starting point of the fibre paths in the corners and therefore the samples were homogenous

in the tested section (comp. Figure 4 right side). As mentioned in the introduction, the printer mandates a chopped carbon fibre outer layer for the continuous glass fibre samples. This is represented as a white line in the figure, whereas the orange line represents the fibre paths. To determine the effect on discontinuous fibre reinforced samples a chopped carbon fibre reinforced filament was used as it shares the same matrix material as the continuous glass fibre reinforced filament. The chopped carbon fibre samples also consist of an outer layer. But instead of a concentric fill pattern, a +/- 45° serpentine fill pattern was used (comp. microscopic image in Figure 30), which is made from the same material as the inner layers. The layer height for both materials was set to 0.1 mm.

Cutting

The cuts were made using a Mutronic Diadisc 4200 high precision saw. The saw is equipped with a water vapor cooling system that sprays water vapor on the saw blade to cool it down. Due to the known water absorption, this system would have altered the polyamide material. But some tests without any cooling showed, that instead of chipping the material, the saw blade melted the plastic, even with long cooldown periods during cutting. Furthermore, the test samples became too hot to touch. To solve this problem, a custom air-cooling system was designed and manufactured using a 3D printer. A nozzle was connected to the air pressure system in the workshop. In the first attempt it was pointing at a 25° angle to blow the chips of the blade. Even though it was expected to cause vibrations, their intensity was underestimated and would have certainly caused damage to the bearings. In the second iteration the nozzle was set to be pointing straight at the blade. This setup caused no notable vibrations, even when operated at 5 bars, and significantly increased the cutting quality.

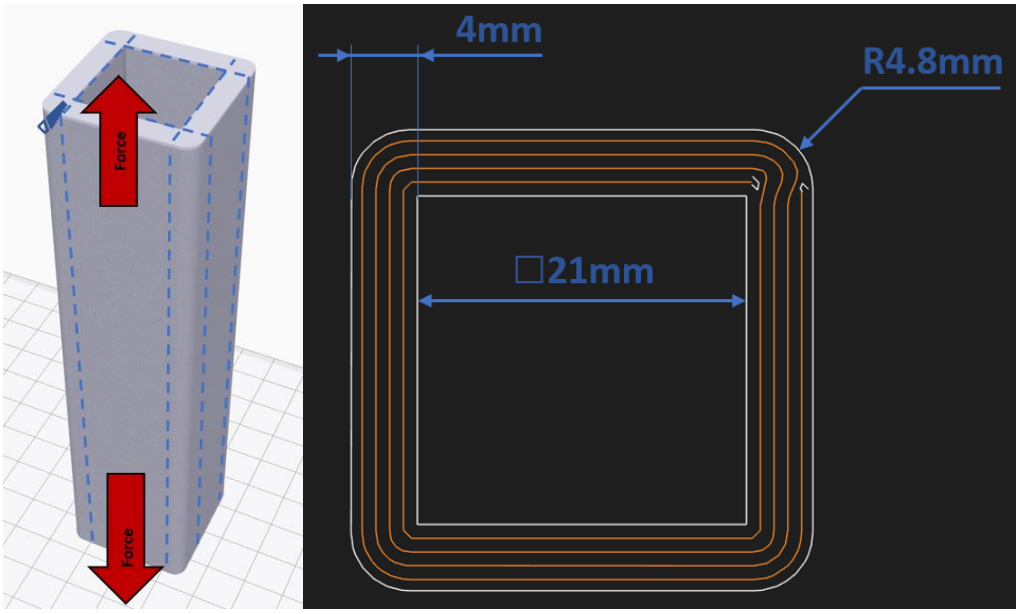

Figure 11: Rectangular tube with cutting patterns for the extraction of the X3 test samples (left), Cross-section of the rectangular tube. The fibre paths are orange and the Onyx paths are white. Starting point of the fibre path is in the top right corner (right).

3.2.7 Geometric and weight changes

Any thermal treatment is expected to have an effect on the dimensions and shape of a plastic part. To determine the extent of the geometric changes the samples were measured before and after the heat treatment to determine the amount of change. For the test samples the length, as well as the height and width at the centre were measured using a calliper. The flatness before and after the annealing process was measured using a Zeiss Eclipse coordinate measurement machine. All samples were weighed using a "Sartorius MC21" micro scale, that has an accuracy of 0.1 mg, before and after the heat treatment to verify any reduction in moisture levels.

3.2.8 Heat treatment

A "Memmert 100-800" oven, which allows the setting of ramp up and cooldown heat-rate was used. It has two P100 temperature sensors built in, which are positioned at the top of the chamber. The air circulation fan was set to its maximum speed to make sure no temperature gradient was shaped inside the heat chamber. This was verified by manually measuring the temperature at multiple points inside the chamber.

3.3 Pre-study

A pre-study was conducted to get an understanding of how the material behaves, when subjected to heat, and to evaluate if this undergoing should be further pursued. X3 test samples were manufactured as described in the previous section. They were cut and then heated to 150°C with air circulating around them and the temperature was held for 1, 6 and 10 hours. The main observation of the pre-study was the significant warping of the test samples after the heat treatment, which led to 50% of the test samples in each run breaking at the clamp even though tabs were used. Since the test samples were put on trays during the heat treatment, it was suspected that the tray cooled down too slow during the cooldown phase which led to thermal stresses resulting in warping. The annealing process was delayed for two weeks due to lab closure. On return to the lab, the non-treated but already cut samples showed the same warping as the previously annealed samples. This led to the conclusion that the warp causing stresses came from the printing process and not the heat treatment process. Annealing was done prior to cutting the tubes for verification purposes. A comparison of the warping between an annealed test sample and a non-annealed one both stored at room temperature for two weeks is shown in Figure 12. The annealed test samples were completely flat and remained that way which confirms residual stresses from the printing process to be the major cause of warping. The initial tests were repeated with test samples first being heated and then cut, the averaged results of which are shown in Figure 13.

As can be seen, the Young's modulus increased, but all test samples became very brittle, which indicates that either the moisture content was reduced or that polymer oxidation took place. To determine if oxidization affected the samples, it was decided to heat up the test tube in oil and then cut the test samples. The tube was placed inside a glass beacon filled with paraffin oil. When submerging the test tube in oil, no air bubbles were observed. Since the oil, as well as the glass beacon act as thermal insulators, the oil temperature was measured to be 139°C when the oven reached 150°C. Therefore, the oven temperature was increased by 10°C. This led to an increase in both tensile strength and elongation at break compared to the test samples annealed in air. None the less, the elongation at break was less than half than that of the non-annealed test sample. This is most likely because of large air-inclusions inside the material causing a notch effect, which will be discussed in a later section. For this reason, the oxidation might also not have happened to such a great extent as the stress-strain

diagram suggests. A slight oxidization of the outer surface, leading to embrittlement, might just be enough to amplify the notch effect without large amounts of the material oxidizing.

Figure 12: Comparison of a "X3" test sample annealed before cutting showing no warping (left) with a non-annealed test sample with significant warping (right) both after being stored two weeks at room temperature

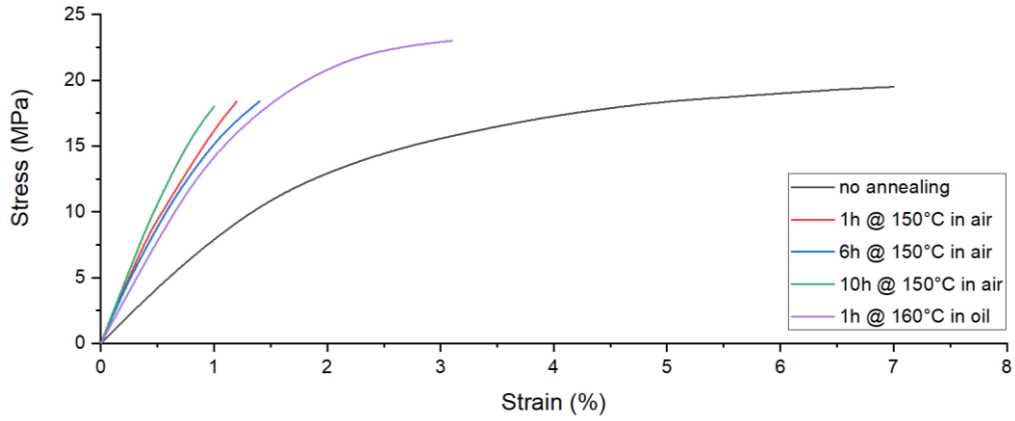

Figure 13: Test results of heating samples in air and oil for different annealing times

In conclusion, the pre-study showed, that the Young's modulus significantly increased as a result of the annealing process. Furthermore, it was determined, that the samples heated in air became more brittle than the ones heated in oil. This suggests that the filament either contains no or not enough oxidization protection when exposed to high temperatures for several hours. Thus, an inert atmosphere during the annealing process was required. If the test samples were first annealed and then cut, residual stresses are eliminated without a deformation of the part – at least when using the heating and cooling rates described in the next section.

3.4 Design of Experiment

The post treatment strength is expected to be a function of the annealing temperature, annealing time as well as the heat up and cooldown rate. Based on the literature, a heat up rate of 15 K/h and a cooldown rate of 10 K/h were chosen, which were also used for the pre-

study. Due to their low magnitude, no thermal stresses should be induced, and the part should be uniformly heated up and cooled down. Since both polymers in the chopped carbon fibre and the continuous glass fibre reinforced filaments are Polyamide 6, the annealing temperatures revolved around the recommend 160°C determined in the literature. Samples were heated up and kept at 130°C, 160°C and 185°C for 0.5 h, 2h and 6h respectively. Due to the fact, that no significant deformation occurred at those temperatures, 200°C was also tested. The wide spans in temperature and time were used to highlight the effect of each parameter.

Since the polymer matrix is very similar in both the chopped and continuous fibre reinforced material and the matrix dominates the material properties perpendicular to the fibre direction, the chopped fibre material was used for determining the ideal temperatures and times. Accordingly, the continuous glass fibre reinforced material was annealed at 200°C for 6h as these settings showed the best increase in performance as will be discussed in following sections.

Since both the pre-study and literature review have shown, that polyamide oxidizes if heated in the presence of oxygen, causing its mechanical degradation, an inert atmosphere was required. For this purpose, a nitrogen oven could be used. An alternative to nitrogen is paraffine oil, which does not interact with polyamide since it does not have polar groups. Compared to nitrogen, paraffine oil has a heat conductivity that is three times higher. Also, the density of ~0.8 g/cm³ at room temperature of paraffin oil is 800 times higher than the 0,001 g/cm³ of nitrogen. Since the density of the chopped fibre reinforced polyamide is 1.2 g/cm³ and for the glass fibre reinforced polyamide 1.5 g/cm³, the resulting buoyant force was expected to act as a support and thus prevent large deformations caused by gravity during the annealing process [132].

In the context of the scientific investigation, it was necessary to design a container that has very little mass and uses materials with high thermal conductivities and low heat capacities, to avoid a big temperature difference between the container and the oven. Aluminium was chosen for the container because of its high heat conductivity. Figure 14 shows a cross-section of the heat container with the test sample inside. At the bottom of the test sample a spacer provided clearance to allow for oil circulation. A measurement of the temperature difference

between the oven and oil temperature is shown in Figure 15. During the heating cycle the temperature difference remained at 3°C and only 0.9°C during the cooling cycle.

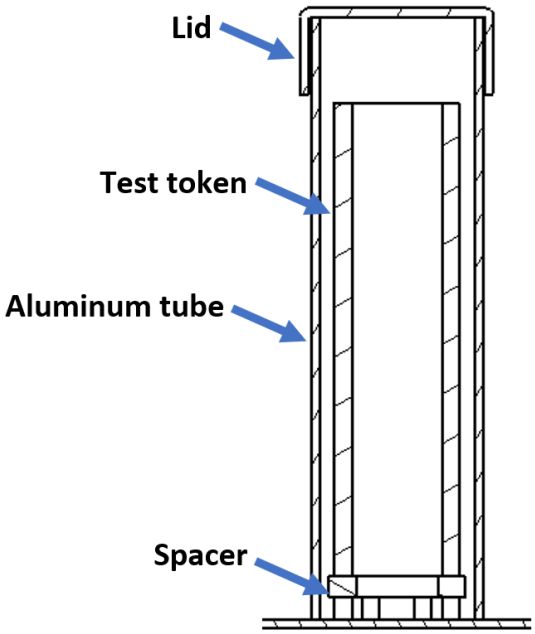

Figure 14: Cross-section of the heat container with the test sample inside

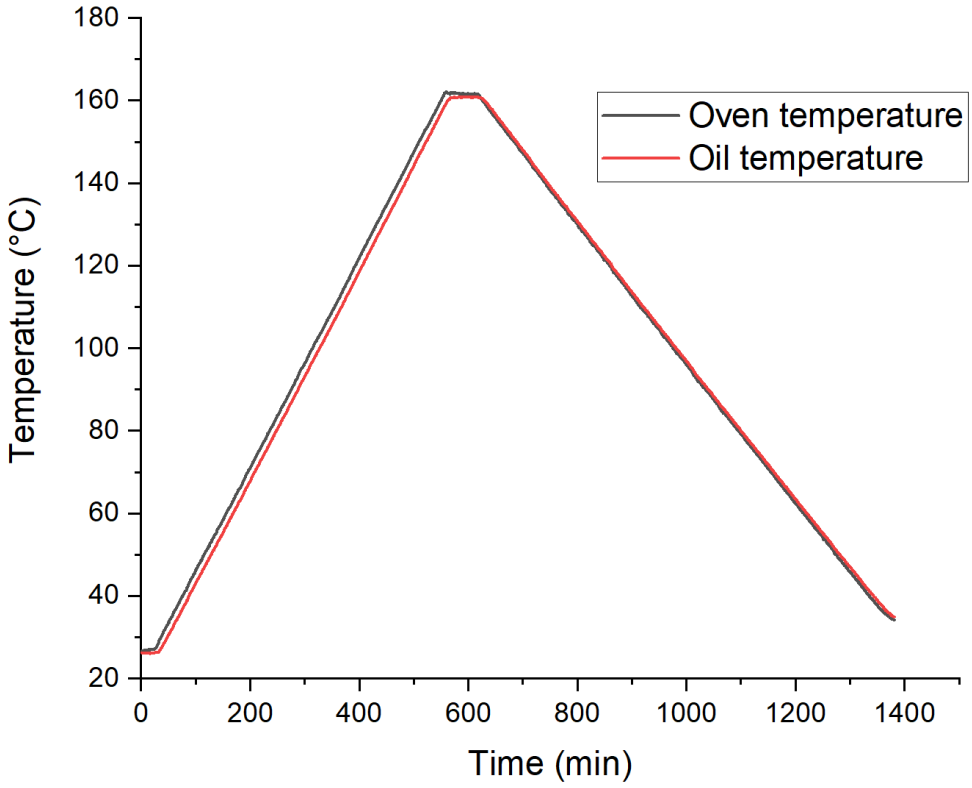

Figure 15: Temperatures inside and outside the container showing the minimal Insulating effect of the heat treatment container

3.5 Testing results

In this section, the results of the infrared, DSC and XRD analysis as well as the mechanical testing will be presented.

3.5.1 Infrared spectroscopy

The infrared spectrum for both the chopped carbon and continues glass fibre reinforced plastics are shown in Figure 16. Due to the higher fibre content of the glass fibre filament, the overall intensity of the peaks was less compared to the carbon fibre filament. The peak at 3300 cm^{-1} is caused by a stretching vibration of the hydrogen/nitrogen (N-H) molecules. At 2930 cm^{-1} and 2850 cm^{-1} the symmetric and asymmetric stretching of the CH_2 molecule is absorbing the radiation. The peaks at 1665 and 1539 cm^{-1} are where stretching of the C=O molecule as well as a bending of the N-H molecule happens, which is typical for the amide group. Up to this point, the two materials have an identical spectrum typical for polyamide 6 [133]. Between 1200 and 900 cm^{-1} the glass fibre filament was slightly more absorbent. Although, no definite explanation was found, a suspected cause would be a coupling agent that is used to increase the adhesion between the fibres and the matrix material. Alkoxysilane compounds are commonly used for this purpose and do absorb radiation in that frequency range [134] [135].

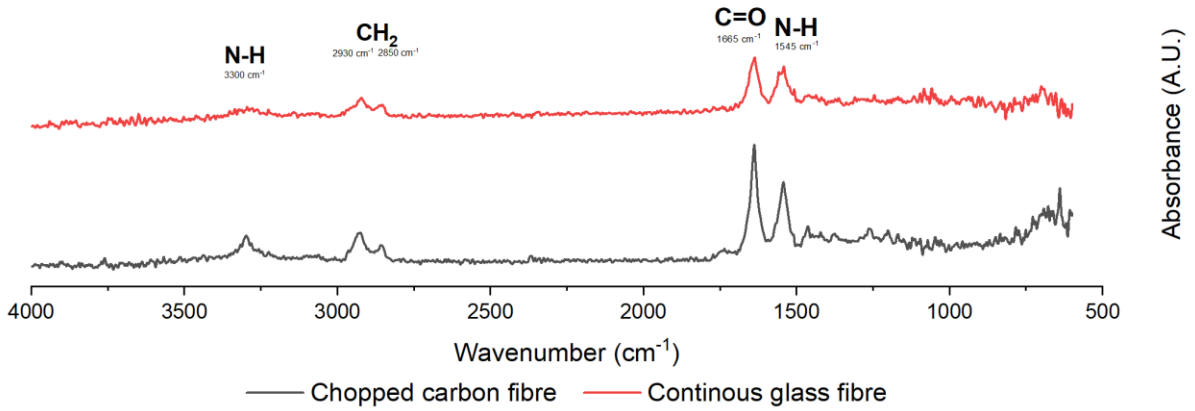

Figure 16: Infrared absorption spectra of the chopped carbon fibre and continuous glass fibre reinforced plastics

Figure 17 shows the absorption spectra of the chopped carbon fibre material for different annealing durations. Since there were no differences between the individual temperatures, only one graph per temperature is shown. It was observed that the double peak of the CH_2 molecule at 2900 cm^{-1} and 2850 cm^{-1} significantly increases, while the double peaks of the

amide group (NHCO) decreased. This shows that the gamma phase of the polyamide 6 converted into the alpha phase [136]. Similar observations have been reported for polyamide 12, which has the same bonds but six more CH_2 molecules in-between [137]. The same observation was made for the continuous glass fibre material when annealed at 200°C as shown in Figure 18.

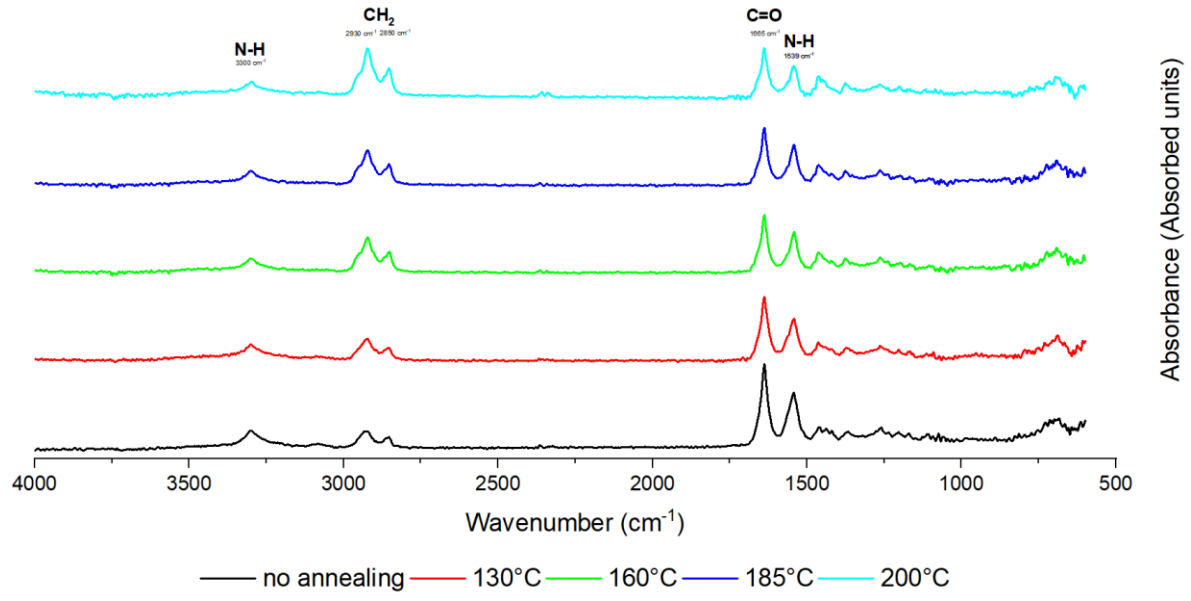

Figure 17: Infrared absorption spectra of the chopped carbon fibre reinforced plastics for different annealing temperatures

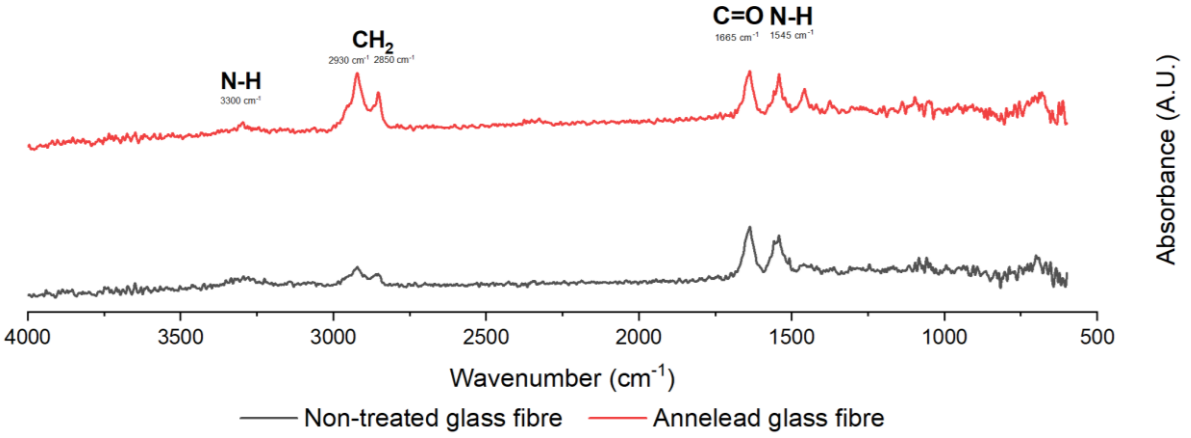

Figure 18: Infrared absorption spectra of the non-treated and annealed continuous glass fibre reinforced plastics

3.5.2 DSC analysis

Analysis results for the raw and processed chopped carbon fibre and glass fibre filament are shown in Figure 19. Flat but wide peaks that stretch from 80°C to 140°C show an endothermic process caused by absorbed moisture which evaporates. This manifested in an average weight loss of 3.8% for the chopped carbon fibre reinforced samples and 3.1% for the glass fibre reinforced samples, which was determined by weighing the samples before and after the DSC measurements. These values are similar to the ones published by Pascual-Gonzalez et.al [86]. The lack of a distinct glass transition peak can be attributed to the high crystallinity of Polyamide 6. The reason for the chopped carbon fibre peaks being higher than those of the glass fibre reinforcement was the higher fibre content in the glass fibre samples. Since the total weight was the same, the amount of plastic was less in the latter.

None of the tests showed exothermic “cold crystallization” peaks, which would be located between the glass transition temperature and the melting temperature. In the first heating run, only one melting peak was observed, whereas for the second heating run, two peaks were observed. The two peaks were present in both materials, but a lot more defined in the glass fibre reinforced plastic. Investigations of polyamide 6 yarn have shown that this behaviour is caused by the super positioning of melting and recrystallisation processes [138] [139]. When most of the crystallization is completed during the cooldown process, the remaining amorphous regions have a lack of place and chain mobility which leads to imperfect crystals. These imperfect crystals start melting, but almost simultaneously a recrystallisation occurs leading to a formation of a new crystal structure, which almost immediately starts melting, forming the second peak. The double peaks being further apart in the continuous glass fibre than in the chopped carbon fibre material was most likely due to the fibres acting as nucleation sites. Since the randomly aligned carbon fibres triggered crystal growth in more places and different orientations than the regularly aligned continuous glass fibres, the probability of imperfect crystals appearing was less likely. The fibres acting as nucleation sites also explains why the crystallisation in the chopped fibre filament started 10°C earlier. Similar observations have been made for fibre reinforced polypropylene [140].

To determine the melting enthalpies according to ASTM D3418, the mass of the plastic in the composite material was calculated using the densities (ρ) and fibre volume contents (φ) from Table 8 as

$$m_{plastic} = m_{total} * (1 - \varphi * \frac{\rho_{Fibre}}{\rho_{total}}) \quad (3.1)$$

The evaporated moisture was subtracted from the total mass. As can be seen in Table 9, the melting enthalpies in the first heating run were almost identical. The minor difference is most likely due to inaccuracies in the fibre content. If a 33% fibre content for the glass fibre composite is assumed, the melting enthalpies would be identical.

The degree of crystallinity K is defined as

$$K = \frac{\Delta H_{meassured}}{\Delta H_{100\%}} \quad (3.2)$$

where $\Delta H_{meassured}$ is the measured melting enthalpy and $\Delta H_{100\%}$ is the melting enthalpy for a 100% crystalline material. While there is a discord about the exact value, most researchers have agreed on 230 J/g for Polyamide 6 [141]. The chopped carbon fibre material had a crystallinity of 23% in the non-annealed state and 21% if slowly cooled from the melt. Annealing for 6h at 160°C and 185°C caused a slight increase of the crystallinity to 27% (63 J/g). These values are in good accordance with those reported in literature for polyamide 6 [142].

Table 8: Parameters for the calculation of the plastic mass for each sample

Parameter	**Value**	**Source**
Glass fibre filament density	1.5 g/cm³	[132]
Glass fibre volume fraction	30.6%	[86]
Glass fibre density	2.6 g/cm³	[143]
Chopped carbon fibre filament density	1.2 g/cm³	[132]
Chopped carbon fibre volume fraction	10.9%	[86]
Chopped carbon fibre density	1.9 g/cm³	[144]

Both the Infrared and the later described XRD analysis showed, that the gamma phase was prevailing in the non-annealed samples, which indicates a fast cooldown during the manufacturing process. In regular polyamide 6 (without fibre reinforcement), nucleation starts if chain segments randomly align. But those nucleation sites can be destroyed by the chains moving due to heat [145]. This makes it more likely that the nucleation effect of the fibres at faster cool rates is less, resulting in similar levels of crystallinity, which are observed in the first heating run. When slowly cooling the material from the melt (in the first cooling run), it is assumed that the nucleation effect of the much more randomly aligned chopped fibres played a more significant role as they provide more nucleation sites. This resulted in a higher crystallinity of the chopped carbon fibre filament in the second heating run. However, a more in-depth analysis is required to confirm this hypothesis. Since both the alpha and gamma phases are reported to have similar melting enthalpies, the phase change can be ruled out as a reason for the change in enthalpy [146]. The characteristic melting temperatures and graphs for the unprocessed filament confirm the values reported in literature [86].

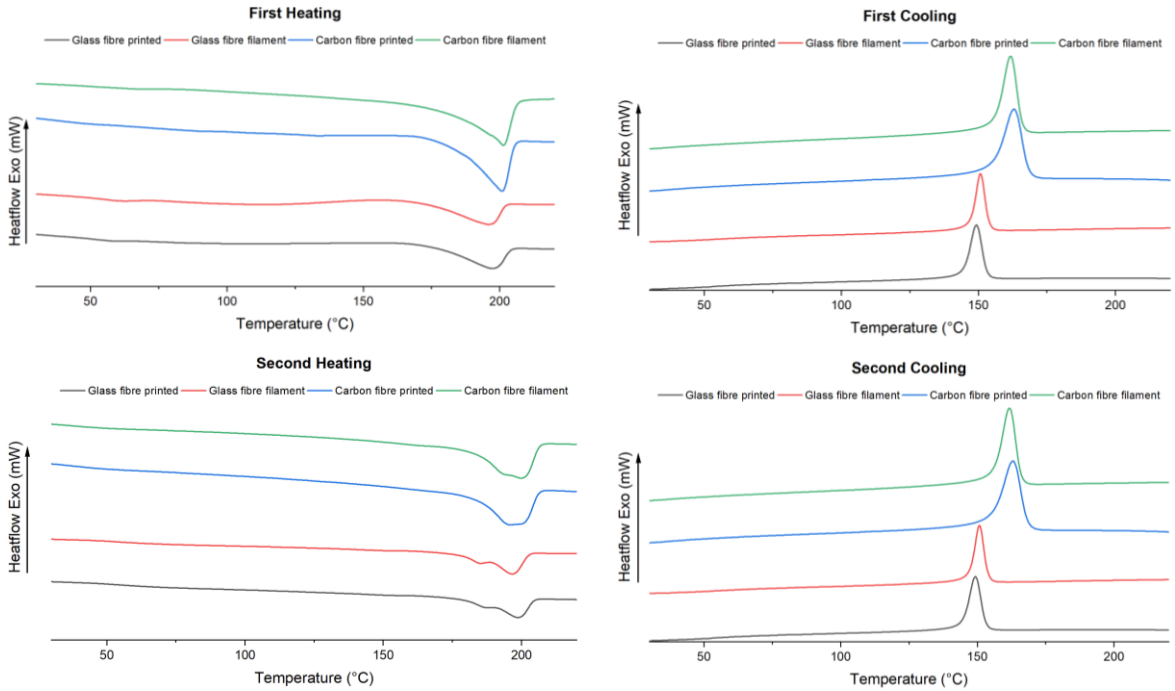

Figure 19: DSC results for the first and second heat run (10 K/min) and the first and second cooling run (10 K/min) of the raw filament as well as the processed chopped carbon fibre and continuous glass fibre material.

Table 9: DSC Results for the 10 K/min heating program with 5 mg samples. The water loss and fibre content have been considered for the calculation of the enthalpies.

	Melting Temperature T_M 1st heating [°C]	**Melting Temperature T_M 2nd heating [°C]**	**Crystallisation Temperature T_C [°C]**	**Melting enthalpy 1st heating [J/g]**	**Melting enthalpy 2nd heating [J/g]**
Glass fibre filament	196	185/197	151	49	41
Glass fibre printed	197	187/198	150	49	42
Carbon fibre filament	201	195/200	163	52	48
Carbon fibre printed	200	195/200	162	52	47

3.5.3 XRD analysis

The results of the XRD analysis for the chopped carbon fibre reinforced polyamide are shown in Figure 20. The peaks at 23.4° and 28° are caused by the alpha phase, whereas the peak at 24.9° is caused by the gamma phase. The right shift when plotting the reflection over the angle compared to values from most of the literature is because a cobalt cathode was used instead of a copper one [147]. The d-spacings calculated using the Bragg's equation, which resulted in 0.441nm and 0.369nm for the α (200) and α (002)/(202) peaks and 0.412nm for the γ (200) peak were in good accordance with values reported in literature for polyamide 6 [148]. As a result, the densities of the crystalline phase are reported to slightly change from 1.16 g/cm³ (γ -phase) to 1.21 g/cm³ (α -phase). As can be expected, the density of the amorphous phase, where the distances between the polymer chains are greater, is only 1.09 g/cm³ [146].

The gamma phase was dominant in the untreated material, but the alpha phase was also present, which is indicated by the shoulders besides the gamma peak. The presence of the gamma phase indicated, a fast cooldown during printing. As the annealing temperature increased the alpha phase became more prevalent with almost no gamma phase left at 185°C and with it completely having disappeared at 200°C. This phenomenon, with the occurrence of phase transitioning below the melting temperature in the materials solid state, is referred to as the Brill transition [149]. A study analysing nylon 66 suggests that this phenomenon

could be caused by the relaxation of the amorphous phase. Increased chain mobility in the non-crystalline phase allows for the phase transition to take place [150]. Instead of applying the energy in the form of temperature, this transition can also be enabled by applying mechanical energy in the form of material deformation [151]. As can be seen in Figure 12 the Brill transition fully developed after 0.5h of annealing time since the alpha peaks are identical for each of the different exposure times at the given temperatures. Since the chain mobility of the amorphous regions also is expected to have increased with temperature this observation was in accordance with the early stated explanation.

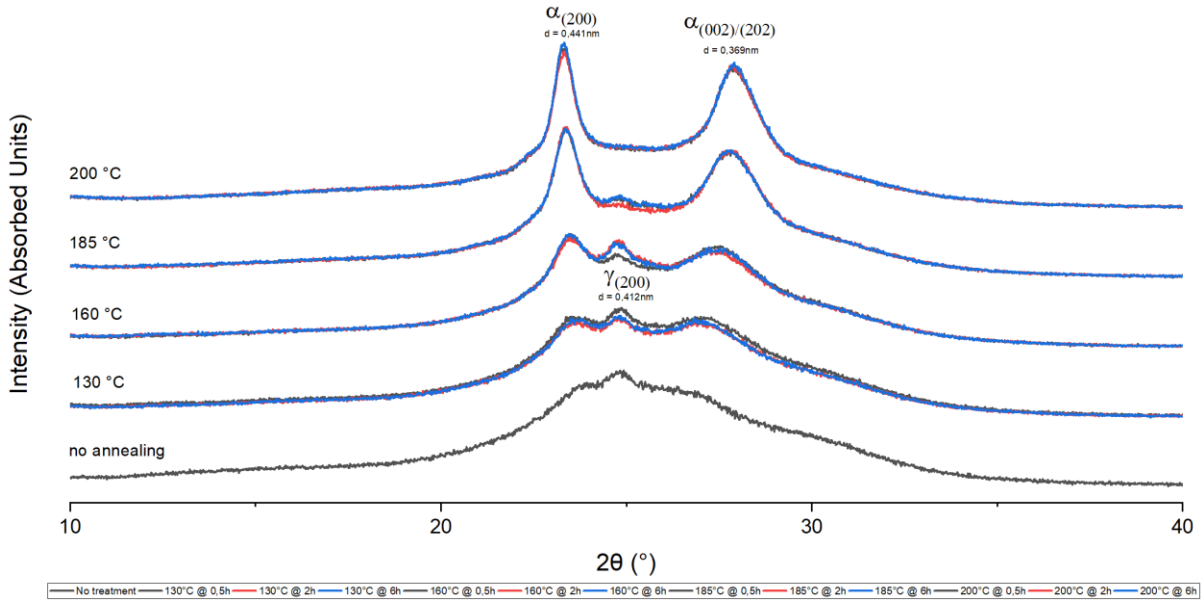

Figure 20: XRD analysis of the chopped carbon fibre filament for the different annealing times and temperatures

Figure 21 shows the XRD analysis for the continuous glass fibre material with no heat treatment as well as annealed at 200°C for 6h. The intensity of the signal and peaks was significantly lower compared to chopped carbon fibre material. This was because of the higher fibre content, which covers a larger area of the measured surface. Additionally, the noise appears to have increased as well. None the less, the same transition from the gamma phase to the alpha phase was observed.

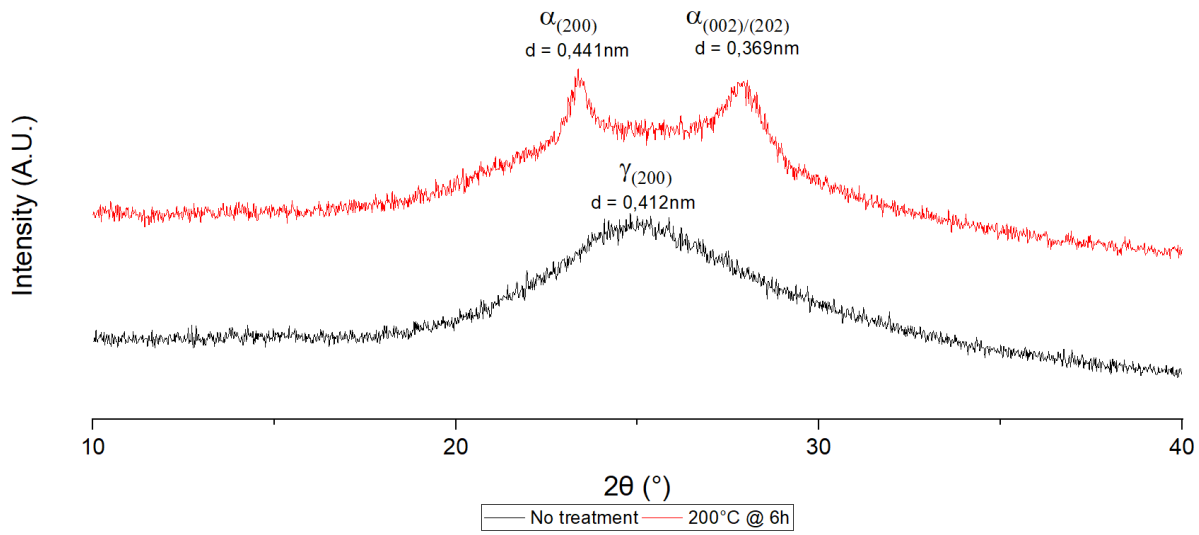

Figure 21: XRD analysis of the processed glass fibre material with no heat treatment applied (bottom) and annealed at 200°C for 6h (top)

3.5.4 Tensile Testing

Averaged Stress-Strain graphs for the mechanical tensile tests of the chopped carbon fibre are shown in Figure 22 and the corresponding mechanical properties are shown in Figure 23. The Young's modulus was calculated at a 1% strain. It was observed that all properties changed in a similar way if annealed at 0.5 and 2h. At 6h the material became slightly stiffer and more brittle, while the ultimate tensile strength (UTS) did not change significantly.

The untreated material has a tensile strength of 19MPa, a Young's modulus of 0.75 GPa and breaks at 7.1% elongation. The following mentioned mechanical properties refer to the samples annealed for 6 hours. Annealing at 130°C did not lead to any significant improvements in the UTS or the Young's modulus, but the elongation at break decreased to 4.1%. At 160°C the Young's modulus and UTS increased to 1.1 GPa and 21 MPa, whereas the elongation at break decreased to 3.7%. A further decrease to 1.9% occurs and the UTS and Young's modulus increase to 24 MPa and 1.8 GPa respectively when annealed at 185°C. At 200°C the highest UTS and Young's modulus of 29 MPa and 2.4 GPa were measured, but also the lowest elongation at break of 1.2%. The latter two Young's moduli are even higher than the manufacturers specification, which reports 1.4 GPa [132].

All curves, except for the samples annealed at 200°C for 6h, show a curvature that increases with increasing strain. This viscoelastic behaviour is typical for semi crystalline plastics like

polyamide 6 [152]. The test samples annealed at 200°C for 6h failed at 1.2% strain with only a linear stress-strain relation. While the Young's modulus and ultimate tensile strength continuously increased the elongation at break decreased as the annealing temperature was increased.

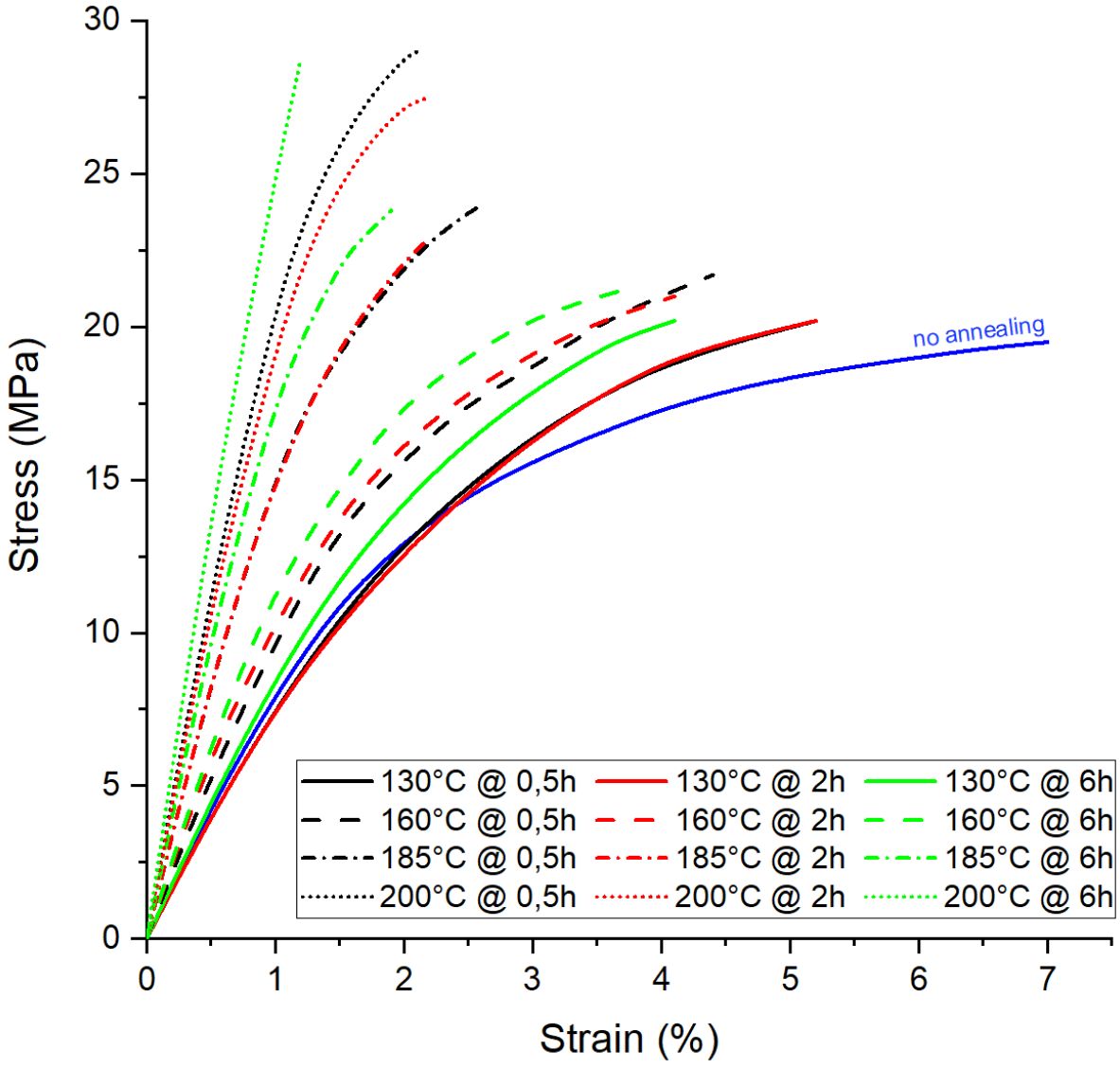

Figure 22: Tensile tests in "X3" direction of the annealed chopped carbon fibre reinforced test samples. The bottom graph is the non-annealed material as a reference

The tensile test of the non-annealed glass fibre test sample showed a failure in three steps as can be seen in Figure 24. At a stress of 7.3 MPa the continuous glass fibre layer ruptured, but the outer chopped carbon fibre layers were still intact holding the test sample together. At 13% elongation, the outer layers broke as well, and the two halves of the test sample were

only held together by a few loose fibres. One end of the fibre was stuck to the top half of the test sample, the other end to the bottom half. As the elongation increased, the fibres were slowly pulled out accompanied by high pitch sounds. Annealing completely changed the failure mode. As can be seen in Table 10 the Young's modulus and UTS almost increased by a factor of three. When fracture occurred, the inner continuous glass fibre layer and the outer chopped carbon fibre layer snapped simultaneously.

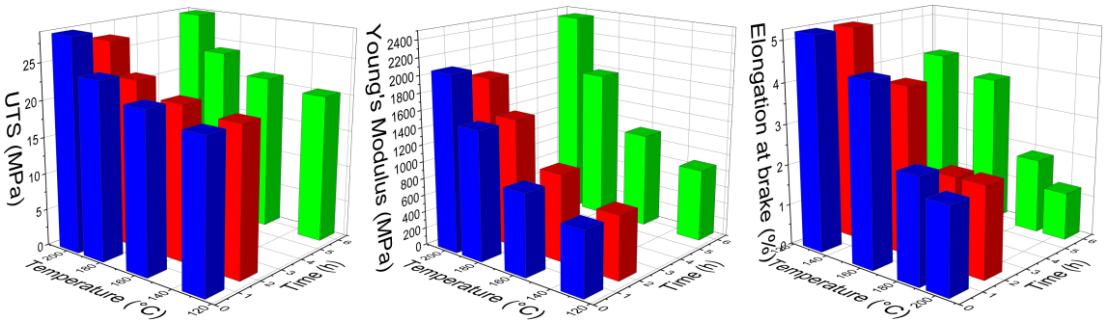

Figure 23: Ultimate tensile strength (left), Young's modulus (middle) and Elongation at brake (right) of the chopped carbon fibre test samples. Note that the temperature scale is reverse for the last diagram.

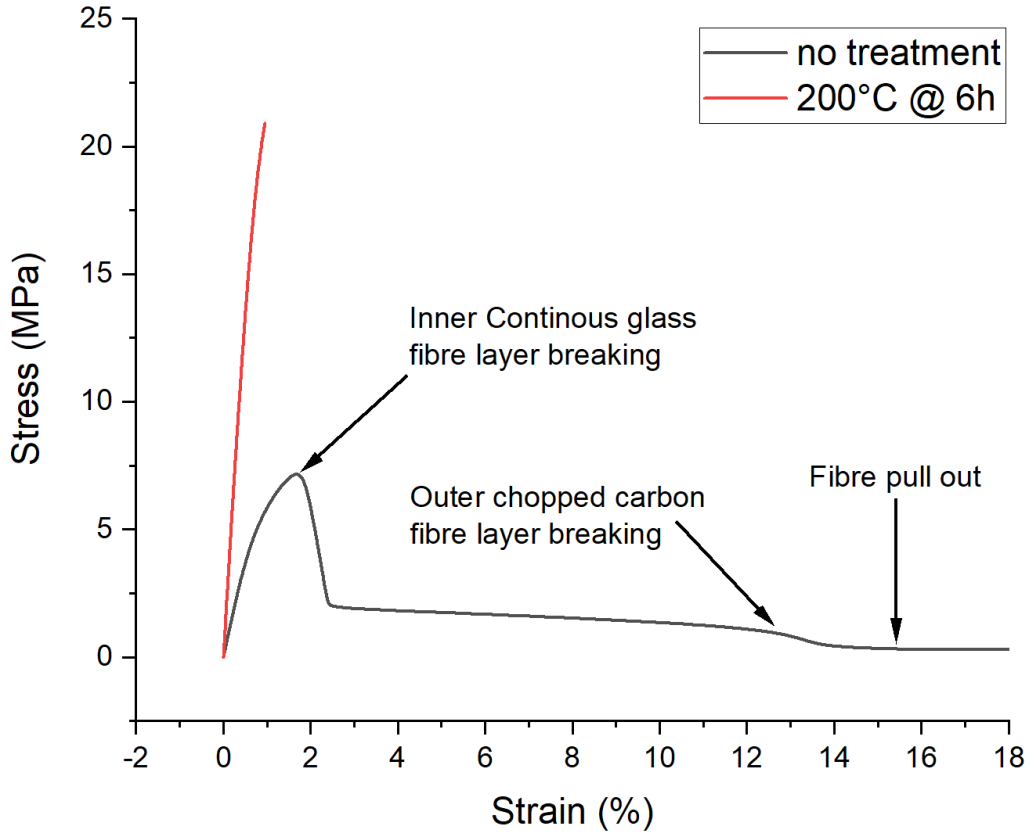

Figure 24: Stress-Strain diagram of the continuous glass fibre material with no heat treatment applied and annealed at 200°C for 6h

Table 10: Mechanical properties of the continuous glass fibre material before and after annealing.

	UTS [MPa]	**Elongation at break** [%]	**Young's modulus** [GPa]
GF no treatment	**7** ± 1	**1.7** ± 0.4	**0.6** ± 0.1
GF 200°C @ 6h	**21** ± 3.5	**1** ± 0.2	**1.9** ± 0.4

3.5.5 Geometric changes

The average flatness of the chopped carbon fibre test samples was 0.044mm with a standard deviation S_X of 0.015mm. The changes in flatness for each of the different test tubes is shown in Table 11. As can be seen, the flatness decreases slightly during the annealing process, but there was no pattern indicating a correlation with temperature or time. For the thickness and width no significant changes were measured. However, the changes in the tube height illustrated in Figure 25 decreased and showed a correlation with the annealing temperature. As the temperature was increased from 130°C to 160°C to 185°C the shrinkage increased from 0.3mm to 1mm to 2mm when annealed for 0.5h. A further increase to 200°C did not lead to a further decrease in height. When looking at the three annealing times there was also a slight increase. At 160°C the shrinkage increased from 1mm to 1.16mm to 1.57mm when annealed at 2h and 6h. Since the decrease in flatness has no correlation with time or temperature, but the height shrinkage does, it can be concluded that no creep happened during the annealing process and that the part shrunk uniformly. Flatness in the continuous glass fibre test samples annealed for 6h at 200°C decreased from 0.085mm to 0.246mm, while the height decreased by 1.4mm. Since the fibre content was higher and the fibres do not shrink it is to be expected that the shrinkage is smaller compared to the chopped carbon fibre test samples. Although it was not possible to capture on a picture, the decrease in flatness was caused by a slight rotation of the tube along the "X3" axis. When the annealed test tube was placed on a flat surface, only three corners were in contact with the surface while the fourth one was slightly above the ground.

The loss in weight for the chopped carbon fibre sample after the annealing process was 1% on average. No correlation between the annealing time and temperature can be observed, which is to be expected since even the lowest annealing temperature is 30°C above the boiling point of water. This is less than the 4.2% weight loss reported in the DSC section. Since the

DSC measurements were conducted with very low masses, water from the air could easily be absorbed while they were stored. So that value represents the saturated material. Since the parts were annealed right after the printing process, there was no time for the water content to saturate and therefore the weight loss is expected to be lower. But even if the material was saturated, the difference could be explained by moisture that escapes from the material but gets trapped inside the large air voids (comp. next section).

Table 11: Changes in flatness in mm for the chopped carbon fibre test tubes

Flatness [mm]		Annealing Time		
		0,5h	2h	6h
Annealing Temperature	130°C	+0,015	+0,002	+0,006
	160°C	+0,004	+0,006	+0,006
	185°C	+0,012	+0,009	+0,005
	200°C	+0,011	+0,009	+0,009

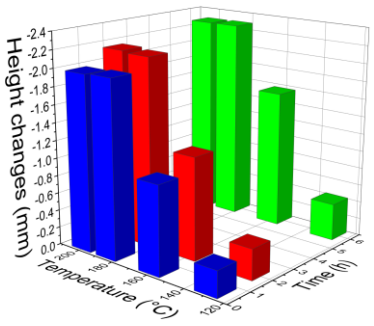

Figure 25: Changes in height for the chopped carbon fibre samples

3.5.6 Optical microscopy

Figure 26 shows the fracture surfaces of the chopped carbon fibre test samples. The one on the left was annealed at 130°C for 6 hours and it is clearly visible that fracture surface was smooth and planar without any visible deformation. It almost creates the impression, that the print had finished at that layer. This is a clear indication, that failure took place at the interface between two layers. The air inclusions between the strands were also clearly visible.

The right side of Figure 26 shows the fracture of the sample annealed at 200°C for 6 hours. The air inclusions were still clearly visible. But when looking at the interface of the wall layer with the 45° inner layer (at the upper part of the picture) it looks like the layers merged together. Furthermore, the failure did not create a planar fracture surface. Instead, parts of the underlying layers got ripped out, which indicated that the material failure extended over multiple layers.

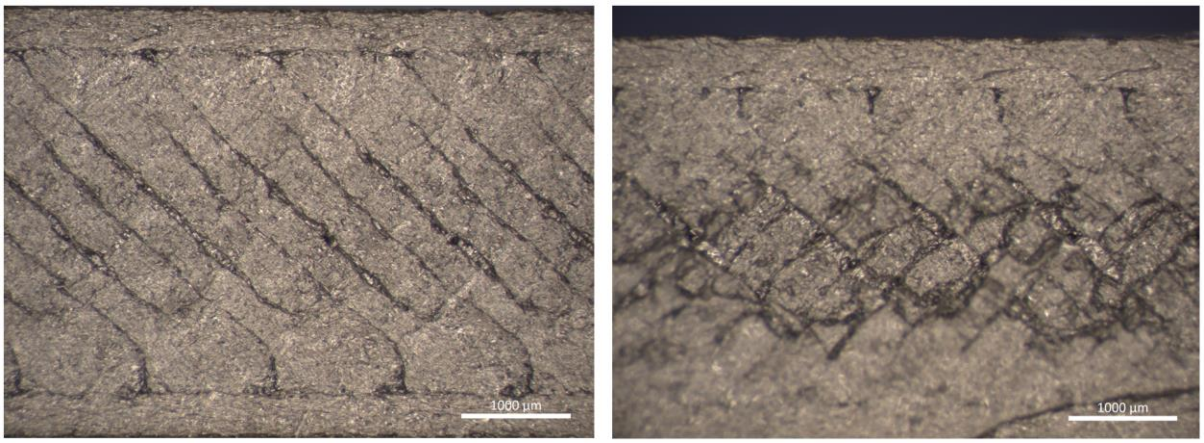

Figure 26: Fracture surfaces of the chopped carbon fibre annealed at 130°C (left) and 200°C (right) at a 1.6x magnification. To illustrate the depth of the failure surface, the focus on the right-hand side is put on the lowest level of the fracture surface making the top layers appear out of focus. The scale applies to the focussed layer, which makes the part on the right appear larger even though the same magnification is used.

After cutting the samples out of the tube and before testing them the glass fibre test samples were inspected via optical microscopy. On the left side of Figure 27 the non-annealed sample is shown with only small air inclusion, that were caused by the printing process. On the right-hand side, a test sample annealed at 200°C for 6 hours is shown. The number and size of air inclusions increased significantly compared to the non-annealed sample. Both rows of air inclusions were located exactly between the different strands, which are roughly 900 µm wide. Since microscopic images only provide information about an individual cross-section a large number of images at different planes would be required for a statistical significance. For precise calculations of the air-void ratio, computer tomography would be required. Unfortunately, this technology was not available and should be used in future studies.

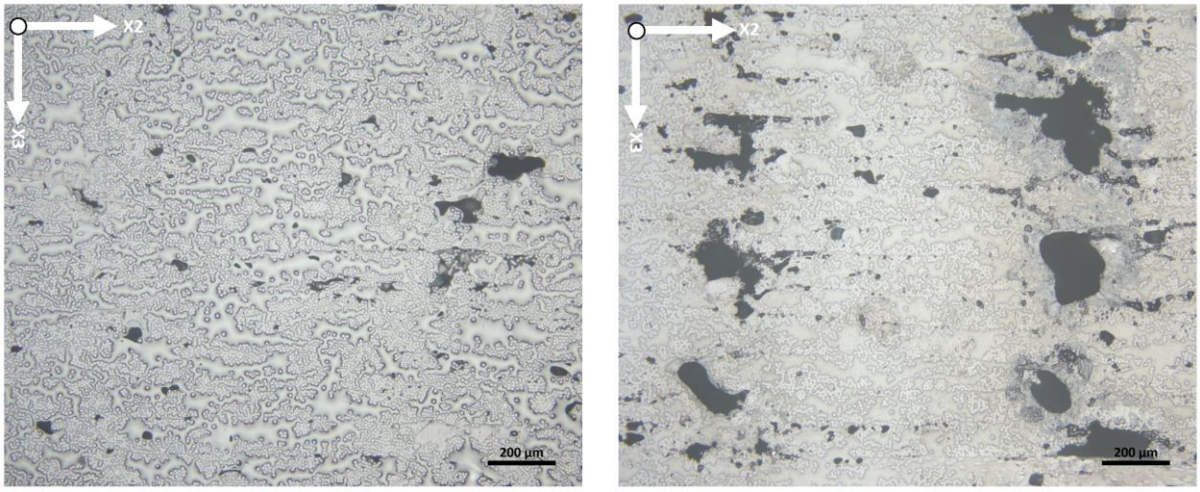

Figure 27: Microscopic images showing small air-inclusions caused by the printing process in the non-annealed sample (left) and large air-inclusions after the annealing process (right).

In Figure 28, the fracture surfaces of the non-treated continuous glass fibre reinforced test sample as well as of the annealed one are shown. The fibre pull-out previously described in the mechanical testing section is illustrated for the non-annealed sample, whereas the annealed sample shows no signs of fibre pull-out.

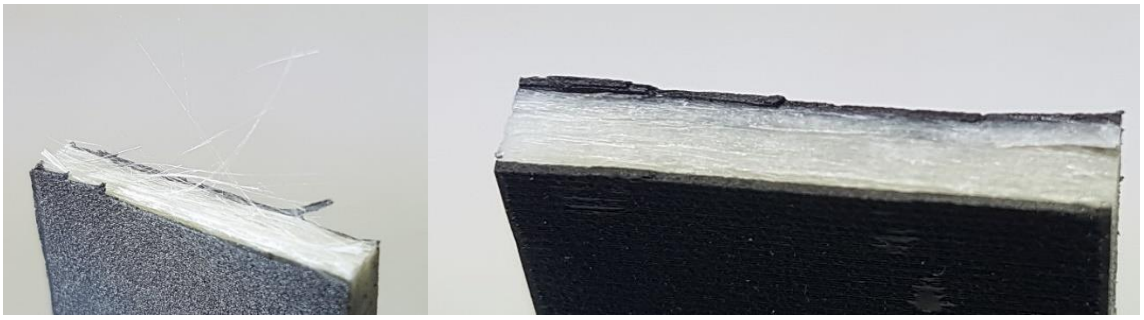

Figure 28: Failure surfaces of the continuous glass fibre filament with no treatment applied (left) and annealed at 200°C (right)

3.6 Discussion

The exact composition of the two filaments used for this study was unknown at the beginning, as the manufacturer did not disclose any information about them. The infrared spectroscopy revealed that the matrix material for both the chopped carbon fibre and the continuous glass fibre filament by “Markforged” are polyamide 6. The same results were obtained by Pascual-Gonzalez et al. who published their results while this project was ongoing [86].

The DSC analysis of the processed material showed no cold crystallization peaks. “Cold crystallization” refers to the freezing of the polymer chains in their amorphous state when rapidly cooling a crystalline plastic from its liquid state. This happens when there is not enough time for the crystals to form. When reheating a material in such a state, an endothermic peak between the glass transition and the melting point is caused by the formation of crystals. As shown in the literature review, this phenomenon is not uncommon in the FDM process. However, this was not the case for the materials and process parameters investigated in this study.

X-Ray diffraction analysis as well as the infrared analysis showed that the gamma phase was prevalent in the non-annealed parts. Since the gamma phase is thermally unstable, its existence suggested a rapid cooldown of the material after it has been extruded through the nozzle. These investigations also showed that annealing caused a transition from the gamma to the alpha phase. While the latter has a slightly higher density, the decreased tube height is most likely also caused by a decrease in the air void ratio. Due to the lack of appropriate measurement equipment, like a CT scanner, this aspect could not be investigated. The change in air void ratio and the phase transition are suspected to be the primary cause of the increase in Young’s modulus for the test samples annealed for 0.5h and 2h. A similar increase of the alpha phase at higher annealing temperatures has been reported for thin isotropic polyamide 6 samples [153]. At an annealing temperature of 200°C the elongation at break was reported to decrease by 50% and the strength to increase by 25% compared to an annealing temperature of 120°C. Another study used nanoindentation to determine the modulus of samples annealed at 60 and 200°C [154]. They found a correlation between an increase in the alpha phase and the modulus. A possible explanation for the slightly higher increase in stiffness when annealed at 6h is the additional diffusion or entanglement of the polymer chains between two layers, as the changes in height did no suggested a significant change in the air void ratio and an increased phase transformation was also not observed. In literature the processed of increased entanglement is referred to as autohesion for which the annealing time has been reported as an important parameter [155]. The crystallinity did slightly increase from 23% to 27% when annealed for 6h at 160°C, which is also expected during the autohesion process. But there was no further increase when annealed at 185°C. This indicates that the change in crystallinity during the annealing process did not have a large influence on

the improvement of the mechanical properties as the Young's modulus did increase when comparing those two annealing temperatures. However, this needs to be investigated in more detail since not only the degree of crystallinity but also the crystal structure has an influence on the mechanical properties [154].

Optical microscopy revealed that the chopped carbon fibre test samples have large air inclusions between the adjacent strands. Since the printing directions altered between +/- 45° the layers did not have a continuous contact surface. When loaded with tension these air inclusions are expected to cause a stress concentration at the layer interface (notch effect) and act as crack initiators causing the part to fail prematurely. As the material becomes stiffer due to the heat treatment, the notch effect increased as the stress concentration at lower elongations at the layer interface was higher. Furthermore, the oxygen trapped inside the part probably will partially oxidize the internal surfaces resulting in localized embrittlement, which worsens the influence of the notch effect even more. So, while it seems that the annealing makes the material more brittle the notch effect is making the material appear more brittle than it is.

For the untreated continuous glass fibre composite, the weak bonding between layers is suspected to be the main cause of the observed brittle behaviour. Additionally, the brittle behaviour is expected to be caused by the continuous fibres. Since the fibres have a significantly higher Young's modulus than the polyamide 6, at the fibre-matrix interface there is a sudden change in the materials' stiffness. This leads to a high stress concentration in the areas between two fibres, which initiates material failure [156]. Generally, the brittle behaviour of continuous fibre reinforced plastics has nothing to do with the printing or the annealing process and also occurs when conventional manufacturing methods are used. However, optical microscopy showed that air-voids were present as a result of the printing process and the air void ratio significantly increased during the annealing process, causing further increase of the notch effect. The increase in air-void ratio was a result of energy stored in the bend fibres. As the fibres are bend around the 90° corners of the tube, energy is stored, like a hairspring. Heating the polyamide 6 softens it, allowing for the continuous glass fibres to release tension by moving apart. The fact that the air inclusions appear mainly between the different strands, shows the poor adhesion between layers and the inhomogeneity of the material. If the material was completely homogenous, the air inclusions would have been

distributed equally across the whole cross-section. The fibre pull-out after failure, which was observed for the non-annealed samples, most likely was a result of both the inhomogeneous stress distribution caused by the air inclusions and fibres as well as the low UTS. The energy released at the point of failure is not enough to separate the whole cross-section simultaneously and local areas remain connected. Since the tensile test was not stopped at this point the few remaining fibres attached to both halves of the failed sample were slowly pulled out as the test continued. The much higher stress at failure for the annealed test samples caused simultaneous separation of the whole cross-section and therefore no fibre pull-out was observed.

3.7 Future research needs

While the heat treatment has led to a significant increase in the Young's modulus, the microscopy analysis showed that the test samples still had a high air-void ratio. A detailed analysis of the distribution and size of the air-voids should be carried out using computer tomography. The high air-void ratio could be addressed by applying pressure during the annealing process, which is investigated in the next chapter. The mineral oil, which was used to prevent the oxidization of the material, would be suited for this purpose, as the incompressible characteristic of the oil allows for its use to simultaneously apply pressure and heat. For industrial applications small throughput times are important, which is why a study analysing the effect of different heating- and cooling rates on the materials properties should be conducted. Furthermore, it would be interesting to see, how the size and structures of the crystals changes during the annealing process as a function of annealing time and temperature. This could be done using transmitted light microscopy with polarized light.

3.8 Conclusions

In this chapter the effect of annealing on the mechanical properties in build-up direction of chopped carbon fibre and continuous glass fibre reinforced polyamide 6 parts produced by fused filament fabrication was investigated. It was shown that the strength and stiffness in build-up direction was significantly improved by applying a heat treatment. The best results were achieved by annealing the parts at 200°C, which is the melting point of the material, for 6h. The Young's modulus for the chopped carbon fibre and continuous glass fibre increased

from 0.75 GPa and 0.6 GPa to 2.4 GPa and 1.9 GPa respectively, while the UTS increased from 19 MPa and 7.3 MPa to 29 MPa and 20.9 MPa. Decrease in the elongation at break was observed, which was most likely caused by air inclusions inside the material causing a notch effect. For the chopped fibre material, the reinforcement had no effect on the failure mode as the large air voids still dominate the material failure. However, for the continuous fibre reinforced material the fibres played a significant role as the energy stored in the fibre bends caused a significant increase in the air voids.

3.9 Application in practice

The containers for the heat treatment process in this study were tailored to the geometry of the test samples. This was done to only have a small temperature difference between the air in the oven and the test sample. Of course, this approach is not practical in industrial applications since every part would need its own container. A concept that might work is shown in Figure 29. The oil is kept in circulation by a pump thus avoiding the build-up of a temperature gradient within the container. Temperature changes are realized by either pumping the oil through a heater or a cooler.

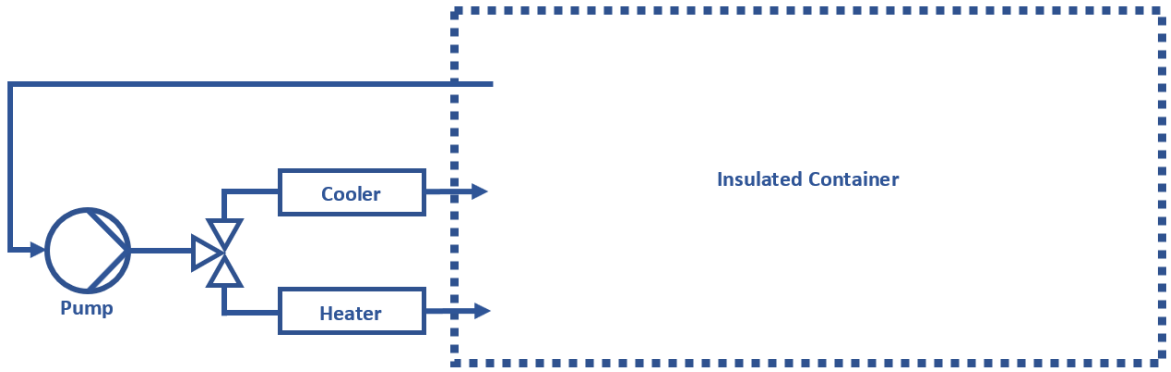

Figure 29: Concept for using the heat treatment process in practice

Chapter 4

Pressure Treatment

As shown in the previous chapter, the annealed test tokens contained large air-voids after the annealing process. In order to reduce the air-void-ratio and further increase the mechanical performance a pressure treatment study was conducted. The purpose was to determine how different pressure levels affect the air inclusions. Contrary to the previous chapter the mechanical properties in both the build-up direction as well as the direction perpendicular to it were investigated. This was done to determine if the pressure treatment results in a transverse isotropic material. Based on a literature review the research gap was identified and the experiments were designed accordingly. After presenting and discussing the testing results the future research needs are elaborated. The results of this chapter were published in the “Progress in additive manufacturing” journal [157].

4.1 Literature Review

While this research was ongoing, a study similar to the previous chapter was conducted by Wang et al. They made similar observations regarding the air-inclusions when analysing the annealing effects of continuous carbon fibre-reinforced amorphous thermoplastic for temperatures varying between 50°C and 200°C [158]. As was the case for the continuous glass fibre reinforced thermoplastic, their material contained air-voids due to the printing process

before the heat treatment process. While annealing at 100°C for 4h lead to a 1% decrease in air-voids, annealing at 200°C led to a 6% increase.

There has also been some research regarding the effects of pressure on the annealing process. Qinghao et al. subjected additively manufactured parts to 5MPa of pressure for 10 minutes after heating them to 230°C [159]. Instead of applying constant pressure they chose to use spacers to control the materials thickness. The spacer thickness was chosen so that the final thickness in theory have zero void content. The initial air-void content of 12% was reduced to 6% and the flexural strength increased by 93% as a result. While they assumed that the matrix material to be Polyamide 6, an in-depth investigations of the filament showed that it is actually an amorphous thermoplastic [86]. Pascual-González et al. conducted similar experiments but with temperatures between 70°C and 270°C and applying a constant 1 MPa of pressure for 15 minutes with samples heated on a heating plate [160]. While temperatures of up to 170 °C led to a significant decrease in porosity large air-voids close to the edges of the part remained after the treatment. Almost complete consolidation was observed for temperatures at 210 °C and above. However, the parts' thickness decreased due to the application of force from the top while the width and length increased as the annealing temperature was increased. As a result, annealing at 150°C was recommended.

The main purpose of this study was to determine to what extend the strength and stiffness can be increased and the air-void ratio decreased by applying pressure and heat to the additively manufactured continuous fibre reinforced parts. As reported in the previous paragraph other studies have reported that the material runs away when just applying pressure from one side. Consequently, a mould press was chosen for this study. The mould prevents the diffluence of the high viscosity polyamide and was expected to create an environment similar to that in an autoclave. The difference between the existing studies and the present one is the material that is being used as well as the method for pressure application. In this work a semicrystalline glass fibre reinforced thermoplastic was investigated, whereas previous works focused on a carbon fibre reinforced amorphous thermoplastic. In addition, a pressure-controlled mould press was used instead of applying the pressure only from one side. Furthermore, the effect of different pressures was investigated, to determine if commonly available autoclaves provide a sufficient amount of pressure.

4.2 Experimental setup

The experimental setup was similar to the one presented in the previous chapter, so there is some overlap in this section.

4.2.1 Materials

This work focuses on parts produced by a Markforged “Mark Two”. The proprietary software that controls the printer mandates that all parts must be surrounded by at least one layer of Onyx, which is polyamide mixed with chopped carbon fibres, on all sides. Before processing the material was continuously stored in a dehumidified storage box at room temperature, as recommended by the manufacturer

4.2.2 X-Ray radiography

To quantitatively compare the reduction of air voids within the material, X-Ray radiography was used. Images were taken with a “Y.Cheetah” X-Ray System from “YXLON International” set to 100 kV and 39 µA.

4.2.3 Microscopy

Magnified images of the fracture surfaces of the different test tokens were captured by a Leica MZ6 with an Axiocam 305 Color attached to it. For higher magnifications, a LEO 1430 scanning electrode microscope was used with the beam voltage set to 20 kV.

4.2.4 Caloric Characterization

A “DSC821e” differential scanning calorimeter (DSC) from “Mettler Toledo“ with a “FRS5” sensor was used to analyse the samples with a temperature rate of 10 K/min with 5 mg samples in standard 40 µl pierced aluminium pans starting from 30°C and up to 230°C according to ASTM D3418 [9]. Calibration of the measurement device was conducted according to the user manual and standard by using Indium as a reference material. The test chamber was purged with 50 ml/min of nitrogen, and each measurement was repeated twice. Samples were extracted with a sharp cutting tool such that a flat surface resulted. The degree of crystallinity K was calculated as described in the previous chapter.

4.2.5 X-Ray Diffraction

X-Ray diffraction (XRD) measurements were performed using a Malvern Panalytical Empyrean. The machine was equipped with a cobalt cathode (wavelength = 1.7890100 Å), and the voltage and current were set to 40 kV and 30 mA. The intensity data were collected from 10° to 40° every 0.02° for a period of 0.7 s.

4.2.6 Mechanical Testing

Tensile testing was performed on an Instron 5966 machine. The strain rate was set to 0.01/min as recommended by ASTM D3039 to achieve a quasi-static load [131]. Notch effects, which can result from using mechanical gages, were avoided by using an Instron 2663-901 video extensometer for non-contact strain measurements. The length, height and width at the centre were measured using a calliper.

All test tokens are designed according to the ASTM D3039 standard with a length of 110 mm. In our previous study, aluminium tabs were used, and the test samples produced acceptable failure modes (failure within the gauge section). However, the pressure-treated samples failed directly at the tabs. As reported, the materials' inner defects in the previous study led to failure, which most likely overshadowed any inhomogeneities at the tabs. The standard does not dictate a specific material; thus, epoxy-laminated circuit board was tested, as recommend by Adams [161]. This test also led to tab failure; therefore, polyamide tabs were tested, which produced acceptable failure modes.

The coordinate axes were named in accordance with previous works on conventional fibre-reinforced plastics. "X1" refers to the fibre direction, "X2" is perpendicular to "X1" and on the same plane and "X3" is perpendicular to the printing bed (often referred to as the lay-up or build-up direction). In transverse isotropic materials, the stiffnesses and strengths in the "X2" direction are the same as in the "X3" direction (comp. Figure 1). This work focuses on the material performance in the "X2" and "X3" directions.

Tensile samples:

As in the previous chapter, a rectangular tube with a concentric fill pattern was printed, from which the tokens for the build-up strength test ("X3" direction) were extracted (comp. Figure 11). The "start rotation percent," which determines the location of the starting point, was

chosen to be either 1%, 26%, 51% or 76%. Through this method, the starting point of the fibre paths was in the corners and the samples were therefore homogenous in the tested section. The starting point is illustrated in Figure 11 in the top right corner. As mentioned previously, the printer mandates a chopped carbon fibre outer layer for the continuous glass fibre samples. The chopped carbon fibre layer is represented as a white line in the figure, whereas the orange line represents the glass fibre paths. The layer height for both materials was 0.1 mm. The test tokens for the "X2" direction were printed individually with the dimensions shown in Figure 30. After the pressure treatment, the edges were milled off to achieve homogenous samples with no connecting ends.

Cutting:

The cuts were made using a Mutronic Diadisc 4200 high precision saw equipped with a custom air-cooling system that uses high pressure air from the system in the workshop.

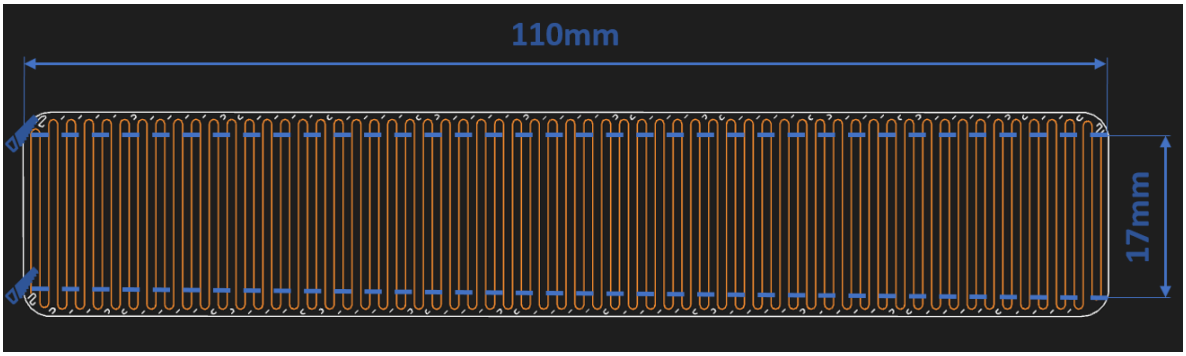

Figure 30: X2 tensile test geometry with cutting patterns. The fibre paths are orange and the onyx paths are white

4.2.7 Damping and modal frequencies

The influence of the pressure treatment on the damping and modal frequencies of the X2 tensile test tokens was evaluated using Siemens "LMS Test.Lab". A Polytec PDV-100 laser vibrometer was used to measure the vibrations. This option was chosen, because attaching an accelerometer would significantly influence the mass and damping resulting in inaccurate measurements.

Vibration excitation via a loudspeaker was tested (comp. Figure 31). However, due to the small sample area, it was not possible to sufficiently transfer enough energy into the sample even at elevated sound levels. The result was very distorted signals, which did not provide reliable information. However, the same setup was successfully tested with larger composite plates, producing accurate results. The samples were consequently exited with a “PCB 084A17” impulse hammer that is designed for low mass (comp. Figure 32). For each point, the measurement was performed out five times and the coherence and frequency response functions were monitored. The measurement was discarded and repeated in if any error was detected (e.g., pushing the sample instead of giving an impulse).

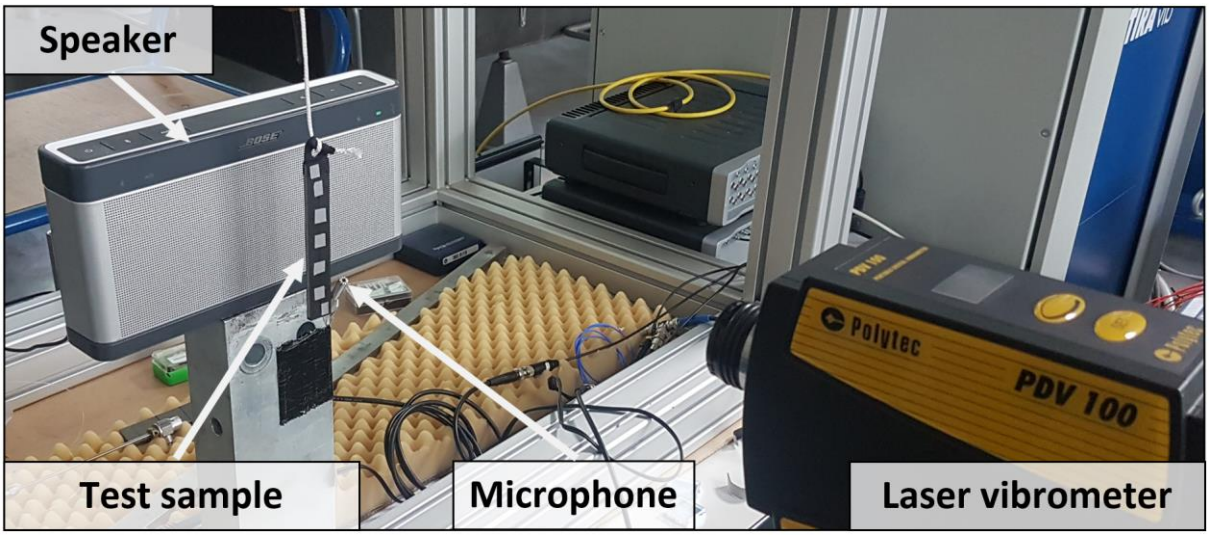

Figure 31: Vibration excitation via loudspeaker

Figure 32: Vibration excitation via impulse hammer

4.2.8 Heat treatment

A “Memmert 100-800” oven, which allows the setting of ramp-up and cool-down heat rate as well as the hold temperature in between, was used. This oven has two P100 temperature sensors built in, which are positioned at the top of the chamber. The air circulation fan was set to its maximum speed to ensure that no temperature gradient built up inside the heat chamber.

4.2.9 Finite Element Analysis

For the finite element analysis, the structural analysis and simulation software from ANSYS® was used. The mesh was created using the auto meshing feature with a 0.5 µm mesh size, and tetrahedral elements were used.

4.3 Design of Experiment

The post-treatment strength is expected to be a function of the annealing temperature, annealing time and heat-up and cool-down rates. In the preceding investigation, a heat-up rate of 15 K/h and a cool-down rate of 10 K/h were chosen. To improve the throughput time and thereby achieve a higher practical relevance, a heating rate of 60 K/h and a cooling rate of 40 K/h were used in the present study. Figure 39 illustrates the XRD analysis for the increased heating and cooling rates without any pressure applied. The gamma phase, which forms when the polyamide is fast cooled from the molten state, gets transformed into the alpha phase [162]. Thus, this increase did not cause a change in the phase transformation compared to the slower cooling rate. Any observed changes were caused by the applied pressure.

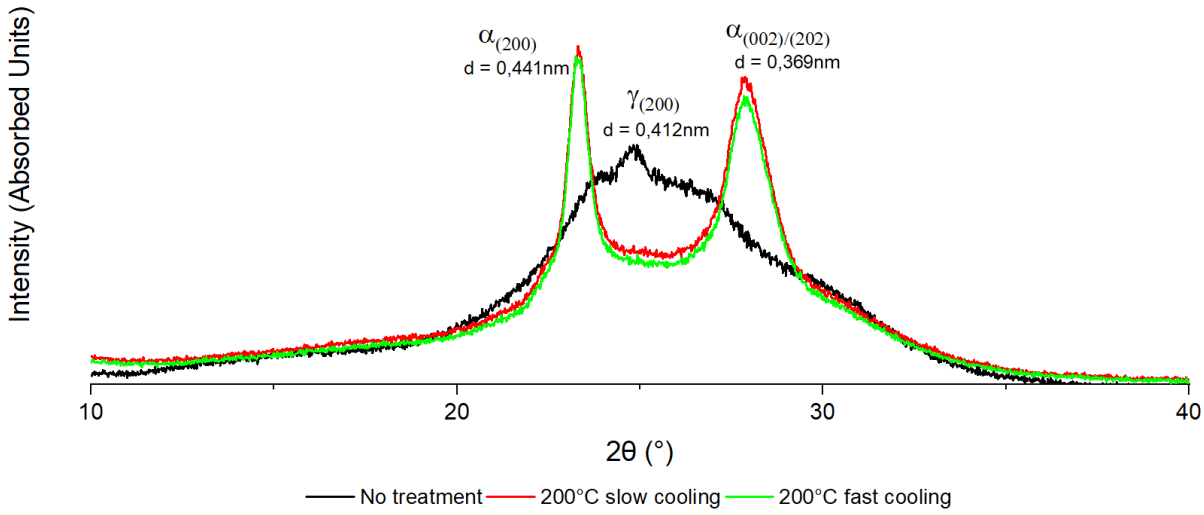

Figure 33: Effect heating and cooling rates on the crystalline phases

While the previous study presented in the chapter showed that paraffine oil is a suitable annealing medium, the simultaneous application of pressure was deemed too dangerous in the context of a university project. A failure of the container containing 200°C hot oil at a pressure of 6 MPa (60 bars) would be a very serious health hazard.

Therefore, a mould press was designed to create the pressure. Figure 34 presents the different components. A steel stamp and mould are connected by six screws with a M10 thread. Disc springs are used to apply and sustain the pressure. The device containing the test tokens was heated up to 200°C and the pressure was then applied using disc springs. After 30 minutes, the pressure was released and the part cooled down at the defined cooling rate.

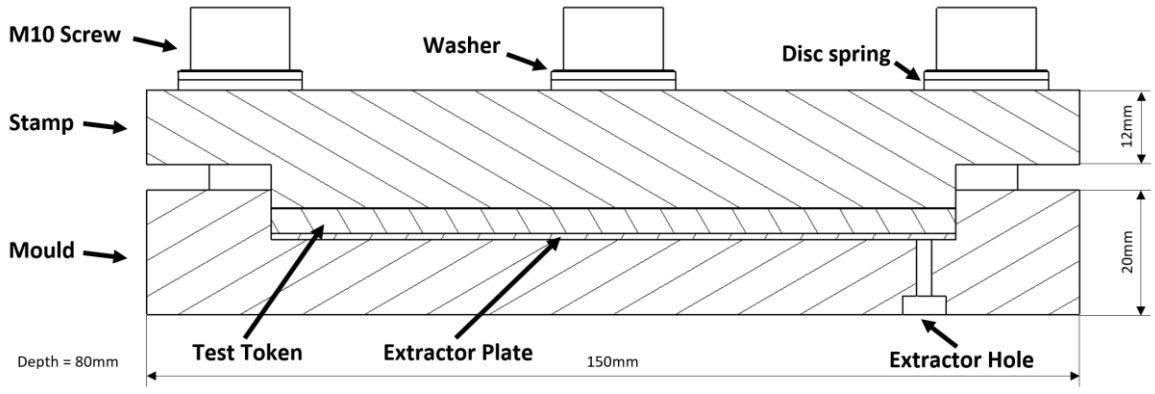

Figure 34: Cross-section of the pressure device.

4.4 Testing results

This section presents the results of the DSC, XRD, damping, optical analysis and the mechanical. The following section discusses the results in further detail.

4.4.1 DSC analysis

Figure 35 presents the results of the DSC analysis. The top curve represents the non-treated material as a reference. The wide melting peak indicates the presence of mixed crystal sizes [163]. The second curve from the top shows the sample annealed at 200°C for 6 h at atmospheric pressure. The peak is significantly narrower than the reference curve, which makes it likely that the crystals have grown/merged. The increase in melting temperature due to annealing was previously observed for polyamide 12 and was attributed to an improvement in the crystalline order [164]. The tokens annealed under pressure at 200°C (but only for 30 minutes) also exhibited a significantly narrower peak. However, the melting temperature did not increase. The different pressures also had no significant effect on the degree of crystallinity, which was measured to be 17.8% on average. This level is slightly lower than the 20.4% crystallinity measured for the samples annealed at 6 h.

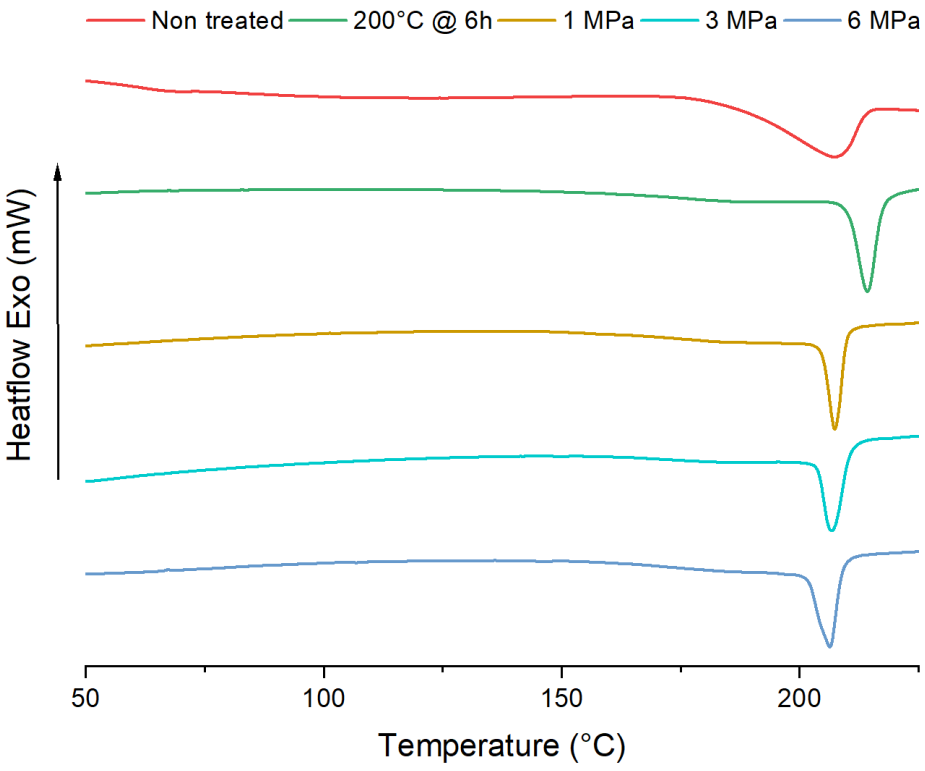

Figure 35: DSC analysis of the non-annealed, heat- and pressure treated samples.

4.4.2 XRD analysis

Figure 36 illustrates the results of the XRD analysis for the different annealing pressures, including both the gamma phase at 24.9° as well as the alpha phase with peaks at 23.4° and 28°. In the untreated material, the gamma phase was dominant, but the broad shoulders show small amounts of the alpha phase. As reported in the previous study, the heat treatment process causes a solid-state phase transition [108]. For the pressure treatment similar observations were made. The gamma phase fully transitioned into the alpha phase as was the case when no pressure was applied. However, the 28° alpha peak was a little more pronounced than the 24.9°, which was the other way around for the heat treatment.

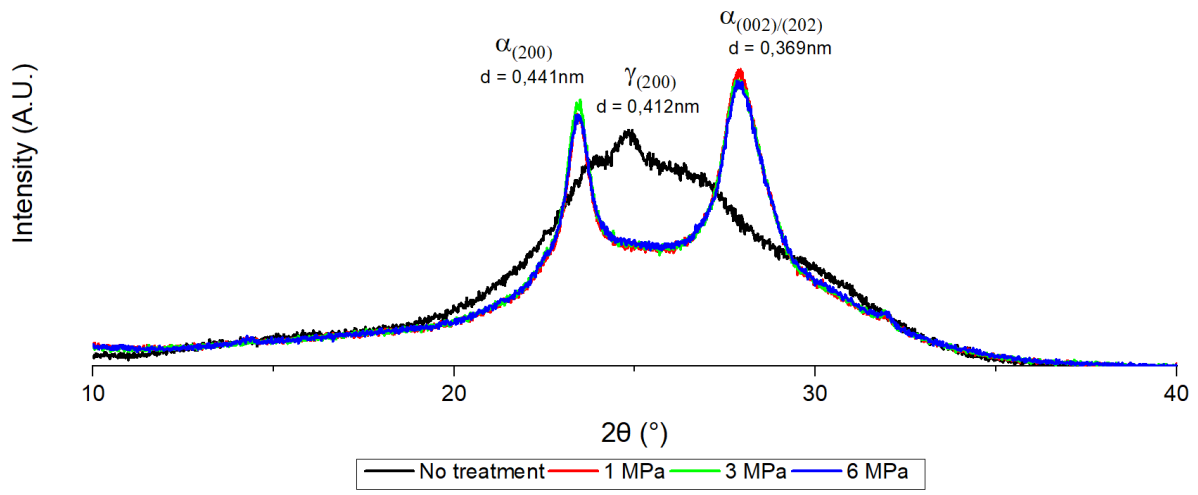

Figure 36: XRD analysis for the different pressures

4.4.3 Tensile Testing

Figure 37, Table 12, Table 13 and Table 14 present the results of the tensile tests for both the X2 (dashed line) and X3 (continuous line) directions. For the untreated samples (black line), the Young's modulus in the X3 direction was eight times smaller (0.6 GPa vs 4.3 GPa) and the ultimate tensile strength four times smaller (7 MPa vs 29 MPa) than in the X2 direction.

However, when applying 1 MPa of pressure (red line), the Young's moduli are almost equal, with 4.9 GPa in the X3 direction and 5.2 in the X2 direction. The ultimate tensile strength increased to 55 MPa for the X2 direction and 34 MPa for the X3 direction. While an increase in pressure to 3 MPa led to a 0.5 GPa increase in the Young's modulus, a further increase to 6 MPa did not lead to a further increase in the Young's modulus in the X2 direction. The same observation was made for the tensile strength. In the X3 direction, an increase to 3 MPa led

to a 0.2 GPa decrease for the Young's modulus and a 7 MPa decrease for the tensile strength. However, these tensile strength results in X3 direction do not represent the full potential of the material, as further discussed in section **4.5**.

Figure 38 presents the unedited stress-strain diagrams for an untreated and pressure-treated X2 sample. There are two phenomena visible: noise from the very beginning for both graphs and "steps" occurring only in the pressure treated samples. These "steps" occurred for all pressure-treated samples in both directions starting at strains between 0.3% and 0.5%. It is very likely that these "steps" represent crack growth along the fibre-matrix interface. However, this hypothesis should be verified using computed tomography (CT) imaging.

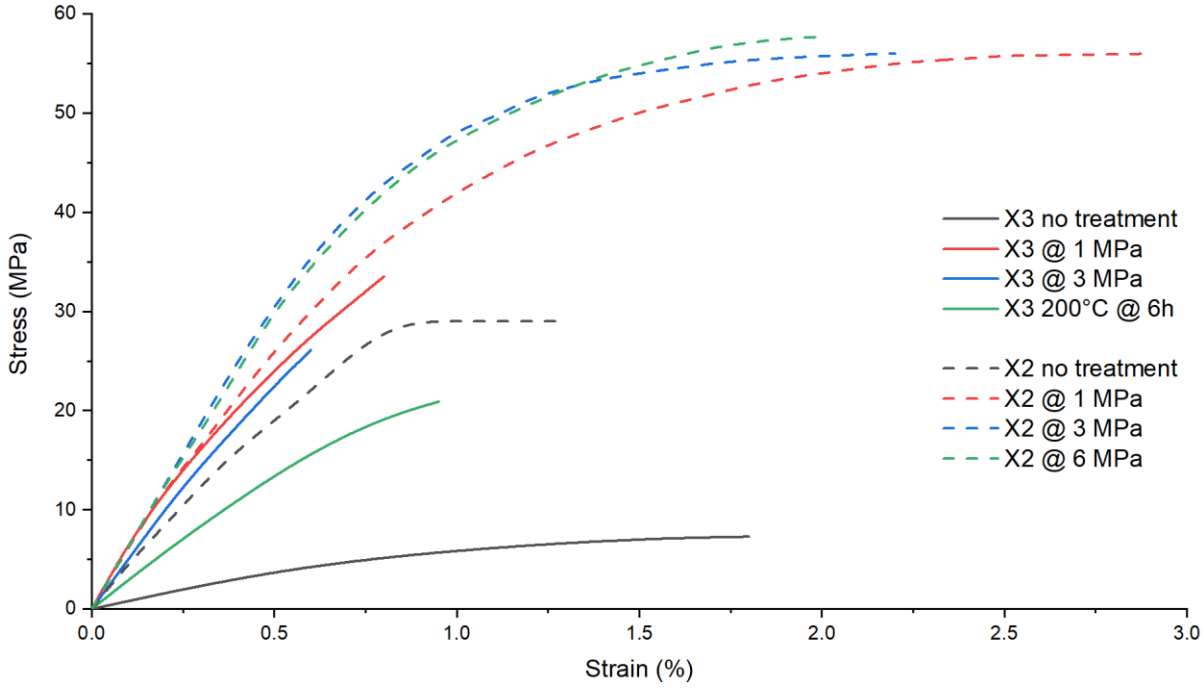

Figure 37: Averaged Stress Strain diagram for X2 and X3 direction for different pressures.

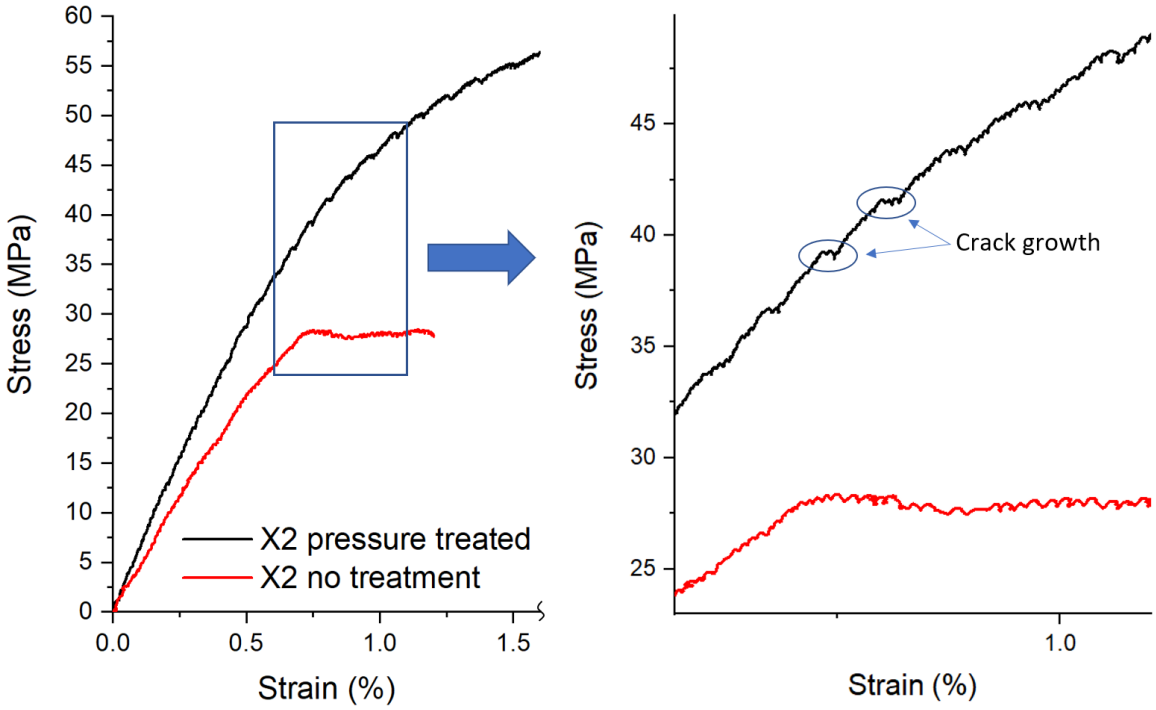

Figure 38: Unedited stress strain diagrams for pressure treated and non-treated samples

Table 12: Ultimate Tensile strength for the different pressures and testing directions

UTS [MPa]	-	1 MPa	3 MPa	6 MPa
X3	**7** ± 1	**34** ± 5	**27** ± 4	-
X2	**29** ± 3	**55** ± 3	**56** ± 3	**57** ± 2

Table 13: Young's modulus for the different pressures and testing directions

Young's Modulus [GPa]	-	1 MPa	3 MPa	6 MPa
X3	**0.6** ± 0.1	**4.9** ± 0.2	**5.1** ± 0.3	-
X2	**4.3** ± 0.7	**5.2** ± 0.3	**5.7** ± 0.4	**5.6** ± 0.3

Table 14: Strain at failure for the different pressures and testing directions

Strain at failure [%]	-	1 MPa	3 MPa	6 MPa
X3	**1.7** ± 0.38	**0.7** ± 0.14	**0.5** ± 0.05	-
X2	**1.4** ± 0.66	**2.9** ± 0.05	**2.1** ± 0.10	**1.9** ± 0.22

4.4.4 Geometric changes

Table 15 presents the dimensions of the test tokens before and after the pressure treatment. The width of the test tokens was not affected by the pressure treatment, whereas the height and length decreased. It should be noted that the width of the X3 test tokens was a result of the cutting process and not the printing process. At 1 MPa, the length is decreased by 1.6% on average and the height by 8.5% for the X2 test tokens. While there was no further length decrease when 3 MPa of pressure were applied, the height decreased by a further 5%. An increase in pressure to 6 MPa did not lead to further dimensional changes. The changes in the X3 samples were similar.

Table 15: Geometric changes measured at the centre of the test tokens

[mm]	**Before**			**1 MPa**		
	Length	Height	Width	Length	Height	Width
X2	110.19 ± 0.09	3.99 ± 0.05	20.95 ± 0.08	108.40 ± 0.28	3.65 ± 0.03	21.04 ± 0.05
X3	109.57 ± 0.07	3.91 ± 0.02	20.92 ± 0.09	107.84 ± 0.32	3.52 ± 0.03	21.00 ± 0.07
	3 MPa			**6 MPa**		
	Length	Height	Width	Length	Height	Width
X2	108.33 ± 0.31	3.50 ± 0.02	21.03 ± 0.06	108.48 ± 0.16	3.48 ± 0.04	21.01 ± 0.05
X3	107.29 ± 0.24	3.39 ± 0.06	21.05 ± 0.05	-	-	-

4.4.5 X-Ray radiography

Figure 39 depicts the results for the X-Ray radiography analysis, where the brightness is indirectly proportional to the density (white = low density). To make the air inclusions clearly visible, the brightness and contrast of the images were increased. As this measurement projects a three-dimensional part onto a two-dimensional plane, only quantitative information could be obtained. Computer tomography would allow for more detailed information, but this technology was not available. Nonetheless, the images reveal that the non-treated sample has bright stripes located close to the fibre bends and the centre. These stripes were most likely caused by large air inclusions, as the density of air (0.0012 kg/m³) is significantly less than the density of polyamide 6 (1.2 g/cm³) and the density of glass fibre (2.5 g/cm³). Thus, the air voids appear brighter. Furthermore, there are ± 45° lines visible. These lines resulted from the mandatory non-reinforced layers mentioned in section 4.2.1.

The stripes at the bends became smaller when 1 MPa of pressure was applied and disappeared in the parts centre. At 3 and 6 MPa, no bright stripes could be observed. Furthermore, at 3 and 6 MPa, the images' overall brightness became slightly darker in direct comparison to the other images, meaning that the air void content further decreased.

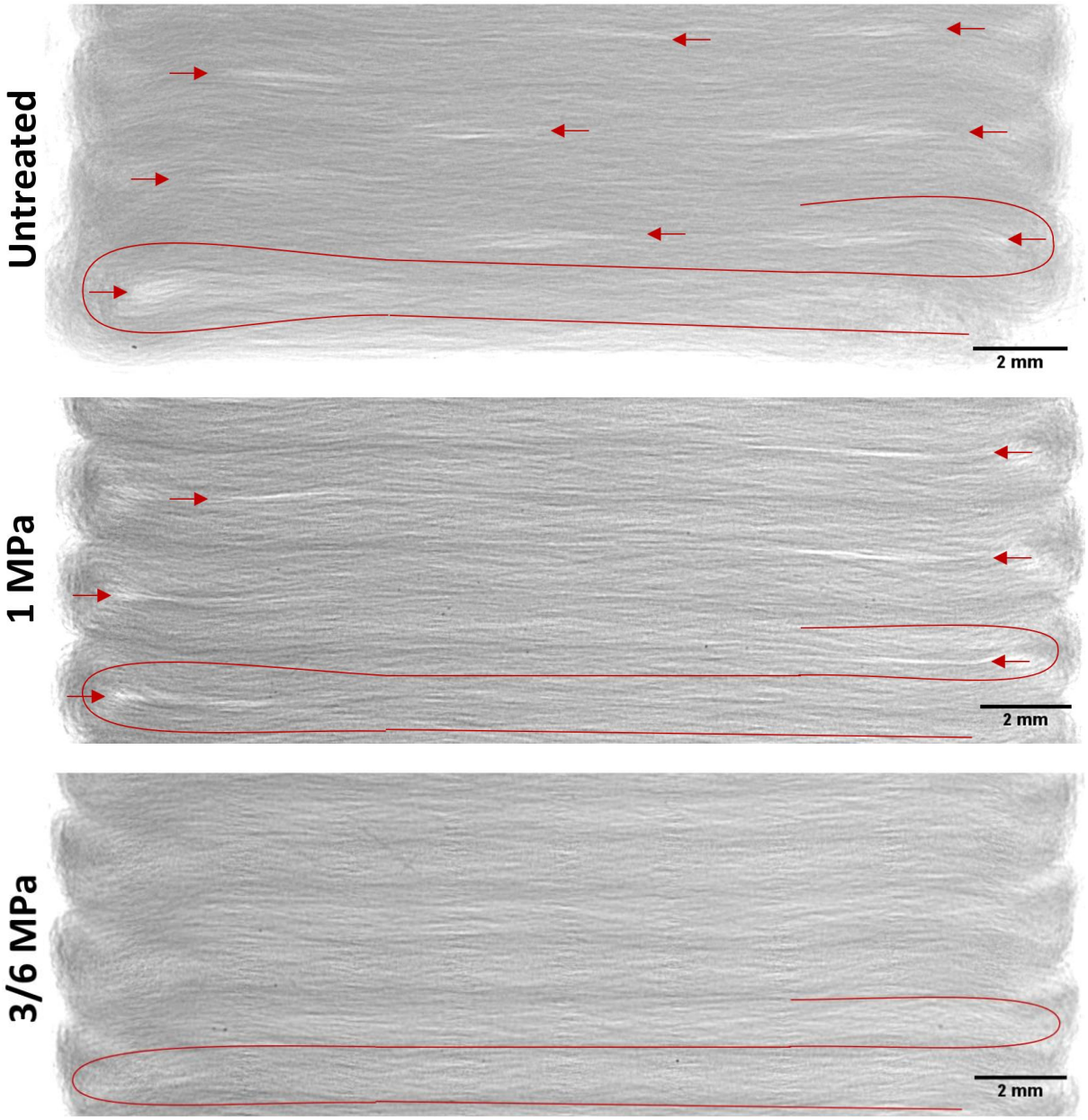

Figure 39: X-Ray radiographic images of the non-treated and post processed "X2" test tokens. To contrast and brightness were increased for a better visualization. The continuous red line indicates the fibre path and the arrows mark large air-inclusions. Brighter colors corelate with a lower density. The slightly visible +/-45° lines for the untreated sample origing from the non-reinforced layers. At three and six Megapascal of pressure, there were no visible differences between the X-Rax images, so only one was included.

4.4.6 Optical Microscopy

Optical microscopy of the samples' cross-sections allowed for a more detailed analysis of the decrease in air voids. Based on the X-Ray analysis, the air voids were expected to decrease as the distance from the fibre bends increased. The cross-sections at the fibre bends and close to the centre were consequently analysed. As illustrated in Figure 40, the non-treated sample has both large columns as well as a significant number of small air inclusions. When treated with 1 MPa, the small air inclusions were greatly reduced, but the large air columns remained. This change led to a drop from 10.5% to 5.5% in air inclusions. Although the air void ratio significantly dropped when further increasing the pressure, the difference between the 3 MPa (0.5%) and 6 MPa (0.3%) pressure treatment was only minor.

The cross-sections illustrated in Figure 41 close to the centre exhibited a similar pattern. While the air inclusions significantly reduced compared to the ones close to the fibre bends, the air void ratio was still 3.8%. It is important to note here that some of the embedding material found its way into the non-treated sample. As a result, the air voids in the centre of the figure appear bright instead of dark. In contrast to the cross-section close to the fibre bends, the 1 MPa treatment achieved a large reduction of the air voids in the parts centre, similar to the reduction at 3 MPa (0.5%) and 6 MPa (0.3%). The change of air inclusions is summarised in Table 16. These observations align with the results from the X-Ray analysis; however, to achieve a higher statistical relevance, a CT-analysis should be conducted.

To determine to what extend the air-voids were also present in larger parts, cross-sectional images at increasing distances from the fibre bend of a rectangular beam with a total length of 160mm were analysed. Figure 42 and Figure 43 present the results of the analysis. As with the previous samples epoxy resin infiltrated some of the air voids, which made the air voids appear bright white instead of black. At a distance of 10mm large air columns repeating every two strands can be observed with some smaller air-inclusions in-between them. The distance between the (imaginary) centre lines of the large air-void columns was 1760µm on average. At a layer height of 100µm the width of two layers without the air voids would be 1700µm. This calculation is based on the cross-sectional area of the filament which is $8.5*10^3$ µm² (comp. Figure 44). As the distance from the fibre-bends increases these large air-columns became smaller. However, air-void columns were observed between the large air-columns.

At a distance of 40mm from the bends the additional columns were clearly visible. While the large air-columns did become smaller they were still clearly present at a distance of 80mm from the bend. Nonetheless, the overall air-void ratio decreases. At 10mm from the bend it was measured to be 4.8% whereas at 80mm it is 2.1%. As mentioned in the previous paragraph, a CT analysis should be used for a more in-depth analysis in future studies.

Figure 45 depicts the fractured X3 (left) and X2 (right) samples. The X3 samples, which were not milled off after annealing, exhibited oxidation on the outside, indicated by the brown surface. As the X2 samples were milled off to eliminate the fibre connections, there was no oxidised layer. While the mould itself was closed during the whole heating cycle, it was not airtight.

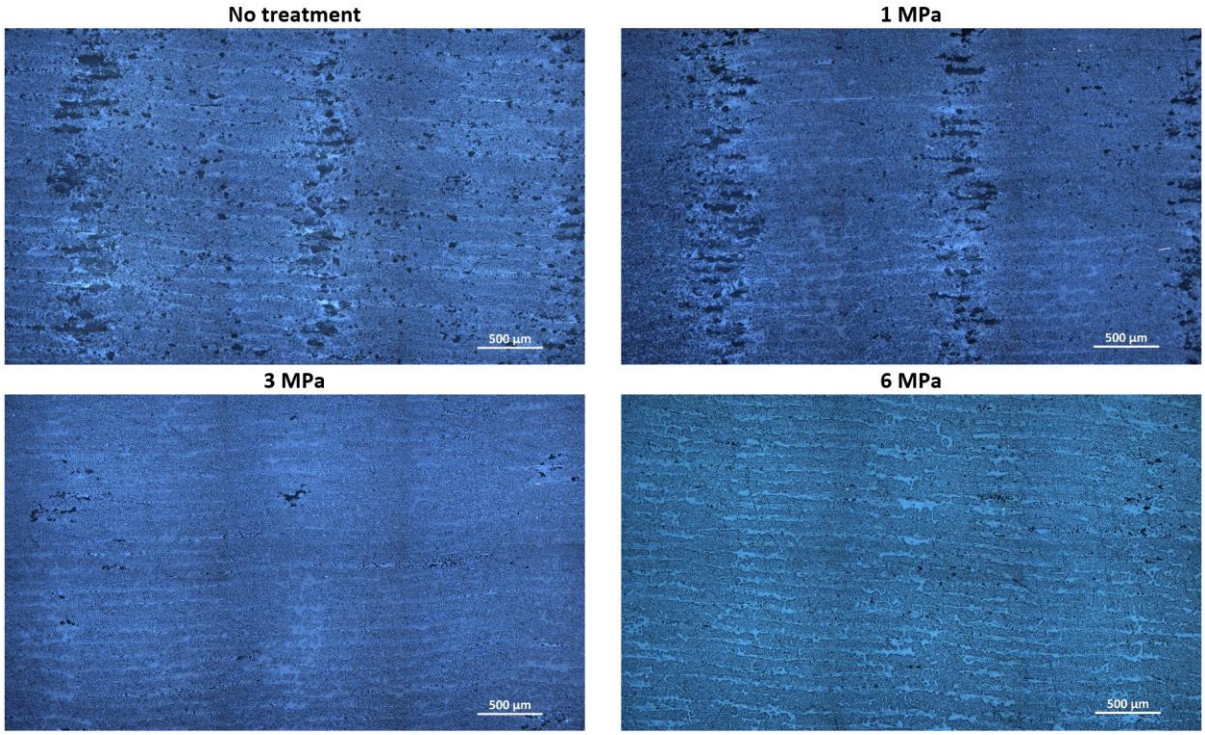

Figure 40: Air inclusions in the X2 samples close to the fibre bends

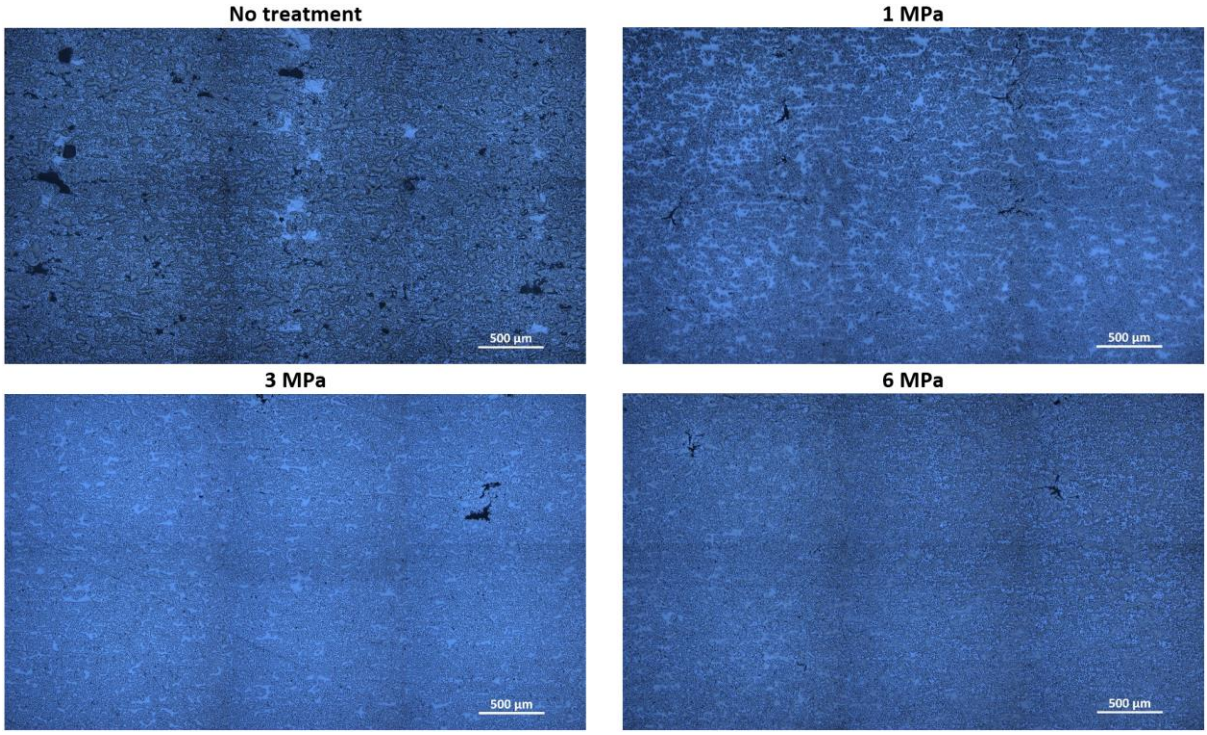

Figure 41: Air inclusions in the X2 samples close to the samples centre

Table 16: Percentage of air inclusions close to the bends and the middle for different pressures

Pressure	Border [%]	Middle [%]
No treatment	**10.5** ± 1.6	**3.8** ± 0.9
1 MPa	**5.5** ± 0.5	**0.5** ± 0.1
3 MPa	**0.5** ± 0.1	**0.5** ± 0.1
6 MPa	**0.3** ± 0.1	**0.3** ± 0.1

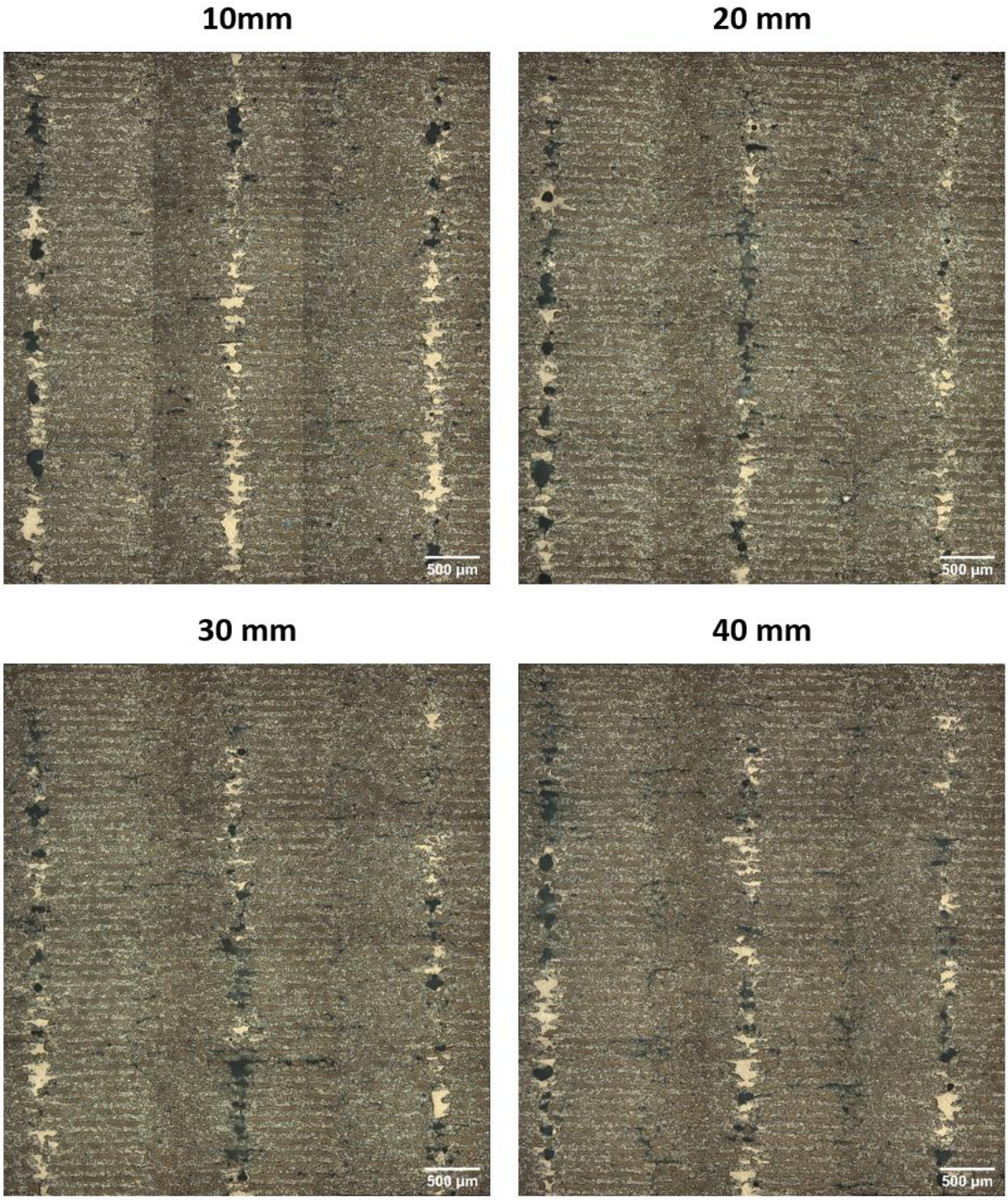

Figure 42: Microscopic images of cross-sections at distances of 10-40mm from the fibre bends. Air voids (black) were partially filled with Epoxy resin (white) during the polishing preparation process.

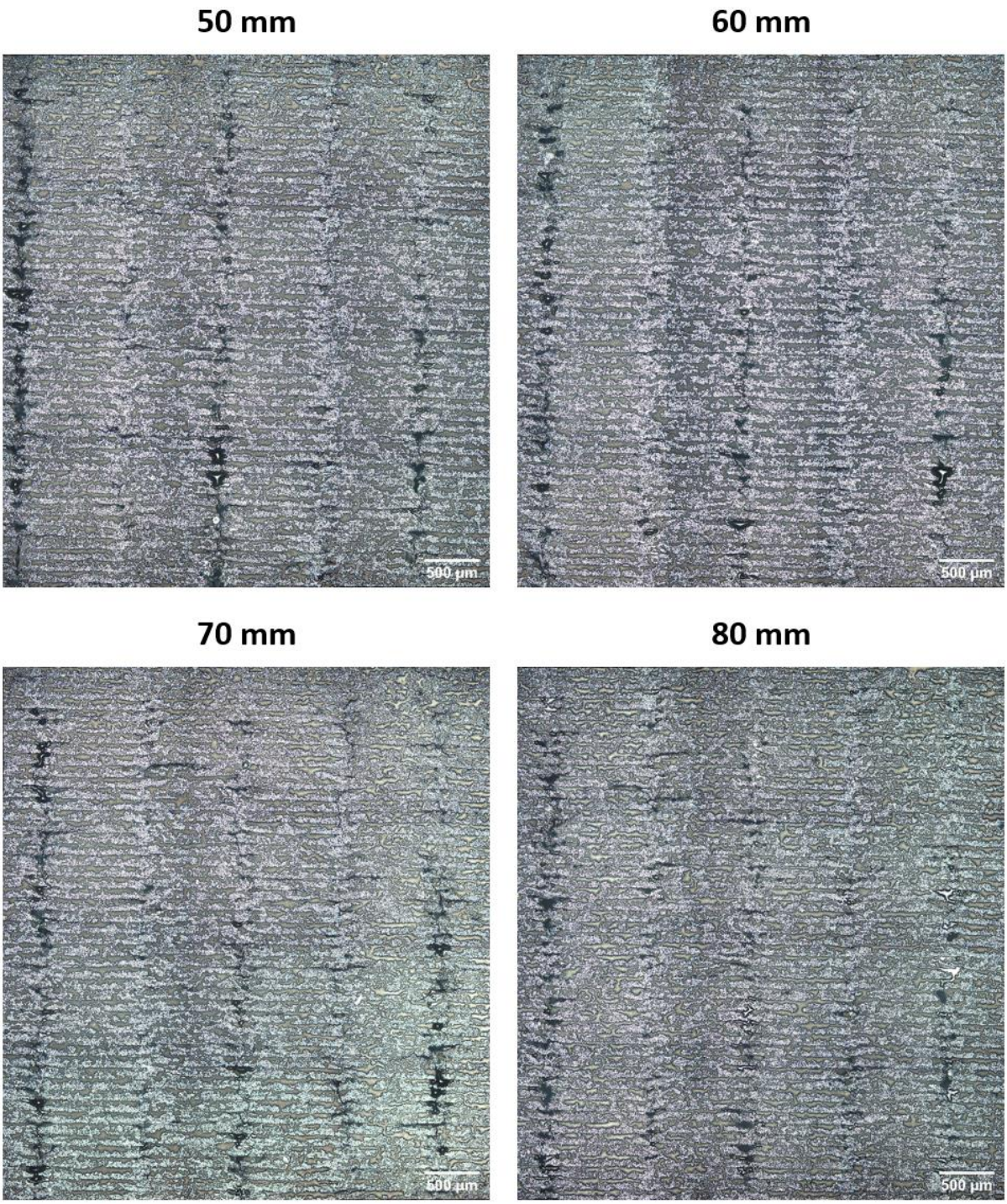

Figure 43: Microscopic images of cross-sections at distances of 50-80mm from the fibre bends. Air voids (black) were partially filled with Epoxy resin (white) during the polishing preparation process.

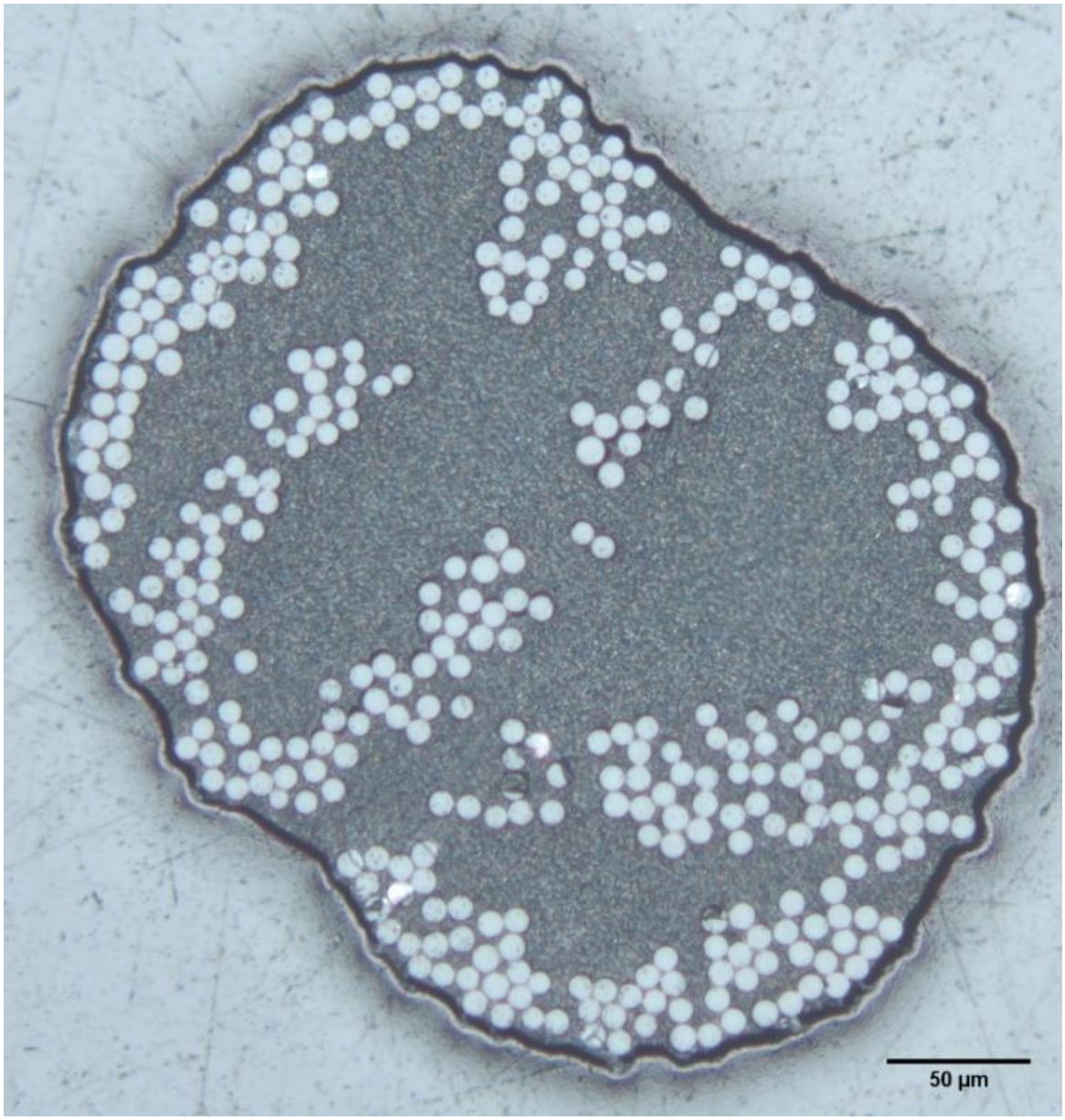

Figure 44: Cross section of the raw glass fibre filament.

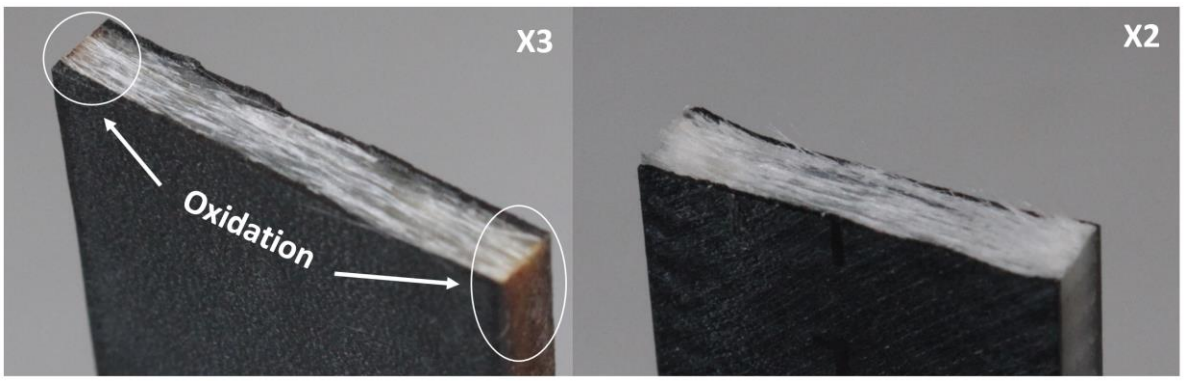

Figure 45: Fracture surface of the X3 sample (left) with visible oxidation and X2 sample (right) with milled-off sides.

4.4.7 Scanning electron microscopy

Figure 46 presents magnified images of the fracture surface for the non-treated X2 sample taken with the scanning electron microscope. As illustrated in Figure 46a) and b), most fibres on the surface have almost no matrix material on them, as if it has been stripped of. While these images only illustrate a small frame, they are representative of the whole fracture surface. At 10,000x magnification (Figure 46 c), partial delamination can be observed. A piece of polyamide is partially detached from the fibre (right-hand side) the and the other half is still attached to it. In the upper half of the image, there is residue visible on the fibre. It is unclear whether it is the fibre coating that is breaking off or matrix material. The image could not be focused any further beyond a magnification of 20,000x, but as is illustrated in Figure 47, the residue is most likely matrix material adhering to the fibre, as the infrared analysis in the previous study indicated the use of alkoxysilane compounds as a sizing agent [108]. These compounds would not exhibit such ductile behaviour. This ductile deformation at the fibre-matrix interface indicates a good connection between the glass fibre and the polyamide.

The magnified fracture surfaces of the pressure-treated X2 samples demonstrate a different pattern of damage (comp. Figure 48). Compared to the non-treated sample, much more matrix material is still adhering to the fibres. The same partial delamination (Figure 48 c) can be observed, but in many more places. In addition, instead of only small pieces still adhering to it, much of the fibre's surfaces is still covered by or connected to the matrix material (please note that the magnification is 5,000x). For both the untreated and postprocessed samples, many broken-off fibres are visible.

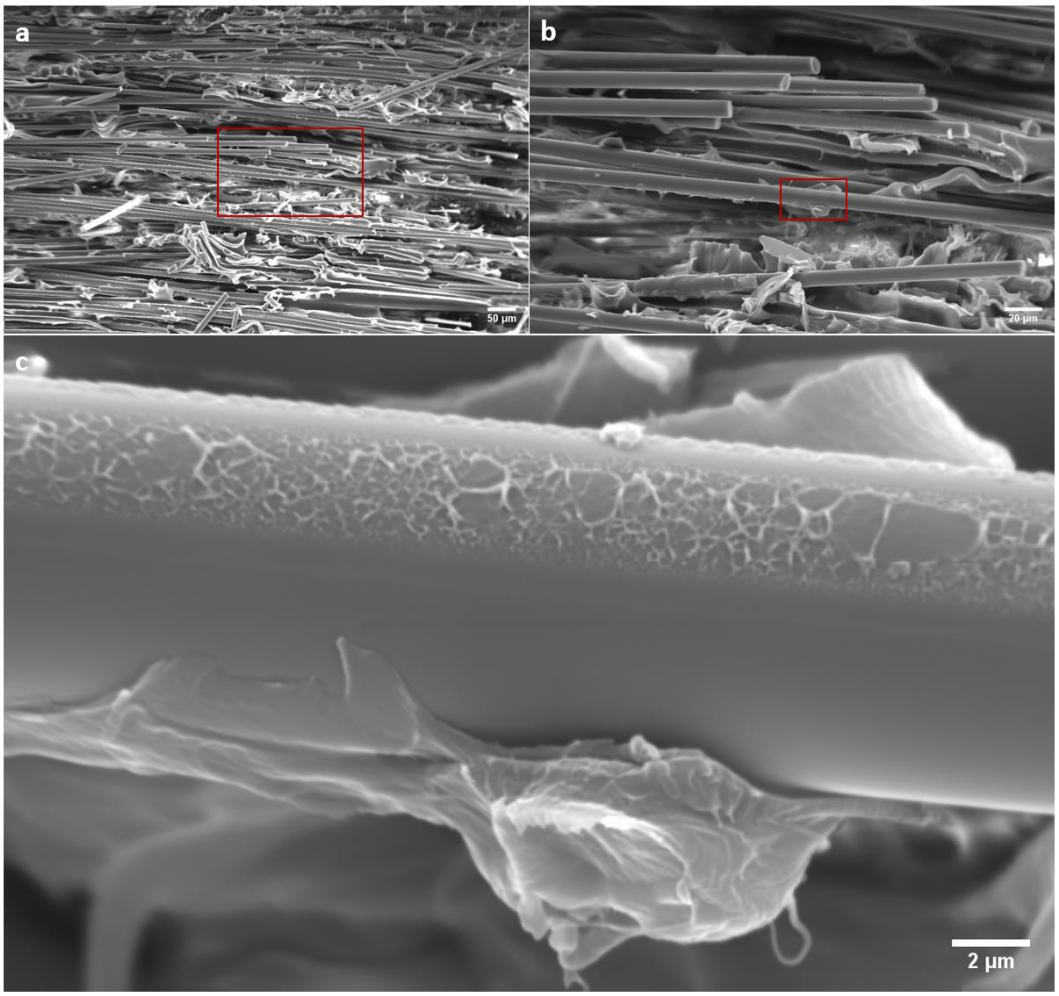

Figure 46: Fracture surface of the non-treated X2 sample magnified 300x (a), 1000x (b) and 10000x (c)

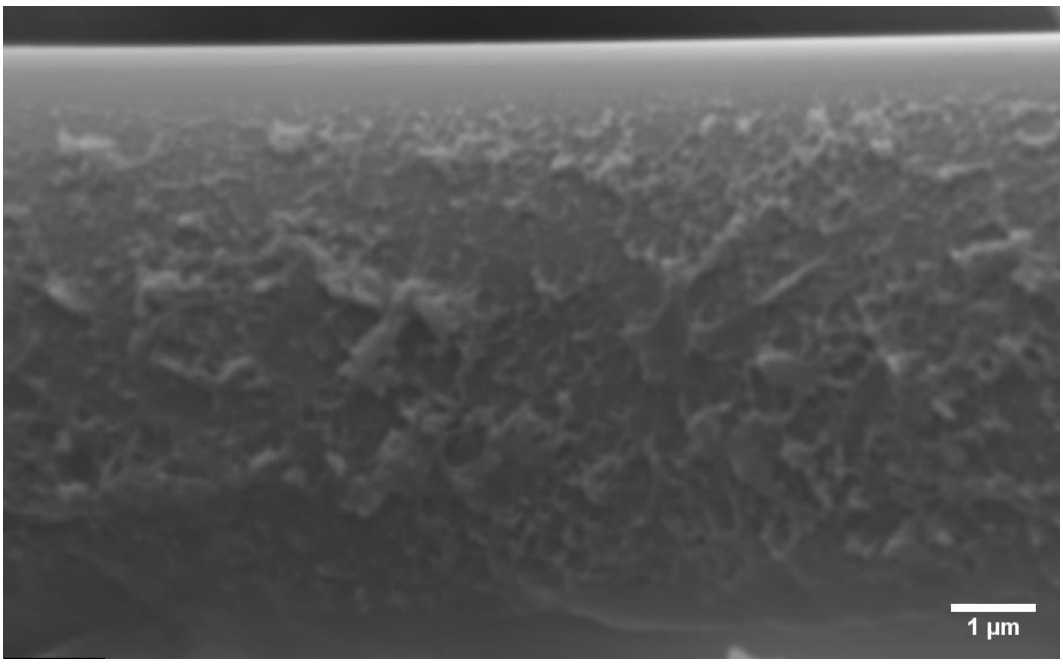

Figure 47: Residue on the fibre at a 20000x magnification.

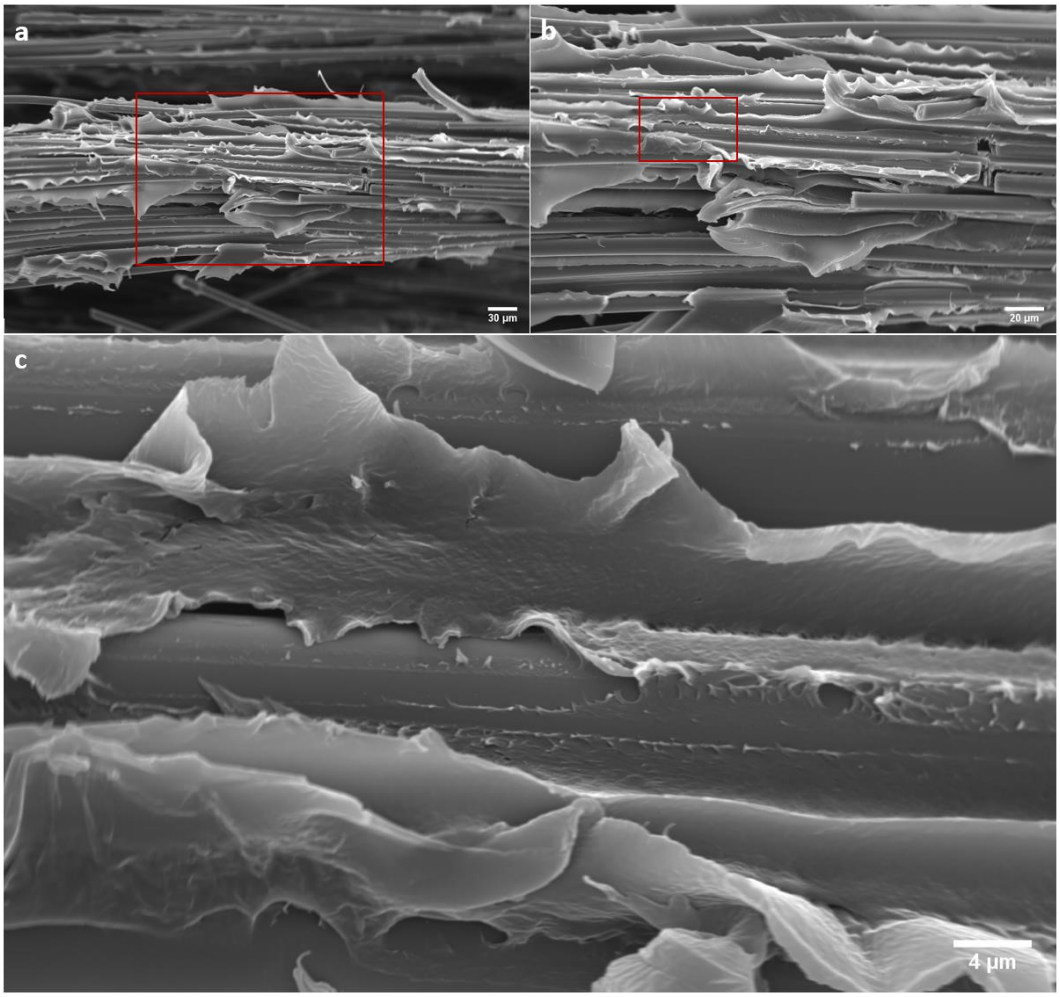

Figure 48: Fracture surface of the pressure treated X2 sample magnified 500x (a), 1000x (b) and 5000x (c)

4.4.8 Damping and Modal Frequencies

Figure 49 shows the first and second modes determined by the impact measurement. All of the signals are of equal quality, which allows for comparison with one another. The frequencies and damping values are listed in Table 17. The heat and pressure treatment had no significant influence on the material damping. Changes in the frequencies were caused by changes in the geometry and in the Young's modulus.

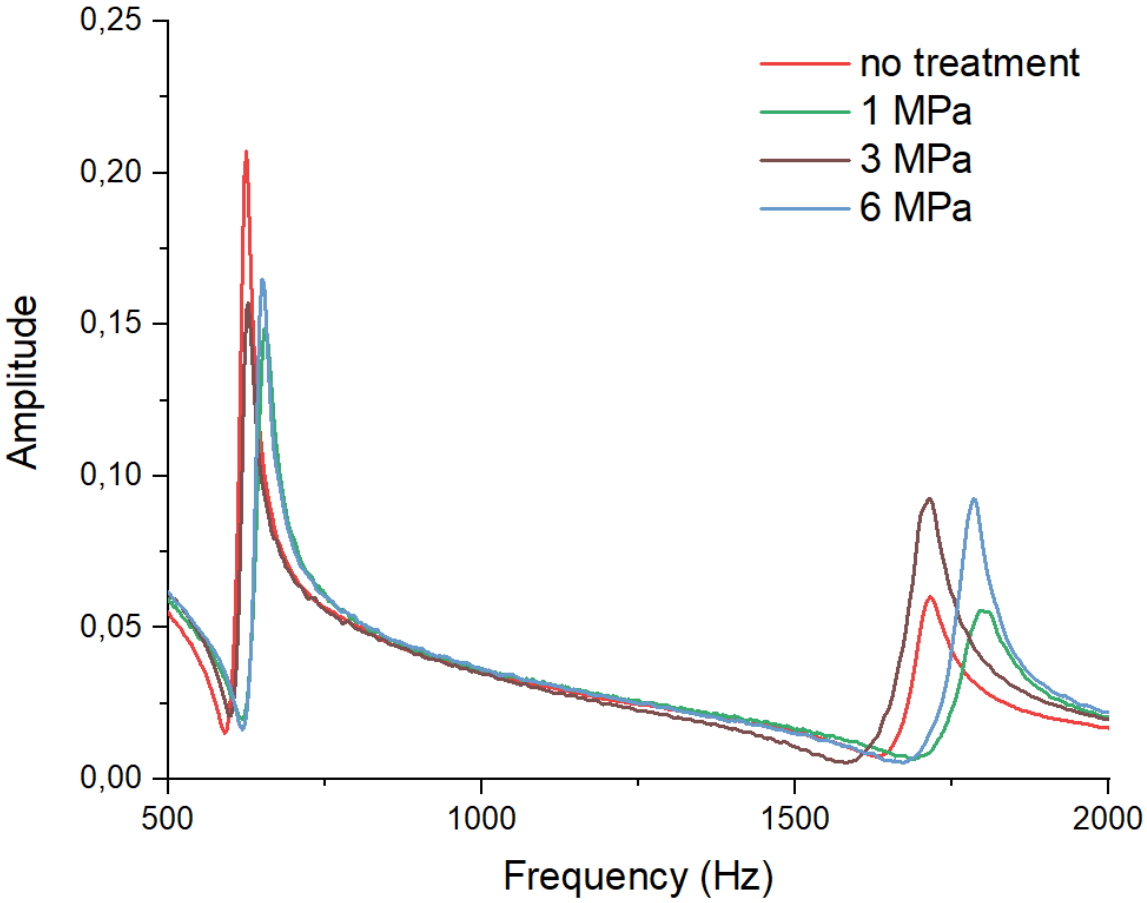

Figure 49: Results of the impact measurements showing the first and second Eigenfrequency.

Table 17: Frequencies and damping values determined for the test samples

	-	1 MPa	3 MPa	6 MPa
Frequency 1st mode [Hz]	623	635	624	645
Damping 1st mode [%]	1.67	1.37	1.38	1.21
Frequency 2nd mode [Hz]	1709	1795	1711	1783
Damping 2nd mode [%]	1.53	1.35	1.59	1.28

4.4.9 FEM Unit cell analysis

To determine the theoretical maximum material performance, the constituent's properties were used to calculate the composite's elastic properties. For this purpose, it was assumed that the fibre distribution is homogenous and that the element shown in Figure 50 is a

repeating pattern within the material. The boundary surface S of this element is subjected to constant homogenous strain ε_{ij}^0:

$$u_i(S) = \varepsilon_{ij}^0 x_j. \tag{4.1}$$

It was assumed that the average strains $\bar{\varepsilon}_{ij}$ of the composite equal the strains at the boundary surface ε_{ij}^0. A derivation can be found in [165]. The displacement field created by ε_{kl}^0 = 1 (ε_{11}^0 = 1, ε_{12}^0 = 1,…) can be written using $u_i^{(kl)}(x)$ as:

$$u_i(x) = \varepsilon_{kl}^0 u_i^{(kl)}(x). \tag{4.2}$$

with a summation over *k* and *l*. The resulting strains can be expressed as:

$$\varepsilon_{ij}(x) = \frac{1}{2}\varepsilon_{kl}^0\left(u_{i,j}^{(kl)} + u_{j,i}^{(kl)}\right). \tag{4.3}$$

Using Hook's law, the resulting stresses are calculated as

$$\sigma_{ij}(x) = \frac{1}{2}C_{ijpq}(x)\varepsilon_{kl}^0\left(u_{p,q}^{(kl)} + u_{q,p}^{(kl)}\right). \tag{4.4}$$

where $C_{ijpq}(x)$ represents the location-dependent elasticity tensor for the fibre and matrix material. The average stress is calculated by averaging the stress over the volume element:

$$\bar{\sigma}_{ij} = C_{ijkl}^* \bar{\varepsilon}_{kl} = \frac{1}{V}\int_V \sigma_{ij} dV, \tag{4.5}$$

where C_{ijkl}^* is the desired elasticity tensor of the composite. The FEM calculations were performed according to section 4.2.9 using the values shown in Table 18 with a 32% fibre volume content [86]. As polyamides are known to change their properties when absorbing water, calculations for both the dry and conditioned material state were performed. The results are listed in

Table 19. As expected, the Young's modulus in the fibre direction was only slightly affected by the change of the matrix properties whereas the Young's modulus in the directions perpendicular to the fibres significantly dropped when the polyamide was conditioned.

.

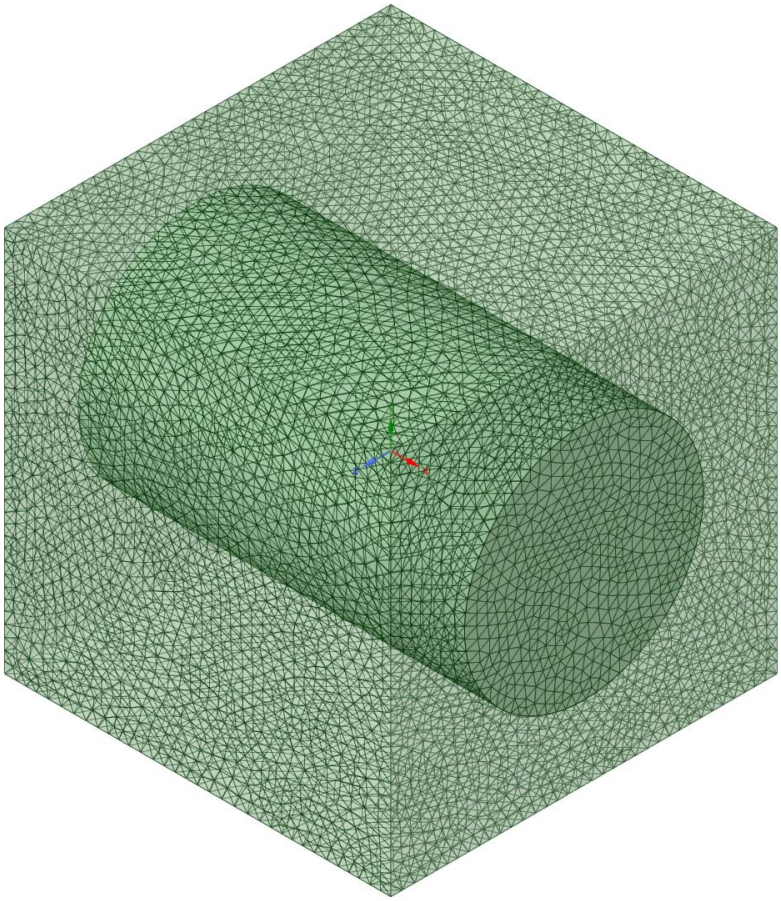

Figure 50: Representative volume element used to determine the elastic properties with a 9.2µm fibre.

Table 18: Young's moduli and Poisson's ratios for polyamide 6 and glass fibre

	Young's Modulus [GPa]	**Poisson's ratio**
Polyamide 6 (dry/conditioned)	3.0/1.0 [166]	0.39/0.45 [167]
Glass fibre	82 [86]	0.18 [168]

Table 19: Elastic properties of the annealed material for a dry and conditioned matrix

	Dry	**Conditioned**
Young's modulus - E1 [GPa]	26.7	25.3

Young's Modulus – E2/E3 [GPa]	6.3	2.6
Shear modulus G12/G31 [GPa]	1.9	0.6

4.5 Discussion

The XRD analysis demonstrated that applying pressure while the material was heated above the melting point did not significantly change the crystalline structure compared to annealing without pressure, nor did the increased heating rate of 60 K/h or cooling rate of 40 K/h. While the DSC analysis revealed no difference in the degree of crystallinity between the different pressures, the sample annealed for 6h in the previous study exhibited a slightly higher degree of crystallinity and melting point. This finding could explain, why the samples from the previous study showed a slight increase in Young's modulus independent from the temperature when annealed for 6 h compared to shorter annealing periods.

Analysis of the geometric changes indicated that the width of the samples is not affected by the pressure treatment. This result was expected, as the fibres were aligned in that direction. Unlike the matrix material, the fibres remain solid at the annealing temperature and do not experience any plastic deformation. Thus, unless the fibres are moved during the annealing process, the width cannot be affected. The change in the test token length can be attributed to thermal contraction. When the pressure is applied, the test token takes the shape of the mould at a temperature of 200°C. During the cool-down phase, the polyamide contracts. This process is independent of the pressure, which is why the decrease in length was almost the same for all pressure levels. The decrease in height is an indicator of the reduction of air voids. However, if the geometry is used for density calculations, the 3D contour should be measured using a coordinate measurement machine. Furthermore, it must be taken into account that the polyamide 6 phases exhibit different densities [146].

The X-Ray analysis indicated an inhomogeneous distribution of air voids, with larger air-inclusions located at the fibre bends. Microscopic analysis confirmed this observation, which is likely a result of the high bending rigidity of the fibres (comp. Figure 51). At the 180° turns, the bending moment causes a displacement of the strands from their ideal path. The bending moment decreases as the printing nozzle moves further away from the bend. The same effect was reported for carbon fibre-reinforced plastics [159]. As a result, the air voids decrease as

the distance to the fibre bends increase. These fibre bends are also likely the reason why, at a pressure of 1 MPa, there were still large air voids present. The compaction process requires a higher pressure to push the fibres closer to each other. A pressure of 3 MPa seems to be high enough, as the large air inclusions at the fibre bends almost completely disappeared. A further increase to 6 MPa did not lead to a significant further decrease in the air void ratio. While these observations align with the measured mechanical properties, the microscopic and X-Ray measurements can only be considered as an indicator. For a more precise analysis, a computer tomography analysis is required to determine the 3D distribution of air voids inside the part.

Nonetheless, the observed insignificant difference between 3 MPa and 6 MPa seems plausible. The high viscosity of the plastic hinders the small remaining air bubbles from escaping. Instead of being squeezed out, they are compressed and remain inside the material. The same effect can be observed in conventional fibre-reinforced plastics manufactured from prepregs, where the high viscosity of the uncured matrix material causes air bubbles to be trapped inside the material [169].

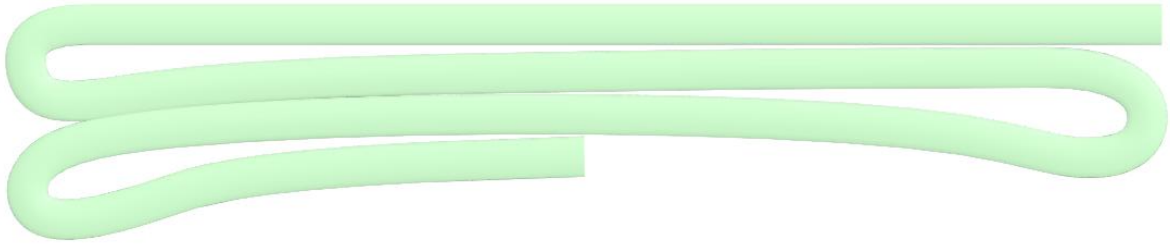

Figure 51: Air Voids caused by fibre bends

The mechanical tests revealed a high standard deviation in both the untreated and post-processed samples. This result is most likely caused by the air inclusions, the fibre orientation, and the poor layer adhesion. Variations in the size and distribution of the air voids can lead to localised stress concentrations and premature failure. Misaligned fibres will also influence the mechanical properties, as the fibres have a greater effect on the mechanical properties if they are oriented in the tensile direction. As illustrated in Figure 51, the fibre bends already cause a slight fibre misalignment at the bends in the untreated state. When pressure is applied, the bends will be squeezed together. However, it cannot be guaranteed that the fibres will align perfectly in this process. Beyond the effect on the Young's modulus, local fibre misalignment can also cause local stress concentration and therefore premature failure.

However, despite the deviations, the measurements were able to indicate the effects of different pressure levels on the mechanical properties, which are discussed in the following paragraphs.

In the untreated state, tensile tests revealed that the material exhibited vastly different properties in the X2 and X3 directions. This difference can be attributed to the poor layer adhesion, which mainly affects the build-up (X3) direction. This factor is an important aspect to consider when applying failure criteria that assume transverse isotropic material properties [170]. After the application of 1 MPa of pressure, the Young's moduli in both directions significantly increased with the Young's modulus in the build-up direction still slightly lower. This difference was most likely due to the oxidation of the outer layer, which only remained in the X3 samples as they were not milled off prior to testing. As most studies investigating oxidation behaviour focus on low temperature oxidation, there is no data available for temperatures of 200°C. However, at 160°C, a study indicated that short exposure times of under 1 h cause significant breaking of the polymer chains [171]. Oxidation is also the probable cause of the significant 20 MPa difference in the ultimate tensile strengths between the two testing directions. The very brittle oxidised outer layers are expected to initiate crack growth, leading to premature material failure. Long-term studies have shown that oxidation must also be taken into consideration when using polyamide at temperatures as low as 70°C [172]. While stabilisation agents have been proven to prevent a drop in tensile strength, the elongation at brake inevitably decreases at prolonged exposure to high temperatures [173].

A further increase of pressure to 3 MPa lead to a further increase in the Young's modulus. This result can be explained by the air voids in the fibre bends, which remained at 1 MPa of pressure. As the air inclusions increase the cross-section used for the calculation of the Young's modulus, the Young's modulus appears lower. At 3 MPa, these air voids almost completely disappeared, which is also why a further increase to 6 MPa did not affect the Young's modulus and tensile strength. Comparison with the theoretical Young's modulus determined by the finite element method indicates that the post-processed material nearly matches the theoretically achievable Young's modulus. The difference between the ideal model and the experimental data can be explained by the non-reinforced outer layers.

The small "steps" observed in the stress-stain diagram were most likely caused by localised delamination, evidence of which was found in the SEM images. Similar behaviour can be

observed in conventional fibre-reinforced composites, where cracks propagate along the fibre matrix interface [174] [175] [176]. This hypothesis should be verified using *in-situ* tomography tensile testing. For the untreated X2 samples, the primary cause of failure is most likely the large air-inclusions. These air-inclusions cause a notch effect and thereby localised stress concentration, initiating part failure. However, as the fibres were not aligned perfectly, they still connected the two halves of the failed test sample. As the tensile test continued, the fibres were slowly pulled out of the matrix, which shows as a horizontal line in the stress-strain diagram. This event would explain the absence of matrix material on the fibres on the fracture surface of the non-treated test tokens as well as the broken-off fibres. As not all fibres were aligned in the same angle, some were pulled out and others broke off. As the pressure treatment significantly reduced the air inclusions, significant strength is built up in the pressure-treated samples, as indicated by the increased ultimate tensile stress. When the part failed, the two halves were separated more abruptly and the fibres were not be pulled out. Therefore, the fracture images of the post-processed samples show much more matrix material still adhering to the fibres.

While dry polyamide 6 has a tensile strength of up to 80 MPa, the achieved strength of 55 MPa is most likely very close to the material's optimum performance. This is because the Young's modulus of the fibres is significantly higher than the Young's modulus of the matrix materials. At a given stress level, the elongation within the matrix is significantly higher than the elongation in the matrix. The fibres also limit the contraction of the matrix material. These effects cause an inhomogeneous stress/strain distribution within the matrix [170]. An illustration of this effect is presented in Figure 52, where light refraction shows the inhomogeneous stress/strain distribution in a transparent matrix material. Local stress accumulation causes crack initiation, leading to material failure. For conventional composites, the effect has a stronger impact, as thermosets are much more brittle, leading to tensile strengths below 50 MPa [177]. Simulations have demonstrated that this effect causes the crack growth along the fibre/matrix interface, as described in the previous paragraph [178].

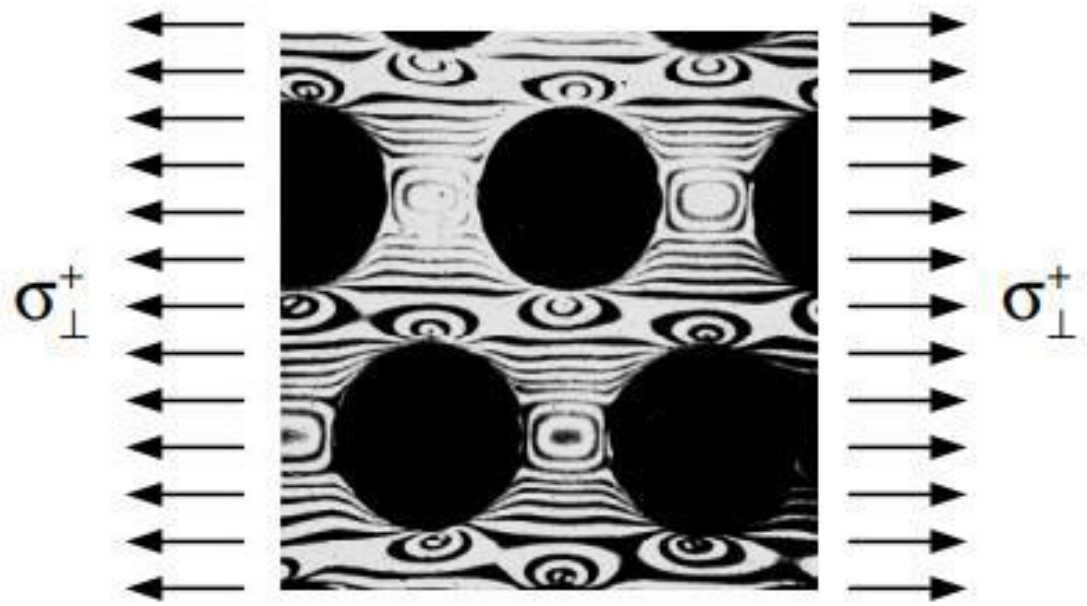

Figure 52: Image of the stress concentration within the transparent matrix [179]

This effect also explains why a further increase in pressure did not significantly increase the tensile strength. As the microscopic and X-Ray analysis indicated, there were more air-inclusions present at 1 MPa than at 3 MPa and 6 MPa. In homogenous materials, these inclusions would initiate the crack growth and be the limiting factor. However, for this material, the inhomogeneous stress distribution caused by the embedded fibres seemed to overshadow the influence of the small remaining air inclusion.

4.6 Future research needs

All of the experiments in this study were conducted using a mould press. Using such a press in practice would take away the benefits of the additive manufacturing process, which does not require a mould. The investigated pressure levels of 1 MPa and 3 MPa can be achieved by commonly available autoclaves that are currently used to cure conventional thermosetting composite materials. However, pressure of 6 MPa can only be achieved by using an actual mould press. Nonetheless, as the results indicate that there is no significant difference between 3 MPa and 6 MPa, there is no need to use the higher pressure. Future studies should consequently investigate using an autoclave to post-process the additively manufactured composite. When heating the polyamide up to its melting point without a mould, gravity will

presumably cause significant material deformation. As shown in a previous study, this effect can be prevented by submerging the parts in mineral oil. The buoyancy effect prevents deformation and protects the polyamide from oxidation. Future research should also investigate how much the heating and cooling rates can be increased to decrease the overall processing time.

As the analysis of the RVE indicated that the composites' properties significantly change when the polyamide is saturated, this aspect should also be explored. Moisture absorption is a slow process. The test samples used in this study are expected to take roughly nine months to reach equilibrium at normal temperature and air moisture levels [130]**.** During that time, the outer parts of the material will be saturated, whereas the inner parts will remain dry, which is a factor to consider.

4.7 Conclusion

The study presented in this chapter analysed the effects of a post-processing pressure treatment on the mechanical properties and the air void ratio of additively manufactured continuous fibre-reinforced plastics. The tests focused on the properties in perpendicular directions to the fibres. Three different pressure levels were investigated using a mould press. The researchers observed that 1 MPa of pressure significantly decreased the air void and increased the mechanical performance, with a Young's modulus increase from 4.3/0.6GPa to 5.2/4.9GPa and a tensile strength increase from 29/7MPa to 55/34MPa in the "X2"/"X3" direction. However, air voids close to the fibre bends remained. At a pressure of 3 MPa, these air voids disappeared, leaving only small air voids. The Young's modulus also increased to 5.7/5.1GPa. A further increase of pressure (6 MPa) had no significant effect on the air voids or the tensile strength. However, since no protective atmosphere was used, oxidation occurred, which led to a premature failure of the test tokens in the "X3" direction. The "X2" test tokens were milled off and did not prematurely fail. As a result, the ultimate tensile strength of the "X3" test tokens was significantly lower. Nonetheless, the Young's modulus in both directions was almost identical after the pressure treatment process. This finding does not hold true for the as-printed state, which demonstrates that the pressure treatment process homogenises the additively manufactured composite material. Based on an FEM analysis and the shape of the stress-strain graph, the values obtained for the post-processed

“X2” samples are likely to represent the materials’ maximum performance. Future studies should focus on a post-pressure-treatment process using an autoclave and optimisation of the process parameters. Furthermore, an analysis of the failure behaviour under combined loads should be performed.

Chapter 5

Failure modelling

It was shown in the previous chapter, that annealing under pressure can eliminate most air voids in additively manufactured continuous glass fibre reinforced polyamide 6. In this chapter a multi-scale modelling approach is presented, to analyse the practical uses of the postprocessed additively manufactured composite. A part of the results discussed in this chapter were presented at the “Landshuter Leichtbau-Colloquium (LLC)” [180].

A composite material can be modelled on three different levels: micro-level, meso-level or the macro-level (comp. Figure 53) [181]. On the micromechanical level, the individual constituents of the composite material are modelled. For continuous fibre reinforced materials this includes the fibre, the matrix as well as the fibre-matrix interface. Damage initiation and localized debonding, which take places in areas with a high fibre density, as well as the crack propagation along the interfaces can be modelled directly [182]. At the meso level, which is often referred to as a layer wise model, a single layer of the composite is considered. The mechanical properties at this scale can either be obtained through experiments or by using the micromechanical modelling approach. Since the individual constituents are not considered anymore, localized effects must be modelled using state variables. Occurring damage, which must be considered as it changes the mechanical properties, can be modelled using smeared crack models (SCM) or discrete crack models

(DCM) [183]. At the macro scale the materials behaviour is even further homogenized with the whole part assumed to be a homogenous anisotropic material.

Since the real damage takes place on the microlevel, the most accurate results would be obtained by modelling a whole part on the microlevel. But even with today's technology, modelling a whole part on the microscale is not possible. However, the micro-level approach can be used to determine the properties of the meso-scale which provides the foundation for the macro scale. This approach is referred to as multi-scale modelling or virtual testing and has been successfully implemented in different studies [184] [185] [186] [187]. The most relevant papers are discussed in detail in the next section.

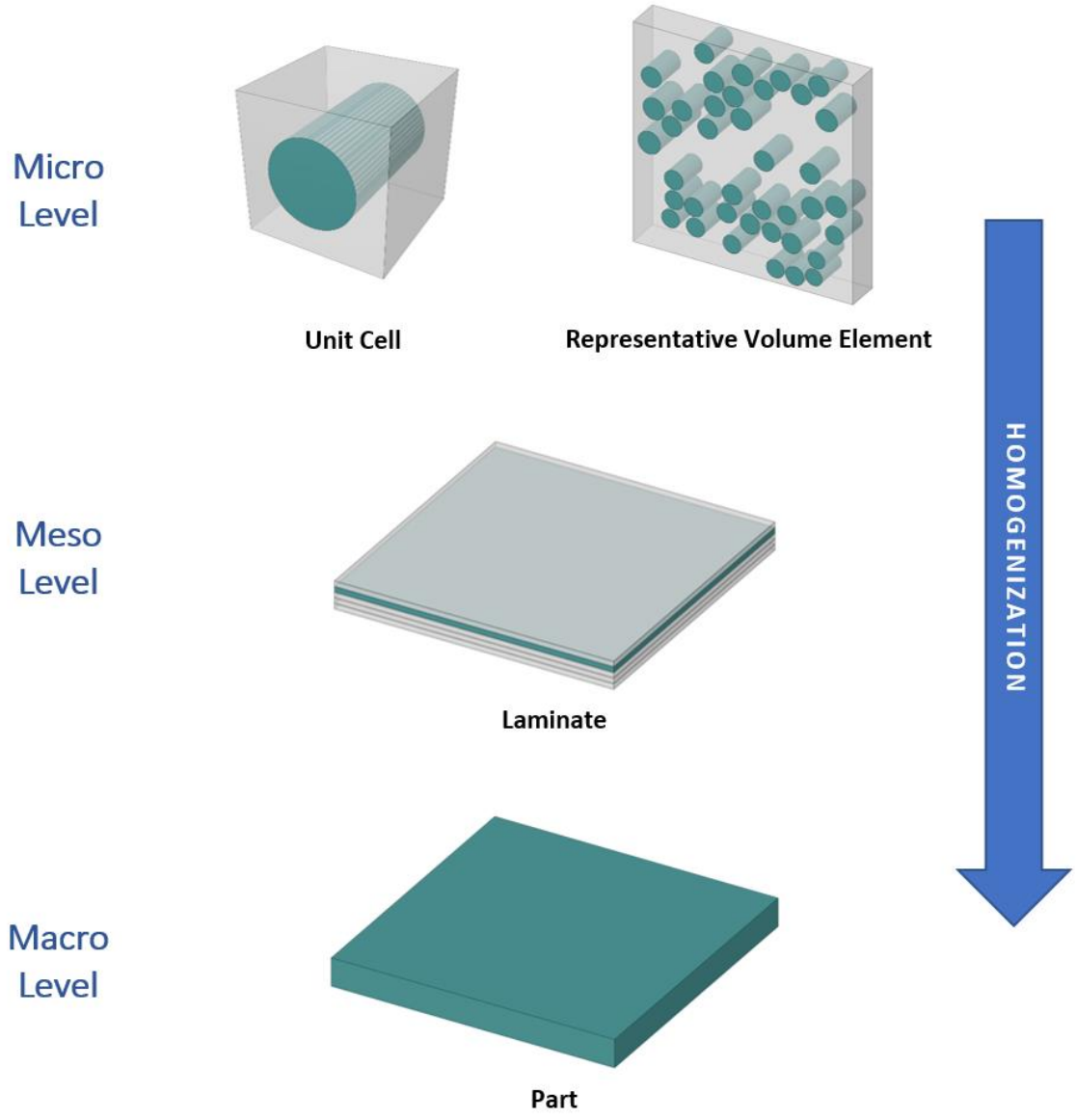

Figure 53: Different modelling level approaches.

5.1 Literature review

Pulungan et al. investigated the transverse tensile failure behaviour of continuous glass fibre reinforced polypropylene [188]. The fibre volume content was determined to be 47% with an average fibre diameter of 16.4µm. Test tokens were manufactured using unidirectional prepreg tape. The Drucker-Prager model was used to simulate the plasticity of the polypropylene matrix. Its degradation was captured by the ductile damage model integrated into Abaqus. It was assumed that the damage initiation for shear is three and for compression ten times larger compared to the tensile load. For the fibre-matrix interface a strength of 20 MPa and a critical displacement of 1µm were assumed. Using the standard deviation of the elastic parameters the minimum size of the representative volume element was determined to be 300x255 µm². A comparison with a unit cell showed good agreement in the initial response but could not capture the failure caused by localized stress concentration.

Liu et al. investigated the failure behaviour of a glass fibre reinforced polycarbonate under transverse tension and shear [189]. The void nucleation and growth in the matrix material was modelled using the Gurson-Tevgrad-Needlman model. A homogenous fibre distribution was assumed and a square RVE with a size of 46µm containing eight fibres was chosen for the analysis. With a diameter of 10µm this resulted in a fibre volume content of 30%. By assuming a fracture angle of 47° it was found that the determined fracture curve was in good agreement with the curve predicted by Puck's failure criterion.

The failure behaviour of an additively manufactured carbon fibre reinforced thermoplastic was investigated by Dutra et al [190]. The minimum size for the RVE was determined by calculating the elastic properties based on the fibre distribution taken from microscopic images. Values were found to converge at a size of 200x200µm². For combined load cases the failure of the fibre, matrix and interface were analysed. Material failure was assumed when one of the three components failed. This is a reasonable approach for the matrix and the fibre. However, it is a very conservative assumption for the interface as interface failure only initiates the material failure. This was even stated by the authors themselves. Furthermore, the matrix was considered to have failed when yielding occurs instead of considering the actual fracture. This is also very conservative as thermoplastics are very ductile. On the other hand, the anisotropy caused by the weak bonding of the layers as well

as the air-inclusions were not considered. So, unintentionally, the analysis was carried out for the post processed material. They found a good agreement between their failure prediction and Puck's failure theory.

Schramm et al. investigated the temperature dependent failure behaviour of continuous glass and carbon fibre reinforced polyamide 6 and polypropylene [191]. Samples were manufactured using a conventional tube winding process. The glass fibre reinforced PA6 was stated to have a mass content of 60%. Using the densities of the constituents it can be calculated that this equals a 40% volume content. The test samples were conditioned before testing, so the PA6 is saturated. It was found that even at elevated temperatures Puck's failure criterion can be applied to this material.

The literature review has shown that previous studies have successfully used micromechanical models to predict the macroscopic failure of thermoplastic composites. However, there has been no study focusing on the simulation of glass fibre-reinforced polyamide 6 with a low fibre volume content. Therefore, a micromechanical model for the post-processed additively manufactured composite was created and used as a foundation for a mesomechanical failure model. The mesomechanical model was used to evaluate a practical use case of the material.

5.2 Experimental setup

5.2.1 Optical Microscopy

Magnified images of the fracture surfaces of the different test tokens were taken by a Leica MZ6 microscope with an Axiocam 305 color attached to it. Samples were polished using a Strueters polishing machine. The glass fibres have a much higher Young's modulus and strength than the Nylon matrix material. As a result, polishing was quite challenging as the matrix did not provide enough support during the polishing process, causing the fibres to fragment if the applied polishing forces were too high (Figure 54 left). While this is no problem for the characterisation of the air-voids that were presented in the previous chapters, it does make it harder for the segmentation algorithm to distinguish between fibres and matrix. It also leads to a worse image quality due to light reflections. An extensive investigation of the ideal polishing parameters showed that the best results were obtained with a pressing force

of 5N and using the following grain sizes: 18µm (until plane), 6µm (until fibres are clearly visible) and 3µm (300s). A final polishing step using fumed silica suspension with a grain size of 0.25µm slightly improves the surface quality. The result is illustrated Figure 54 on the right side. The bright reflection is caused by remaining damaged fibres which cannot be completely avoided. The areas of matrix material in between the fibre groups are out of focus. That is because the soft matrix material was removed more quickly than the hard glass fibres despite the low forces. This effect is discussed in more detail in section 5.9.

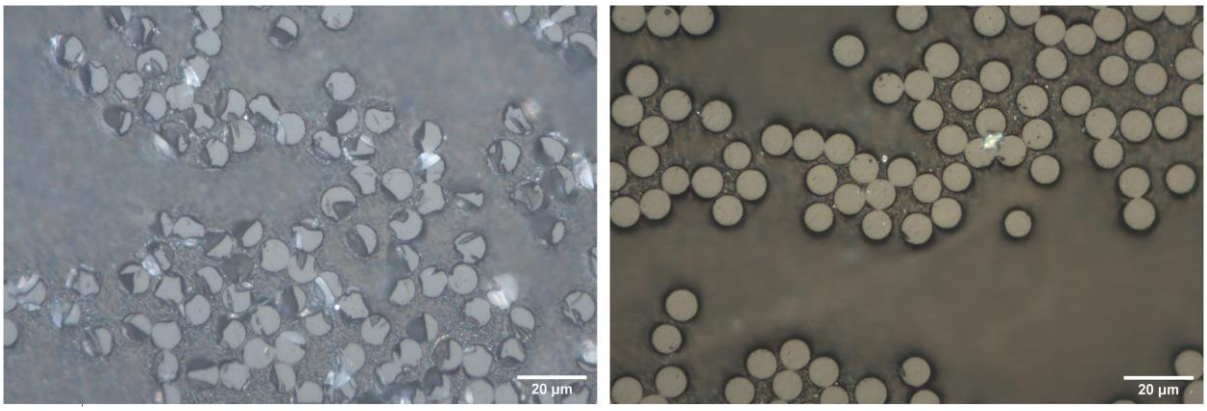

Figure 54: Damaged fibres due to high polishing forces (left) and good polishing results (right).

5.2.2 Image Processing

To transfer the microscopic images into an FEM program, a four-step process using the Fiji image analysis software was applied. Due to the fact, that the fibres and matrix have very similar colours, machine learning must be used to separate the fibre and matrix areas. This was done using the "Trainable Weka Segmentation" plugin. Multiple areas in the microscopic image were either assigned to a matrix or a fibre class. Based on this data the algorithm was trained and then used to classify the image. In case the algorithm did not assign all fibre/matrix areas correctly, parts of these areas were added manually to the right class and the training/classification was repeated. An edge finding algorithm was applied to the classified image to detect the borders of the fibres. The Hough-Transformation was used to extract the fibre coordinates and diameters. Due to some damage inflicted during the polishing process not all circles can be detected or are detected not correctly (comp. Figure 55). As a result, some post-processing in the CAD program was required.

5.2.3 Nanoindentation

A Hysitron TI Premier equipped with a Berkovich tip was used for the nanoindentation measurements.

5.2.4 FEM Software

The micromechanical model was created in Abaqus Version 2021 and the mesomechanical failure criterion was implemented as a user subroutine (UMAT).

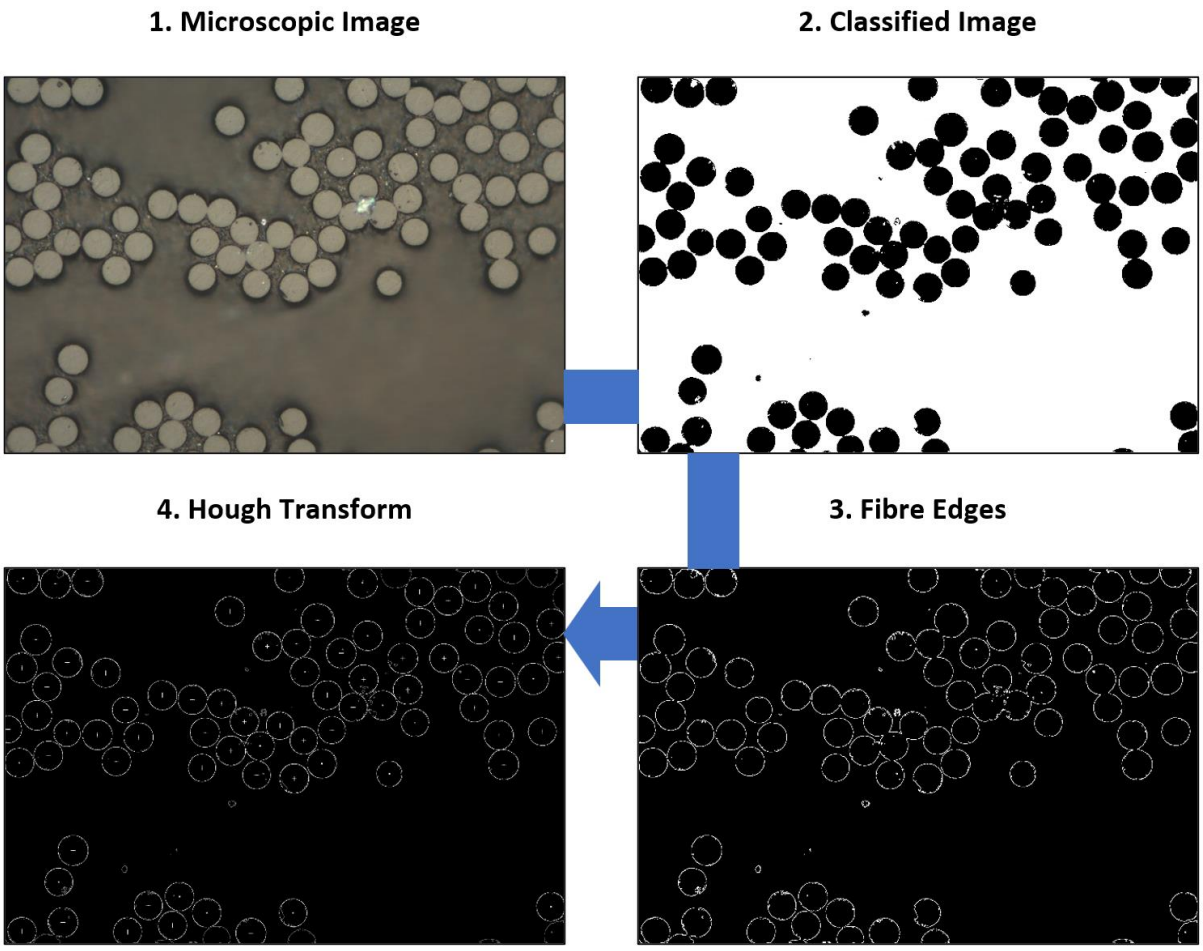

Figure 55: Four step process to extract the fibre diameters and coordinates from the microscopic images.

5.3 Representative Volume Element

A Representative Volume Element (RVE) could be used to study a materials behaviour and to determine its mechanical properties. This approach has been successfully used in numerous

studies to predict the behaviour of a composite material [192] [188]. Per definition an RVE "is entirely typical of the whole mixture on average".

5.3.1 Periodic Boundary conditions

For small RVEs, displacement boundary conditions lead to an overestimation in stiffness due to all the outer surfaces of the RVE remaining flat [193]. Researchers therefore preferred periodic boundary conditions (PBCs) for the microscopic investigation of composite and porous materials [194] [195] [196] [197]. The PBC were achieved by constraining the displacement of opposite nodes of the RVE

$$u_j^{i+} - u_j^{i-} = \varepsilon_{ij}^0 l_i \ (i,j = x,y,z) \tag{5.1}$$

where u_j^i are the node displacements, ε_{ij}^0 the macroscopic strain tensor and l_i the length of the RVE. The macroscopic strain was applied via reference nodes located on the top, right and front side of the RVE. The stresses were calculated according to Okereke et al using the reaction forces *RF* of the reference nodes

$$\langle \boldsymbol{\sigma} \rangle = \frac{1}{V} \sum_k^{N_k} x_k \otimes RF_k \tag{5.2}$$

where *k* is the index of the reference node, V the volume of the RVE and *x* the coordinate position of the reference node [198]. An overview of different implementation methods of the PBCs into the FE code can be found in [199]. In this work the equations proposed by Li et al were used [200]. Their correct implementation was verified by assigning each section of the RVE the same homogenous elastic material and applying different load cases. The resulting stress and strain fields were perfectly uniform and therefore the boundary conditions were implemented correctly. Based on the stresses and strains it was verified that the calculated material properties (e.g., Young's modulus) matched the input parameters.

5.3.2 Size determination

The fibre distribution in the printed material was very inhomogeneous because the fibre distribution in the raw filament already was inhomogeneous (comp. Figure 44). To determine the minimum size of the RVE, the influence of the width and height on the homogenised

properties were analysed. A fibre modulus of 73 GPa and a matrix modulus of 1.7 GPa were used [201] [132]. For the determination of the minimum height of the RVE random sections with a fixed width of 1500µm were modelled. The difference between the maximum and minimum values of the properties was then plotted. It was ensured that there were no air-inclusions present in the segments. To allow for clean meshing, a MATLAB script was used to decrease the diameter of fibres iteratively until a minimum distance of 0.5µm was reached. This caused the fibre volume content to decrease from 29.4% to 27.3%. As the position of the fibres was not changed the decrease was assumed to be negligible. Fibres on the borders were moved inside the RVE and it was paid attention that the fibre volume content was not changed by this process. For each height three segments were calculated and the difference between the minimum and maximum values for each elastic property was calculated. As shown in Figure 56 the mechanical properties only showed very little variation with a 200µm element height. The influence of the RVE width was then determined by applying the same methodology using a fixed height of 200µm and modelling different widths (comp. Figure 57). Due to the limited number of models the graph has steps in it but a downwards trend is clearly visible.

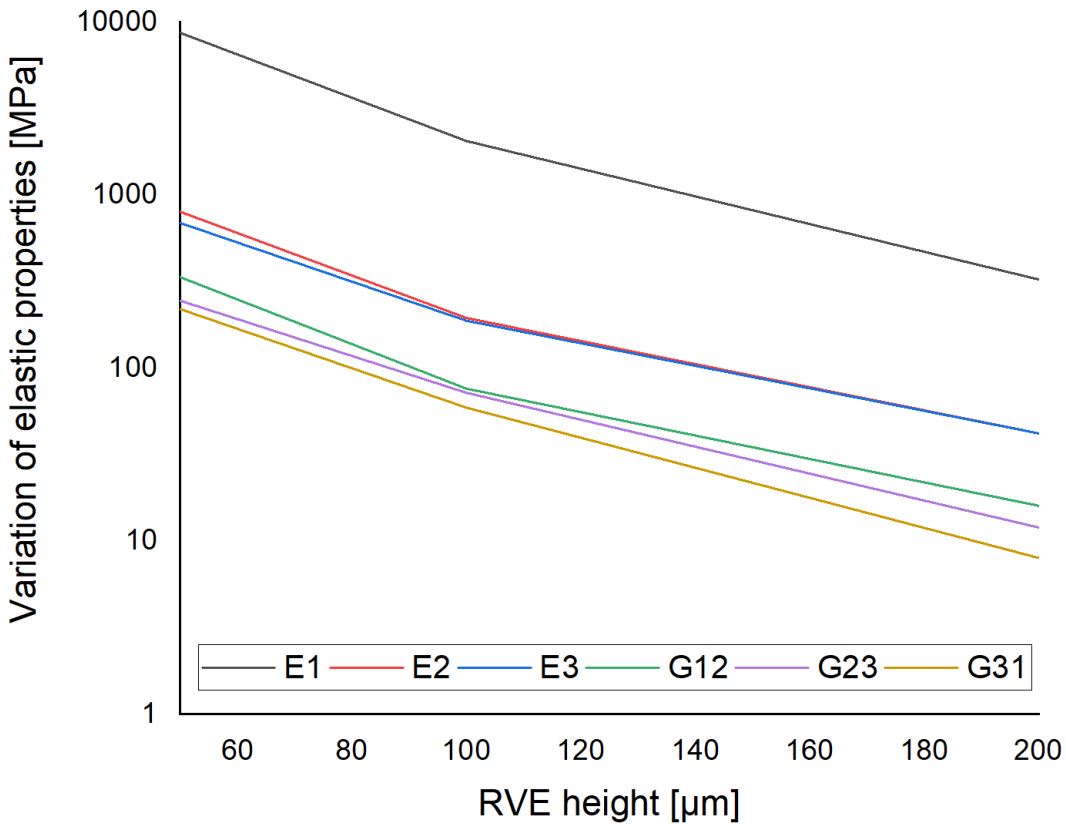

Figure 56: Influence of the height on the variation of the elastic properties for a constant width of 1500µm.

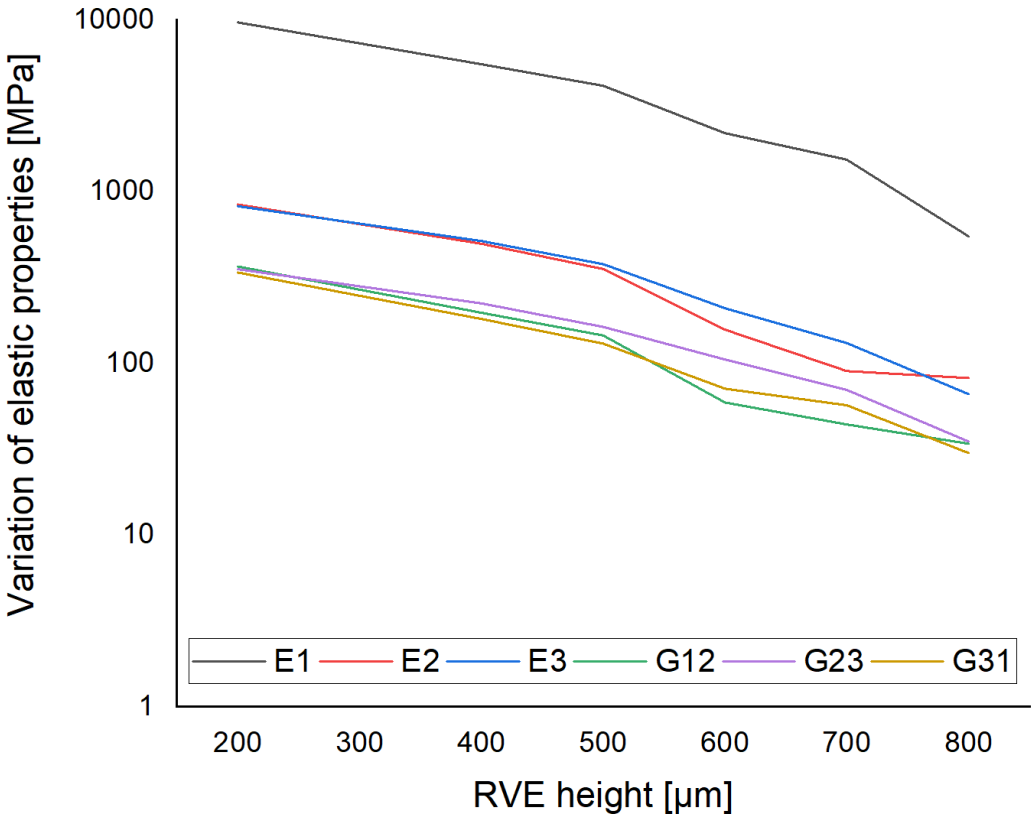

Figure 57: Influence of the width on the variation of the elastic properties for a constant height of 200µm.

Consequently, an RVE with a size of 800x200 µm² is expected provide a good representation of the materials response (comp. Figure 58 and Table 20). However, this model is too large for the failure analysis given the computational power that was available. While the calculation of the homogenised properties already required a lot of resources, especially for the larger RVEs, all the non-linear effects and fine meshing that was required for the failure analysis results in a significant higher computational effort. Furthermore, the periodic boundary conditions are handled in a way that increases the per-increment calculation time by orders of magnitude (compared to displacement boundary conditions). Therefore, it was not possible to analyse the failure of the RVE. Instead, this study will focus on a 15µm x 15µm unit cell with a depth of 6µm containing a single Ø9.3µm fibre. This unit cell represents an ideal version of the material where all fibres are distributed equally. Nonetheless, the RVE that was identified in this study, could be used in future studies.

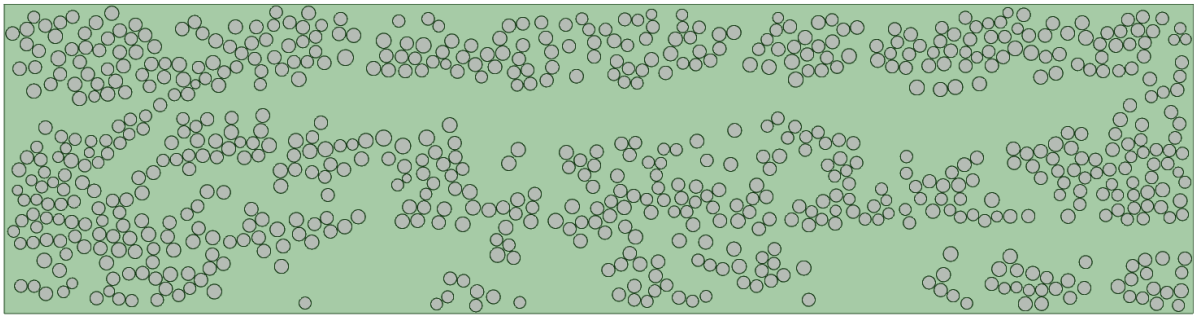

Figure 58: 800x200 µm² RVE

Table 20: Homogenized properties of the 800x200 RVE with a reduced fibre volume content and fibre modulus of 75 GPa and a matrix modulus of 1.7 GPa

	E1	E2	E3	G12	G23	G31
1500x200	20.2	3.2	3.1	1.2	1.1	1.0
800x200	20.6	3.2	3.1	1.2	1.1	1.0

5.4 Constitutive Model

5.4.1 Glass Fibre

The average fibre diameter, which was determined by optical microscopy, is 9.3µm with a normal distribution shown in Figure 59. While the manufacturer does not disclose any information about the fibre properties a study has determined an average Young's modulus of 82 GPa and a tensile strength of 2.2 GPa by extracting fibres via pyrolysis [86]. Since these results were not known prior to the start of the homogenization, slightly different fibre properties were used in the previous section. Ultrasonic vibration analysis has shown that glass fibres are isotropic, consequently they will be modelled as a linear elastic isotropic material and a Poisson's ratio of 0.18 is used [202] [168].

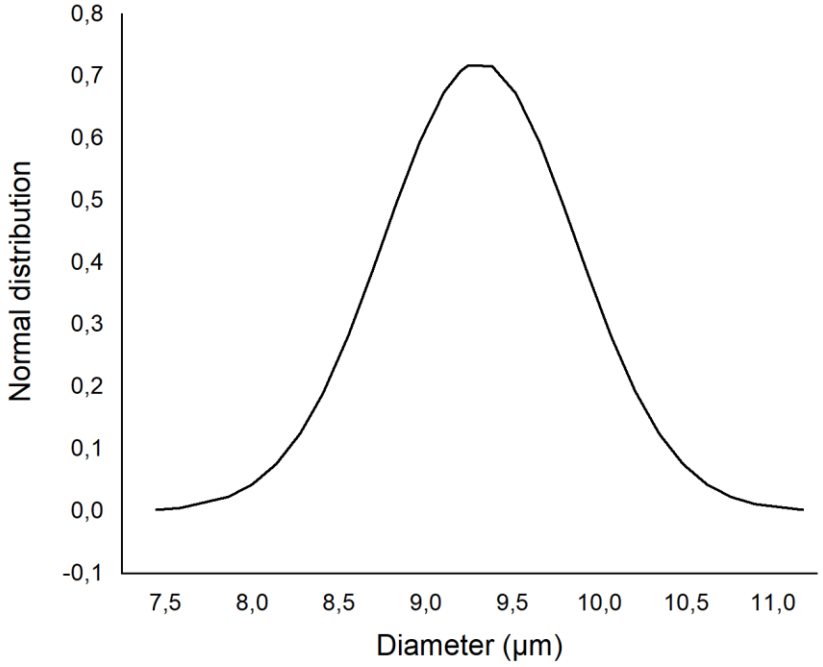

Figure 59: Normal distribution of the fibre diameter

5.4.2 Fibre-Matrix Interface

The fibre-matrix interface failure behaviour was model using a bilinear traction separation law shown in Figure 60 where the elastic behaviour is

$$\boldsymbol{t} = \begin{Bmatrix} t_n \\ t_s \\ t_t \end{Bmatrix} = \begin{bmatrix} K_{nn} & 0 & 0 \\ 0 & K_{ss} & 0 \\ 0 & 0 & K_{tt} \end{bmatrix} \begin{Bmatrix} \Delta_n \\ \Delta_s \\ \Delta_t \end{Bmatrix} = \boldsymbol{K}\Delta \tag{5.3}$$

with the traction vector t and the separation Δ comprising of three components (normal, shear and tangential direction). The initial/elastic compliance $\boldsymbol{K}$, the interface strength $\boldsymbol{T}$ and fracture separation Δ^{fail} define the fracture energy rate G_C (area under the curve). $\boldsymbol{K}$, is defined by the critical separation Δ^c and the interface strength $\boldsymbol{T}$:

$$K_{nn} = \frac{T_n}{\Delta_n^c}, K_{ss} = \frac{T_s}{\Delta_s^c}, K_{nn} = \frac{T_t}{\Delta_t^c} \tag{5.4}$$

To maintain a homogenous stress/strain field, researchers have used values ranging from 10^5 to 10^{10} GPa/m [189] [203] [188] [204] [205]. In this study 0.3* 10^5 GPa/m and an interface thickness of 0.1 µm were used. A study investigating the fibre/matrix interface of conditioned polyamide 6 and glass fibres has determined a fracture energy rate of 165 J/m² for unsized fibres [206]. While this value seems plausible for a conditioned polyamide 6, which exhibits a

ductile fracture behaviour, for a dry polyamide 6 the fracture energy is likely to be much lower. For polycarbonate a fracture energy rate of 45 J/m² resulted in a good agreement between the experiments and simulation [189]. For polypropylene a value of 10 J/m² led to accurate results [188]. A study analysing the failure of a thermoset composite used a fracture energy rate of 5 J/m² [204]. In a later study the same research group applied a machine learning algorithm to determine the fracture parameters and found that a tensile fracture energy rate of 2 J/m² provides the most accurate results [205]. For this study 40 J/m² were used like the one for polycarbonate. However, future studies should investigate the fracture energy of dry polyamide reinforced with glass fibres.

If the maximum stress in either the normal (T), shear (S_1) or tangential (S_2) direction is reached, the elements stiffness is linearly degraded with the help of the degradation parameter *d*. Due to a lack of available experimental data, it will be assumed that the initial stiffnesses, fracture energy rates and the interface strengths are equal in all directions (K_{nn} = K_{ss} = K_{tt}, G_{IC} = G_{IIC} = G_{IIC}, T_N=T_S=T_T).

Liu et al. has achieved good agreement between simulated and experimentally determined properties of glass fibre reinforced polycarbonate by using an interface strength equal to the yield strength of the matrix material [189]. Therefore, an interface strength of 70 MPa was used in this study.

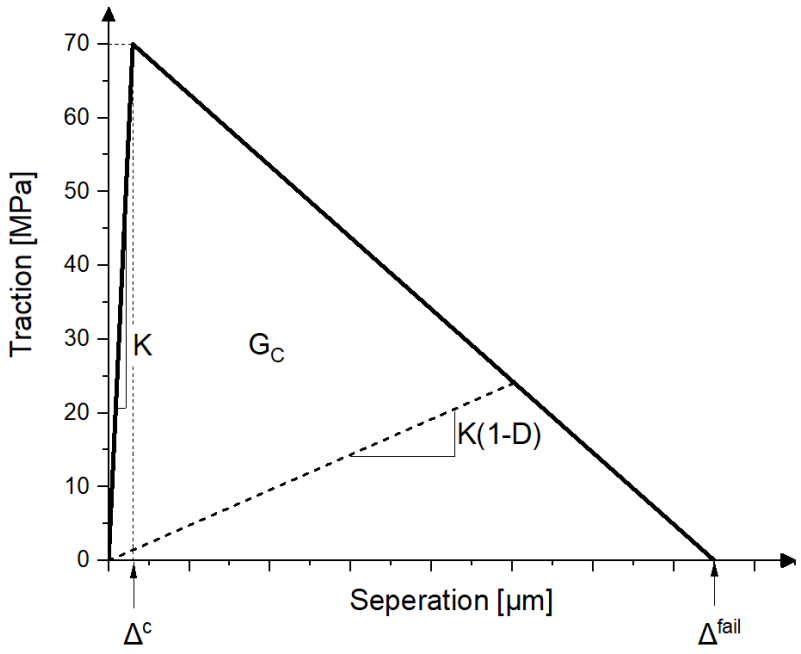

Figure 60: Bilinear Traction separation law. The area under the curve is equal to the energy release rate G_C

5.4.3 Polyamide 6

Polyamide 6 is known to have significantly different mechanical properties depending on the water saturation level [207]. Since the focus was put on the heat-treated samples, a dry polyamide was assumed. While the simulation requires true stress-strain data most published work only contains the engineering stress strain data. The engineering stresses and strains can be converted to true stresses and strains using

$$\varepsilon_{True} = \ln(1 + \varepsilon_{Eng}) \tag{5.5}$$

$$\sigma_{True} = \sigma_{Eng} * (1 + \varepsilon_{Eng}) \tag{5.6}$$

However, this relationship is only true for incompressible materials and only until necking begins. For polyamide 6 the start of necking was reported to occur at the yield point [208]. But even if it did not, these equations would only provide a rough estimate for polyamide 6, as it cannot be considered incompressible. So, in order to get accurate results, a constant measurement of the current cross-section during mechanical testing is required to get accurate results. The only publication containing true stress-strain data for dry Polyamide that could be obtained was published by Felder et al [209]. Their work also provides value information for future research regarding the temperature and strain rate dependence of the material. However, as shown in Table 21, the mechanical properties of dry polyamide 6 stated in the manufacturer's datasheets vary significantly depending on the manufacturer/specific blend. As Felder et al sourced their material from BASF, their determined Young's modulus of 2600 MPa and yield strength of 70 MPa seem plausible but are overall lower than the material provided by other manufacturers.

Table 21: Mechanical properties of dry polyamide 6 from different manufacturers

Manufacturer	**Young's modulus** [MPa]	**Yield strength** [MPa]	**Elongation at yield** [%]	**Elongation at break** [%]
BASF [210]	2800	70	3,5	-
Akro-Plastic [211]	3200	80	4	20
Direct Plastics [212]	3300	84	5	37
Dupont [213]	3600	92	3.8	9

An analysis of the failure behaviour of Polyamide 6 by Selles et al. has shown that failure is initiated by nanometric voids [214]. Void growth and coalescence eventually result in material failure [208].

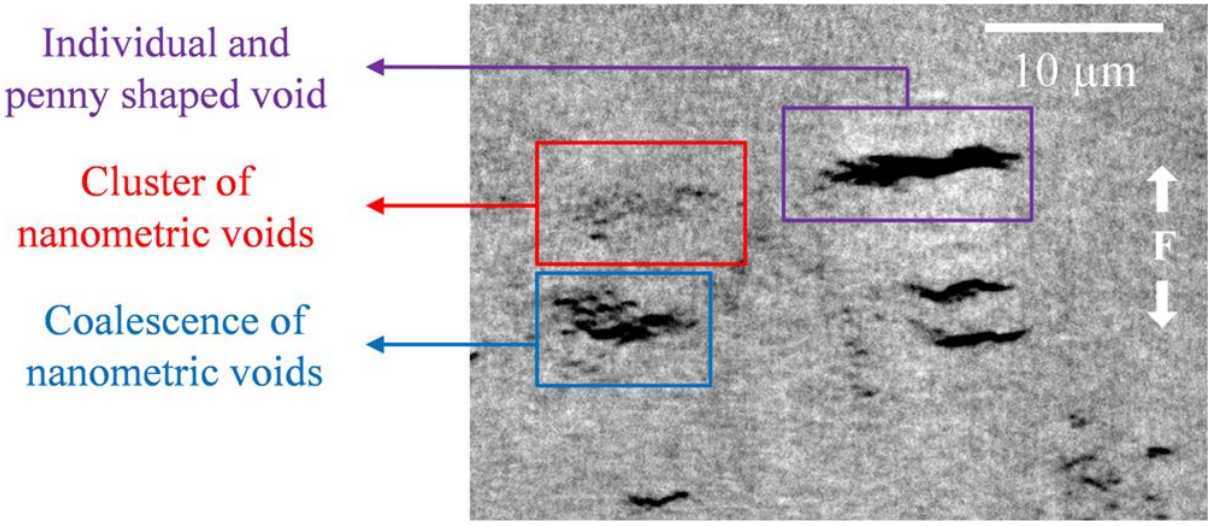

Figure 61: Different voids observed in Polyamide 6 [214]

The Gurson-Tvergaard-Needleman (GTN) model could potentially be used to model this behaviour. It was developed by Gurson and later modified by Tvergaard and Needleman [215] [216] [217]. Void nucleation, void growth and void coalescence are assumed to be correlated to the void volume fraction of the material. Jeridi et al. used the GTN model for predicting the creep behaviour of Polyamide 6. Good agreement between experimental and simulated values were achieved by differentiating between the amorphous and crystalline phase [218]. The GTN model was also used by Liu et al for the failure simulation of polycarbonate and good a good match with experimental results was achieved. While Polycarbonate (PC) and Polyamide 6 are very similar in their mechanical properties and failure mechanisms there is currently not enough data available for this model to be used for the failure modelling PA6 [219] [220].

Instead, based on recommendation from the research community, the failure was modelled using a phenomenological model that captures the failure mechanisms based on the fracture energy G_f of the material [221]

$$G_f = \int_{\bar{\varepsilon}_0^{pl}}^{\bar{\varepsilon}_f^{pl}} L\sigma_y d\bar{\varepsilon}^{pl} = \int_0^{\bar{u}_f^{pl}} \sigma_y d\bar{u}^{pl} \tag{5.7}$$

where *L* is the characteristic element length, $\bar{\varepsilon}_0^{pl}$is the equivalent plastic strain at yielding, $\bar{\varepsilon}_f^{pl}$the equivalent plastic strain at failure and $\bar{u}_f^{pl}$ the equivalent plastic displacement at failure. At the onset of yielding the damage variable *D* is used to degrade the material stiffness

$$E_{Damaged} = (1 - D)E_{Undamaged} \tag{5.8}$$

In this model the damage is initiated when

$$\omega_D = 1 \; with \; \Delta\omega_D = \frac{\Delta\bar{\varepsilon}^{pl}}{\bar{\varepsilon}_D^{pl}(\eta, \dot{\bar{\varepsilon}}^{pl})} \geq 0 \tag{5.9}$$

where $\bar{\varepsilon}^{pl}$ is the equivalent plastic strain, $\bar{\varepsilon}_D^{pl}$ the equivalent plastic strain at the onset of damage and η the stress triaxiality. Due to a lack of experimental data, a linear degradation is assumed

$$\dot{D} = \frac{\dot{\bar{u}}^{pl}}{\bar{u}_f^{pl}} \tag{5.10}$$

Due to the previously elaborated void-related failure behaviour, the compressive strength was expected to be higher than the tensile strength, because voids do not open when being loaded under compression. For calibrating the model, the true stress-strain graphs until failure would be required. However, there is no publication containing this data. Different authors were contacted, but none of them was willing to share their data. Thus, based on the data published by Felder et al. and Parodi et al., a failure onset for uniaxial tension was assumed to begin a plastic strain $\bar{\varepsilon}_D^{pl}$ of 0.08 [209] [222]. Like the approach taken by Pulungan et al., the damage onset for shear and uniaxial compression was chosen to be three and six times greater than for uniaxial tension and a 0.15 µm displacement at failure was assumed [188].

To account for the pressure dependent plasticity [223], the extended linear Drucker-Prager yield criterion was used, which is defined as

$$F = t - ptan\beta - d = 0 \; where \; t = \; 0.5q\left[1 + \frac{1}{K} - \left(1 - \frac{1}{K}\right)\left(\frac{r}{q}\right)^3\right] \tag{5.11}$$

where *q* is the Mises equivalent stress, *K* is the ratio of the yield stress in triaxial tension to the yield stress in triaxial compression, *r* is the third invariant of the deviatoric stress, *p* is the equivalent pressure stress and β is the friction angle of the material (slope of the linear yield surface in the p-t plane). *d* is the cohesion of the material and defined based on the tensile yield stress

$$d = \left(\frac{1}{K} + \frac{1}{3} tan\beta\right) \sigma_t \tag{5.12}$$

The plastic flow is modelled as

$$G = t - p tan\psi \tag{5.13}$$

where ψ is the dilation angle in the p-t plane. It is assumed, that β = ψ (associated flow rule). For a crosshead speed of 1mm/min, which can be considered as quasi static, the friction angle for conditioned polyamide 6 was determined to be 11.8°, which was used in this study [223].

5.4.4 Simulation parameters

To avoid convergence issues the simulations were carried out using ABAQUS/Explicit. The displacements were applied via a smooth step function with a final displacement of 2 µm for the uniaxial load. For combined loading the tensile/compressive load was also set to 2 µm and the shear displacement was varied. Mass scaling was used to accelerate the simulation, with the target time increment set to $8*10^{-6}$ s. It was verified that the kinetic energy is below 10% of the total internal energy to ensure that the mass scaling did not influence the results. The same verification was carried out for the artificial strain energy, to ensure that hourglassing was not a problem. The energies for the uniaxial load case are shown in Figure 62. The fibre and matrix were meshed using linear hexagonal elements (C3D8R) with reduced integration and enhanced hourglass control and a mesh size of 0.5 µm. The interface was meshed using linear cohesive elements (COH3D8). The maximum element degradation was limited to 0.99.

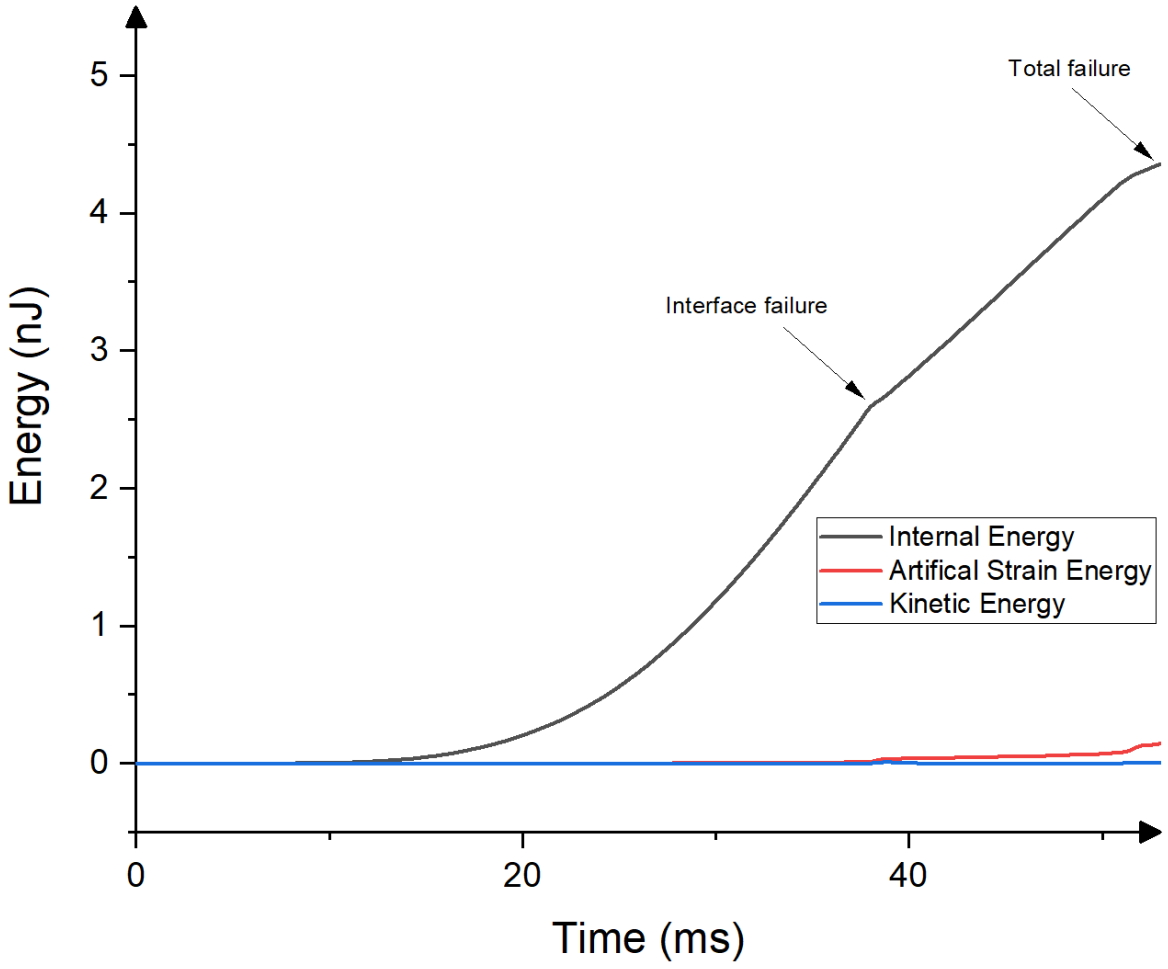

Figure 62: Internal, artificial strain and kinetic energy for the uniaxial tension loading of the unit cell

5.5 Results and discussion

In this chapter the results of the micromechanical analysis will be presented and discussed.

5.5.1 Uniaxial Tension

Figure 63 shows the stress-strain data from the simulation of the uniaxial tensile load case. Furthermore, the experimental data from the post-processed material is included for comparison. It is important to remind the reader, that the test tokens had non-reinforced outer layers, which were mandated by the printer's software. As discussed in the previous chapter, the waviness in the experimentally determined stress-strain curve most likely results from localised delamination, which eventually results in material failure.

The unit cell exhibited a multistage failure, which is shown in more detail in Figure 64 (element degradation) and Figure 65 (equivalent plastic strain). First, the degradation started at the centre of the interface (1). The degradation propagated along the interface (2) causing a strain concentration within the matrix, which led to failure initiation within the matrix (3). Failure of the interface (4) was followed by a crack growth in the matrix along the interface (5), which led to part failure (6). A similar multistage failure behaviour of a unit cell was observed for fibre-reinforced polypropylene [188].

The simulation for uniaxial tension was carried out with the Young's modulus from Felder et al. (2.6 GPa) as well as with a Young's modulus of 3 GPa. The plasticity data was not changed. The deviation between the experimental stress strain curve and the simulated one in the range of 1% and 2% strain was reduced when assuming the higher Young's modulus, whereas it increased above 2%. This change in the overall shape proves, that the properties of the polyamide have a significant influence on the overall response. This is a result of the low fibre volume fraction. As already mentioned in the previous section, the stress-strain data used for the simulation is on the lower end regarding the Young's modulus compared to other manufacturers. The simulation results indicated, that Markforged most likely uses one of the stiffer polyamide 6 blends. As the unit-cell does not consider the inhomogeneous fibre-distribution, it is also to be expected, that the strain at failure is higher than the experimentally determined one. In an RVE, stress is expected to accumulate in fibre dense areas, initiating crack growth resulting in a lower elongation at break. Also factors like the remaining air-voids and fibre-misalignment were not considered, which are also expected to affect the results.

In order to give future research projects an insight how the different parameters affect the stress-strain response a sensitivity analysis was conducted. This was done, by increasing single input parameters by 20% and leaving the others at their initial value. Figure 66 and Figure 67 show the influence of different matrix, interface and fibre parameters on the stress-strain response. The parameters with most significant influence were identified to be the matrix and interface strength. Due the small fibre volume fraction, the matrix makes up a large portion of the RVE and therefor it can be expected the matrix strength has a significant influence on the stress-strain response of the composite. The increase of the interface strength resulted in the interface having a higher strength than the matrix. As result, some matrix elements

close to the fibre failed, which shows in a slight drop in the stress before the eventual interface failure. Future studies should investigate both interface and matrix behaviour and these parameters can be used to further calibrate the FEM model as already discussed in section 5.4.2.

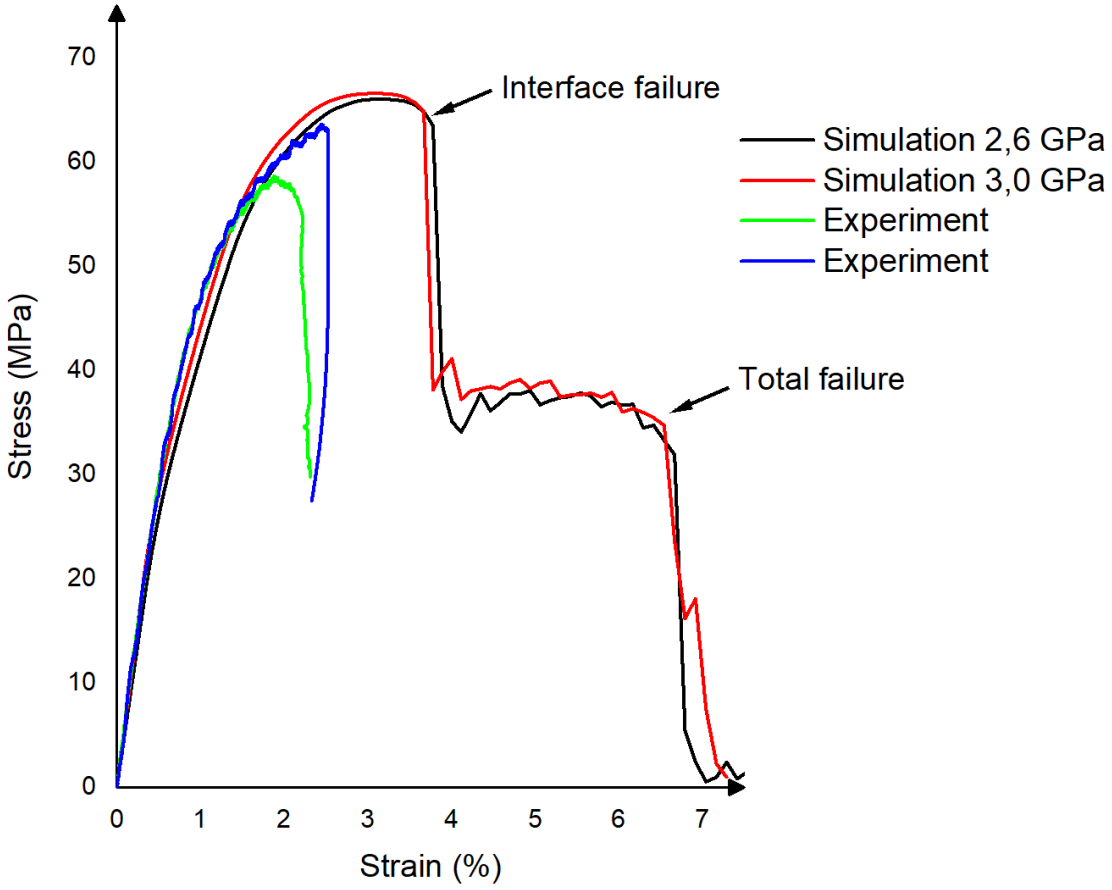

Figure 63: Stress-strain diagrams for the uniaxial tensile load case. The experimental data refers to the post-processed samples from the previous chapter.

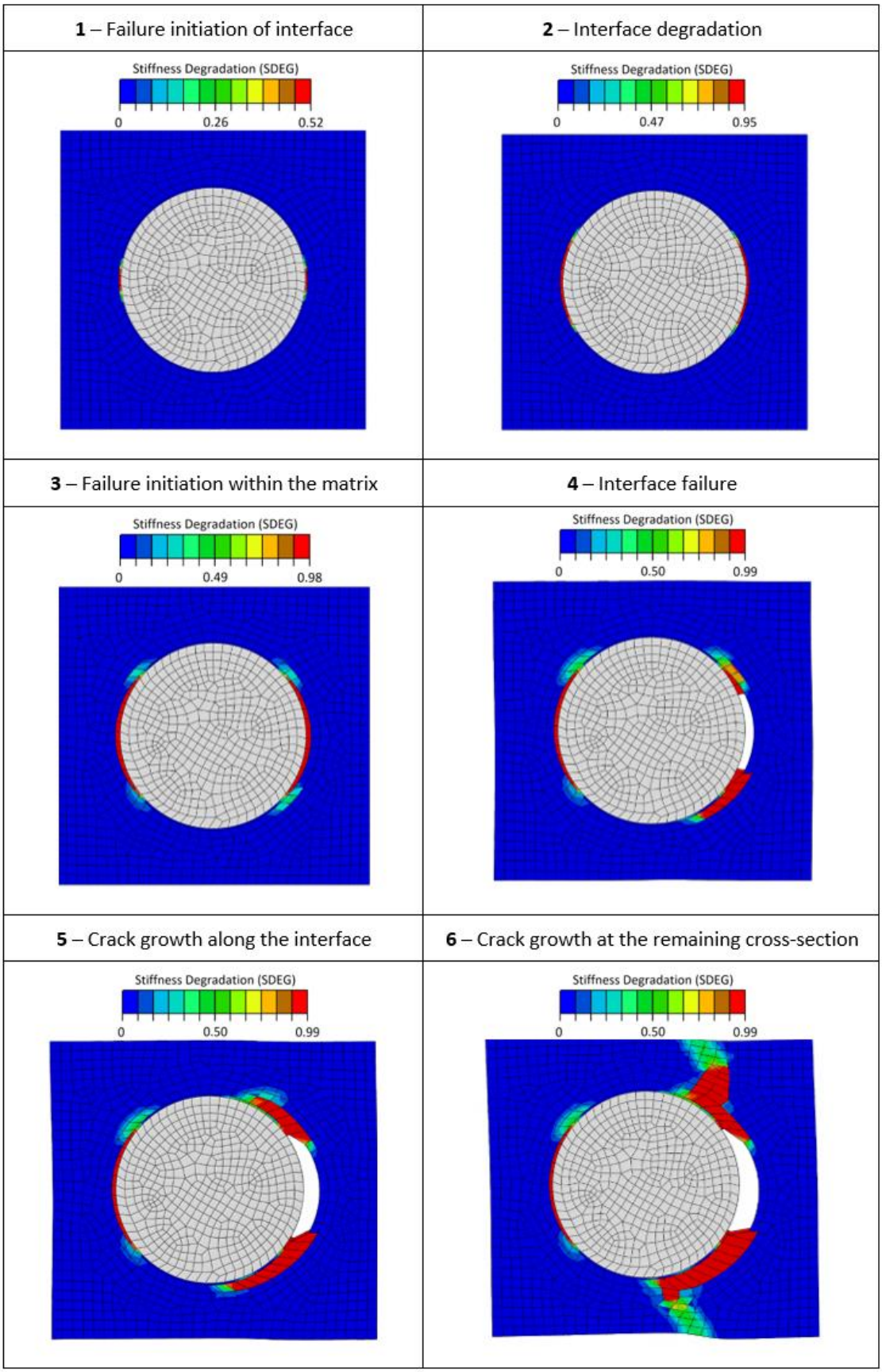

Figure 64: Element degradation during the uniaxial tensile loading. The element deletion of the matrix was deactivated for a better illustration.

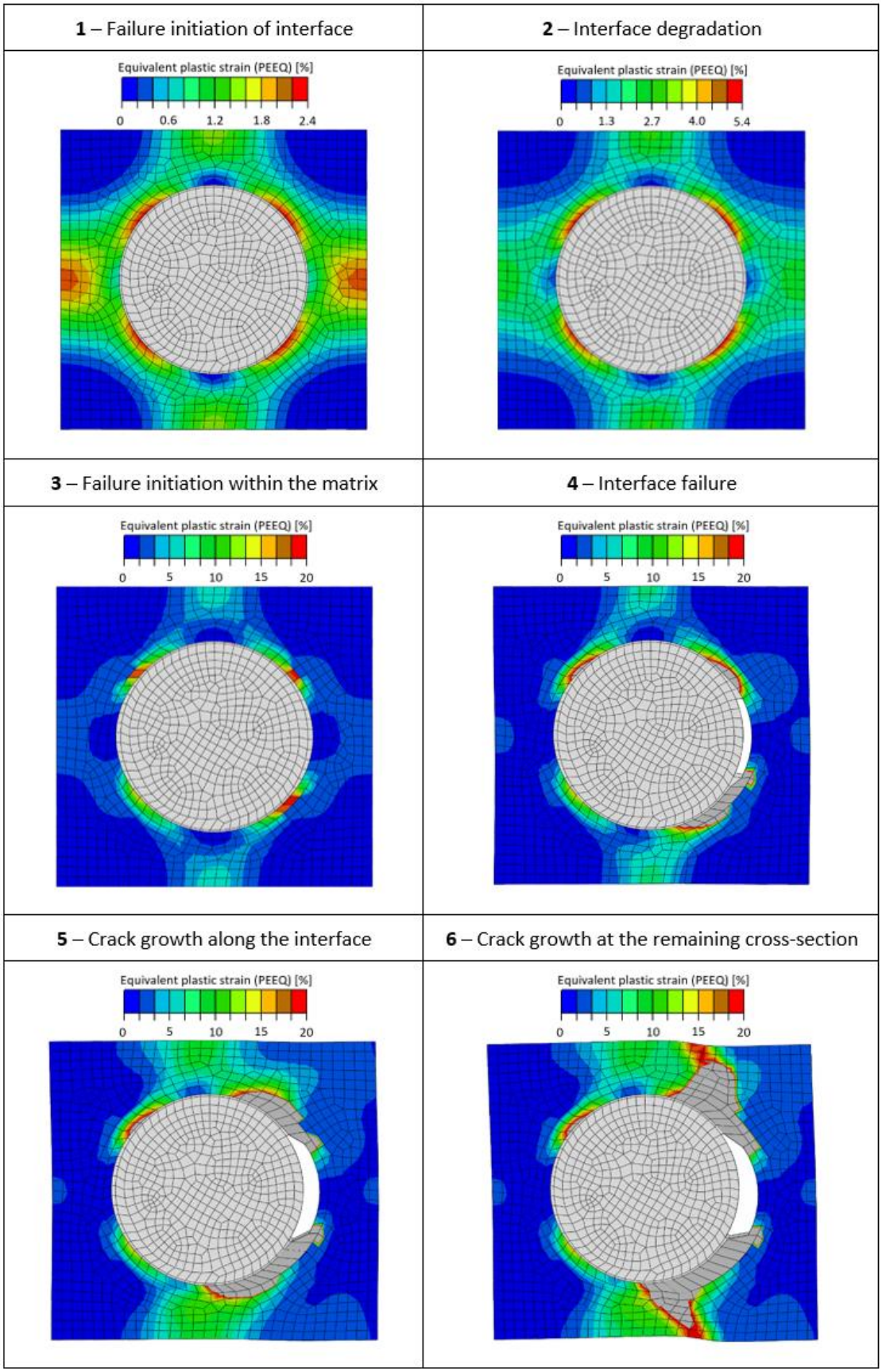

Figure 65: Equivalent plastic strain (PEEQ) during the uniaxial tensile loading. The element deletion of the matrix was deactivated for a better illustration.

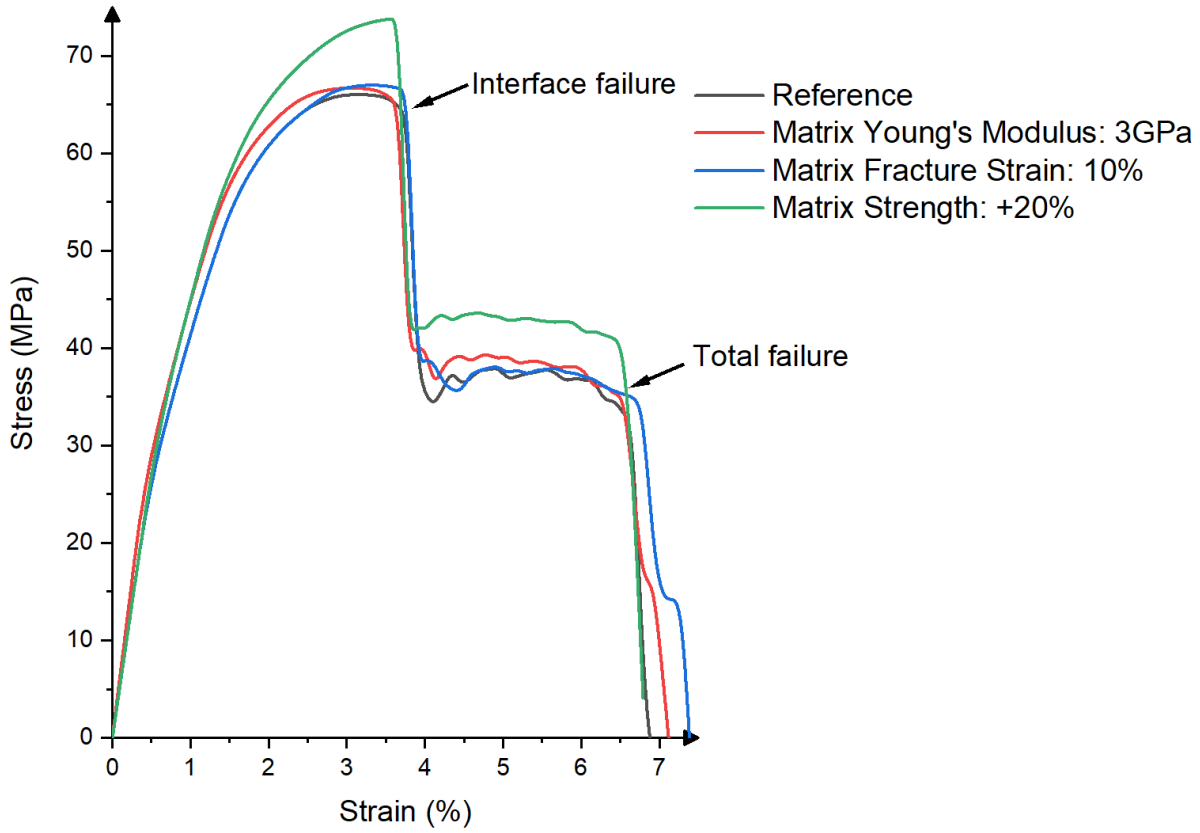

Figure 66: Effects of a 20% increase of different matrix parameters on the stress-strain response.

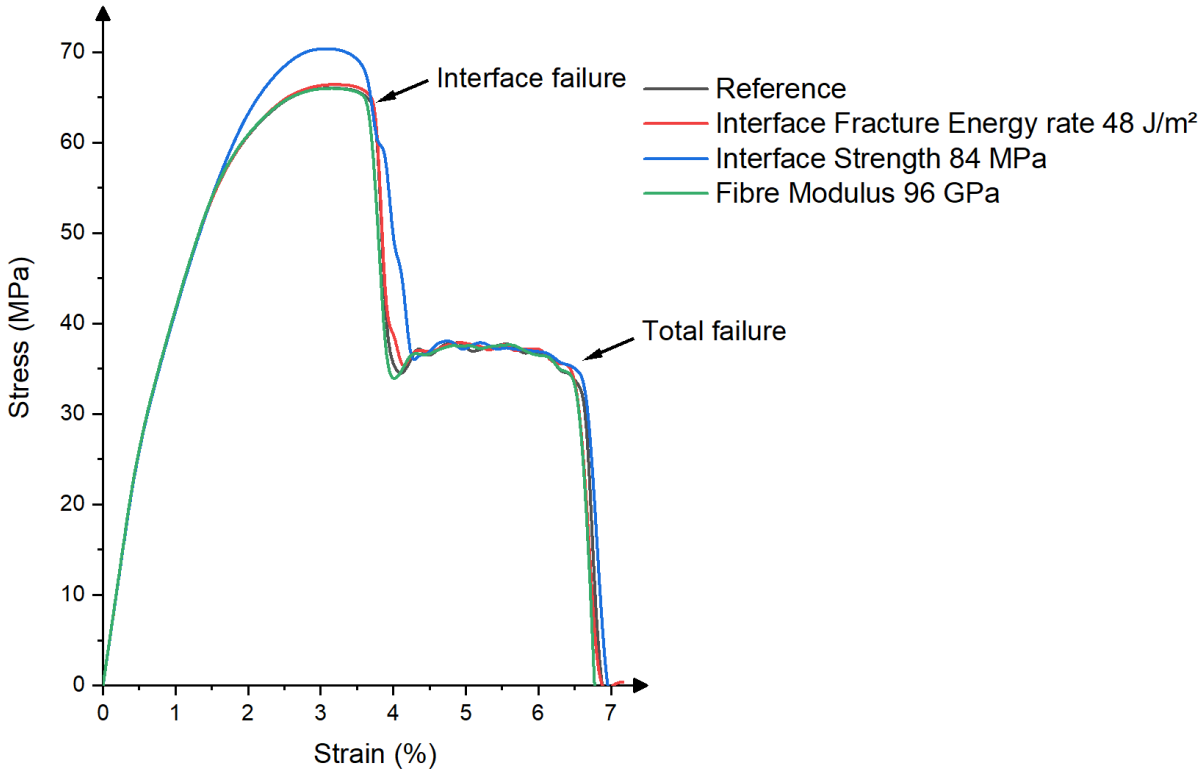

Figure 67: Effects of a 20% increase of different matrix parameters on the stress-strain response

5.5.2 Combined loading

The stress response under displacement controlled combined loading is presented in Figure 68 and the fracture mode for each load case is illustrated in Figure 69 and Figure 70. For all combined load cases with a tensile stress, the fracture plane was parallel to the plane where the load was applied to. This was also the case for the longitudinal shear load case. However, for pure compression, the fracture angle changes. The transition of the fracture angle was observed between a compression/shear load ration of -0.25 and -0.5. However, it is important to remind the reader, that the determined transition point can only be considered an indicator, as the unit cell does not take the fibre distribution into account. Besides the change of the fracture angle, it was observed, that the shear stress at failure was increased, when simultaneously applying a compressive load, before decreasing again. For a combined tensile and shear load, the shear load at failure immediately decreases. The inhomogeneous fibre distribution is expected to have an influence on both the fracture envelope as well as the transition of the fracture angle. Therefore, a more detailed analysis of the gradual failure process under combined loading should be carried out with the RVE presented in section 5.3.2.

Both the change in fracture angle and the increase in shear stress at failure for combined shear and compressive loading are considered by Puck's failure theory [13]. Puck's failure theory will be elaborated in more detail in the next section, but the predicted failure envelope is included in Figure 68. Overall, Puck's predicted failure envelope was in good agreement with the micromechanical model. One of the tests, that was proposed by Puck to verify if his failure theory is applicable, is a transverse compression test. A fracture angle of 54° (±3°) is a strong indicator, that Puck's failure theory can be applied to the composite material. For this study, a compression test was carried out using test tokens, that were not pressure treated. The test token geometry as well as a failed test token is shown in Figure 71. Before testing, the front and back surfaces were milled off to avoid any influence from the fibre loops. At the front of the test token, the fracture angle of 57° predicted by Puck was clearly visible. One back side however, separation of the individual strands was observed. This was most likely caused by the large air-inclusions, which were discussed in more detail in the previous chapter. In future studies, this test should be repeated with pressure treated test tokens.

The only publication the failure envelope determined in this study can be compared to was published by Schramm et al [191]. They tested conditioned polyamide 6 with a 40% glass fibre volume content and found a good agreement between their experimental data and Puck's failure theory under combined loading. For the uniaxial test cases they measured a tensile strength of 25 MPa, a shear strength of 30 MPa and a compressive strength of 75 MPa at 23°C. These strengths are significantly lower than the ones determined in this study. The difference can be explained by the change in mechanical properties of polyamide 6, because the tensile strength decreases significantly as the water saturation increases [207] [224]. As the tensile strength predicted in this study was experimentally validated, the obtained fracture envelope seems plausible. Nonetheless, the macroscopic failure analysis in section 5.7 was carried out for both the strengths of the dry composite determined in this study as well as the ones for the conditioned composite determined by Schramm et al.

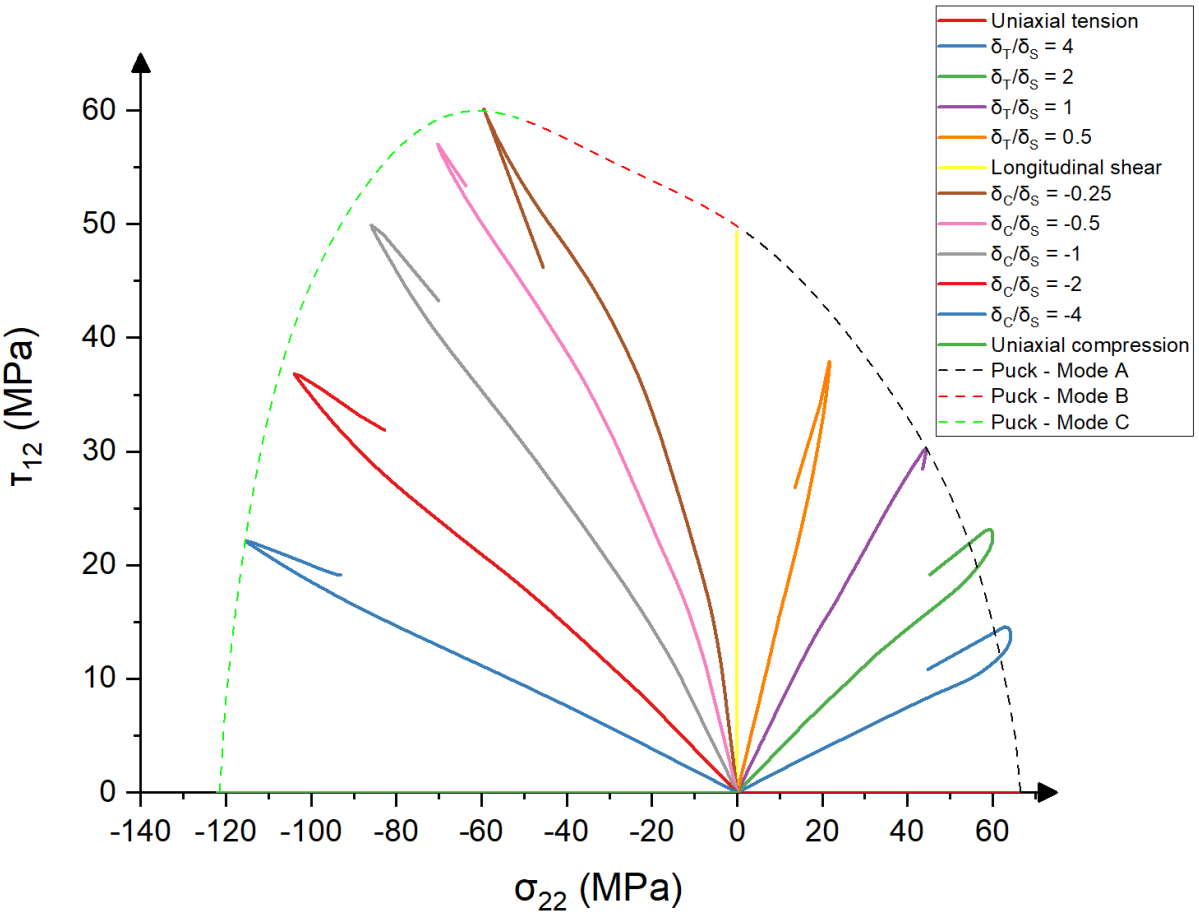

Figure 68: Fracture for combined longitudinal shear and transverse tension/compression.

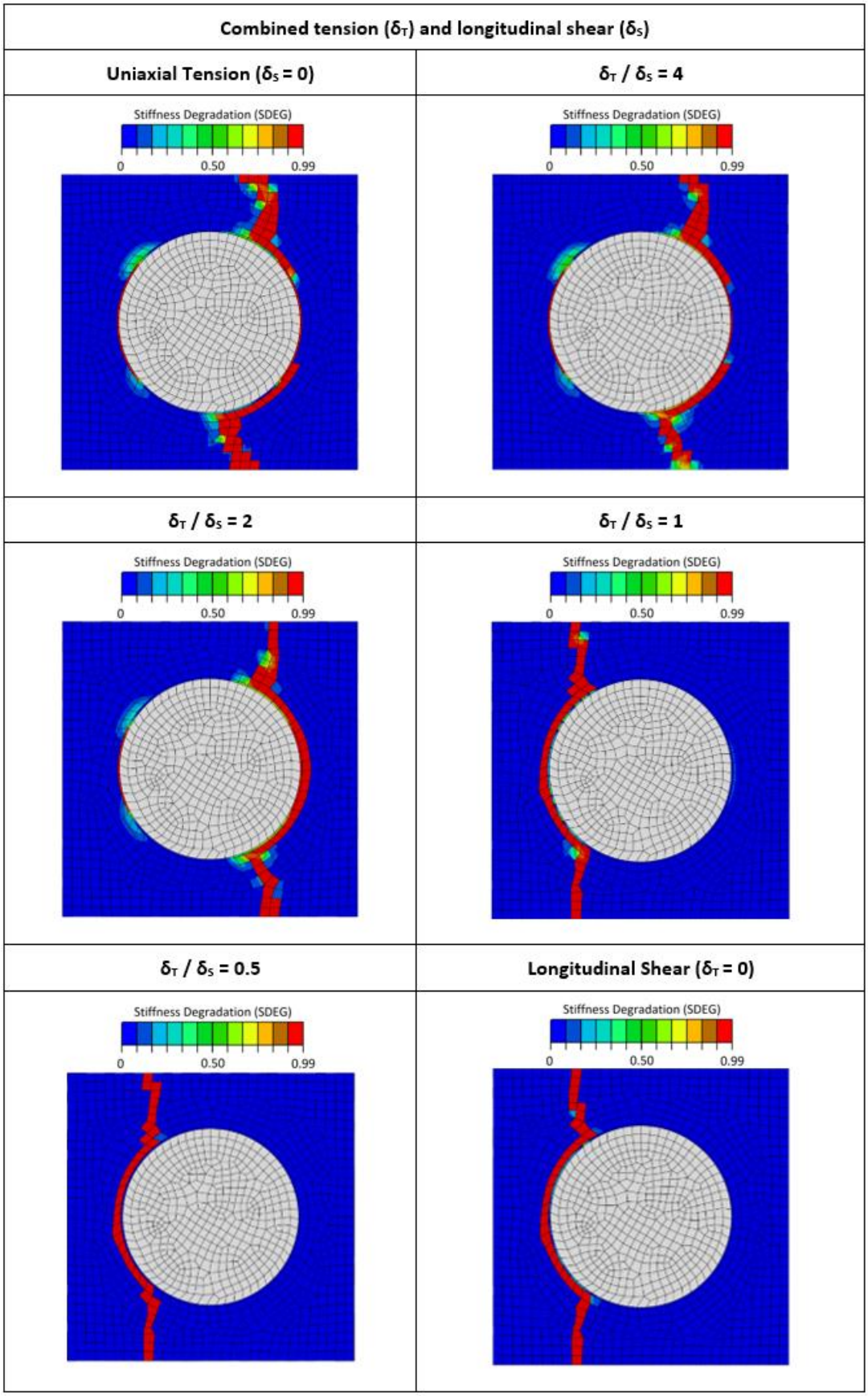

Figure 69: Fracture modes for combined tensile and longitudinal shear loads. The stiffness degradation was mapped onto the undeformed shape for a better illustration.

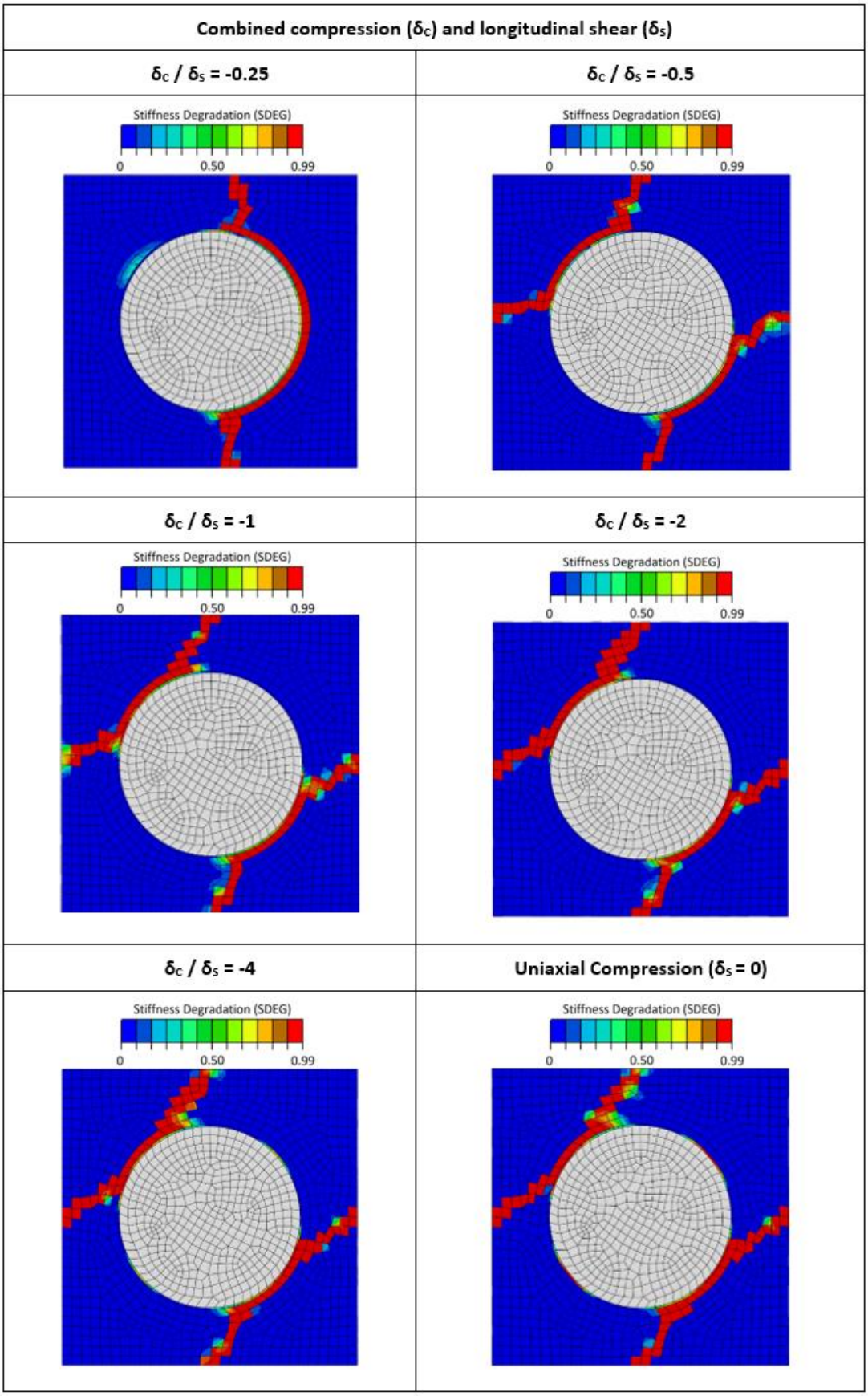

Figure 70: Fracture modes for combined compressive and longitudinal shear loads. The stiffness degradation was mapped onto the undeformed shape for a better illustration.

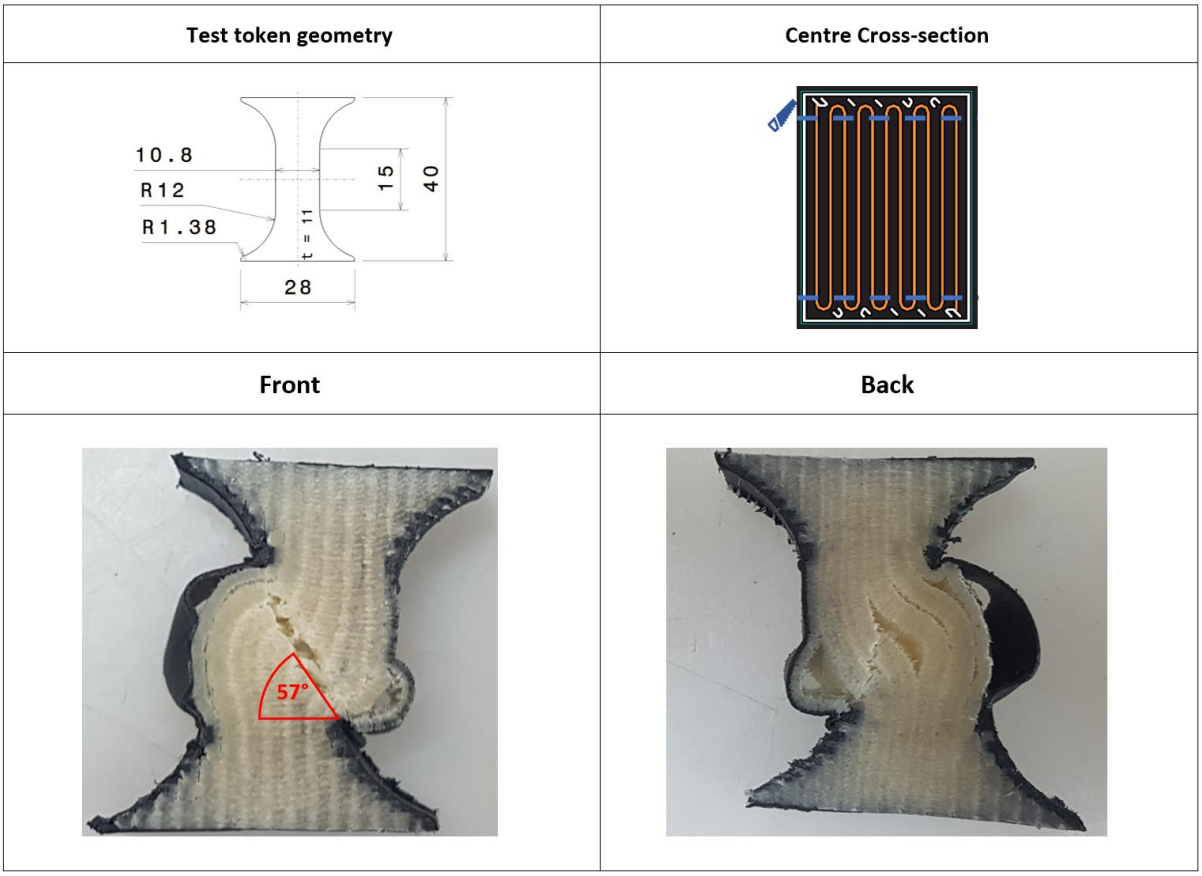

Figure 71: Geometry of the compression test token and a failed test token.

5.6 Puck's 2D fracture criterion

The change of the fracture angle under combined transverse compression/longitudinal shear and the increased shear strength for that load case is not unique to this material but has also been observed in conventional composites. Based on Mohr's failure theory for brittle isotropic materials and with the change in fracture angle in mind, Alfred Puck formulated his failure theory, which was published in 1996 in Germany only [13]. Publications in English were made for the "worldwide failure exercises", where numerous failure prediction models were evaluated and compared to each other. But it wasn't until 2008 that his work got fully translated into English by Martin Knops [225]. The sophistication of Puck's model showed in the different world-wide failure exercises. Puck's failure theory was declared the winner in the first "worldwide failure exercise" [14] [15] and was among the final top four theories in the second one [226]. The failure criterion is formulated based on the stress exposure f_E and differentiates between fibre-failure (*FF*) and inter-fibre-failure (*IFF*). The material fails when

f_E = 1. For the interested reader, a short summary of Puck's failure theory as well as its implementation in Abaqus is included in Appendix A and B.

For a three-dimensional stress state, there are no analytical solutions and algorithms must be used to find the fracture stresses. However, for a two-dimensional stress state (σ_2, τ_{12}), there is an analytical solution. Figure 72 illustrates the corresponding fracture curve in the σ_2-τ_{12} domain, as well as the different failure modes. The identification of these failure modes is one of the main strengths of Puck's failure theory. If fracture mode A or B are occurring, adjacent plies in a laminate will "bridge" the gaps and therefore it is not considered a criterial load. Mode C, however, will cause a wedge effect which can cause delamination and total part failure as a result. The stress exposure for the different failure modes is calculated as follows:

Mode A (θ_{fp} = 0°):

$$f_{E,IFF} = \sqrt{[\left(\frac{1}{R_{\perp}^{t}} - \frac{p_{\perp\parallel}^{t}}{R_{\perp\parallel}}\right) * \sigma_2]^2 + (\frac{\tau_{21}}{R_{\perp\parallel}})^2} + \frac{p_{\perp\parallel}^{t}}{R_{\perp\parallel}} * \sigma_2, for\ \sigma_2 \geq 0 \quad (5.14)$$

Mode B (θ_{fp} = 0°):

$$f_{E,IFF} = \sqrt{(\frac{p_{\perp\parallel}^{c}}{R_{\perp\parallel}} * \sigma_2)^2 + (\frac{\tau_{21}}{R_{\perp\parallel}})^2} + \frac{p_{\perp\parallel}^{c}}{R_{\perp\parallel}} * \sigma_2, for\ \sigma_2 < 0\ and\ |\frac{\sigma_2}{\tau_{21}}| \leq |\frac{R_{\perp\perp}^{A}}{\tau_{21,c}}| \quad (5.15)$$

Mode C ($\theta_{fp} \neq 0°$):

$$f_{E,IFF} = \left[\left(\frac{\tau_{21}}{2 * (1 + p_{\perp\perp}^{c}) * R_{\perp\parallel}}\right)^2 + \left(\frac{\sigma_2}{R_{\perp}^{c}}\right)^2\right] * \frac{R_{\perp}^{c}}{-\sigma_2}, for\ \sigma_2 < 0\ and\ \left|\frac{\sigma_2}{\tau_{21}}\right| > |\frac{R_{\perp\perp}^{A}}{\tau_{21,c}}| \quad (5.16)$$

$$\cos(\theta_{fp}) = \sqrt{\frac{1}{2 * (1 + p_{\perp\perp}^{c})} * [(\frac{R_{\perp\perp}^{A} * \tau_{21}}{R_{\perp\parallel} * \sigma_2})^2 + 1]} \quad (5.17)$$

Mode B transitions to Mode C at the point:

$$\sigma_2 = -R_{\perp\perp}^{A}, \tau_{21,c} = R_{\perp\parallel} * \sqrt{1 + p_{\perp\perp}^{c}} \tag{5.18}$$

with

$$R_{\perp\perp}^{A} = \frac{R_{\perp}^{c}}{2(1 + p_{\perp\perp}^{c})} \tag{5.19}$$

where $R_{\perp}^{t}/\ R_{\perp}^{c}$ is the tensile/compressive strength in perpendicular direction to the fibres, $R_{\perp\parallel}$ is the longitudinal shear strength and the variables p are calibration parameters. The derivation for these equations can be found in [227].

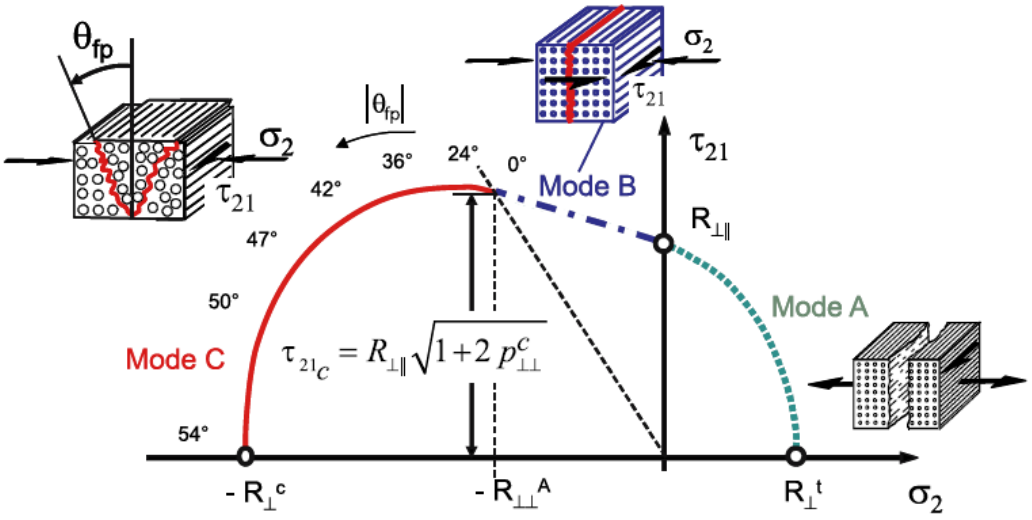

Figure 72: Matrix fracture modes according to Puck's failure theory [225].

For the curve shown in Figure 68 the parameters shown in Table 22 were used. Puck's prediction of the change in fracture angle did not perfectly match the micromechanical model. However, as mentioned in the previous section, this is most likely due the unit cell not taken the inhomogeneous fibre distribution into account.

Table 22: Parameters for Puck's failure criterion based on the micromechanical model

$R_{\perp}^{t}$	$R_{\perp}^{c}$	$R_{\perp\parallel}$	$p_{\perp\parallel}^{t}$	$p_{\perp\parallel}^{c}$	$p_{\perp\perp}^{c}$
65 MPa	120 MPa	50 MPa	0.3	0.2	0.2

5.7 Application in practice

Together with racing team of the Technische Hochschule (university of applied sciences) Ingolstadt the universities race car was analysed towards potential use cases of the additively manufactured composite. With the help of the aerodynamics team, especially Fabian Wein (student), the front splitter was selected and analysed regarding the aerodynamic load [228]. The acting pressures were determined at the car's maximum speed of 130 km/h and are shown in Figure 73. The circled flap was selected for this study, as it had the highest force of 25 N acting on it (-22 N lift and 11N drag). According to the "Formula student" racing rules, aerodynamic parts with a face area smaller than 225 cm² are not allowed to deflect more than 25 mm at a test force of 50 N [229]. Furthermore, a misuse load case was considered. This takes unforeseen events into account, like for instance a mechanic stepping on the part. For this purpose, an equally distributed load of 500N was applied.

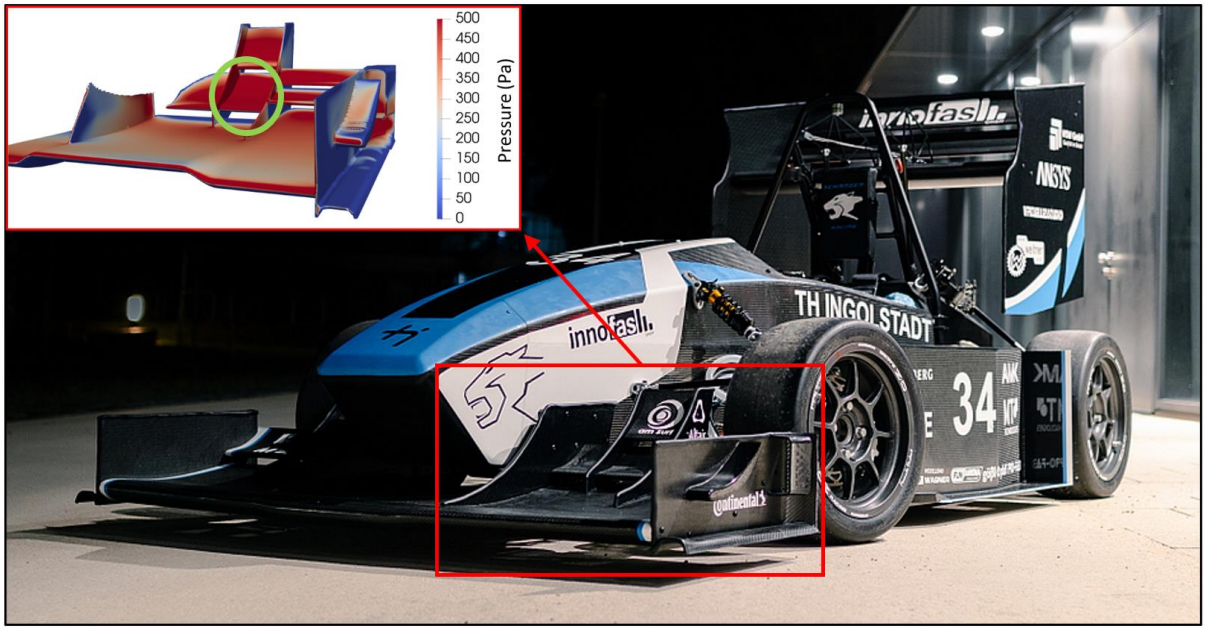

Figure 73: Race car of the Technische Hochschule Ingolstadt. The pressure distribution at 130 km/h is shown in the top left corner [228]. The image of the car is taken from [230].

5.7.1 Simulation parameters and modelling

The previously determined parameters from Table 22 and the material properties shown in Table 23 were used for the simulation. The elastic properties were extracted from the micromechanical model (comp. chapter **4.4.9**), whereas the tensile and compressive strength

in fibre direction was taken from [191] and [56]. Furthermore, the mechanical properties published by Felder et al for conditioned glass fibre reinforced polyamide 6 were used to analyse the effect of the reduced longitudinal shear and transverses tensile strength [209]. Since the elastic properties were not included in the publication, the micromechanical model was used to determine these values (comp. Table 24). The strength in fibre direction was not changed.

Table 23: Material properties used for the failure analysis of a dry polyamide 6

E_1	E_2	G_{12}	ν_{12}	ν_{23}	E_{Fibre}	$\nu_{Fibre12}$	$R_{\parallel}^{t}$	$R_{\parallel}^{c}$
26.7 GPa	6.3 GPa	1.9 GPa	0.319	0.507	82 GPa	0.18	530 MPa	85 MPa

Table 24: Material properties used for the failure analysis of a conditioned polyamide 6

E_1	E_2	G_{12}	ν_{12}	ν_{23}	E_{Fibre}	$\nu_{Fibre12}$	$R_{\parallel}^{t}$	$R_{\parallel}^{c}$
25.3 GPa	2.6 GPa	0.6 GPa	0.364	0.710	82 GPa	0.18	530 MPa	85 MPa

The part and the boundary/load conditions are illustrated in Figure 74. The left and right side of the flap were constrained with a fixed support and the load was applied as a surface pressure. The load was applied over one second and eight node linear brick elements were used. Due to the restrictions of the printing process, the fibres were laid out in only one direction (indicated by the orange lines). A wall-thickness of 0.9mm was used, which is the minimum width that can be printed by the Markforged “Mark Two” printer.

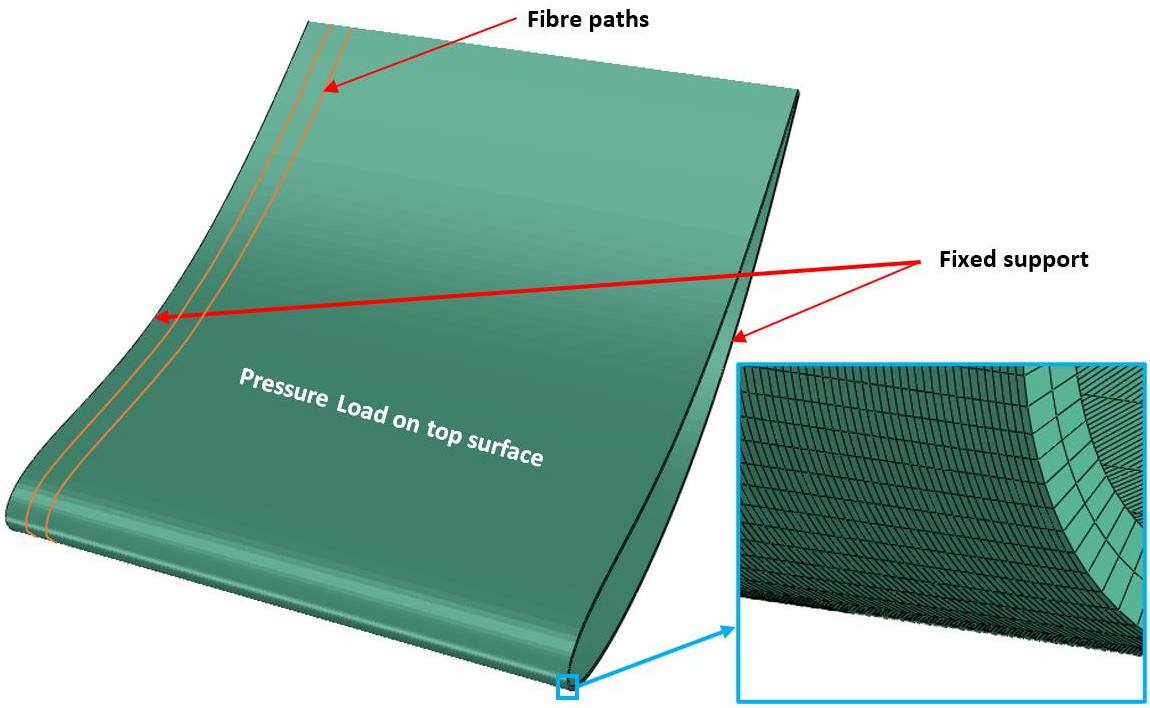

Figure 74: Flap with boundary conditions, fibre paths (orange) and mesh

5.7.2 Misuse load case

As both the aerodynamic load and the test case required by the racing rules did not result in failure, only the misuse load case is discussed, the results of which are illustrated in Figure 75. As the part was not close to fibre failure, only the matrix failure under tension and the deformation are included in the figure. For the dry composite, the maximum deformation at the bottom of the flap is 1.3 mm and no matrix failure was observed. For the conditioned material, the maximum deformation is 2.5 mm. This significant increase in deformation compared to the dry material was a result of the decrease in Young's modulus perpendicular to the fibres. Furthermore, matrix failure caused by tension was observed at the supports in the bottom section of the flap as well as at the corners at the top. The failure was caused by the significant strength decrease of the conditioned composite.

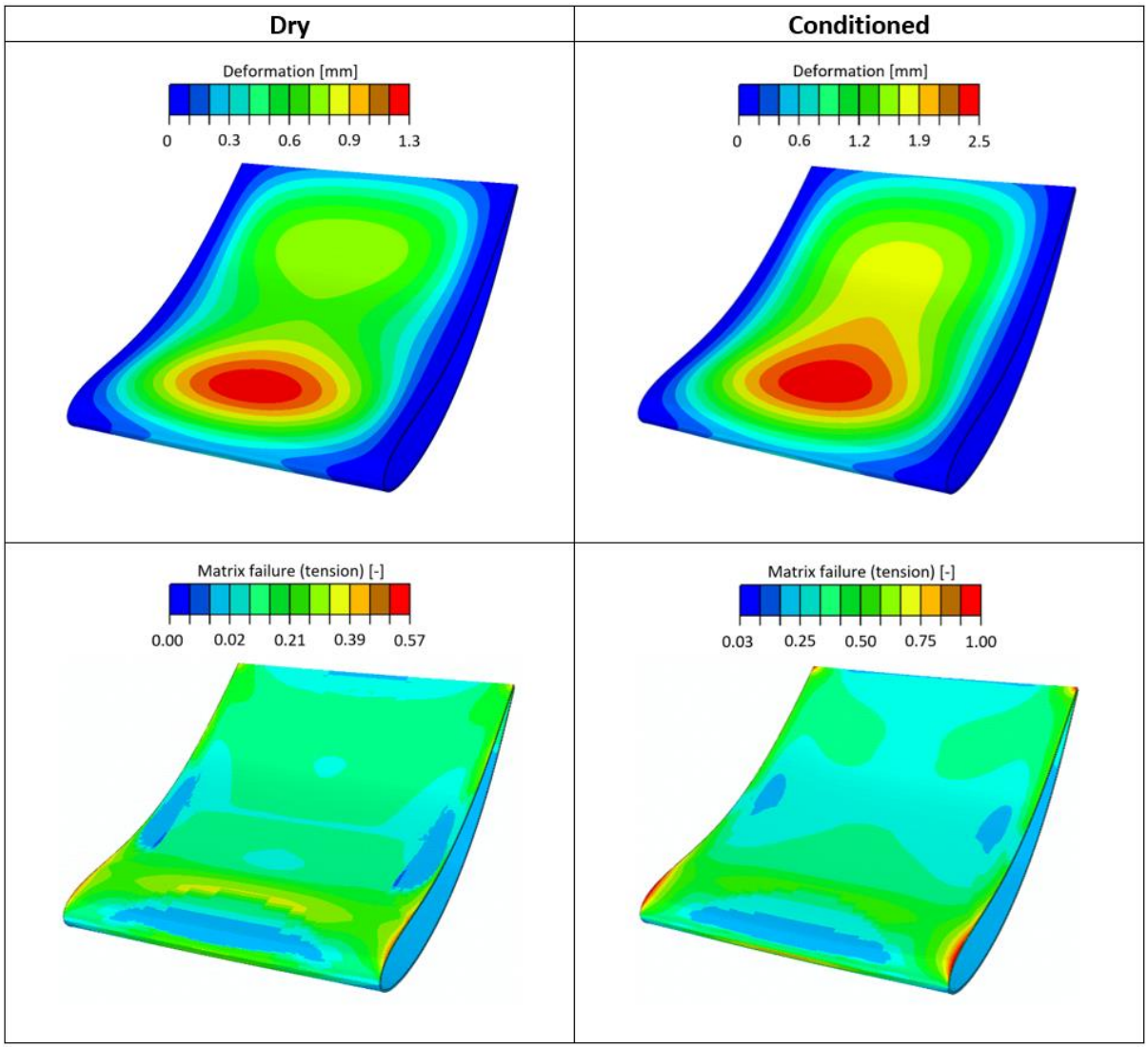

Figure 75: Deformation and matrix failure for the dry and conditioned composite

5.7.3 Misuse load case with a strut

To address the large deformation at the centre, a strut was added in the lower section of the flap to increase the stiffness. In practice, this strut would have to be printed separately and then glued into place. However, for the purposes of the simulation, the whole part was assumed to be homogenous. The reinforcement resulted in a significant decrease in the front section of the flap but did not improve the deformation of the upper section (comp. Figure 76). Furthermore, the matrix failure in the matrix failure in the lower section was addressed and only remained on top edges. An additional strut in the upper section could be used to prevent the matrix failure. Alternatively, the flap could be filled with a lattice structure for add additional reinforcement and increased bending stiffness.

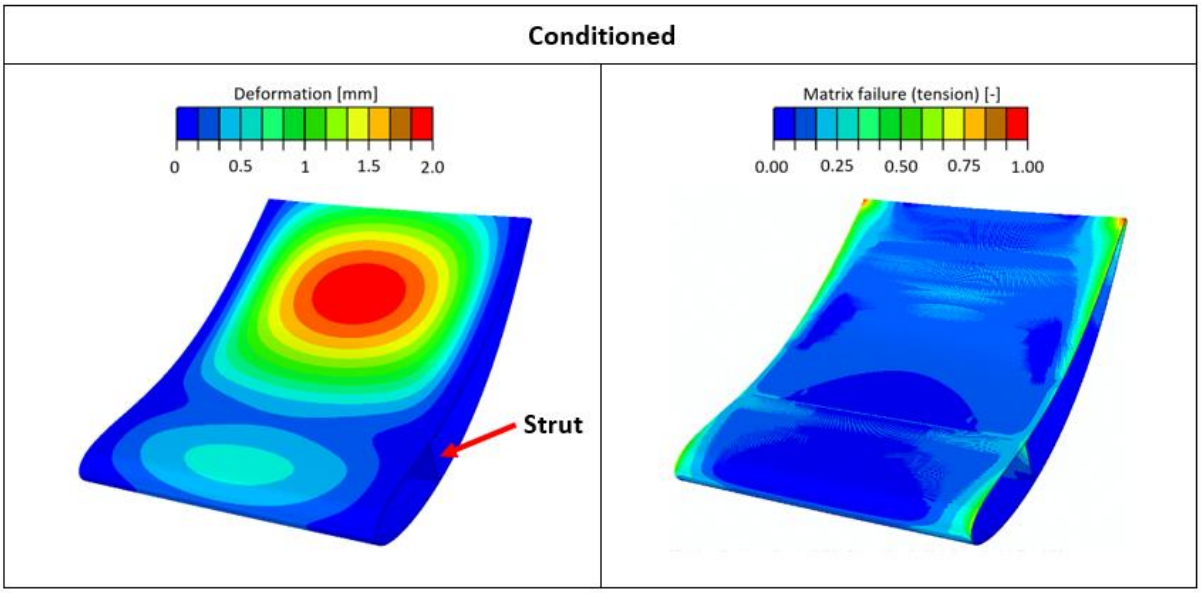

Figure 76: Deformation and matrix failure for the conditioned composite

5.8 Comparison with conventional solution

In the current version of the race car, the flap is manufactured from two layers of carbon fibre-reinforced epoxy which are oriented at 0° and 45° with a total thickness of 0.4 mm. The mechanical properties of the conventional composite used for the simulation are listed in Appendix C and the deformation for the misuse load case is shown in Figure 77 (left). For comparative reasons, the same part was also simulated with the mechanical properties of the conditioned polyamide 6 (comp. Figure 77 right). The deformation of the conventional solution was significantly lower than the additively manufactured part without a strut. In part, this was due to the different fibre reinforcement, as the carbon fibre has a Young's modulus that is three times greater than of the glass fibre. Furthermore, the fibre volume content of the conventional part was 50%, whereas the post-processed additively manufactured part only had a 30% fibre volume fraction. But most importantly, the fibres in the conventional part were oriented in different directions. That this made a major difference was illustrated by the deformation of the post-processed additively manufactured (Figure 77 right), which had the same deformation as the additively manufactured part with layers only oriented in one direction but with twice the thickness (Figure 75 right). This example illustrates, that is important to further develop and research on FDM printers, that have more degrees of freedom and allow for the fibres to be placed across layers. However, the solution with the additional strut, which was proposed in the previous section, illustrates, that it is already

possible to additively manufacture parts with a similar performance. But this comes at the cost of increased mass, with the additively manufactured flap with a strut having twice the mass compared to the conventional composite flap (29.4g vs. 59.2g). The additively manufactured flap shown in Figure 77 on the right side only weighs 25.1g.

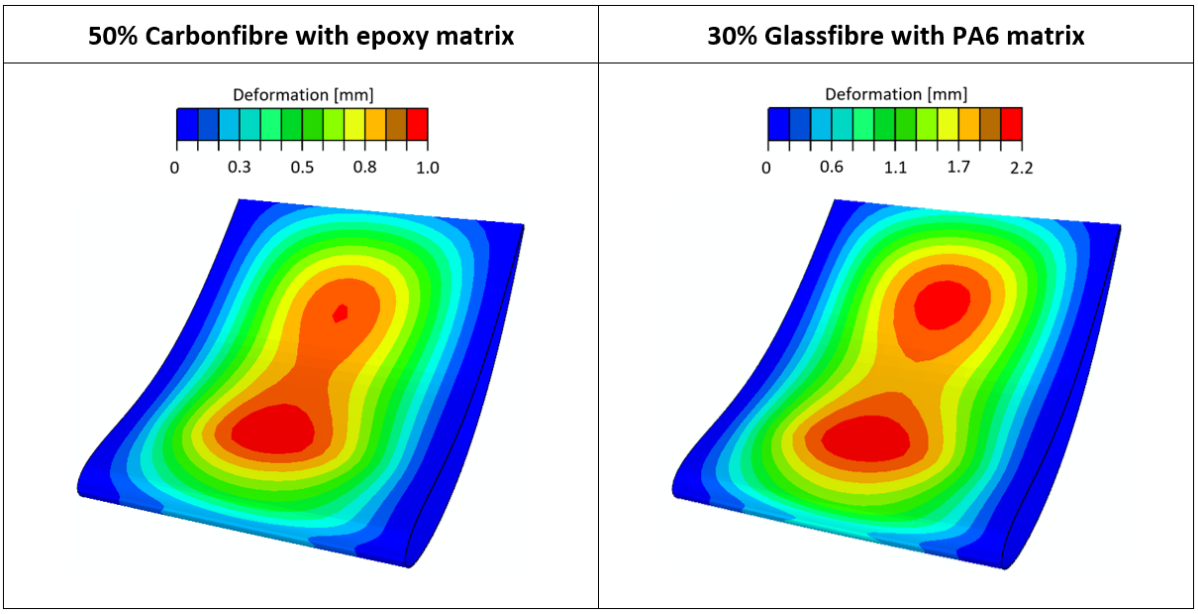

Figure 77: Deformation for the misuse load case of conventional carbon fibre reinforced epoxy with a 50% fibre volume content (left) and glass fibre reinforced conditioned PA6 with a fibre volume content of 30%. Both materials have the same layer sequence (0° and 45°).

5.9 Future research needs

The failure envelope created in this study for the postprocessed additively manufactured composite was based on a unit cell. Due to a lack of available computational power, it was not possible to simulate an entire RVE. The unit cell neglects the influence of the inhomogeneous fibre distribution within the material. The simulation should be repeated with the RVE proposed in section 5.3.2 . As the unit cell showed a higher strain of failure than the experiments, the parameters selected based on the literature review seem to provide a good foundation for the simulation. Despite the good agreement between the simulation and the experiment for the tensile load case, it is also important to further validate the simulation results. Future research studies should focus on shear and compression tests of the post processed material as well as the failure under combined loads. The material properties of polyamide 6 used in this study were taken from the literature and the shear/compressive

failure was based on assumptions. These assumptions should be experimentally validated. Furthermore, as shown in the comparison of manufacturer data, the properties of polyamide 6 can vary significantly depending on the manufacturer. For future studies, the true stress-strain data until failure for tensile, compression and shear load cases should be determined to have solid foundation for the model.

With the currently available desktop printers it is only possible to orient the fibres within one layer. Therefore, cross ply laminates that extend over multiple layers cannot be manufactured. This issue could be addressed by mounting the nozzle on a robotic arm. There already have been some studies published investigating this approach [231] [232]. This research should be applied to a system that can print continuous fibre reinforced filament.

In the literature review in chapter 2.4 different optimization approaches were presented. The fracture analysis presented in this chapter can be used as a basis for these algorithms to determine the ideal fibre path in the post-processed additively manufactured parts. Future research studies could also focus on the failure analysis of printed parts without postprocessing. To do this, a characterization of the interlayer is a crucial task. Studies have shown that there is enough time for reptation and as a result the interpenetration depth is sufficient [7] [87] [88]. The weak bonding between layers was found to be caused by areas of aligned polymer chains close to the interface, which is referred to as residual alignment. It is caused by the flow of the molten plastic through the nozzle, which aligns the polymer chains along the flow direction at the filament nozzle interface. The aligned chains cannot anchor the adjacent material properly and thus weaken the material. A study analysing the weld strength of PLA has found, that lower printing speed and higher printing temperature can reduce this effect [88]. Furthermore, it was determined that the filament-filament interface makes up 12% of the total thickness. Despite the material used in this study having continuous fibre reinforcement the underlying mechanisms are most likely similar. Since the material is also extruded through a nozzle, the polymer chains at the nozzle-filament interface are also expected to align in flow direction. Future studies should investigate, how the continuous fibre reinforcement affects the residual alignment and crystallinity at the interface. At the interlayer, the Young's modulus is expected to decrease, which could be measured by nanoindentation. However, there are still challenges that must be overcome before useable results can be obtained. As was mentioned in section 5.2.1, the polishing process resulted in

the formation of trenches between the fibre rich areas. A depth analysis for the samples polished as described in the microscopy section is shown in Figure 78. At the edge of the fibres there is a sudden drop and then an 8-10% slope with the lowest point being in between the fibre rich areas. This a problem because an inclined surface leads to measurement errors of the Young's modulus. The slope occurs most likely because the soft matrix material is removed faster as the fibres push into the polishing disc as illustrated in Figure 79. Measurements have shown that the trenches are already present at the 4000-grain polishing step. The last polishing steps then cause the fibre to protrude. Additionally, this effect also creates a visibly rough polymer surface (comp. Figure 78.). If researchers do find a way to polish the material in way that results in flat surfaces, inaccuracies caused by factors like the surface roughness could still pose a problem. Furthermore, research has shown that thermoplastics require large indentation depths or otherwise high scatter in the data is observed [233]. For measurements close to fibres this could lead to falsified results as the fibre hinder the deformation of the polymer.

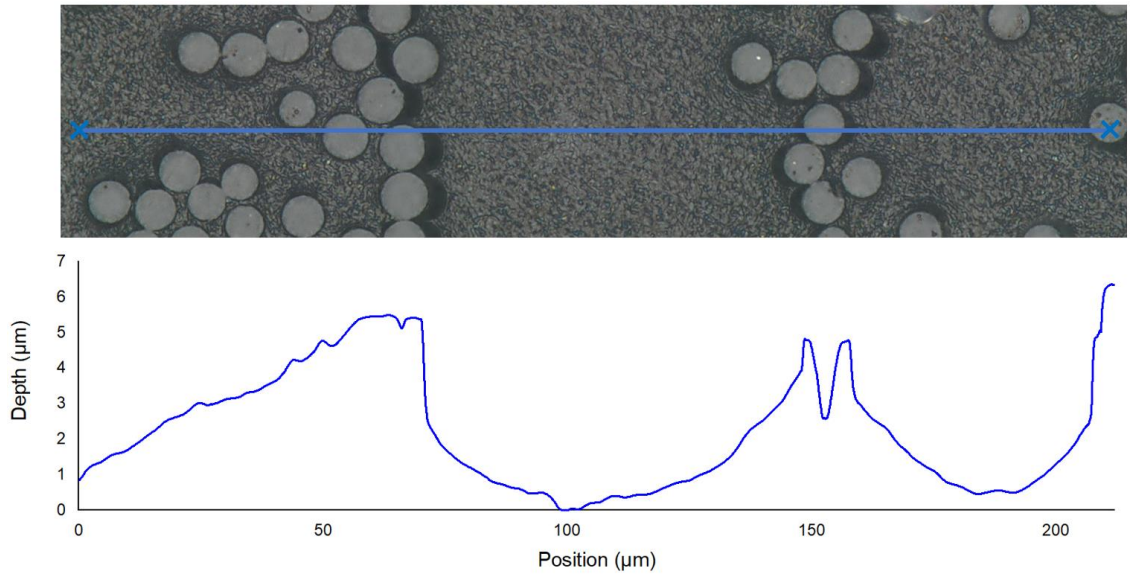

Figure 78: Depth profile of the polished samples

Figure 79: Suspected cause of the depth profile

5.10 Conclusion

In this chapter a micromechanical simulation approach for the post processed material was presented. For the micromechanical model the Drucker-Prager yield criterion and ductile failure was used to model the polyamide 6 matrix. The interface was modelled with a bilinear traction separation law. An analysis of the elastic properties based on microscopic images indicated, that a representative volume element with a size of 800µm x 200µm would be sufficiently large. However, due to a lack of computational power, the failure analysis was applied to a unit cell containing a single fibre. The micromechanical model showed a good agreement with the tensile test data but predicted a higher elongation at break. This was expected, as the unit cell neglected the influence of the inhomogeneous fibre distribution. An analysis of the failure under combined loads showed good agreement with the Puck failure criterion despite the low fibre volume content. The micromechanical model also predicted the change in fracture angle. However, the exact point of transition should be confirmed by a failure analysis of the RVE. Future research should also focus on an experimental validation of the fracture envelope. For the failure analysis of the additively manufactured parts that have not been post-processed, the mechanical properties of the interlayer should be determined.

A mesomechanical analysis of a flap on the universities race car using Puck's failure criterion showed, that this material can be used in secondary components and even handle misuse load cases. This is despite the fact, that the fibre orientation is currently limited by the layer-by-layer build process that prohibits the additive manufacturing of cross-ply laminates when using desktop printers. To address this issue, future research should focus on an additive manufacturing process that has more degrees of freedom.

Chapter 6

Conclusion and Recommendations

The objective of the research described in this thesis was to determine the effects of a temperature and pressure treatment on the mechanical performance of an additively manufactured continuous glass fibre reinforced polyamide 6 composite. Furthermore, the fracture stresses and fracture angles of the post-processed material, which had a fibre volume that was significantly lower than that of conventional composites, was investigated. In this chapter, the research approaches and key findings are summarized after which the future research needs are elaborated.

6.1 Conclusion

A thorough literature review revealed that there had been different studies published regarding the effects of a temperature treatment of additively manufactured plastics. However, none of the studies analysed fibre reinforced composites. Studies that did analyse additively manufactured composites mainly focused on the mechanical properties in the non-postprocessed state. These studies also revealed that the fibre volume content of these additively manufactured materials was roughly 30%. This is significantly lower than the fibre volume content of conventional composites, which commonly have a fibre volume fraction of 50-65%. Furthermore, air inclusions as well as the poor adhesion between layers was found to decrease the mechanical performance. A summary of the literature review was published as a review paper [16].

In chapter 3 these shortcomings were addressed by conducting an in-depth analysis of the effects of an annealing process on the strength of the additively manufactured composite in build-up direction. The effects of different annealing times and temperatures was evaluated

using chopped fibre reinforced polyamide 6. The Young's modulus and tensile strength were found to increase as function of the annealing temperature, whereas no significant difference was found for annealing times of 0.5h and 2h. An annealing time of 6h resulted in slightly improved mechanical properties. XRD analysis revealed a temperature dependent phase transition. Furthermore, it was found that the use of mineral oil as an annealing medium prevented gravity caused deformation due to the buoyancy effect. This fact allowed for annealing temperatures of up to 200°C, which is the melting point of polyamide 6, without causing any significant deformation. Annealing at 200°C at 6h resulted in the highest Young's modulus and tensile strength. Thus, these settings were applied to the continuous fibre reinforced polyamide 6. In the as-printed state, the composite had a very low tensile strength of only 7.3 MPa and a Young's modulus of 0.6 GPa. These values increased to 20.9 MPa and 1.9 GPa because of the heat treatment. However, the heat treatment caused a decrease in the elongation at break for both the chopped and continuous fibre reinforced composites. This was most likely caused by large air-voids that were still present after the annealing causing a notch effect. Furthermore, a change in water content was also expected to have an influence, as dry and conditioned polyamide 6 have different properties. For the continuous fibre-reinforced composite the air-void ratio was even found to increase. This was most likely caused by energy stored in the bent fibres, that was released as the polyamide was heated up and weakened. These findings were published as a research paper [108].

Based on these findings a pressure treatment process was investigated in chapter 4 to reduce the air-void ratio and further improve the mechanical performance. Test tokens were annealed at pressures of 1 MPa, 3 MPa and 6 MPa using a mould press to determine the influence of the pressure level. Contrary to annealing study, tensile tests were conducted with samples in build-up direction and samples printed parallel to the printing bed to determine if the material was transverse isotropic. To determine the change in the air-void ratio X-Ray analysis and microscopic imaging was used. These measurements provided further prove that the bend fibres contributed to the large air-void ratio. It was shown, that at 1 MPa the air-void ratio was significantly reduced. However, 3 MPa were required to also reduce the air-void ratio close to the fibre bends. A further increase of the pressure did not lead to a further improvement of the mechanical performance nor a reduction in the air-void ratio. It is important to point out, that the microscopic and X-Ray analysis can only be considered an

indicator regarding the obtained air-void ratios. More detailed information could be obtained by computer tomography, but this technology was not available. Nonetheless, the improvement of the mechanical properties was in alignment with the measured decrease in air-voids. The tensile tests showed that in the printed state, the strength continuous glass fibre reinforced polyamide 6 is not transverse isotropic. Most likely this was caused by the weak layer adhesion that effects the strength in build-up direction to a greater extend compared to samples printed parallel to the printing bed. As there was no nitrogen oven available, the mould was heated up in a regular oven. This resulted in some oxidation of samples, which led to premature failure in the test tokens in build-up direction. As the samples printed parallel to the printing bed were milled of after the pressure treatment, to eliminate the connecting fibre bends, they did no fail prematurely. For the samples printed perpendicular to the printing bed and treated at a pressure of 3 MPa, an ultimate tensile strength of 56 MPa and a Young's modulus of 5.7 GPa was measured. The Young's modulus for the samples in build-up direction was slight lower (5.1 GPa), which was most likely due to the oxidization. Nonetheless, these results strongly indicate, that the pressure treatment homogenizes the additively manufactured continuous fibre reinforced composite making it transverse isotropic. These findings are currently under publication as a research paper.

To determine the fracture stresses and fracture angles of the post-processed material for transverse tension/compression in combination with longitudinal shear, a micromechanical model was created for virtual testing. The polyamide 6 material was modelled with the Drucker-Prager yield criterion and ductile damage model was used to predict the failure. The fibre-matrix interface was modelled with a bilinear traction separation law. The size of an appropriate representative volume element was identified to be 800x200 µm². However due to limitations in the available computational power, the calculations were carried out using a unit cell containing a single fibre. For a uniaxial tensile load case, the simulation showed good agreement with the experimentally determined data in terms of Young's modulus and tensile strength. The elongation at break was predicted to be higher than in the experiments, but this was expected, as the unit cell does not take the inhomogeneous fibre distribution into account. The fracture envelope determined for combined longitudinal shear and transverse tension/compression showed a good agreement with Puck's failure criterion. The micromechanical model also predicted a change in the fracture angle under transverse

compression and longitudinal shear. As a practical use-case, the front flap of the universities race car was selected. Simulations were carried out for both the dry composite, which would be the state right after the pressure treatment, and for conditioned composite. It was shown, that for a misuse load case, the reduced strength of the conditioned composite led to material failure. Furthermore, it was shown, that the limitation in fibre orientation currently pose a significant drawback as it is not possible to manufacture cross-ply laminates across multiple layers with the currently available desktop printers that are able to process continuous fibre reinforced filament. Nonetheless, it was shown that this drawback could be addressed, for instance by adding struts in the right places.

6.2 Future research needs

The effects of the pressure treatment of the mechanical properties in this study were carried out using a mould press for both cost and safety reasons. Theoretically, it would be possible to design a sealed steel container and fill it with mineral oil. Due to the high thermal expansion coefficient of mineral oil, high pressures could be achieved by simply heating the container up. However, a more practical solution would be to post-process the parts in an autoclave. The investigated pressure levels in this study were chosen with this in mind. A pressure of 3 MPa is on the upper end of what commonly used autoclaves can achieve. So future studies should focus on investigating this approach and use CT scanning to determine the precise change of the air-void ratio. Putting the parts in a mineral oil bath during this process, as was done in this study, can prevent gravity caused deformation when annealing parts at elevated temperatures. Additionally, the effect of different heating and cooling rates should be investigated to improve throughput times for practical applications.

For long term uses the Fatigue behaviour of the additively manufactured composite should be determined. Based on the observed increase of the layer adhesion, it is expected that the annealing significantly increases the durability of the additively manufactured parts. The pressure treatment likely will result in a further increase of the fatigue strength, as air-voids, which were shown in this study to be significantly reduced when applying pressure during the annealing process, are likely to cause crack formation. Similar investigations could be carried out to investigate the creep behaviour.

The virtual failure analysis of the post-processed composite should be repeated with the proposed representative volume element to determine the influence of the inhomogeneous fibre distribution. Furthermore, the mechanical properties of dry polyamide 6 for uniaxial compression and shear should be experimentally determined to have a solid foundation for the simulation. It is also necessary to experimentally validate the fracture envelope. The micromechanical investigations did take the low fibre content into account, which is typical for additively manufactured continuous fibre reinforced composites. However, there are still other factors related to the FDM process that need to be addressed for which the proposed model can provide the foundation. By adding both the interlayer and the air-voids, the fracture behaviour in the as-printed state could be determined. To do this, it is necessary to characterise the mechanical properties of the interlayer. One possibility would be to use transmitted light microscopy to determine the thickness and nanoindentation to determine the Young's modulus. However, before nanoindentation can be used, a surface treatment must be found that does not change the materials properties and results in a flat surface. The strength of the interlayer could be determined by using uniaxial load cases of the non-post processed composite.

One aspect that was not addressed is the deformation caused by the heat treatment. While the chopped fibre-reinforced samples used in the annealing study did not exhibit any distortion, the continuous fibre reinforced tube slightly twisted around its centre axis. This difference was most likely a result of the different printing patterns. The chopped fibre reinforced samples contained an alternating ± 45° pattern, whereas all layers of the continuous fibre reinforced tube were printed in a clockwise pattern. For the pressure treatment study, this was not an issue at all, as the mould press prevented any deformation. It is very likely, that geometric changes will occur for more complex structures. Residual stresses caused by the layer-by-layer manufacturing process, where a hot polymer is printed onto a cold surface, are known to cause residual stresses and even warpage. This is even observed if no heat treatment is applied. However, recent studies created models to predict theses stresses and warpage based on the printing-process parameters [234] [235]. This allows for detailed virtual investigation of the ideal process parameters and prediction of the warping. The same approach should be applied to the continuous fibre reinforced material to be able to predict the deformation caused by the annealing process. Special attention would

have to be paid to the energy stored in the bent fibres. The structure could then be printed in a way, that results in the desired geometry after the pressure treatment process. In an interview the CEO of the company “Relativity Space”, which focuses on additively manufacturing metal rockets, states that the company uses a similar approach: “We have invented software that reverse warps the whole part before printing it. […] The robots are printing a wobbly/weird shape […] but in the end it comes out perfectly straight” [236].

Bibliography

[1] X. Zhang, Y. Chen and J. Hu, “Recent advances in the development of aerospace materials,” *Progress in Aerospace Sciences,* vol. 97, pp. 22-34, 2018.

[2] K. Jin-Woo and L. Deon-Gi, “Effect of Fiber Orientation and Fiber Contents on the Tensile Strength in Fiber-Reinforced Composites,” *Journal of Nanoscience and Nanotechnology,* vol. 10, no. 5, pp. 3650-3653, 2010.

[3] D. S. Cousins, Y. Suzuki, R. E. Murray, J. R. Samaniuk and A. P. Stebner, “Recycling glass fiber thermoplastic composites from wind turbine blades,” *Journal of Cleaner Production,* vol. 209, pp. 1252-1263, 2019.

[4] P. T. Mativenga, N. A. Shuaib, J. Howarth, F. Pestalozzi and J. Woidasky, “High voltage fragmentation and mechanical recycling of glass fibre thermoset composite,” *CIRP Annals,* vol. 65, no. 1, pp. 45-48, 2016.

[5] W. Gao, Y. Zhang, D. Ramanujan, K. Ramani, Y. Chen, C. B. Williams, C. C. Wang, Y. C. Shin, S. Zhang and P. D. Zavattieri, “The status, challenges, and future of additive manufacturing in engineering,” *Computer-Aided Design,* vol. 69, pp. 65-89, 2015.

[6] A. Bacciaglia, A. Ceruti and A. Liverani, “Additive Manufacturing Challenges and Future Developments in the Next Ten Years,” in *International Conference on Design, Simulation, Manufacturing: The Innovation Exchange*, Modena, Italy, 2019.

[7] C. McIlroy and R. Graham, “Modelling flow-enhanced crystallisation during fused filament fabrication of semi-crystalline polymer melts,” *Additive Manufacturing,* vol. 24, p. 323–340, 2018.

[8] A. Todoroki, T. Oasada, Y. Mizutani, Y. Suzuki, m. Ueda, R. Matsuzaki and Y. Hirano, “Tensile property evaluations of 3D printed continuous carbon fiber reinforced

thermoplastic composites," *Advanced Composite Materials,* vol. 29, no. 2, pp. 147-162, 2020.

[9] C. Casavola, A. Cazzato, V. Moramarco and G. Pappalettera, "Residual stress measurement in Fused Deposition Modelling parts," *Polymer Testin,* vol. 58, pp. 249-255, 2017.

[10] M. A. Caminero, J. M. Chacón, I. García-Moreno and J. M. Reverte, "Interlaminar bonding performance of 3D printed continuous fibre reinforced thermoplastic composites using fused deposition modelling," *Polymer Testing,* vol. 68, pp. 415-423, 2018.

[11] R. T. L. Ferreira, I. A. Ashcroft, S. Li and P. Zhuo, "Optimisation of Fibre-Paths in Composites produced by Additive Manufacturing," in *6th International Conference on Engineering Optimization*, Lissabon, 2018.

[12] H. A. Adabi, H.-T. Thai, V. Paton-Cole and V. Patel, "Elastic properties of 3D printed fibre-reinforced structures," *Composite Structures,* vol. 193, pp. 8-18, 2018.

[13] A. Puck, Festigkeitsanalyse von Faser-Matrix-Laminaten, München Wien: Carl Hanser Verlag, 1996.

[14] P. Soden, M. Hinton and A. Kaddour, "A comparison of the predictive capabilities of current failure theories for composite laminates," *Composites Science and Technolog<,* vol. 58, pp. 1225-1254, 1998.

[15] M. Hinton, A. Kaddour and P. Soden, "A comparison of the predictive capabilities of current failure theories for composite laminates, judged against experimental evidence," *Composites Science and Technology,* vol. 62, pp. 1725-1797, 2002.

[16] M. Handwerker, J. Wellnitz and H. Marzbani, "Review of mechanical properties of and optimisation methods for continuous fibre-reinforced thermoplastic parts manufactured by fused deposition modelling," *Progess in Additive Manufacturing,* 2021.

[17] Markforged, “Markforged Mark Two,” Markfoged, [Online]. Available: https://markforged.com/mark-two/. [Accessed 28 05 2020].

[18] Anisoprint, “Anisoprint Composer,” Anisoprint, [Online]. Available: https://anisoprint.com/product-composer. [Accessed 05 28 2020].

[19] Desktop Metal, “Fibre series,” Desktop Metal, [Online]. Available: https://www.desktopmetal.com/products/fiber. [Accessed 28 05 2020].

[20] CEAD, “CFAM Prime,” CEAD, [Online]. Available: https://cead-am.com/wp-content/uploads/2019/09/FOLDER-CFAM.pdf. [Accessed 28 05 2020].

[21] S. S. Wicks, G. R. de Villoria and B. L. Wardle, “Interlaminar and intralaminar reinforcement of composite laminates with aligned carbon nanotubes,” *Composites Science and Technology,* vol. 70, no. 1, pp. 20-28, 2010.

[22] M. W. Czabaj and J. G. Ratcliffe, “Comparison of intralaminar and interlaminar mode I fracture toughnesses of a unidirectional IM7/8552 carbon/epoxy composite,” *Composites Science and Technology,* vol. 89, pp. 15-23, 2013.

[23] A. Goel, K. Chawla, U. Vaidya, N. Chawla and M. Koopman, “Characterization of fatigue behavior of long fiber reinforced thermoplastic (LFT) composites,” *Materials Characterization,* vol. 60, no. 6, pp. 537-544, 2009.

[24] F. H. Bhuiyan and R. S. Fertig, “A Physics-Based Combined Creep and Fatigue Methodology for Fiber-Reinforced Polymer Composites,” in *58th AIAA/ASCE/AHS/ASC Structures, Structural Dynamics, and Materials Conference*, Texas, 2017.

[25] M. Eftekhari and A. Fatemi, “Variable amplitude fatigue behavior of neat and short glass fiber reinforced thermoplastics,” *International Journal of Fatigue,* vol. 98, pp. 176-186, 2017.

[26] *ASTM D3039 / D3039M-17, Standard Test Method for Tensile Properties of Polymer Matrix Composite Materials, ASTM International, West Conshohocken, PA, 2017, www.astm.org.*

[27] *ASTM D6641 / D6641M-16e1, Standard Test Method for Compressive Properties of Polymer Matrix Composite Materials Using a Combined Loading Compression (CLC) Test Fixture, ASTM International, West Conshohocken, PA, 2016, www.astm.org.*

[28] *ASTM D3410 / D3410M-16, Standard Test Method for Compressive Properties of Polymer Matrix Composite Materials with Unsupported Gage Section by Shear Loading, ASTM International, West Conshohocken, PA, 2016, www.astm.org.*

[29] "ASTM D6484 / D6484M-14, Standard Test Method for Open-Hole Compressive Strength of Polymer Matrix Composite Laminates, ASTM International, West Conshohocken, PA, 2014, www.astm.org".

[30] *ASTM D5766 / D5766M-11(2018), Standard Test Method for Open-Hole Tensile Strength of Polymer Matrix Composite Laminates, ASTM International, West Conshohocken, PA, 2018, www.astm.org.*

[31] *ASTM D6742 / D6742M-17, Standard Practice for Filled-Hole Tension and Compression Testing of Polymer Matrix Composite Laminates, ASTM International, West Conshohocken, PA, 2017, www.astm.org.*

[32] *ASTM D6264 / D6264M-17, Standard Test Method for Measuring the Damage Resistance of a Fiber-Reinforced Polymer-Matrix Composite to a Concentrated Quasi-Static Indentation Force, ASTM International, West Conshohocken, PA, 2017, www.astm.org.*

[33] *ISO 527-4:1997: Plastics — Determination of tensile properties — Part 4: Test conditions for isotropic and orthotropic fibre-reinforced plastic composites, Geneva, Switzerland, www.iso.org.*

[34] *ISO 12817:2013, Fibre-reinforced plastic composites — Determination of open-hole compression strength, Geneva, Switzerland, www.iso.org.*

[35] *ISO 14126:1999, Fibre-reinforced plastic composites — Determination of compressive properties in the in-plane direction, Geneva, Switzerland, www.iso.org.*

[36] *ISO 11566:1996, Carbon fibre — Determination of the tensile properties of single-filament specimens, Geneva, Switzerland, www.iso.org.*

[37] *ASTM D5379 / D5379M-19, Standard Test Method for Shear Properties of Composite Materials by the V-Notched Beam Method, ASTM International, West Conshohocken, PA, 2019, www.astm.org.*

[38] *ASTM D2344 / D2344M-16, Standard Test Method for Short-Beam Strength of Polymer Matrix Composite Materials and Their Laminates, ASTM International, West Conshohocken, PA, 2016, www.astm.org.*

[39] *ASTM D3518 / D3518M-18, Standard Test Method for In-Plane Shear Response of Polymer Matrix Composite Materials by Tensile Test of a ±45° Laminate, ASTM International, West Conshohocken, PA, 2018, www.astm.org.*

[40] *ASTM D5467 / D5467M-97(2017), Standard Test Method for Compressive Properties of Unidirectional Polymer Matrix Composite Materials Using a Sandwich Beam, ASTM International, West Conshohocken, PA, 2017, www.astm.org.*

[41] *ASTM D4255 / D4255M-15a, Standard Test Method for In-Plane Shear Properties of Polymer Matrix Composite Materials by the Rail Shear Method, ASTM International, West Conshohocken, PA, 2015, www.astm.org.*

[42] *ASTM D3846-08(2015), Standard Test Method for In-Plane Shear Strength of Reinforced Plastics, ASTM International, West Conshohocken, PA, 2015, www.astm.org.*

[43] *ISO 14130:1997, Fibre-reinforced plastic composites — Determination of apparent interlaminar shear strength by short-beam method, Geneva, Switzerland, www.iso.org.*

[44] *ISO 14129:1997, Fibre-reinforced plastic composites — Determination of the in-plane shear stress/shear strain response, including the in-plane shear modulus and strength,*

by the plus or minus 45 degree tension test method, Geneva, Switzerland, www.iso.org.

[45] *ISO 15310:1999, Fibre-reinforced plastic composites — Determination of the in-plane shear modulus by the plate twist method, Geneva, Switzerland, www.iso.org.*

[46] *ASTM D7264 / D7264M-15, Standard Test Method for Flexural Properties of Polymer Matrix Composite Materials, ASTM International, West Conshohocken, PA, 2015, www.astm.org.*

[47] *ASTM D6272-17, Standard Test Method for Flexural Properties of Unreinforced and Reinforced Plastics and Electrical Insulating Materials by Four-Point Bending, ASTM International, West Conshohocken, PA, 2017, www.astm.org.*

[48] *ASTM D6415 / D6415M-06a(2013), Standard Test Method for Measuring the Curved Beam Strength of a Fiber-Reinforced Polymer-Matrix Composite, ASTM International, West Conshohocken, PA, 2013, www.astm.org.*

[49] *ISO 14125:1998, Fibre-reinforced plastic composites — Determination of flexural properties, Geneva, Switzerland, www.iso.org.*

[50] *ASTM D3479 / D3479M-19, Standard Test Method for Tension-Tension Fatigue of Polymer Matrix Composite Materials, ASTM International, West Conshohocken, PA, 2019, www.astm.org.*

[51] G. W. Melenka, B. K. Cheung, J. S. Schonfield, M. R. Dawson and J. P. Carey, "Evaluation and prediction of the tensile properties of continuous fiber-reinforced 3D printed structures," *Composite Structures,* vol. 153, pp. 866-875, 2016.

[52] A. N. Dickson, J. N. Barry and K. A. D. D. P. McDonnell, "Fabrication of continuous carbon, glass and Kevlar fibre reinforced polymer composites using additive manufacturing," *Additive Manufacturing,* vol. 16, pp. 146-152, 2017.

[53] M. Scrocco, T. Chamberlain, C. Chow, L. Weinreber, E. Ellks, C. Halford, P. Cortes and B. Conner, "Impact Testing of 3D Printed Kevlar-Reinforced Onyx Material," in *29th*

Annual International Solid Freeform Fabrication Symposium, Austin, Texas, USA, 2018.

[54] *ASTM E23-18, Standard Test Methods for Notched Bar Impact Testing of Metallic Materials, ASTM International, West Conshohocken, PA, 2018, www.astm.org.*

[55] G. Goh, V. Dikshit, A. Nagalingam, G. Goh, S. Agarwala, S. Sing, J. Wei and W. Yeong, "Characterization of mechanical properties and fracture mode of additively manufactured carbon fiber and glass fiber reinforced thermoplastics," *Materials & Design,* vol. 137, pp. 79-89, 2018.

[56] J. Justo, L. Távara, L. García-Guzmán and F. París, "Characterization of 3D printed long fibre reinforced composites," *Composite Structures,* vol. 185, pp. 537-548, 2018.

[57] A. N. Dickson, J. N. Barry, K. A. McDonnell and D. P. Dowling, "Fabrication of continuous carbon, glass and Kevlar fibre reinforced polymer composites using additive manufacturing," *Additive Manufacturing,* vol. 16, pp. 146-152, 2017.

[58] L. Blok, M. Longana, H. Yu and B. K. S. Woods, "An investigation into 3D printing of fibre reinforced thermoplastic composites," *Additive Manufacturing,* vol. 22, pp. 176-186, 2018.

[59] F. van der Klift, Y. Koga, A. Todoroki, M. Ueda, Y. Hirano and R. Matsuzaki, "3D Printing of Continuous Carbon Fibre Reinforced Thermo-Plastic (CFRTP) Tensile Test Specimens," *Open Journal of Composite Materials,* vol. 6, pp. 18-27, 2016.

[60] J. N. Lozada, H. Ahuett-Garza, P. Orta-Castañón, W. M. Verbeeten and D. Sáiz-González, "Tensile properties and failure behavior of chopped and continuous carbon fiber composites produced by additive manufacturing," *Additive Manufacturing,* vol. 26, pp. 227-241, 2019.

[61] T. A. Dutra, R. T. L. Ferreira, H. B. Resende and A. Guimarães, "Mechanical characterization and asymptotic homogenization of 3D-printed continuous carbon fiber-reinforced thermoplastic," *Journal of the Brazilian Society of Mechanical Sciences and Engineering,* vol. 41, no. 133, 2019.

[62] J. Zhang, Z. Zhou, F. Zhang, Y. Tan, Y. Tu and B. Yang, " Performance of 3D-Printed Continuous-Carbon-Fiber-Reinforced Plastics with Pressure," *Materials,* vol. 13, no. 2, p. 471, 2020.

[63] A. Imeri, I. Fidan, M. Allen, D. A. Wilson and S. Canfield, "Fatigue analysis of the fiber reinforced additively manufactured objects," *The International Journal of Advanced Manufacturing Technology,* vol. 98, pp. 2717 - 2724, 2018.

[64] *ASTM D7791-17, Standard Test Method for Uniaxial Fatigue Properties of Plastics, ASTM International, West Conshohocken, PA, 2017, www.astm.org.*

[65] A. D. Pertuz, S. Díaz-Cardona and O. A. González-Estrada, "Static and fatigue behaviour of continuous fibre reinforced thermoplastic composites manufactured by fused deposition modelling technique," *International Journal of Fatigue,* vol. 130, p. 105275, 2020.

[66] G. Höhne, W. F. Hemminger and H.-J. Flammersheim, Differential Scanning Calorimetry, Berlin Heidelberg: Springer-Verlag, 2003.

[67] K. P. Menard, Dynamic Mechanical Analysis: A Practical Introduction, Boca Raton: CRC Press, 2002.

[68] P. J. Haines, Thermal Methods of Analysis, Dordrecht: Springer, 1995.

[69] J. Alemán, A. Chadwick, J. He, M. Hess, K. Horie, R. Jones, P. Kratochvíl, I. Meisel, I. Mita, G. Moad, S. Penczek and R. F. Stepto, "Definitions of terms relating to the structure and processing of sols, gels, networks, and inorganic-organic hybrid materials (IUPAC Recommendations 2007)," *Pure Appl.Chem.,* vol. 79, no. 10, p. 1801–1829, 2007.

[70] *ASTM D3171-15, Standard Test Methods for Constituent Content of Composite Materials, ASTM International, West Conshohocken, PA, 2015, www.astm.org.*

[71] *ASTM D2734-16, Standard Test Methods for Void Content of Reinforced Plastics, ASTM International, West Conshohocken, PA, 2016, www.astm.org.*

[72] S. Garcea, Y. Wang and P. Withers, “X-ray computed tomography of polymer composites,” *Composites Science and Technology,* vol. 156, pp. 305-319, 2018.

[73] *ASTM D3418-15, Standard Test Method for Transition Temperatures and Enthalpies of Fusion and Crystallization of Polymers by Differential Scanning Calorimetry, ASTM International, West Conshohocken, PA, 2015, www.astm.org.*

[74] *ASTM E1356-08(2014), Standard Test Method for Assignment of the Glass Transition Temperatures by Differential Scanning Calorimetry, ASTM International, West Conshohocken, PA, 2014, www.astm.org.*

[75] *ISO 11357-1:2016, Plastics — Differential scanning calorimetry (DSC) — Part 1: General principles, International Organization for Standardization, Geneva, Switzerland, 2016, www.iso.org/.*

[76] *ISO 11357-2:2020: Plastics — Differential scanning calorimetry (DSC) — Part 2: Determination of glass transition temperature and step height, Geneva, Switzerland, 2020, www.iso.org/.*

[77] *ISO 11357-3:2018: Plastics — Differential scanning calorimetry (DSC) — Part 3: Determination of temperature and enthalpy of melting and crystallization, Geneva, Switzerland, 2018, www.iso.org/.*

[78] *ISO 11357-4:2014: Plastics — Differential scanning calorimetry (DSC) — Part 4: Determination of specific heat capacity, , Geneva, Switzerland. www.iso.org.*

[79] *ISO 11357-5:2013: Plastics — Differential scanning calorimetry (DSC) — Part 5: Determination of characteristic reaction-curve temperatures and times, enthalpy of reaction and degree of conversion, Geneva, Switzerland. www.iso.org.*

[80] *ASTM D7028-07(2015), Standard Test Method for Glass Transition Temperature (DMA Tg) of Polymer Matrix Composites by Dynamic Mechanical Analysis (DMA), ASTM International, West Conshohocken, PA, 2015, www.astm.org.*

[81] *ASTM E1641-18, Standard Test Method for Decomposition Kinetics by Thermogravimetry Using the Ozawa/Flynn/Wall Method, ASTM International, West Conshohocken, PA, 2018, www.astm.org.*

[82] *ASTM E1131-20, Standard Test Method for Compositional Analysis by Thermogravimetry, ASTM International, West Conshohocken, PA, 2020, www.astm.org.*

[83] *ISO 11358-1:2014, Plastics — Thermogravimetry (TG) of polymers — Part 1: General principles, Geneva, Switzerland. www.iso.org.*

[84] *ISO 11667:1997: Fibre-reinforced plastics — Moulding compounds and prepregs — Determination of resin, reinforced-fibre and mineral-filler content — Dissolution methods, International Organization for Standardization, Geneva, Switzerland, www.iso.org.*

[85] *ASTM E2533-17e1, Standard Guide for Nondestructive Testing of Polymer Matrix Composites Used in Aerospace Applications, ASTM International, West Conshohocken, PA, 2017, www.astm.org.*

[86] C. Pascual-González, M. Iragi, A. Fernández, J. Fernández-Blázquez, L. Aretxabaleta and C. Lopes, "An approach to analyse the factors behind the micromechanical response of 3D-printed composites," *Composites Part B: Engineering,* vol. 186, p. 107820, 2020.

[87] M. A. G. Cunha and M. O. Robbins, "Effect of Flow-Induced Molecular Alignment on Welding and Strength of Polymer Interfaces," *Macromolecules,* vol. 53, p. 8417−8427, 2020.

[88] A. Costanzo, R. Spotorno, M. V. Candal, M. M. Fernández, A. J. Müller, R. S. Graham, D. Cavallo and C. McIlroy, "Residual alignment and its effect on weld strength in material-extrusion 3Dprinting of polylactic acid," *Additive Manufacturing,* vol. 36, p. 101415, 2020.

[89] M. Kawai and S. Saito, “Off-axis strength differential effects in unidirectional carbon/epoxy laminates at different strain rates and predictions of associated failure envelopes,” *Composites Part A: Applied Science and Manufacturing,* vol. 40, no. 10, pp. 1632-1649, 2009.

[90] A. Vijayachandran, P. Acar, V. Sundararaghavanz and A. Waas, “Fiber path optimization of a symmetric laminate with a cutout for thermal buckling, using a novel finite element algorithm.,” in *Structures, Structural Dynamics, and Materials Conference*, San Diego, California, USA, 2016.

[91] P. Acar, A. Vijayachandran, V. Sundararaghavan, A. Waas and M. Rassaian, “Optimization of spatially varying fiber paths for a symmetric laminate with a circular cutout under remote uniaxial tension,” *SAE Int. J. Mater. Manf.,* vol. 9, no. 1, pp. 75-80, 2016.

[92] X. Legrand, D. Kelly, A. Crosky and D. Crépin, “Optimisation of fibre steering in composite laminates,” *Composite Structures,* vol. 75, pp. 524-531, 2006.

[93] E. Lund, “Discrete Material and Thickness Optimization of laminated composite structures including failure criteria,” *Structural and Multidiciplinary Optimization,* vol. 57, no. 6, p. 2357–2375, 2018.

[94] C. Kiyono, E. Silva and J. Reddy, “A novel fiber optimization method based on normal distribution function with continuously varying fiber path,” *Composite Structures,* vol. 160, pp. 503-515, 2017.

[95] M. Bruyneel, “SFP—a new parameterization based on shape functions for optimal material selection: application to conventional composite plies,” *Structural and Multidisciplinary Optimization,* vol. 43, no. 1, pp. 17-27, 2011.

[96] M. Bruyneel, P. Duysinx, C. Fleury and T. Gao, “Extensions of the Shape Functions with Penalization Parameterization for Composite-Ply Optimization,” *AIAA Journal,* vol. 49, no. 10, 2011.

[97] T. Gao and W. Zhang, “A bi-value coding parameterization scheme for the discrete optimal orientation design of the composite laminate,” *Numerical Methods in Engineering,* vol. 91, no. 1, pp. 98-114, 202.

[98] A. Malakhov and A. Polilov, “Design of composite structures reinforced curvilinear fibres using FEM,” *Composites Part A: Applied Science and Manufacturing,* vol. 87, pp. 23-28, 2016.

[99] Y. Zhu, J. Liu, D. Liu, H. Xu, C. Yan, B. Huang and D. Hui, “Fiber path optimization based on a family of curves in composite laminate with a center hole,” *Composites Part B: Engineering,* vol. 111, pp. 91-102, 2017.

[100] G. Huang, H. Wang and G. Li, “An efficient reanalysis assisted optimization for variable-stiffness composite design by using path functions,” *Composite Structures,* vol. 153, pp. 409-420, 2016.

[101] Y. T. A. U. M. H. Y. M. R. Yamanaka, “Fiber line optimization in single ply for 3D printed composites,” *Open Journal of Composite Materials,* vol. 6, pp. 121-131, 2016.

[102] M. Montemurro and A. Catapano, “On the effective integration of manufacturability constraints within the multi-scale methodology for designing variable angle-tow laminates,” *Composite Structures,* vol. 161, pp. 145-159, 2017.

[103] E. Lemaire, S. Zein and M. Bruyneel, “Optimization of composite structures with curved fiber trajectories,” *Composite Structures,* vol. 131, pp. 895-904, 2015.

[104] Z. Hashin, “Failure criteria for unidirectional fibre composites,” *ASME Journal of Applied Mechanics,* vol. 47, no. 2, pp. 329-334, 1980.

[105] Markforged, “Composites Datasheet,” Markforged, 5 10 2019. [Online]. Available: https://static.markforged.com/markforged_composites_datasheet.pdf. [Accessed 28 05 2020].

[106] J. Frenkel, “Viscous Flow of crystalline bodies under the action of surface tension,” *J. Phys.,* vol. 9, p. 385–391, 1945.

[107] F. Wohlgemuth, D. Lellinger and I. Alig, “Modelling of Pore Collapse during Polymer Sintering: Viscoelastic Model with Enclosed Gas,” *Materials,* vol. 14, no. 9, p. 2182, 2021.

[108] M. Handwerker, J. Wellnitz, H. Marzbarni and U. Tetzlaf, “Annealing of chopped and continuous fibre reinforced polyamide 6 produced by fused filament fabrication,” *Composites Part B: Engineering,* vol. 223, no. 15, p. 109119, 2021.

[109] Y. Li and W. A. Goddard, “Nylon 6 Crystal Structures, Folds, and Lamellae from Theory,” *Macromolecules,* vol. 35, pp. 8440-8455, 2002.

[110] R. A. Wach, P. Wolsczak and A. Adamus-Wlodarczyk, “Enhancement of Mechanical Properties of FDM-PLA Parts via Thermal Annealing,” *Macromolecular Materials and Engineering,* vol. 303, no. 9, 2018.

[111] G. Perego, G. D. Cella and C. Bastioli, “Effect of Molecular Weight and Crystallinity on Poly(lactic Acid),” *Mechanical Properties. J. Appl. Polym. Sci.,* vol. 59, pp. 37-43, 1996.

[112] T. Huang and M. Yamaguchi, “Effect of Cooling Conditions on the Mechanical Properties of Crystalline Poly(lactic Acid),” *J. Appl. Polym. Sci.,* vol. 134, no. 20, 2017.

[113] C. Benwood, A. Anstey, J. Andrzejewski, M. Misra and A. K. Mohanty, “Improving the Impact Strength and Heat Resistance of 3D Printed Models: Structure, Property, and Processing Correlationships during Fused Deposition Modeling (FDM) of Poly(Lactic Acid),” *ACS Omega,* vol. 3, no. 4, pp. 4400-4411, 2018.

[114] Y. Liao, C. C. B. Liu, G. Barra, L. Di Maio, L. Incarnato and K. Lafdi, “Effect of Porosity and Crystallinity on 3D Printed PLA Properties,” *Polymers,* vol. 11, no. 9, p. 1487, 2019.

[115] S. Wang, L. Daelemans, R. Fiorio, M. Gou, D. R. D'hooge, K. De Clerck and L. Cardon, “Improving Mechanical Properties for Extrusion-Based Additive Manufacturing of Poly(Lactic Acid) by Annealing and Blending with Poly(3-Hydroxybutyrate),” *Polymers,* vol. 11, no. 9, p. 1529, 2019.

[116] Y. Wangwamg, X. Wang, E. Ferraris and J. Zhang, “Melt crystallization of PLA/Talc in fused filament fabrication,” *Materials & Design,* vol. 182, p. 108013, 2019.

[117] H. Simmons, P. Tiwary, J. E. Colwell and M. Kontopoulou, “Improvements in the crystallinity and mechanical properties of PLA by nucleation and annealing,” *Polymer Degradation and Stability,* vol. 166, pp. 248-257, 2019.

[118] S. Bhandari, R. A. Lopez-Anido and D. J. Garnder, “Enhancing the interlayer tensile strength of 3D printed short carbon fiber reinforced PETG and PLA composites via annealing,” *Additive Manufacturing,* vol. 30, p. 100922, 2019.

[119] D. Vaes, M. Coppens, B. Goderis, W. Zoetelief and P. V. Puyvelde, “Assessment of Crystallinity Development during Fused Filament Fabrication through Fast Scanning Chip Calorimetry,” *Applied Sciences,* vol. 9, no. 13, p. 2676, 2019.

[120] R. M. Dunn, K. R. Hart and E. Wetzel, “Improving fracture strength of fused filament fabrication parts via thermal annealing in a printed support shell,” *Progress in Additive Manufacturing,* vol. 4, no. 3, p. 233–243, 2019.

[121] I. M. Fouda, M. M. EL-Tonsy and A. Shaban, “Evaluation of the structural behaviour of annealed nylon 6 fibres from density measurements,” *Journal of Materials Science,* vol. 26, pp. 5085-5092, 1991.

[122] D. D. Kopeliovich, “Annealing of plastics,” Substech, 01 08 2013. [Online]. Available: http://www.substech.com/dokuwiki/doku.php?id=annealing_of_plastics. [Accessed 01 07 2020].

[123] P. International, “ANNEALING OF NYLON & REINFORCED NYLONS,” Plastics International, 31 08 2018. [Online]. Available: https://www.plasticsintl.com/media/wysiwyg/Nylon___Reinforced_Nylon_Annealing.pdf. [Accessed 01 07 2020].

[124] B. Plastics, “Annealing Guidelines,” Boedeker Plastics INC, 02 07 2020. [Online]. Available: https://www.boedeker.com/Technical-Resources/Technical-Library/Plastic-Annealing-Guidelines. [Accessed 02 07 2020].

[125] Licharz, “Konstruieren mit technischen Kunststoffen,” Licharz GmbH, 31 03 2020. [Online]. Available: https://www.ktw-gornau.de/media/files/PDF-Dateien/Broschuere_Kunststoffe_Bearbeitung_und_Nachbehandlung.pdf. [Accessed 02 07 2020].

[126] E. M. Mccolm, “Monocomponent artificial filaments or the like of synthetic polymers; Manufacture thereof from homopolycondensation products from polyamides”. United States Patent US3150435A, 18 03 1963.

[127] T. Karstens and V. Rossbach, “Thermo-oxidative degradation of polyamide 6 and 6,6,” *Macromolecules,* vol. 190, pp. 3033-3053, 1989.

[128] W. Dong and P. Gijsman, “Influence of temperature on the thermo-oxidative degradationof polyamide 6 films,” *Polymer Degradation and Stability,* vol. 95, pp. 1054-1062, 2010.

[129] W. H. Bragg and W. L. Bragg, “The reflection of X-rays by crystals,” *Proceedings of the Royal Society,* vol. 88, no. 605, pp. 428-438, 1913.

[130] L. E. Chemistry, “Moisture Absorption in Durethan Polyamide Parts,” 01 05 2005. [Online]. Available: https://techcenter.lanxess.com/scp/americas/en/docguard/PIB_Durethan_Moisture_Absorption.pdf. [Accessed 08 06 2021].

[131] ASTM D3039 / D3039M-17, Standard Test Method for Tensile Properties of Polymer Matrix Composite Materials, ASTM International, West Conshohocken, PA, 2017.

[132] Markforged, “Material Datasheet Composites,” 10 05 2019. [Online]. Available: http://static.markforged.com/downloads/composites-data-sheet.pdf. [Accessed 30 08 2019].

[133] L. Peng, J. Li, S. Y. C. Peng and F. Jiang, “The crystal-form transition behaviours and morphology changes in a polyamide 6 cyclic dimer,” *Royal Society Open Science,* vol. 5, no. 11, p. 180957, 2018.

[134] J. Thomason, “Glass fibre sizing: A review,” *Composites Part A: Applied Science and Manufacturing,* vol. 127, p. 105619, 2019.

[135] National Institute of Standards and Technology, “Silane, triethoxymethyl,” National Institute of Standards and Technology, 01 01 2020. [Online]. Available: https://webbook.nist.gov/cgi/cbook.cgi?ID=C2031676&Mask=80. [Accessed 18 08 2020].

[136] S. Arabnejad and S. Manzhos, “Defects in alpha and gamma crystallinenylon6: A computational study,” *AIP Advances,* vol. 5, p. 107123, 2015.

[137] N. Ma, W. Liu, L. Ma, S. He, H. Liu, Z. Zhang, A. Sun, M. Huang and C. Zhu, “Crystal transition and thermal behavior of Nylon 12,” *e-Polymers,* vol. 20, pp. 346-352, 2020.

[138] M. Todoki and T. Kawaguchi, “Origin of Double Melting Peaks in Drawn Nylon 6,” *JOURNAL OF POLYMER SCIENCE,* vol. 15, pp. 1067-1075, 1977.

[139] P. Frübing, A. Kremmer and R. Gerhard-Multhaupt, “Relaxation processes at the glass transition in polyamide 11:From rigidity to viscoelasticity,” *THE JOURNAL OF CHEMICAL PHYSIC,* vol. 125, p. 214701, 2006.

[140] L. Cui, P. Wang, Y. Zhang, L. Zhang, Y. Chen, L. Wang, L. Liu and X. Guo, “Combined effect of α-nucleating agents and glass fiber reinforcement on a polypropylene composite: a balanced approach,” *RSC Avances,* vol. 7, no. 68, pp. 42783-42791 , 2017.

[141] E. Klata, S. Borysiak, K. Van de Velde, J. Garbarczyk and I. Krucińska, “Crystallinity of Polyamide-6 Matrix in Glass Fibre/Polyamide-6 Composites Manufactured from Hybrid Yarns,” *Fibres and Textiles in Eastern Europe,* vol. 12, no. 3, pp. 64-69, 2004.

[142] M. Bureau, J. Denault, K. Cole and G. Enright, “The role of crystallinity and reinforcement in the mechanical behavior of polyamide-6/clay nanocomposites,” *Polymer Engineering and Science,* vol. 42, no. 9, pp. 1897-1906, 2004.

[143] M. Derradji, J. Wang and W. Liu, “5- Fiber-Reinforced Phthalonitrile Composites,” in *Phthalonitrile Resins and Composites*, Norwich, NY, William Andrew, 2018, pp. 241-294.

[144] B. Fei, “2 - High-performance fibers for textiles,” in *Engineering of High-Performance Textiles*, Sawston, UK, Woodhead Publishing, 2018, pp. 27-58.

[145] G. Ehrenstein and R. P. Theriault, Polymeric materials : structure, properties, applications, Munich: Hanser, 2001.

[146] T. Fornes and D. Paul, “Crystallization behavior of nylon 6 nanocomposites,” *Polymer,* vol. 44, no. 14, pp. 3945-3961, 2003.

[147] Y.-H. Chen, P. Ranganathan, C.-W. Chen and Y.-H. Lee, “Effect of Bis (2-Aminoethyl) Adipamide/Adipic Acid Segment on Polyamide 6: Crystallization Kinetics Study,” *Polymers,* vol. 12, no. 5, p. 1067, 2020.

[148] Y. Liu, L. Cui, F. Guan, Y. Gao, N. E. Hedin, L. Zhu and H. Fong, “Crystalline Morphology and Polymorphic Phase Transitions in Electrospun Nylon 6 Nanofibers,” *Macromolecules,* vol. 40, no. 17, pp. 6283-6290, 2008.

[149] R. Brill, “Behavior of polyamides on heating,” *J. Prakt. Chem.,* vol. 161, pp. 49-64, 1942.

[150] Y. Wolanov, A. Feldman, H. Harel and G. Marom, “Amorphous and crystalline phase interaction during the Brill transition in nylon 66,” *Polymer Letters,* vol. 3, no. 7, pp. 452-457, 2009.

[151] H. Guo, J. Wang, C. Zhou, W. Zhang, Z. Wang, B. Xu, J. Li, Y. Shang, J. de Claville Christiansen, D. Yu and Z. J. S. Wu, “Direct investigations of deformation and yield induced structure transitions in polyamide 6 below glass transition temperature with WAXS and SAXS,” *Polymer,* vol. 70, pp. 109-117, 2015.

[152] Y. Sato, S. Maumizu and K. Sakaue, “Evaluation of viscoelastic non-isochoric plastic behavior of PBT and PA6,” *Mech Time-Depend Mater,* 2022.

[153] N. D. Z. O. M. J. F. S. S. Dencheva, “Relationship between crystalline structure and mechanical behaviour in isotropic and oriented polyamide 6,” *Journal of Applied Polymer Science,* vol. 203, pp. 2242-2252, 2007.

[154] L. Shen, I. Y. Phang and L. Tianxi, “Nanoindentation studies on polymorphism of nylon 6,” *Polymer Testing,* vol. 25, no. 2, pp. 249-253, 2006.

[155] F. Awaja, “Autohesion of polymers,” *Polymers,* vol. 97, pp. 387-407, 2016.

[156] H. Ghayoor, S. V. Hoa and C. C. Marsden, “A micromechanical study of stress concentrations in composites,” *Composites Part B: Engineering,* vol. 132, pp. 115-124, 2018.

[157] M. Handwerker, J. Wellnitz, H. Marzbani and U. Tetzlaff, “ Pressure and heat treatment of continuous fibre reinforced thermoplastics produced by fused filament fabrication,” *Progress in Additive Manufacturing,* 2022.

[158] K. Wang, H. Long, Y. f Chen, M. Baniassadi, Y. Rao and Y. Peng, “Heat-treatment effects on dimensional stability and mechanical properties of 3D printed continuous carbon fiber-reinforced composites,” *Composites Part A,* vol. 147, p. 106460, 2021.

[159] H. Qinghao, H. Wang, F. Kunkun and Y. Lin, “3D printed continuous CF/PA6 composites: Effect of microscopic voids on mechanical performance,” *Composites Science and Technology,* vol. 191, p. 108077, 2020.

[160] C. Pascual-González, P. Martín, A. Fernándeza, A. León, C. Lopes and J. Fernández-Blázquez, “Post-processing effects on microstructure, interlaminar and thermal properties of 3D printed continuous carbon fibre composites,” *Composites Part B,* vol. 210, p. 108652, 2021.

[161] D. O. Adams and D. F. Adams, “TABBING GUIDE FOR COMPOSITE TEST SPECIMENS,” 01 10 2002. [Online]. Available: http://www.tc.faa.gov/its/worldpac/techrpt/ar02-106.pdf. [Accessed 03 08 2021].

[162] Y. Zhang, Y. Zhang, S. Liu, A. Huang, Z. Chi, J. Xu and J. Economy, “Phase stability and melting behavior of the α and γ phases of nylon 6,” *Applied Polymer Science,* vol. 120, no. 4, pp. 1885-1891, 2010.

[163] UserCom 11, METTLER TOLEDO, Greifensee, Switzerland, 2000, p.3.

[164] S. Gogolewski, K. Czerniawska and M. Gasiorek, “Effect of annealing on thermal properties and crystalline structure of polyamides.,” *Colloid and Polymer Science,* vol. 258, no. 10, pp. 1130-1136, 1980.

[165] J. Aboudi, S. Arnold and B. Bednarcyk, “Fundamentals of the Mechanics of,” in *Micromechanics of Composite Materials*, Oxford, United Kingdom, Butterworth-Heinemann, 2013.

[166] Kern GmbH, “Polyamid 6,” 01 08 2021. [Online]. Available: https://www.kern.de/de/technisches-datenblatt/polyamid-pa-6-e?n=1101_1. [Accessed 01 08 2021].

[167] Polymerservice Merseburg, “Lateral Contraction,” 01 08 2021. [Online]. Available: https://wiki.polymerservice-merseburg.de/index.php/Poissonzahl. [Accessed 01 08 2021].

[168] Swiss Composite, “Composite Material Data,” 01 08 2021. [Online]. Available: https://www.swiss-composite.ch/pdf/i-Werkstoffdaten.pdf. [Accessed 01 08 2021].

[169] M. Mehdikhani, L. Gorbatikh, I. Verpoest and S. V. Lomov, “Voids in fiber-reinforced polymer composites: A review on their formation,characteristics, and effects on mechanical performance,” *Journal of Composite Materials,* vol. 53, no. 12, pp. 1579-1669, 2018.

[170] M. Knops, Analysis of Failure in Fiber Polymer Laminates - The Theory of Alfred Puck, Berlin Heidelberg: Springer-Verlag , 2008.

[171] C. El-Mazry, M. Hassine, O. Correc and X. Colin, “Thermal oxidation kinetics of additive free polyamide 6-6,” *Polymer Degradation and Stability,* vol. 98, no. 1, pp. 22-36, 2013.

[172] X. Zhao, X. Li, L. Ye and G. Li, “Stress–Thermooxidative Aging Behavior of Polyamide 6,” *Aplied Polymer Science,* vol. 129, no. 3, pp. 1193-1201, 2013.

[173] Y. Shu, L. Ye and T. Yang, “Study on the long-term thermal-oxidative aging behavior of polyamide 6,” *Applied Polymer Science,* vol. 110, no. 2, pp. 945-957, 2008.

[174] A. Bergan, C. Dávila, F. Leone, J. Awerbuch and T.-M. Tan, “A Mode I cohesive law characterization procedure for through-the-thickness crack propagation in composite laminates,” *Composites Part B: Engineering,* vol. 94, pp. 338-349, 2016.

[175] H. Koerber, P. Kuhn, M. Ploeckl, F. Otero, P.-W. Gerbaud, R. Rolfes and P. Camanho, “Experimental characterization and constitutive modeling of the non-linear stress–strain behavior of unidirectional carbon–epoxy under high strain rate loading,” *Advanced Modeling and Simulation in Engineering Sciences,* vol. 5, no. 17, 2018.

[176] P. V. Kosmachev, V. O. Alexenko, S. A. Bochkareva and S. V. Panin, “ Deformation Behavior and Fracture Patterns of Laminated PEEK- and PI-Based Composites with Various Carbon-Fiber Reinforcement,” *Polymers,* vol. 13, no. 14, p. 2268, 2021.

[177] M. Kawai and S. Saito, “Off-axis strength differential effects in unidirectional carbon/epoxy laminates at different strain rates and predictions of associated failure envelopes,” *Composites Part A: Applied Science and Manufacturing,* vol. 40, no. 10, pp. 1632-1649, 2009.

[178] C. Lüders, “ Nonlinear-Elastic Orthotropic Material Modeling of an Epoxy-Based Polymer for Predicting the Material Behavior of Transversely Loaded Fiber-Reinforced Composites,” *Journal of Composite Sciences,* vol. 4, no. 2, p. 46, 2020.

[179] A. Puck, “Zur Beanspruchung und Verformung von GFK-Mehrschichtverbund-Bauelementen,” *Kunststoffe,* vol. 12, pp. 965-973, 1967.

[180] M. Handwerker, J. Wellnitz and H. Marzbani, “Mikromechanische Betrachtung von additiv hergestellten endlosfaserverstärkten Thermoplasten [Micromechanical investigation of additively manufactured thermoplastics],” in *10. Landshuter Leichtbau-Colloquium (2021)*, Landshut, 2021.

[181] P. Wriggers and M. Hain, “Micro-Meso-Macro Modelling of Composite Materials,” in *Computational Plasticity*, Berlin Heidelberg, Springer, 2007, pp. 105-122.

[182] “Nanoscale in situ observations of crack initiation and propagation in carbon fiber/epoxy composites using synchrotron radiation X-ray computed tomography,” *Composites Science and Technology,* vol. 197, no. 8, p. 108244, 2020.

[183] X. Lu, X. Guo and T. Tay, “From diffuse damage to discrete crack: A coupled failure model for multi-stage progressive damage of composites,” *Computer Methods in Applied Mechanics and Engineering,* vol. 379, p. 113760, 2021.

[184] V.-D. Nguyen, L. Wu and L. Noels, “A micro-mechanical model of reinforced polymer failure with length scale effects and predictive capabilities. Validation on carbon fiber reinforced high-crosslinked RTM6 epoxy resin,” *Mechanics of Materials,* vol. 133, pp. 193-213, 2019.

[185] M. Okereke, A. Akpoyomare and M. Bingley, “Virtual testing of advanced composites, cellular materials and biomaterials: A review,” *Composites Part B: Engineering,* vol. 60, pp. 637-662, 2014.

[186] C. González and J. LLorca, “Virtual fracture testing of composites: A computational micromechanics approach,” *Engineering Fracture Mechanics,* vol. 74, no. 7, pp. 1126-1138, 2007.

[187] D. Mortell, D. Tanner and C. McCarthy, “A virtual experimental approach to microscale composites testing,” *Composite Structures,* vol. 171, pp. 1-9, 2017.

[188] D. Pulungan, G. Lubineau, A. Yudhanto, R. Yaldiz and W. Schijve, “Identifying design parameters controlling damage behaviors of continuous fiber-reinforced

thermoplastic composites using micromechanics as a virtual testing tool," *International Journal of Solids and Structures,* vol. 117, pp. 177-190, 2017.

[189] P. Liu and X. Li, "Explicit finite element analysis of failure behaviors of thermoplastic composites under transverse tension and shear," *Composite Structures,* vol. 192, pp. 131-142, 2018.

[190] T. A. Dutra, R. T. Ferreira and H. B. Resende, "Mechanism based failure of 3D-printed continuous carbon fiber reinforced thermoplastic composites," *Composites Science and Technology,* vol. 213, p. 108962, 2021.

[191] N. Schramm, J. X. Teltschik and L. Kroll, "model, Analytical modelling of continuous fibre-reinforced thermoplastics' thermomechanical properties and implementation into a failure," *Technologies for Lightweight Structures,* vol. 4, no. 1, pp. 18-31, 2021.

[192] F. Naya, C. Lopes, C. González and J. LLorca, "Computational micromechanics strategies for the analysis of failure in unidirectional composites," in *Numerical Modelling of Failure in Advanced Composite Materials*, Cambridge, UK, Woodhead Publishing, 2015, pp. 411-433.

[193] M. Okereke and S. Keates, "Boundary Conditions," in *Finite Element Applications*, Basel, Switzerland, Springer International Publishing, 2018, pp. 243-298.

[194] W. Q. L. Tian, X. Chao, J. Liang and M. Fu, "Periodic boundary condition and its numerical implementation algorithm for the evaluation of effective mechanical properties of the composites with complicated micro-structures," *Composites Part B: Engineering,* vol. 162, pp. 1-10, 2019.

[195] E. Pelukhov and M.-A. Keip, "Computational homogenization of transient chemo-mechanical processes based on a variational minimization principle," *Advanced Modeling and Simulation in Engineering Sciences,* vol. 7, no. 35, 2020.

[196] A. Akpoyomare, M. Okereke and M. Bingley, "Virtual testing of composites: Imposing periodic boundary conditions on general finite element meshes," *Composite Structures,* vol. 160, pp. 983-994, 2017.

[197] J. Alsayednoor, P. Harrison and Z. Guo, “Large strain compressive response of 2-D periodic representative volume element for random foam microstructures,” *Mechanics of Materials,* vol. 66, pp. 7-20, 2014.

[198] M. Okereke and A. Akpoyomare, “A virtual framework for prediction of full-field elastic response of unidirectional composites,” *Computational Materials Science,* vol. 70, p. 82–99, 2013.

[199] D. Garoz, F. Gilabert, R. Sevenois, S. Spronk and W. V. Paepegem, “Consistent application of periodic boundary conditions in implicit and explicit finite element simulations of damage in composites,” *Composites Part B: Engineering,* vol. 168, pp. 254-266, 2019.

[200] S. Li and E. Sitnikova, “An excursion into representative volume elements and unit cells,” in *Comprehensive Composite Materials II*, Amsterdam, Elsevier, 2018, pp. 451-489.

[201] Suter Kunststoffe AG, “Faserverbund-Werkstoffdaten,” 23 12 2020. [Online]. Available: https://www.swiss-composite.ch/pdf/i-Werkstoffdaten.pdf. [Accessed 23 12 2020].

[202] D. Mounier, C. Poilâne, C. Bûcher and P. Picart, “ Evaluation of transverse elastic properties of fibers used in composite materials by laser resonant ultrasound spectroscopy,” in *Acoustics*, Nantes, France, 2012.

[203] T. Vaughan and C. McCarthy, “A micromechanical study on the effect of intra-ply properties on transverse shear fracture in fibre reinforced composites,” *Composites: Part A,* vol. 42, pp. 1217-1228, 2011.

[204] W. Lei, Y. Ismail, P. Zhu, Y. Sheng, J. Liu and D. Yang, “Computational micromechanics-based prediction of the failure of unidirectional composite lamina subjected to transverse and in-plane shear stress states,” *Journal of Composite Materials,* vol. 54, no. 24, pp. 3637-3654, 2020.

[205] J. Chen, L. Wan, Y. Ismail, J. Ye and D. Yang, “A micromechanics and machine learning coupled approach for failure prediction of unidirectional CFRP composites under triaxial loading: A preliminary study,” *Composite Structures,* vol. 267, p. 113876, 2021.

[206] A. Pegoretti, M. Fidanza, C. Migliaressi and A. DiBenedetto, “Toughness of the fiber/matrix interface in nylon-6/glass fiber composites,” *Composites Part A: Applied Science and Manufacturing,* vol. 29, no. 3, pp. 283-291, 1998.

[207] P.-Y. Le Gac, M. Arhant, m. Le Gall and P. Davies, “Yield stress changes induced by water in polyamide 6: Characterization and modeling,” *Polymer Degradation and Stability,* vol. 137, pp. 272-280, 2017.

[208] “Damage of semicrystalline polyamide 6 assessed by 3D X-ray tomography: From microstructural evolution to constitutive modeling,” *Polymer Physics,* vol. 48, p. 1516–1525, 2010.

[209] S. Felder, N. A. Vu, S. Reese and J.-W. Simon, “Experimental and Numerical Investigation of the Material Behavior of semi-crystalline Polyamide 6,” *Technische Mechanik,* vol. 40, no. 01, 2020.

[210] BASF GmbH, “Ultramid B3L - PA6-I,” 02 02 2022. [Online]. Available: https://www.campusplastics.com/material/pdf/160683?sLg=de. [Accessed 01 04 2022].

[211] AKRO-PLASTIC GmbH, “PA6 – Polyamide 6 PA6 AKROMID® B3 3 natural (5772),” AKRO-PLASTIC GmbH, 28 05 2021. [Online]. Available: https://akro-plastic.com/productfilter/pdf/details/5772/. [Accessed 01 12 2021].

[212] D. Plastics, “Nylon Extruded 6 Black,” 01 12 2021. [Online]. Available: https://www.directplastics.co.uk/pdf/datasheets/Nylon%20Extruded%206%20Black%20Data%20Sheet.pdf. [Accessed 01 12 2021].

[213] Dupont, “Zytel 7335F NC010,” 31 03 2022. [Online]. Available: https://dupont.materialdatacenter.com/gb/products/pdf/US/Zytel%C2%AE%207335F%20NC010-gb-US.pdf. [Accessed 01 04 2022].

[214] N. Selles, P. Cloetens, H. Proudhon, T. F. Morgeneyer, O. Klinkova, N. Saintier and L. Laiarinandrasana, “Voiding Mechanisms in Deformed Polyamide 6 Observed at the Nanometric Scale,” *Macromolecules,* vol. 50, no. 11, p. 4372–4383, 2017.

[215] A. Gurson, “Continuum Theory of Ductile Rupture by Void Nucleation and Growth: Part I—Yield Criteria and Flow Rules for Porous Ductile Media,” *J. Eng. Mater. Technol.,* vol. 99, no. 1, pp. 2-15, 1977.

[216] V. Tvergaard, “Influence of voids on shear band instabilities under plane strain conditions,” *International Journal of Fracture,* vol. 17, p. 389–407, 1981.

[217] A. T. V. Needleman, “An analysis of ductile rupture modes at a crack tip,” *Journal of the Mechanics and Physics of Solids,* vol. 35, no. 2, pp. 151-183, 1987.

[218] M. Jeridi, L. Laiarinandrasana and K. Saï, “Comparative study of continuum damage mechanics and Mechanics of Porous Media based on multi-mechanism model on Polyamide 6 semi-crystalline polymer,” *International Journal of Solids and Structures,* vol. 53, pp. 12-27, 2015.

[219] G. C. Ganzenmüller, T. Langhof and S. Hiermaier, “A Constant Acoustic Impedance Mount for Sheet-Type Specimens in the Tensile Split-Hopkinson Bar,” *DYMAT 2018 - 12th International Conference on the Mechanical and Physical Behaviour of Materials under Dynamic Loading ,* vol. 183, p. 02064, 2018.

[220] L. Xie, D. W. Gidley, H. A. Hristov and A. F. Yee, “Evolution of nanometer voids in polycarbonate under mechanical stress and thermal expansion using positron spectroscopy,” *Journal of Polymer Science Part B: Polymer Physics,* vol. 33, no. 1, pp. 77-84, 1995.

[221] Dassault Systèmes, “Damage evolution and element removal for ductile metals,” Dassault Systèmes, 01 01 2017. [Online]. Available: https://abaqus-docs.mit.edu/2017/English/SIMACAEMATRefMap/simamat-c-damageevolductile.htm. [Accessed 01 04 2022].

[222] E. Parodi, G. W. Peters and L. E. Govaert, “Prediction of plasticity-controlled failure in polyamide 6: Influence of temperature and relative humidity,” *Journal of Applied Polymer Science,* vol. 135, p. 45942, 2017.

[223] J. P. Manaia, F. A. Pires, A. M. de Jesus and S. Wu, “Mechanical response of three semi crystalline polymers under different stress states: Experimental investigation and modelling,” *Polymer Testing,* vol. 81, p. 106156, 2020.

[224] E. Parodi, G. W. Peters and L. E. Govaert, “Prediction of plasticity-controlled failure in polyamide 6: Influence of temperature and relative humidity,” *Applied Polymer Science,* vol. 135, no. 11, p. 45942, 2017.

[225] M. Knops, Analysis of Failure in Fiber Polymer Laminates - The Theory of Alfred Puck, Berlin Heidelberg: Springer-Verlag, 2008.

[226] A. Kaddour and M. Hinton, “Maturity of 3D Failure Criteria for Fibre-Reinforced Composites: Comparison Between Theories and Experiments: Part B of WWFE-II,” *Composite Materials,* vol. 47, pp. 925-966, 2013.

[227] A. Puck and H. Schürmann, “Failure analysis of FRP Laminates by means of physically based phenomenological models,” *Comp. Sci. and Techn.,* vol. 58, p. 1045−1067, 1998.

[228] F. Wein, "*Simulationsgestützte Untersuchung zur Anwendbarkeit additiv gefertigter Faserverbundwerkstoffe im Motorsport,*" *M.S. thesis, Technische Hochschule Ingolstadt [university of applied sciences Ingolstadt], 03.03.2022.*

[229] FORMULA STUDENT GERMANY:, “FS-Rules 2022 v1.0.,” 01 01 2022. [Online]. Available: https://www.formulastudent.de/fileadmin/user_upload/all/2022/rules/FS-Rules_2022_v1.0.pdf. [Accessed 01 02 2022].

[230] Technische Hochschule Ingolstadt, “Schanzer Racing Electric,” 01 03 2022. [Online]. Available: https://www.thi.de/studium/studentisches-leben/studentische-vereine-an-der-thi/schanzer-racing-electric-ev. [Accessed 01 03 2022].

[231] C. Wu, C. Dai, G. Fang, Y.-J. Liu and C. C. Wang, “RoboFDM: A robotic system for support-free fabrication using FDM,” in *2017 IEEE International Conference on Robotics and Automation (ICRA)*, Singapore, 2017.

[232] I. B. Ishak and P. Larochelle, “MotoMaker: a robot FDM platform for multi-plane and 3D lattice structure printing,” *Mechanics Based Design of Structures and Machines,* vol. 47, no. 6, pp. 703-720, 2019.

[233] F. Alisafaei and C.-S. Han, “Indentation Depth Dependent Mechanical Behavior in Polymers,” *Advances in Condensed Matter Physics,* p. 391579, 2015.

[234] N. Ramos, C. Mittermeier and J. Kiendl, “Experimental and numerical investigations on heat transfer in fused filament fabrication 3D-printed specimens,” *The International Journal of Advanced Manufacturing Technology,* vol. 118, pp. 1367-1381, 2022.

[235] A. A. Samy, A. Golbang, E. Harkin-Jonse, E. Archer and A. McIlhagger, “Prediction of part distortion in Fused Deposition Modelling (FDM) of semi-crystalline polymers via COMSOL: Effect of printing conditions,” *CIRP Journal of Manufacturing Science and Technology,* vol. 33, pp. 443-453, 2021.

[236] D. Muller, “The Genius of 3D Printed Rockets,” Veritasium, 12 08 2021. [Online]. Available: https://www.youtube.com/watch?v=kz165f1g8-E. [Accessed 14 05 2022].

[237] A. Puck and H. Schürmann, “Failure analysis of FRP Laminates by means of physically based phenomenological models,” *Comp. Sci. and Techn.,* vol. 62, no. 12-13, p. 1633−1662, 2002.

[238] O. Mohr, “Welche Umst¨ande bedingen die Elastizit¨atsgrenze und den Bruch eines Materials,” *Zeitschrift des VDI,* vol. 24, no. 45/46, p. 1524–1541 & 1572–1577, 1900.

[239] H. Deuschle, F. Wittel, H. Gerhard, G. Busse and B.-H. Kröplin, “Investigation of progressive failure in composites by combined simulated and experimental photoelasticity,” *Computational Materials Science,* vol. 1, no. 38, pp. 1-8, 2006.

[240] D. Huybrechts, Ein erster Beitrag zur Verifikation des wirkebenebezogenen Zwischenfaserbruchkriteriums nach Puck, Aachen: Verlag Mainz, 1996.

[241] J. Kopp, Zur Spannungs- und Festigkeitsanalyse für unidirektionalen Faserverbundkunststoff, Aachen: RWTH Aachen, 1999.

[242] R. Cuntze, J. Kopp and D. Huybrechts, Neue Bruchkriterien und Festigkeitsnachweis für unidirektionalen Faserkunststoffverbund unter mehrachsiger Beanspruchung - Modelle und Experimente, Düsseldorf: VDI-Verlag, 1997.

[243] H. M. Deuschle and B.-H. Kröplin, “Finite element implementation of Puck’s failure theory for fibre-reinforced composites under three-dimensional stress,” *Journal of Composite Materials,* vol. 46, no. 19-20, pp. 2485-2513, 2012.

[244] K. Kodagali, *Progressive Failure Analysis of Composite Materials using the Puck Failure Criteria (Doctoral dissertation),* University of South Carolina, 2017.

[245] VDI-Gesellschaft Materials Engineering, *Development of Fibre-Reinforced Plastics components - Analysis,* Berlin: Beuth, 2006-09.

[246] M. H. Deuschle, *3D failure analysis of UD fibre reinforced composites: Puck's failure theory within FEA [Dissertation],* Stuttgart: Universität Stuttgart, 2010.

[247] S. Kuba, *"Implementation of Puck´s failure criterion in FEA," Wissenschaftliches Arbeiten [scientific working], Technische Hochschule Ingolstadt [university of applied sciences Ingolstadt], 06.01.2022.*

[248] A. S. Kaddour and M. Hinton, “Input data for test cases used in benchmarking triaxial failure theories of composites,” *Journal of Composite Materials,* vol. 46, pp. 2295-2312, 2012.

Appendix

Appendix A: Puck's 3D Failure Criterion

Relevance of failure criteria

Contrary to the micromechanical analysis, failure criteria are used to predict failure on the meso/macro level. This approach is necessary, as it is not possible to simulate entire parts on a micro level with the computational power that is available today. The idea behind any failure criterion is to formulate a failure hypothesis that can predict all failure states based on a limited number of know fracture states and auxiliary parameters. In the simplest case, the failure criterion only requires the known fracture states due to fibre parallel/perpendicular tension and compression ($R^t_{\parallel}$, $R^c_{\parallel}$, $R^t_{\perp}$ and $R^c_{\perp}$) as well as in plane and out-of-plane shear ($R_{\parallel\perp}$ and $R_{\perp\perp}$). A failure criterion is formulated as a function of the stresses and strengths, that predicts failure if a certain threshold is exceeded (in most cases "1"). An output lower than "1", doesn't necessarily indicate, how much headroom there is. For this purpose, the stretch factor f_S was introduced. It is the factor, by which number every stress must be multiplied, for failure to occur. The stress exposure f_E, shown in Figure 80, is the reciprocal of f_S and increases linearly with the applied stresses. It indicates the risk of failure.

<Image removed due to copyright restrictions>

Figure 80: Definition of the stress exposure fE [225].

Fibre failure

Per definition, fibre failure occurs, when all the fibres rupture in a ply either due to tensile or compressive stresses (σ1) acting parallel to the fibres. One of the premises of any failure theory, is that a ply is a homogenous material. Therefore, the stresses acting on the ply is used as the failure stress and not the stress acting on the fibres. The simplest formulation for the stress exposure is:

$$f_{E,FF} = \frac{\sigma_1}{R_{\parallel}^{t}}, for\ \sigma_1 > 0$$
$$f_{E,FF} = \frac{\sigma_1}{-R_{\parallel}^{c}}, for\ \sigma_1 < 0 \quad (8.1)$$

What this simple equation does not account for, is the effect of stresses acting perpendicular to the fibres (σ_2, σ_3). Due to the Poisson's effect these stresses too influence fibre fracture. Near the fibre matrix interface, this effect is amplified by the inhomogeneous stress distribution within the matrix.

Therefore, Puck formulated the following definition for fibre failure: Fibre fracture under combined stresses will occur, when the stress in the fibres σ_{1f} is equal to the stresses causing fibre failure under uniaxial tension or compression [13] [227] [237]. The starting point for the formulation of the corresponding failure criterion is the strain in the fibre:

$$\varepsilon_{1f} = \frac{\sigma_{1f}}{E_{\parallel f}} - \frac{\upsilon_{\parallel\perp f}}{E_{\perp f}} * m_{\sigma f} * (\sigma_2 + \sigma_3) \quad (8.2)$$

The magnification factor $m_{\sigma f}$ accounts for the formerly mentioned inhomogeneous stress distribution. The first index of the Poisson's ratio states the direction of the strain caused by the stress acting in the direction of the second index. A subscript "f" refers to the fibre properties. Since the fibres are connected to the matrix, $\varepsilon_{1f} = \varepsilon_1$. With the relationship $\nu_{\parallel\perp f}/E_{\perp f} = \nu_{\parallel\perp f}/E_{\parallel f}$, the fibre stress is calculated as:

$$\sigma_{1f} = E_{\parallel f} * \varepsilon_1 + \nu_{\perp\parallel f} * m_{\sigma f} * (\sigma_2 + \sigma_3) \quad (8.3)$$

This equation serves as the basis for the new fracture condition. To formulate it, the strain e1 is replaced by the elastic law of the unidirectional ply:

$$\varepsilon_1 = \frac{\sigma_1}{E_{\parallel}} - \frac{\upsilon_{\parallel\perp}}{E_{\parallel}} * (\sigma_2 + \sigma_3) \quad (8.4)$$

Then the fibre stress σ_{1f} is replaced by the fracture resistance of the fibre, with $e_{\parallel}$ being the fracture strain from uniaxial σ_1 stress for the fibre and the ply:

$$R_{\parallel f} = E_{\parallel f} * e_{\parallel} \; and \; R_{\parallel} = E_{\parallel} * e_{\parallel} \tag{8.5}$$

With these three equations, the fracture condition can be written as:

$$\frac{1}{\pm R_{\parallel}^{t,c}} * \left[\sigma_1 - \left(\nu_{\perp\parallel} - \nu_{\perp\parallel f} * m_{\sigma f} * \frac{E_{\parallel}}{E_{\parallel} f}\right) * (\sigma_2 + \sigma_3)\right] = 1 \tag{8.6}$$

Since this is a first order equation, the stress exposure can directly be extracted:

$$f_{E,FF} = \frac{1}{\pm R_{\parallel}^{t,c}} * \left[\sigma_1 - \left(\nu_{\perp\parallel} - \nu_{\perp\parallel f} * m_{\sigma f} * \frac{E_{\parallel}}{E_{\parallel} f}\right) * (\sigma_2 + \sigma_3)\right] \tag{8.7}$$

Inter fibre failure

While the fibre failure aspect of Pucks failure assumption is straight forward, the explanation behind the inter-fibre fracture is a lot more complicated. Since Puck's publications contain an in-depth explanation, only a short summary will be given here.

Action-plane failure hypothesis

Puck's failure criterion is based on Mohr's failure theory for brittle isotropic materials, which states: "The fracture limit of a material is determined by the stresses on the fracture plane" [238].

For transverse isotropic materials regarding IFF, three stresses are of importance: The fibre perpendicular stress $\sigma_{\perp}$, the in-plane shear stress $\tau_{\parallel\perp}$ and the through-thickness shear stress $\tau_{\perp\perp}$. In Puck's approach, the stresses acting on a common action plane are related to the strengths of the action plane, which are defined as the amount of exclusive stressing of $\sigma_{\perp}$, $\tau_{\parallel\perp}$ and $\tau_{\perp\perp}$ that plane can withstand. As will be shown later these strengths are not the same as the commonly used strengths and are therefore referred to as the "fracture resistance of the action plane" which are indicated by superscript "A" and defined as [225]:

A fracture resistance of the action plane is the resistance (expressed in the dimension of a stress) by which an action plane resists its own fracture by a single stressing ($\sigma_{\perp}$, $\tau_{\parallel\perp}$ or $\tau_{\perp\perp}$) acting in the action plane under consideration.

When determining the fracture resistance of an action plane, the following question must be answered:

“To which value must the stress $\sigma_{\perp}$ be increased to cause failure **on its** action plane?”

Not:

“To which value must the stress $\sigma_{\perp}$ be increased to cause failure **on any** action plane?”

This is the reason, why it must be determined, if the fracture has occurred on the action plane of the acting force, when determining the material strength. One of the important parts of Puck’s hypothesis is, that there is a maximum of three combined stresses acting on an action plane, which results in three different fracture resistances:

$R^{A}_{\perp}{}^{t}$ Resistance of the action plane against its fracture due to transverse tensile stressing $\sigma_{\perp}{}^{t}$ acting in that plane

$R^{A}_{\perp\perp}$ Resistance of the action plane against its fracture due to transverse tensile stressing $\tau_{\perp\perp}$ acting in that plane

$R^{A}_{\perp\parallel}$ Resistance of the action plane against its fracture due to transverse tensile stressing $\tau_{\perp\parallel}$ acting in that plane

Figure 81 shows that for the transverse tension, the fracture plane equals the action plane of the force, which means that the fracture resistance $R^{A}_{\perp}{}^{t}$ equals the material strength $R^{t}_{\perp}$. A composite will only show this behaviour, if it is intrinsically brittle. The same logic applies to the longitudinal shear stress, which leads to the conclusion, that the fracture resistance $R^{A}_{\perp\parallel}$ equals $R_{\perp\parallel}$. It is worth mentioning, that shear stresses always come in pairs. But since the shear strength $R^{A}_{\parallel\perp}$ is significantly higher as a result of the fibre reinforcement (the fibres would have to be sheared off), this value can be neglected.

As it also can be seen in Figure 81, contrary to those two cases, a $\tau_{\perp\perp}$ will not cause a failure on its action plane but fractures at a 45° angle due to a $\sigma_{\perp}{}^{t}$ stress. This means, that the fracture resistance against transverse tension $R^{A}_{\perp}{}^{t}$ is smaller than the fracture resistance against transverse shear $R^{A}_{\perp\perp}$. This also means, that $R^{A}_{\perp\perp}$ cannot be directly experimentally determined. It can however be calculated from a transverse compression test, where a mixed stress state of transverse shear and transverse compression occurs. The transverse

compression causes friction which makes it also impossible to directly measure $R^A_{\perp\perp}$ from that experiment. If that friction is subtracted $R^A_{\perp\perp}$ can be calculated.

<Image removed due to copyright restrictions>

Figure 81: Fracture planes (grey) for different stresses [225].

As mentioned before, on planes parallel to the fibre only three stresses can occur, namely the normal stress σ_n and the two shear stresses τ_{n1} and τ_{nt} (comp. Figure 82). The three action plane stresses are calculated from the applied stresses as a function of the angle θ:

$$\sigma_n(\theta) = \sigma_2 * \cos(\theta)^2 + \sigma_3 * \cos(\theta)^2 + 2 * \tau_{23} * \sin(\theta) * \cos(\theta) \quad (8.8)$$

$$\tau_{nt}(\theta) = -\sigma_2 * \sin(\theta) * \cos(\theta) + \sigma_2 * \sin(\theta) * \cos(\theta) + \tau_{23} * (\cos(\theta)^2 - \sin(\theta)^2) \quad (8.9)$$

$$\tau_{n1}(\theta) = \tau_{31} * \sin(\theta) + \tau_{21} * \cos(\theta) \quad (8.10)$$

Even though, the two shear stresses τ_{n1} and τ_{nt} behave differently on a micro-mechanical level, if needed they can be summarized to form the stress $\tau_{n\psi}$:

$$\tau_{n\Psi}(\theta) = \sqrt{\tau_{nt}^2(\theta) + \tau_{n1}^2(\theta)} \quad (8.11)$$

The angle, at which fracture occurs is labelled with a subscript “fp”, which stands for fracture plane: θ_{fp}.

Figure 82: Fracture angle and fracture plane stresses according to Puck [225].

Mathematical formulation

To make the following elaborations easier to understand, the result will be forestalled. Figure 83 shows the master fracture body (MFB). Every combination of stresses within this body do not cause failure.

Figure 83: Master fracture body displayed in the action-plane stress state [225].

Due to different failure processes, the MFB consist of two halves. One for compressive σ_n and one for a tensile σ_n. At $\sigma_n = 0$ the MFB intersects the τ_{nt} axis at $\pm R^A_{\perp\perp}$ and the τ_{n1} axis at $\pm R^A_{\perp\parallel}$. The σ_n tensile stress is limited by $R^A{}_\perp{}^t$.

Puck assumed, that the cross-section at $\sigma_n = 0$ can most likely be described by an elliptical function, since both shear stresses are acting on a plane, that is parallel to the fibres and thus it can be assumed, that $R^A_{\perp\parallel}$ and $R^A_{\perp\perp}$ are similar:

$$\left(\frac{\tau_{n\psi}}{R^A_{\perp\Psi}}\right)^2 = \left(\frac{\tau_{nt}}{R^A_{\perp\perp}}\right)^2 + \left(\frac{\tau_{nt}}{R^A_{\perp\parallel}}\right)^2 = 1 \; at \; \sigma_n = 0 \tag{8.12}$$

The factor $R^A_{\perp\Psi}$ is defined as the fracture resistance against the shear stress $\tau_{n\Psi}$. By inserting the relations $\tau_{n1} = \tau_{n\Psi} * \sin(\Psi)$ and $= \tau_{nt} * \cos(\Psi)$ in equation (8.12) and considering the fact, that σ_n has no influence on the angle Ψ, it can also be written as:

$$R^A_{\perp\Psi} = \left[\left(\frac{\cos(\Psi)}{R^A_{\perp\perp}}\right)^2 + \left(\frac{\sin(\Psi)}{R^A_{\perp\parallel}}\right)^2\right]^{-\frac{1}{2}} \tag{8.13}$$

Even though $R^A_{\perp\Psi}$ (Ψ, $R^A_{\perp\parallel}$, $R^A_{\perp\perp}$) is the correct expression, it will only be referred to as $R^A_{\perp\Psi}$.

As a next step, a plane stress state is assumed (σ_2, τ_{21}). If the fracture plane, is the same as the action plane of the acting stresses ($\theta_{fp} = 0°$), $\sigma_n = \sigma_2$, $\tau_{n1} = \tau_{21}$ and $\tau_{nt} = 0$. This is the case, when $\sigma_2 > -0{,}4 * R^c_\perp$. All the resulting fractures for this case, which can easily be experimentally determined, will form a longitudinal hull line in the σ_n, τ_{n1} plane. For $\sigma_n > 0$, Puck decided to model the fracture curve as part of an ellipse that intersects the σ_n axis perpendicularly at $R^A_\perp{}^t$ and the τ_{n1} axis at $R^A_{\perp\parallel}$ with a slope.

Puck further assumed, that all other longitudinal sections can be described in a similar manner. By forming the resulting shear stress as described in equation (8.11) and based on Mohr's fracture envelope, the fracture condition was formulated as:

$$\left(\frac{\tau_{n\Psi}}{R^A_{\perp\Psi}}\right)^2 + c_1 * \frac{\sigma_n}{R^{At}_\perp} + c_2 * \left(\frac{\sigma_n}{R^{At}_\perp}\right)^2 = 1, for \; \sigma_n \geq 0 \tag{8.14}$$

With the help of the boundary condition $\sigma_n = R^{A}{}_{\perp}{}^{t}$ for $\tau_{n\Psi} = 0$ (pure transverse tension), the following relation between c_1 and c_2 can be derived:

$$c_1 + c_2 = 1 \tag{8.15}$$

Furthermore, the inclination at the point $\sigma_n = 0$ is defined as:

$$\left(\frac{\partial \tau_{n\Psi}}{\partial \sigma_n}\right)_{\sigma_n=0} = -p^t_{\perp\Psi} \tag{8.16}$$

By implicitly differentiating the fracture condition at the point ($\sigma_n = 0$, $\tau_{n\Psi} = R^{A}{}_{\perp\Psi}$), the constant c_1 can be determined:

$$\frac{2}{R^A_{\perp\Psi}}\left(\frac{\partial \tau_{n\Psi}}{\partial \sigma_n}\right)_{\sigma_n=0} + \frac{c_1}{R^{At}_{\perp}} = 0 \tag{8.17}$$

This results in the following fracture condition:

$$\left(\frac{\tau_{n\Psi}}{R^A_{\perp\Psi}}\right)^2 + 2 * \frac{p^t_{\perp\Psi} * \sigma_n}{R^A_{\perp\Psi}} + (1 - 2 * \frac{p^t_{\perp\Psi} * R^{At}_{\perp}}{R^A_{\perp\Psi}}) * \left(\frac{\sigma_n}{R^{At}_{\perp}}\right)^2 = 1, for\ \sigma_n \geq 0 \tag{8.18}$$

For $\sigma_n < 0$ a parabolic function is chosen. This accounts for the fact, that the effect of a compressive σ_n increasing the shear strength, reduces as σ_n becomes smaller. But it never intersects with the σ_n axis, which is representing the fact, that a compressive σ_2 stress, will never lead to a fracture on its own action plane. That is why the MFB is open on the negative σ_n axis. The function to describe the parabolic fracture curve is:

$$\left(\frac{\tau_{n\Psi}}{R^A_{\perp\Psi}}\right)^2 + c * \sigma_n = 1, \qquad for\ \sigma_n < 0 \tag{8.19}$$

As with the tensile case, a slope parameter at $\sigma_n = 0$ is defined:

$$\left(\frac{\partial \tau_{n\Psi}}{\partial \sigma_n}\right)_{\sigma_n=0} = -p^c_{\perp\Psi} \tag{8.20}$$

By differentiating equation (8.19) at the point ($\sigma_n = 0$, $\tau_{n\Psi} = 0$), the parameter c can be determined:

$$c = \frac{2 * \ p^c_{\perp\Psi}}{R^A_{\perp\Psi}} \tag{8.21}$$

Which results in the fracture condition for compressive σ_n:

$$\left(\frac{\tau_{n\Psi}}{R^A_{\perp\Psi}}\right)^2 + \frac{2 * \ p^c_{\perp\Psi}}{R^A_{\perp\Psi}} * \sigma_n = 1, \qquad for\ \sigma_n < 0 \tag{8.22}$$

At this point, the unknown parameters are $p^t_{\perp\Psi}$ and $p^c_{\perp\Psi}$. As previously mentioned, for some (σ_n, τ_{n1}) stress states, where $\tau_{nt} = 0$ ($\Psi = 90°$) the fracture curve can be experimentally determined. In that case, the parameters are referred to as $p^t_{\perp\parallel}$ and $p^c_{\perp\parallel}$. For conventional thermosetting fibre reinforced plastics, the values vary between 0.25 and 0.35.

Contrary to those parameters, the inclination parameters at $\Psi = 0°$, referred to as $p^t_{\perp\perp}$ and $p^c_{\perp\perp}$, cannot be experimentally determined. By conducting a pure transverse compression experiment and measuring the fracture angle, the parameter $p^c_{\perp\perp}$ can however be approximated with:

$$p^c_{\perp\perp} = \frac{1}{\cos\left(\theta_{fr}\right)^2} - 1 \tag{8.23}$$

Puck has also given various recommendations for different materials, ranging from 0.20 to 0.30. To achieve a continuous surface of the MFB, an interpolation equation is formulated, for all sections between $\Psi = 0°$ and $\Psi = 90°$:

$$\frac{p_{\perp\Psi}^{t,c}}{R_{\perp\Psi}^{A}} = \frac{p_{\perp\perp}^{t,c}}{R_{\perp\perp}^{A}} * \cos(\Psi)^2 + \frac{p_{\perp\parallel}^{t,c}}{R_{\perp\parallel}^{A}} * \cos(\Psi)^2 \tag{8.24}$$

with

$$\cos(\Psi)^2 = \frac{\tau_{nt}^2}{\tau_{nt}^2 + \tau_{n1}^2} \; and \; \sin(\Psi)^2 = \frac{\tau_{n1}^2}{\tau_{nt}^2 + \tau_{n1}^2} \tag{8.25}$$

With the help of Mohr's circle for uniaxial compression the equation for the parameter $R^A_{\perp\perp}$ can be derived:

$$R_{\perp\perp}^{A} = \frac{R_{\perp}^{c}}{2 * (1 + p_{\perp\perp}^{c})} \tag{8.26}$$

With these equations, Puck's failure criterion is now complete. If the stresses σ_n and $\tau_{n\Psi}$ lead to a number greater than one, the ply will experience IFF. A number lower than one, means no IFF. However, the number does not represent the stress exposure, because it contains quadratic terms. This can be resolved, by dividing all linear stress terms (L) by f_E and all quadratic stress terms (Q) by f_E^2, which leads to the following general solution:

$$f_E = \frac{1}{2} * \left(\Sigma L + \sqrt{(\Sigma L)^2 + 4 * \Sigma Q}\right) \tag{8.27}$$

By applying this to the fracture conditions in equations and the stress exposure for Puck's IFF criterion results.

For $\sigma_n \geq 0$:

$$f_{E,IFF}(\theta) = \sqrt{[\left(\frac{1}{R_{\perp}^{t}} - \frac{p_{\perp\Psi}^{t}}{R_{\perp\Psi}^{A}}\right) * \sigma_n(\theta)]^2 + (\frac{\tau_{nt}(\theta)}{R_{\perp\perp}^{A}})^2 + (\frac{\tau_{n1}(\theta)}{R_{\perp\parallel}})^2} + \frac{p_{\perp\Psi}^{t}}{R_{\perp\Psi}^{A}} * \sigma_n(\theta) \tag{8.28}$$

and $\sigma_n < 0$:

$$f_{E,IFF}(\theta) = \sqrt{(\frac{\tau_{nt}(\theta)}{R^A_{\perp\perp}})^2 + (\frac{\tau_{n1}(\theta)}{R_{\perp\parallel}})^2 + (\frac{p^c_{\perp\Psi}}{R^A_{\perp\Psi}} * \sigma_n(\theta))^2} + \frac{p^c_{\perp\Psi}}{R^A_{\perp\Psi}} * \sigma_n(\theta) \quad (8.29)$$

The fracture angle is determined, by finding the maximum value for $f_{E,IFF}$. The subscript "IFF" is used, to differentiate it from the fibre failure criterion.

For a two-dimensional stress state (σ_2, τ_{12}), these equations have an analytical solution, depending on the acting stresses:

Mode A ($\theta_{fp} = 0°$):

$$f_{E,IFF} = \sqrt{[\left(\frac{1}{R^t_\perp} - \frac{p^t_{\perp\parallel}}{R_{\perp\parallel}}\right) * \sigma_2]^2 + (\frac{\tau_{21}}{R_{\perp\parallel}})^2} + \frac{p^t_{\perp\parallel}}{R_{\perp\parallel}} * \sigma_2, for\ \sigma_2 \geq 0 \quad (8.30)$$

Mode B ($\theta_{fp} = 0°$):

$$f_{E,IFF} = \sqrt{(\frac{p^c_{\perp\parallel}}{R_{\perp\parallel}} * \sigma_2)^2 + (\frac{\tau_{21}}{R_{\perp\parallel}})^2} + \frac{p^c_{\perp\parallel}}{R_{\perp\parallel}} * \sigma_2, for\ \sigma_2 < 0\ and\ |\frac{\sigma_2}{\tau_{21}}| \leq |\frac{R^A_{\perp\perp}}{\tau_{21,c}}| \quad (8.31)$$

Mode C ($\theta_{fp} \neq 0°$):

$$f_{E,IFF} = \left[\left(\frac{\tau_{21}}{2 * (1 + p^c_{\perp\perp}) * R_{\perp\parallel}}\right)^2 + \left(\frac{\sigma_2}{R^c_\perp}\right)^2\right] * \frac{R^c_\perp}{-\sigma_2}, for\ \sigma_2 < 0\ and\ \left|\frac{\sigma_2}{\tau_{21}}\right| > |\frac{R^A_{\perp\perp}}{\tau_{21,c}}| \quad (8.32)$$

$$\cos(\theta_{fp}) = \sqrt{\frac{1}{2 * (1 + p^c_{\perp\perp})} * [(\frac{R^A_{\perp\perp} * \tau_{21}}{R_{\perp\parallel} * \sigma_2})^2 + 1]} \quad (8.33)$$

Mode B transitions to Mode C at the point:

$$\sigma_2 = -R^A_{\perp\perp}, \tau_{21,c} = R_{\perp\parallel} * \sqrt{1 + p^c_{\perp\perp}} \quad (8.34)$$

Accounting for fibre-parallel stress

Since Puck's theory is based on Mohr's failure hypothesis, stresses acting in fibre direction (σ_1) should not have an influence on the IFF, since they don't act on a plane, that is parallel to the fibres. This means the stresses σ_n and $\tau_{n\psi}$ are independent of σ_1. But due do micromechanical effects, there is a measurable influence that requires correction. Experiments have shown, that fibre failure does not occur simultaneously for all fibres, but individual fibres or fibre bundles rupture or kink prematurely [239]. This causes debonding between the fibres and the matrix and micro cracks which increase the risk of IFF. It is assumed, that the weakening effects all fracture modes equally, therefore the fracture angle can be calculated as written above, but the sustainable stress exposure will be lower. For this purpose, a weakening factor η_{W1} is introduced. As can be seen in Figure 84, a progressive influence of σ_1 can be observed [227] [13]. Therefore, Puck decided to model the fracture curve as a section of an ellipse:

$$\eta_{w1} = \frac{c * (a\sqrt{c^2 * (a^2 - s^2) + 1} + s)}{(c * a)^2 + 1}, with\ c = \frac{f_{E,IFF}}{f_{E,FF}}\ and\ a = \frac{1 - s}{\sqrt{1 - m^2}} \quad (8.35)$$

And the reduced stress exposure $f_{E1,IFF}$ is:

$$f_{E1,IFF} = \frac{f_{E,IFF}}{\eta_{w1}} \quad (8.36)$$

The parameters m and s can be chosen between 0 and 1 and are be used to adjust the influence according to experimental data, with m representing the minimum value η_{W1} can reach and s determining the starting point of the deterioration. Per definition, the weakening factor is valid in the following interval:

$$\frac{1}{s} \geq \frac{f_{E,IFF}}{f_{E,FF}} \geq m \quad (8.37)$$

Outside this interval, either no damage to the matrix is caused by σ_1 or the fibre failure is reached before inter-fibre failure is caused.

<Image removed due to copyright restrictions>

Figure 84: Influence of σ_1 on the IFF [225].

Experimental confirmation and parameter acquisition

Over the years different experimental approaches were made to conform Pucks failure theory and to acquire the calibration parameters. This section contains a brief overview [225]. A three-point bending beam consisting of three layers can be used to test different stress states. To achieve a homogenous stress, a thin 90° layer is embedded in two thick 0° layers. Depending on the position of the 90°-layer, different fracture modes can be observed. The shortcoming of this setup is the small test zone that is limited by the layer thickness [240]. By embedding a circular specimen between two gears, that can be used to introduce torque, shear stresses can be tested. Depending on the fibre angle of the specimen, τ_{32} and/or τ_{31} shear stresses occur [241]. The simplest way to determine fracture curve for plane stress combinations, is to use a torsion-tension-compression machine. This machine can simultaneously apply torque and compression/tension to tubular test tokens [242]. Another possible method to produce these stress combinations is to put a test token between two wedges and then apply pressure. The angle of the wedges determines the prevalent stress state. An optimized version of this approach is to include the wedges in the test token

geometry. However, this requires special tools and mechanical treatment [241]. When a pure transverse uniaxial compression stress is acting, Puck predicts failure due to a shear stress. Since both the shear stress and the compressive stress have their peak value at 45°, the compressive stress impedes fracture. At a slightly offset angle, the normal stress is greatly reduced and therefore fracture should occur at a greater angle. For carbon fibre reinforced thermosetting test tokens, an angle of 54° +/- 3° can be observed, which is the same as for cast iron. This test is a good way of verifying whether the composite material is intrinsically brittle or not

Modelling the gradual failure process

In the context of post failure analysis, it is important to note that Puck´s failure criterion is used to predict macroscopic failure over an entire ply. In the case of a laminate the failure of a single or more laminae are not equivalent with the complete disintegration of the laminate. After the point of the first lamina failure, the so-called initial failure stress, a highly nonlinear damage evolution starts in form of a growing crack density. To account for these cracks in a smeared way the stiffness of the respective lamina is reduced. This process is called degradation and resumes until the last lamina in the laminate reaches its failure condition. This state of stress is then called final failure stress which is the highest stress the respective laminate can bear [243].

For the gradual failure process, it is being differentiated between failure mode a and failure modes b and c. The former mode only occurs when a tensile stress is acting on the fracture plane. That means, the crack is being pulled open and there is no contact between the crack surfaces. The latter two on the other hand the crack surfaces are being pushed together, which means that friction occurs, and the material is weakened a lot less then for mode A cracks. Depending on the laminate the load can be increased after the initial failure stress if the load can be redistributed from the degrading lamina to other layers with higher load capacities. This behaviour is excluded in cases where any load has to be transferred through the thickness of the laminate or where the whole laminate is experiencing the same stress exposure. Since no load can be transferred to neighbouring laminae a sudden failure of the laminate occurs [243].

For the sake of simplicity and due to the lack of advanced proposals of laminate behaviour after IFF occurs the degradation process is ruled by the assumption

$$f_{E,IFF} = 1 = constant \tag{8.38}$$

This requirement is met by the successive reduction of the lamina´s stiffnesses as soon as a load results in a stress exposure greater than one. For a given state of strain a reduced stiffness lowers the stresses and therefore the stress exposure. This process is resumed until the degradation δ is sufficient for leading to a stress exposure of the value 1. Experimental work revealed that the normal stiffness is affected more strongly by a growing crack density than the shear stiffness. This is taken into account by reducing the degradation of the shear modulus to 0.6 times compared to the degradation of the normal modulus. The resulting degradation rule is defined as

$$E_{i,deg} = E_i \cdot (1 - \delta) \tag{8.39}$$

$$G_{ij,deg} = G_{ij} \cdot (1 - 0.6 \cdot \delta) \tag{8.40}$$

The degradation value $\delta = [0; 1]$ represents the state of degradation, where $\delta = 0$ is the undamaged material state. This degradation process is only valid in cases where $\sigma_n > 0$ acts on the fracture plane which corresponds to Mode A. As already mentioned in the case of $\sigma_n < 0$ the cracks surfaces are pushed together which results in unchanged stiffnesses [243].

Appendix B: Implementation of Pucks failure criterion

The previously presented equations were implemented in Abaqus as a user-defined material description (UMAT), which allows for a degradation of the stiffness parameters. The UMAT subroutine used in this work was based on the publications of Puck [13], Puck and Schürmann [227], Knops [225], Kodagali [244], Deutschle [243] and the VDI 2014 standard [245]. Quasi-static loading was assumed and therefore an implicit solver was used. Detailed investigations made by Deuschle show the deviation of FEA results depending on the used elements and laminate discretisation compared to analytical solutions [246]. The study has shown, that a denser and higher-order discretisation generally leads to more accurate results along with increasing computational effort. Regarding the stress-based failure prediction of Puck´s failure criterion Deuschle revealed, that a layer-wise discretisation with one linear solid element per lamina is sufficient. This recommend modelling approach was chosen for this study. Figure 85 illustrates the workflow of the subroutine with its inputs and output parameters. The subroutine is provided with the strain at the beginning of the increment, the guessed incremental strain for the current increment and the degradation variables from the previous timestep in form of state variables. If a degradation process was carried out at the previous increment, the stiffness properties are degraded depending on the degradation values δ_i. The stresses, which are calculated based on the orthotropic material law, are used for the fracture analysis. The angle of the fracture plan θ is determined, by calculating the stress exposure for every angle $-90° \leq \theta \leq 90°$ in 1° steps. The plane with the highest stress exposure is the fracture plane. After the calculation of the FF stress exposure $f_{E,FF}$ and the IFF stress exposure $f_{E,IFF}$ the influence of the fibre parallel stress on IFF can are determined. For valid ratios of $f_{E,IFF}/f_{E,FF}$ (comp. equation (8.37)) the weakening factor η_{w1} is calculated which results in a higher $f_{E1,IFF}$. If all stress exposures are ≤ 1 the Jacobian matrix and the state variables are updated. If a stress exposure exceeds the value 1 the respective degradation rule is applied and the iterative process loops until δ_i reached a value where all stress exposures are ≤ 1. The proper implementation of the subroutine was carried out by Sebastian Kuba as a student project under my supervision [247]. For this purpose, two test cases from the world-wide failure exercises were used and compared to Puck's publications [248].

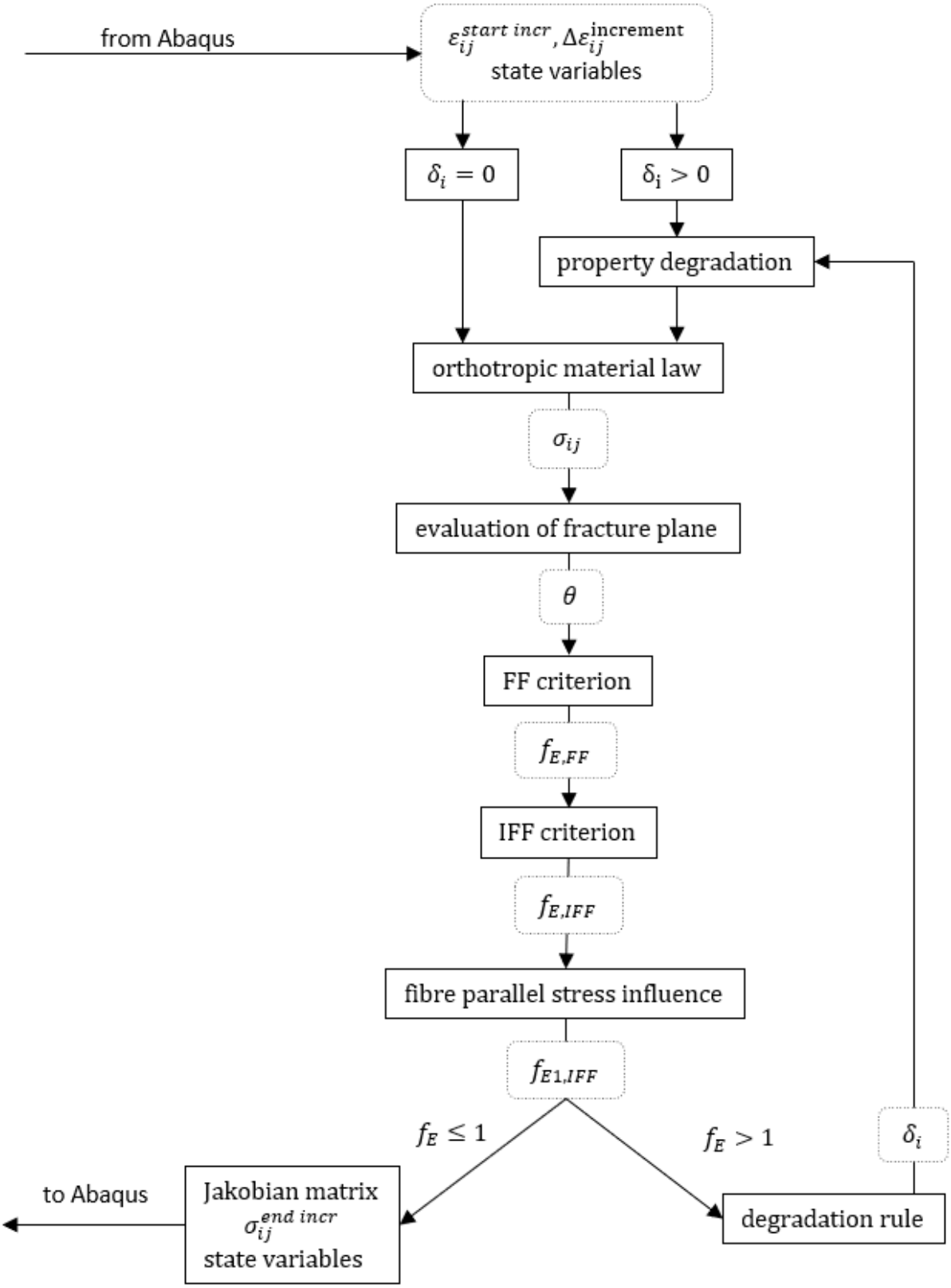

Figure 85: Workflow of user-subroutine including Puck´s failure criterion and degradation models [247].

Appendix C: CFRP properties

Table 25: Properties of the carbon fibre reinforced epoxy [248] [243]

E_1	129 GPa	Ply´s normal modulus in 1-direction
$E_2 = E_3$	5.6 GPa	Ply´s normal modulus in 2- and 3-direction
$G_{12} = G_{13}$	1.33 GPa	Ply´s shear modulus in 12 and 13 plane
$\nu_{12} = \nu_{13}$	0.318	Ply´s Poisson's ratio in 12 plane
ν_{23}	0.5	Ply´s Poisson's ration in 23 plane
E_{f1}	231 GPa	Fibre's normal modulus in 1-direction
ν_{f12}	0.2	Fibre´s Poisson's ration in 12 plane
X_t	1378 MPa	Ply´s parallel tensile strength
X_c	950 MPa	Ply´s parallel compressive strength
Y_t	40 MPa	Ply ´s transverse tensile strength
Y_c	125 MPa	Ply ´s transverse compressive strength
S_{12}	97 MPa	Ply ´s shear strength in 12 plane
$p^t_{\perp\parallel}$	0.35	Inclination parameter
$p^c_{\perp\parallel}$	0.3	Inclination parameter
$p^t_{\perp\perp}$	0.3	Inclination parameter
$p^c_{\perp\perp}$	0.3	Inclination parameter
m_σ	1.1	Stress magnification factor
m	0.5	Weakening parameter for fibre parallel stress
s	0.5	Weakening parameter for fibre parallel stress